Loughborough University

This item was submitted to Loughborough's Institutional Repository (https://dspace.lboro.ac.uk/) by the author and is made available under the following Creative Commons Licence conditions.

creative commons

COMMONS DEED

Attribution-NonCommercial-NoDerivs 2.5

You are free:

- to copy, distribute, display, and perform the work

Under the following conditions:

Attribution. You must attribute the work in the manner specified by the author or licensor.

Noncommercial. You may not use this work for commercial purposes.

No Derivative Works. You may not alter, transform, or build upon this work.

- For any reuse or distribution, you must make clear to others the license terms of this work.
- Any of these conditions can be waived if you get permission from the copyright holder.

Your fair use and other rights are in no way affected by the above.

This is a human-readable summary of the Legal Code (the full license).

Disclaimer

For the full text of this licence, please go to:
http://creativecommons.org/licenses/by-nc-nd/2.5/

Development and Validation of a Pressure based CFD methodology for Acoustic Wave Propagation and Damping.

B.P.N.Gunasekaran

A Doctoral Thesis

Submitted in partial fulfilment of the requirements for the award of Doctor of Philosophy of Lougborough University

© B.P.N.Gunasekaran

June 2011.

To My Parents

ABSTRACT

Combustion instabilities (thermo-acoustic pressure oscillations) have been recognised for some time as a problem limiting the development of low emissions (e.g., lean burn) gas turbine combustion systems, particularly for aviation propulsion applications. Recently, significant research efforts have been focused on acoustic damping for suppression of combustion instability. Most of this work has either been experimental or based on linear acoustic theory. The last 3-5 years has seen application of density – based CFD methods to this problem, but no attempts to use pressure-based CFD methods which are much more commonly used in combustion predictions. The goal of the present work is therefore to develop a pressure-based CFD algorithm in order to predict accurately acoustic propagation and acoustic damping processes, as relevant to gas turbine combustors.

The developed computational algorithm described in this thesis is based on the classical pressure-correction approach, which was modified to allow fluid density variation as a function of pressure in order to simulate acoustic phenomena, which are fundamentally compressible in nature. The fact that the overall flow Mach number of relevance was likely to be low ("mildly compressible" flow) also influenced the chosen methodology. For accurate capture of acoustic wave propagation at minimum grid resolution and avoiding excessive numerical smearing/dispersion, a fifth order accurate Weighted Essentially Non-Oscillatory scheme (WENO) was introduced. Characteristic-based boundary conditions were incorporated to enable accurate representation of acoustic excitation (e.g. via a loudspeaker or siren) as well as enable precise evaluation of acoustic reflection and transmission coefficients. The new methodology was first validated against simple (1D and 2D) but well proven test cases for wave propagation and demonstrated low numerical diffusion/dispersion. The proper incorporation of Characteristic-based boundary conditions was validated by comparison against classical linear acoustic analysis of acoustic and entropy waves in quasi-1D variable area duct flows.

The developed method was then applied to the prediction of experimental measurements of the acoustic absorption coefficient for a single round orifice flow. Excellent agreement with experimental data was obtained in both linear and non-linear regimes. Analysis of predicted flow–fields both with and without bias flow showed that non-linear acoustic behavior occurred when flow reversal begins inside the orifice. Finally, the method was applied to study acoustic excitation of combustor external aerodynamics using a pre-diffuser/dump diffuser geometry previously studied experimentally at Loughborough University and showed the significance of boundary conditions and shear layer instability to produce a sustained pressure fluctuation in the external aerodynamics.

Key words: Gas turbine, Combustion instability, Acoustic Damping, Pressure based Method, WENO and Characteristic boundary condition.

Acknowledgment

I would like to record my sincere gratitude to Prof Jim McGuirk for his supervision, continuous help, patience and support. His technical knowledge, everlasting enthusiasm has provided invaluable contribution throughout this project. I am indebted to him more than he knows.

I would also like to thank all the members of the Loughborough University Technology Centre, past and present for providing invaluable suggestions as well as creating the environment, within I have been very lucky to work. In particular, I would like to thank Mr. Jochen Rupp and Dr. Gavitha Regunath for providing data which are extensively used in this work. I would also like to thank Dr. Jon Carrotte for providing me valuable suggestions especially in latter part of this work.

The financial support from Rolls Royce plc. is also gratefully acknowledged.

Finally, I thank my wife for being very supportive and patient enough to stand beside me to progress with my work.

CONTENTS

List of Figures

List of Tables

1. INTRODUCTION

To set the scene for the engineering application which has motivated the research reported in this thesis, a short introduction to the gas turbine engine and its combustion system is first presented. This is followed by a brief description of the phenomenon of thermo-acoustic combustion instability. Efficient control of thermo-acoustically generated combustion instability is key to many technological advancements in modern/future gas turbine combustion systems such as development of low NOx lean burn combustors. Approaches to minimising or controlling combustion instabilities are reviewed with emphasis on techniques for damping the acoustic modes. Currently thermo-acoustic wave generation/propagation/damping in combustion systems are all typically assessed using experiments and low-order analytical tools; use of Computational Fluid Dynamics (CFD) in this area is growing rapidly but still not common in design practice. This chapter therefore also analyses the challenges for CFD modelling if it is to be used for accurate and efficient analysis of combustion thermo-acoustics, placing particular focus on the prediction of acoustic damping aspects, since this is the principle topic of this thesis.

1.1 THE GAS TURBINE

During World War II, a new type of aircraft engine - the turbojet gas turbine - was developed independently in England by Sir Frank Whittle and in Germany by Hans von Ohain and Max Hahn. Most modern passenger as well as military aircraft are powered by gas turbine engines. A simple gas turbine consist of three main components: compressor, combustion chamber and turbine and the ideal thermodynamic cycle for a simple gas turbine is the Brayton cycle, which consists of isentropic compression, constant pressure combustion and isentropic expansion. Modern gas turbine engines come in a wide variety of shapes and sizes because of the many different aircraft mission profiles. In *turboprop* engines, by the combination of a propeller and gas turbine, optimum propulsive efficiency is achieved for low-speed aircraft and helicopters. *Turbojet* engines produce thrust primarily from the direct impulse of exhaust gases; turbojet engines along with an afterburner are used in supersonic aircraft. For example, the Rolls-Royce Olympus turbojet engine was used to power the Concorde. *Turbofan* engines generate thrust from a combination of a high bypass ratio ducted fan as well as core engine jet thrust; these engines are ideal for high subsonic aircraft speeds; most medium and long haul commercial aircraft use turbofan engines. A typical turbofan gas turbine engine (Rolls-Royce Trent 500) is shown in Figure 1.1.

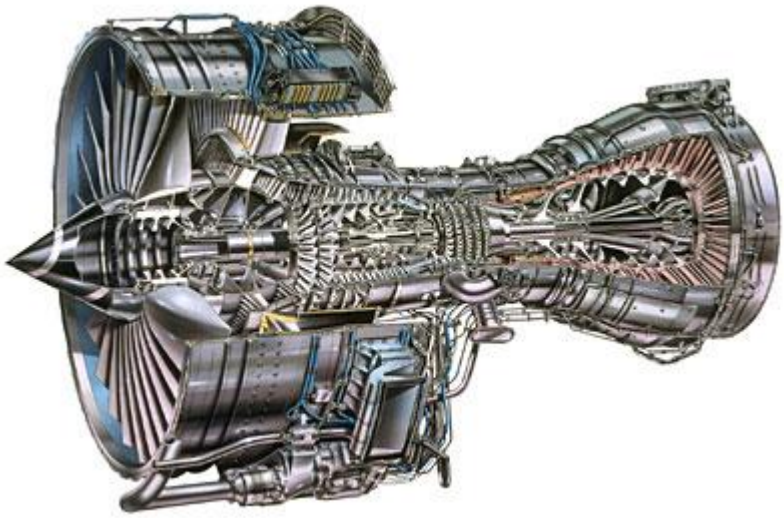

Figure 1. 1– Rolls-Royce Trent 500 – Turbofan engine (www.rolls-royce.com)

1.2 GAS TURBINE COMBUSTION

The combustion system plays a vital role in the overall performance of a gas turbine and its associated pollutant emissions. Unlike an IC engine, combustion in the gas turbine is a continuous process. It is designed to burn a specified fuel-air mixture and deliver the combusted gases to the turbine at a temperature which will not exceed the allowable limit which would compromise cooled turbine blade life. In addition, this must be accomplished with minimum total pressure loss. Fully annular combustion chambers are most commonly used in modern aircraft gas turbine engines. The combustion section comprises the combustion chamber itself, surrounded by a combustion casing. An igniter plug and fuel nozzles are used to initiate combustion and sustain steady state fuel/air mixing, evaporation and chemical reaction. Liquid fuel is introduced at the front end of the combustor via fuel nozzles in a highly atomised spray. Air from the compressor is diffused, first in a pre-diffuser and then in a dump diffuser, and then flows around the combustor and also (at a designed flow split) into the fuel nozzle, where swirl is imparted on the flow and a so-called primary zone flow pattern is created to form a target primary fuel-air mixture. In aircraft engines, fuel injector air currently represents ~ 25 percent of the compressor efflux. The remaining 75 percent of the air is used for: (i) injection into the combustor via primary and secondary jets which control the combustor flow pattern and are used to mix and dilute the ~2500 K combusted primary zone gases to achieve an acceptable combustor exit temperature of ~ 1700K, (ii) to cool the combustor liner via film-cooling holes and thus protect this from the very high radiative and convective heat transfer caused by the flame, (iii) to pass around the combustor into the annular gaps between combustor liner and combustor casing so it can be used for turbine cooling. The combustion chamber must be of light construction to reduce excessive weight and is designed to burn fuel completely in a high velocity air-stream. In nearly all commercial aviation engines, diffusion flames (fuel and air are not

premixed but enter the combustor via separate routes) are extensively used. The *annular* combustion chamber offers the advantages of a larger combustion volume per unit of exposed area, lower material weight and better circumferential uniformity of burned gas temperature, pressure and velocity resulting in an engine of small and compact design. A typical *annular* combustor is shown in figure 1.2.

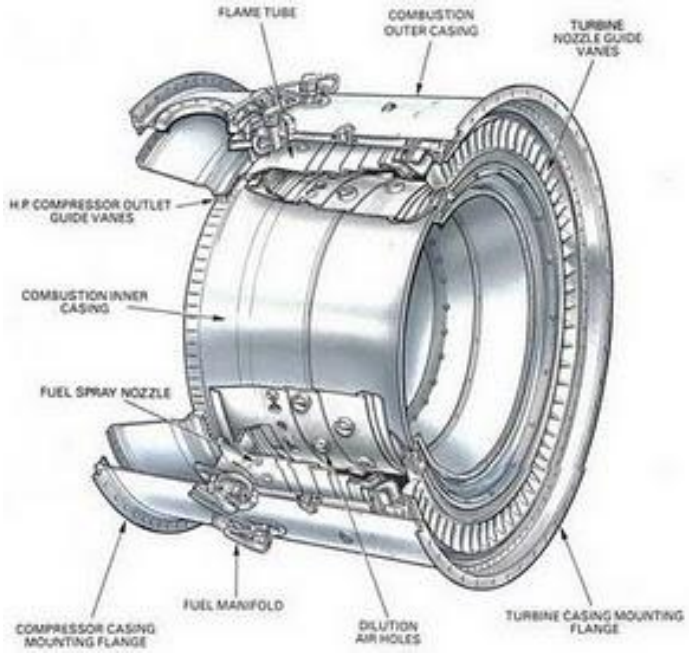

Figure 1. 2 - Annular combustor- Lefebvre (1998)

1.3 EMISSIONS LEGISLATION and REDUCTION TECHNIQUES

The Earth is getting warmer at a much higher rate than ever before. According to NASA (www.nasa.gov): " the 2004 average temperature at the Earth's surface around the world was 0.48˚C above the average temperature from 1951 to 1980". Many scientists believe this is due to global warming exerting an adverse effect on the climatic system. This acute rise in the earth's surface temperature is caused in part by the increase in atmospheric greenhouse gas concentrations (e.g., CO, NOx, CO_2, methane etc.). Increase in greenhouse gases in the atmosphere is argued by many as mainly due to emissions produced from burning fossil fuels, aviation emissions being one contribution. In 1999 a report by the "Intergovernmental Panel on Climate Change" (IPCC) (www.ipcc.ch) estimated that aircraft greenhouse gas emissions could contribute up to 15% of global warming from all human activities by 2050 due to the projected increase in aircraft fleet service. The "International Air Transport Association" (IATA) (www.iata.org) predicted an 8.4% increase in air traffic in China and India annually until 2021. It is thus inevitable that future legislation will continue to force the pace for combustor designs which lead to emissions reduction. In 2001 the Advisory Council for Aeronautics Research in Europe (ACARE) was set up with the goal of developing and implementing a strategic approach to European aeronautics

research. It also set out challenging emission reduction targets, with three key goals aimed to be achieved by 2020 (see, www.acare4europe.com). Those goals are:

- To reduce fuel consumption and CO_2 emissions by 50%.
- To reduce perceived external noise by 50%.
- To reduce NOx by 80%.

In order to achieve the above mentioned emission targets it is believed necessary to introduce new combustor technologies such as Lean Premix Prevapourised (LPP) combustion, Rich-burn, Quick-quench, Lean-burn (RQL) combustion, staged combustion etc (Lefebvre et al. 2010). In such new technologies it is necessary to operate the combustor (and in particular the flame stabilising primary zone region) at lower fuel-air ratios than have been typically used in traditional design practice to lower temperatures, which will lead to lower rates of formation of thermal nitric oxides (NOx). However, in such lean burn systems, unsteady flow oscillations, usually referred to as combustion instability or combustion dynamics, have often emerged as a problem (Lieuwen et al. 2005) and hindered their development.

Conventional diffusion flame combustion chambers inject fuel straight into the primary zone with no premixing with air, resulting in 'hot spots' (regions of stoichiometric fuel/air ratio) producing increased levels of NOx. In lean premixed combustion fuel is premixed with air before injection into the primary zone; the primary zone is thus operated at equivalence ratios closer to the lean extinction limit resulting in lower thermal NOx production but potentially with a more unstable flame. Although NOx levels are drastically reduced in lean burn combustion systems, these systems have proven especially prone to combustion instability as well as auto-ignition and flash-back problems (Lieuwen et al. 2005). Combustion instability was first observed in rocket propulsion (Crocco et al. 1956) where it was given the name 'thermo-acoustic' combustion instability because of the principal driving mechanism involved. It was also found in aero-engine afterburners. In stationary industrial gas turbines, due to the strict legislative requirement for low emissions of NOx, it has become common to shift the combustion process from a non-premixed diffusion flame to a premixed flame type. In the late 1980's stationary gas turbine premixed combustion system design faced many problems due to intense thermo-acoustic combustion instabilities (Sreenivasan et al. 2000). It was thus inevitable that such difficulties would also be faced when lean burn systems were designed for aircraft applications. The following section provides a brief introduction to thermo-acoustic combustion instability.

1.4 THERMO-ACOUSTIC COMBUSTION INSTABILITY

In any unsteady combustion process, the flame in general possesses intrinsic instabilities. Unsteady coupling between static pressure oscillations and chemical reaction in the flame can lead to sustained unstable combustion, a phenomenon commonly called combustion

instability or combustion dynamics. It can be explained in principle as follows. When a fluid element is heated during the combustion process, it expands and produces a propagating pressure wave, which, at least initially, is of sufficiently low amplitude that it may be referred to as an acoustic wave. This radiates into the surrounding gas propagating at the speed of sound relative to the surrounding gas flow. Due to the presence of solid and other possibly reflecting boundaries of the combustion system (e.g. the upstream compressor interface or downstream turbine interface) this pressure wave will undergo reflection or part reflection, part transmission from these boundaries, which then return to interact with the flame. Pressure wave interactions can be of various kinds, for example an incident pressure wave can introduce changes in the incoming air at the fuel nozzle and hence change the air/fuel ratio. A reflected pressure wave or a convected perturbation in equivalence ratio can affect the mixing and chemical reaction in the combustion zone, which might produce a reinforced pressure disturbance. If the pressure increase and the resulting heat release perturbation have an appropriate phase relationship, a self-sustained feedback mechanism (resonant interaction) can be formed. Whether this feedback loop reaches a limit cycle and at what amplitude, depends also on the acoustic damping characteristics of the combustor. These to a large extent depend on the various openings for air admission into the combustor (fuel injector, primary and dilution ports, liner-wall cooling holes), since these provide paths for acoustic energy to leave the system. Specific acoustic damping devices (e.g. Helmholtz resonators) can also be introduced into the combustor design. It has been found that, in general for lean burn combustors, acoustic damping is usually too weak and a large amplitude limit cycle thermo-acoustic pressure oscillation can result. There are thus many possible mechanisms and system characteristics which play key roles in determining the stability of the combustor. Candel (2002) has shown the basic mechanisms involved in combustion instability, see figure 1.3. Note that this figure indicates that acoustic waves play two roles in combustion instability. The first is related to their influence on the source of acoustic pressure oscillations (the unsteady heat release). The second is the interaction with the acoustic nature of upstream/downstream boundary conditions (reflection and transmission characteristics) which obviously play a role in source generation but also cause damping effects on the combustion instability.

Large pressure oscillations can affect the survival of the flame and hence limit the operating range of a combustion system. Combustion instability can produce intense vibrations and cause structural damage. The extent of pressure oscillation depends on the nature of the resonant interaction. If the interaction takes place in the low frequency range, the acoustic wavelength greatly exceeds the typical transverse dimension of the combustor and thus wave propagation is essentially longitudinal (plane waves). On the other hand if the resonance features a higher frequency (f > 1kHz), the wavelength is of the order of or less

than the transverse dimension of the chamber (Candel 2002) and can lead to circumferential modes (spinning waves).

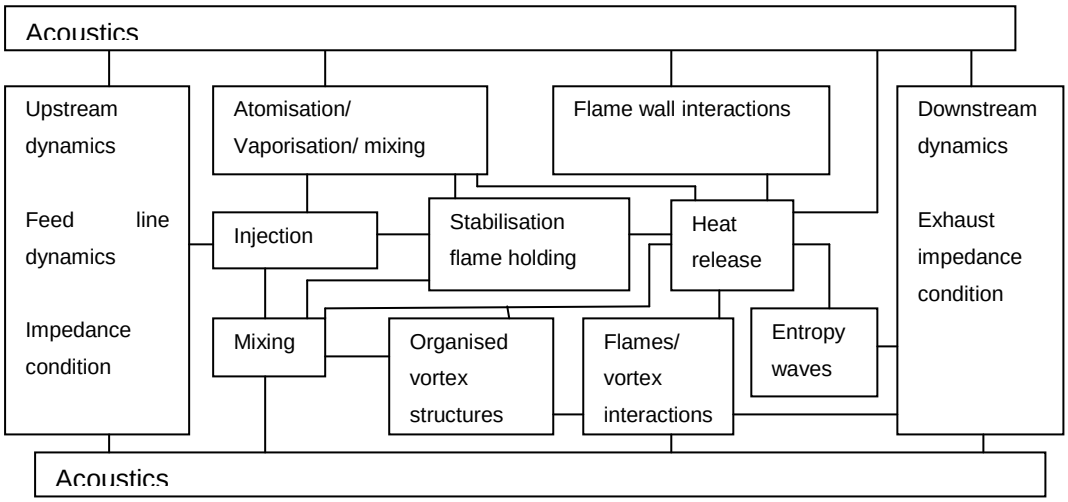

Figure 1. 3 - Basic interactions leading to combustion instabilities, Candel (2002).

The following figures illustrate the level of severity of structural damage caused by combustion dynamics that has been found in industrial gas turbines. Figure 1.4, shows the damage to a centre body fuel injector and Figure 1.5, shows the effect of combustion instability on the transition piece (connection between a can combustor and a sector of the annular turbine inlet), both in GE stationary industrial gas turbines.

Figure 1. 4 - Damage to a GE- 7EA (80 MW) fuel nozzle due to combustion dynamics, (Lieuwan et al. 2003).

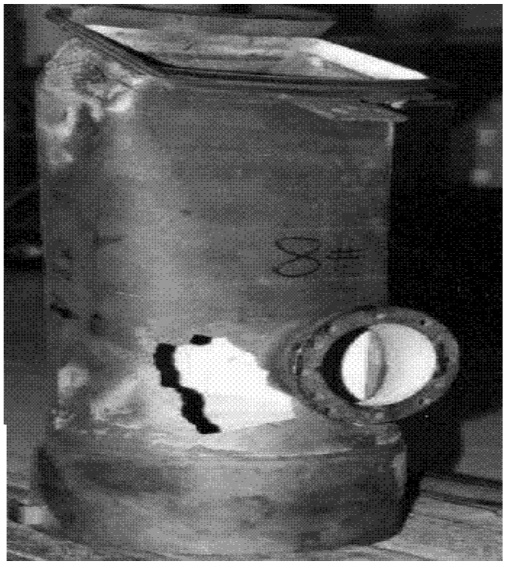

Figure 1. 5 - Failure of transition piece due to combustion instability and also due to high thermal stress, (Lieuwan et al. 2003)

1.5 CONTROL OF COMBUSTION INSTABILITY

To operate a combustion system effectively in lean-premix mode, it is necessary to control the combustion instabilities. In order to do so, it is essential to understand the cause of the instability as well as its nature, i.e., what determines whether an initial disturbance will grow or decay in time. Rayleigh (1945) first obtained a relation which has traditionally served as the primary criterion for establishing the nature of thermo-acoustic instability. This criterion states that when the pressure fluctuations and the unsteady heat release are in phase, the acoustic mode will tend to make the system unstable (instabilities will grow until damped out or reach a limit cycle stationary state). This criterion may be written as:

$$\int_0^T q'(t)\,p'(t)dt > 0 \qquad (1.1)$$

where T is the period of oscillation, q'(t) is the unsteady heat release, p'(t) is the static pressure fluctuation. The above inequality can be satisfied either when heat release increases at a time of compression, or when heat release reduces during expansion. There are many ways in which feedback can result in the favourable phasing of heat release and the pressure. It has been pointed out by Dowling (1995), that consideration of the Rayleigh criterion alone is not sufficient to identify stability or instability, since, for example, the interaction between heat release generated entropy waves (convected hot spots) and the combustor exit boundary can also lead to self-sustained thermo-acoustic instabilities. In addition, since the criterion is in the form of an inequality rather than a precise condition, there is an outstanding question as to how strong the correlation between heat release and pressure fluctuations needs to be before instability growth occurs. Also, when the combustion instability approaches the limit cycle, acoustic processes may no longer be linear, whereas the criterion was derived in a linear framework (Poinsot et al. 2005). Thus, it is difficult to quantify completely the nature of thermo-acoustic instabilities using a simple relationship such as 1.1. However, the Rayleigh criterion emphasises the need for detailed knowledge of the phase relationship between pressure oscillation and various processes controlling the heat release, as key to any stability analysis.

In order to establish and quantify the heat release fluctuations in a combustion system, it is paramount to analyse the flame response to perturbations from acoustic wavefields. This is best expressed via a flame transfer function (Schuller et al. 2002). This function relates heat release fluctuations to incident acoustic perturbations impinging on the flame in both amplitude (gain) and phase (time delay) contexts. Much experimental work has been carried out to obtain the relationship between the various mechanisms (mentioned in figure 1.3) which drive combustion instability and also ways to eradicate such instability (McManus et al. 1998, Pascheret et al. 1999, Richards et al. 1997, Lee et al 2003, Venkataraman et al.1999, Preetham et al. 2007) as well as obtaining flame transfer functions for various incoming perturbations (Candel 2002). Many of these works have used artificial, controlled

acoustic excitation provided by a loudspeaker or siren to provide a measured flame response for a range of excitation frequencies. Experimental studies such as these to determine flame transfer functions for configurations of technical interest is difficult (and expensive for design purpose if carried out at pressure and pre-heat temperatures relevant to engine operation conditions). Analytical models have also been proposed for the phenomenon of pressure wave-flame interactions (Dowling et al. 2003, Ducroix et al. 2003, Lieuwen et al. 2003, Schuller et al. 2002). These are mainly linear acoustic network models in which simple models are used for heat release fluctuation computation (Dowling et al. 2003). Ducroix et al. (2003) on the other hand solved the governing equations for combustion instability by using detailed reaction kinetics. In both cases, the information relating to flame response to acoustic perturbations were fed into low order acoustic network models. Once the acoustic response of the basic flame/combustion system is known then, using active combustion control (McManus et al. 1993, Lieuwen et al. 2005), which uses sensors and feedback control loops, (for example fuel injection control) combustion instability can be controlled/reduced. Alternatively, passive control methods have been studied more recently (Lieuwen et al. 2005, Eldredge et al. 2003, Noiray et al. 2007). In these the acoustic energy created at the flame is dissipated before it can return to the flame by augmenting acoustic damping effects in the overall system, thus eventually reducing/controlling the combustion instabilities. Although active control may become a preferred stabilisation strategy in future, at the present time, passive control methods are more commonly used in both stationary and aviation gas turbine industries. In the context of the present research, attention is here focussed on various damping techniques since interest within the design community has increased significantly in the last few years on development of an improved understanding of acoustic damping.

Use of passive control damping devices to control combustion instability was begun in the 1950's in early rockets, since acoustic instabilities were a major problem hindering the development of efficient rocket motors. Control strategies during this period typically consisted of inclusion of baffles and/or simple geometric modifications (Lieuwen et al. 2005 & Williams 1985). However, unlike rocket motors, combustion instabilities in lean burn gas turbine systems can be excited via multiple causes as described above, and involve interaction with and between rotating machinery, fuel mixing, multiple flame mechanisms etc. Therefore, more robust solutions other than simple geometry changes were needed to overcome these instabilities. One technique which is widely used across gas turbine industries is the Helmholtz resonator (Dupere et al. 2005). This consists of a cavity with a neck connected to the combustion system through a small orifice. Near its resonant frequency, the resonator experiences large-amplitude acoustic oscillations in its neck. These oscillations dissipate acoustic energy by means of vortex shedding at the neck-combustor interface via enhanced viscous effects (Bellucci et al. 2000). A Helmholtz

resonator, however, is only effective in damping acoustics in a limited bandwidth near its resonance; also the resonant oscillation in the neck is heavily dependent on the external pressure fluctuations, so the resonator fails to dissipate acoustic energy if placed near a pressure node location in the combustor. Another passive damping mechanism which is gaining interest is referred to as a “perforated liner with bias flow” (Eldredge et al. 2003). This consists of an array of orifices across the length and circumference of a region of the combustor liner wall with airflow provided through the liner and injected into the “bias flow”, i.e. the combusting flow inside the liner. This scenario is of course already provided in combustor designs to cool the liner walls via various devices such as film, slot cooling, effusion cooling etc. Hence, this technique explores the use of liner cooling as an acoustic damping mechanism as well as a heat transfer device. Harmonic pressure differences across each orifice excite periodic vortex shedding and the shed vortices are convected away by the bias flow (Howe 1979). These shed vortices convert the acoustic energy into fluid kinetic energy, which is eventually dissipated by turbulence and viscous processes into internal energy. Unlike a localised Helmholtz resonator, a liner with perforations over the length of a duct is effective over a (relatively) larger range of frequencies and locations. Even though the Helmholtz resonator and perforated liner have different operability ranges, the fundamental mechanism in which both absorb sound energy is fluid mechanic (due to vortex shedding and subsequent turbulence dissipation). The growing interest in these fluid mechanically driven damping devices poses the question of whether their performance can be acceptably predicted by a fluid mechanics modelling approach (CFD); this topic is covered in the following section.

1.6 PREDICTION OF PASSIVE DAMPING DEVICE PERFORMANCE

For effective and efficient use of passive damping devices it is essential to understand the amount of damping required in specific situations and also the performance of passive damping devices for various incident acoustic wave energy (amplitude and frequency). The low-order, linear acoustic network modelling approach (Dowling et al. 2003, Rehman et al. 2007) has been extended to study the behaviour of passive damping devices placed in various combustion systems by analysing transmission, reflection, and absorption coefficients of various components in the system based on linear acoustic wave propagation theory (in particular using Rayleigh conductivity theory (Rayleigh 1945) for predicting sound absorption in the system with and without passive damping devices). By coupling linear acoustic network models of the system with flame transfer models entire system instability could in principle be analysed. More details of various experimental and analytical work on sound absorption in damping devices is presented below in Chapter 4. This will include in particular recent measurements of Rupp et al. 2010 whose experimental data represent a detailed survey of a classical problem i.e. unsteady flow through an orifice. With recent increase in computational power, Hsiao et al. 1998, studied combustion instabilities in a 3-D model of an annular combustor using Large Eddy Simulation (LES); the CFD modelling

results were then incorporated into a low order acoustic model for predicting instabilities. A similar approach of coupling CFD and low-order acoustic modelling was also employed by Steele et al. (2000) on a Solar Turbines Mars combustor family with promising results. However, in all of these approaches, the acoustic impact of reflected acoustic waves at the boundaries of the system, as well as inclusion of any passive devices like Helmholtz resonators or perforated liners, has been ignored. Even though low-order, linear acoustic modelling tools, either stand alone or with some CFD coupling, can produce useful results, with increased geometric complexity of the combustor component(s) whose acoustic performance/responsiveness has to be considered (cooling liner holes, resonator design etc), and also if acoustic non-linear effects (limit cycle) are to be captured, the limitations of network modelling will be reached and a more general approach needs to be considered.

1.7 SCOPE FOR USING CFD/CAA TO PREDICT THERMO-ACOUSTIC COMBUSTION INSTABILITY AND ASSOCIATED DAMPING EFFECTS

Geometric complexities and non-linear wave interactions in a combustion system can be analysed by numerical solution for the flow field and the acoustic characteristics simultaneously. However, the desire to carry out combined flow/acoustic prediction of combustors and their component parts uncovers an important and classical computational strategy question. Acoustic phenomena are inherently compressible in nature – this favours a density-based CFD approach (Choi et al. 1985, Tam et al. 2001). Whilst some successful CFD approaches for combustion systems have been based on compressible density-based CFD algorithms (Selle et al. 2004, Menon et al. 2006, Chong et al. 2010, Foller et al. 2010), the majority of CFD methods used for low Mach number combustion prediction (particularly those commonly adopted in the gas-turbine industry) are traditionally derived from incompressible pressure-based approach (Anand et al. 1999, Snyder et al. 2001, James et al. 2008). This is especially the case for Large Eddy Simulation (LES) formulations because of the computational efficiency gained by having a time-step not limited by the speed of sound. This raises the following question: which methodology is better when both low Mach number flow and acoustic waves occur simultaneously? In such situations, a method is needed, which will be optimally accurate and efficient, both in high and low Mach number flows. Another key issue which must be addressed for direct solution of both flow and acoustics is the best choice of convective discretisation scheme to be used. For incompressible 3D complex flows involving swirl, jet penetration and impingement and rapid mixing, low order (2^{nd}) schemes with upwind bias providing bounded numerical solutions with no (or small) spatial oscillations are often preferred. On the other hand, for accurate spatial resolution of acoustic waves and small numerical dissipation and dispersion, higher order (5^{th} or even 10^{th}) are usually selected in Computational Aero Acoustic (CAA) approaches, see Tam et al. (2001). Which alternative is best suited to low Mach number acoustic flow simulations needs to be identified. Finally, since the interaction between

acoustic waves and solution domain boundaries will needs to be modelled accurately, the question of accurate acoustic boundary condition representation will play an important role.

The following sub-sections contain an overview of previous work on these three specific aspects. Firstly various extensions of density-based methods to the low Mach number regime and also pressure-based method extensions for compressible and acoustic phenomena are addressed. Next a brief introduction to spatial discretisation schemes currently available for accurate capture of pressure wave propagation is given. Finally, the important question of proper choice of acoustic boundary conditions is discussed.

1.7.1 Unified CFD Methods For Low/High Mach No. Flow

In general the use of classical (density-based) compressible methods for low Mach number flow or classical (pressure-based) incompressible methods for high Mach number flow will gives rise to large computational inefficiencies: very small time steps, convergence problems, or even divergence. What is needed is a CFD algorithm which works well in both incompressible as well as compressible regimes; this is often referred to as a 'Unified method' or a method 'for all flow speeds'.

It is possible broadly to classify Unified methods into three main categories. The first is where the low Mach number behaviour of a density-based method has been improved. Here the most notable method is pre-conditioning (Choi et al. 1993) usually incorporated into a time-marching algorithm. For compressible density-based methods time-marching algorithms are widely used; for low Mach number, this approach gives rise to stiffness issues in the convective term and also converges very slowly to a steady state solution (the time step is defined using a Courant number based on the high speed acoustic velocity, whereas the development time scale of the solution is more limited to the low speed flow convecting time scale). To remove the stiffness in the eigenvalues, the coefficient matrix resulting from the discretised equations is pre-multiplied by a pre-conditioning matrix which scales the eigenvalues of the algebraic equations to the same order of magnitude. Choi et al. (1985) used such a pre-conditioning matrix to modify the energy equation introducing additional terms containing time derivatives of ρ, ρu, ρv, ρw. Just by preconditioning the energy equation alone, Choi et al. (1985) showed the pre-conditioned compressible method was effective for a wide variety of inviscid low Mach number calculations, although it was unstable for low Reynolds number flows. Later, Choi et al. (1993) improved the method for viscous flow using another form of pre-conditioning matrix which introduced an artificial compressibility term into the continuity equation in non-conservative form. A reference Mach number was also employed in order to avoid the pre-conditioning matrix becoming singular if the flow approaches zero Mach number. At very low Reynolds number (~ 50) the viscous time step parameter ($\mu\Delta t / \rho\Delta x^2$) becomes important and makes the convergence slow. Thus, in order to control the stability of the calculation at low Reynolds number,

simultaneous control of the CFL number and viscous time step parameter were needed. The main drawback of this type of preconditioning method is that it falsifies the time-dependence, making time-accurate unsteady computations inefficient. Although this can be overcome using dual time-step techniques, this approach can handle very small Mach number (~ <0.05) only at increasing computational expense. Another approach to improve the low Mach number behaviour of compressible methods is to perturb the equations with artificial compressibility by replacing the physical acoustic modes by artificial acoustic modes (Merkle et al. 1988, McMurtry et al. 1986). This method also usually falsifies the time dependence, making time-accurate unsteady computation inefficient.

A second category of Unified method is known as the asymptotic approach, based on a series expansion of any defined variable in Mach number (eg, $\emptyset(x,t) = \emptyset_o(x,t) + M\emptyset_1(x,t) + M^2\emptyset_2(x,t)$). Klein's (1995) paper developed this method for the low Mach number asymptotic limit of the Euler equations (mainly for combustion applications, with strong variable density flow). The 'pressure' in the asymptotic approach therefore exhibits three distinct roles: (i) thermodynamic (p_0), (ii) acoustic waves (p_1), (iii) as a balancing agent for inertial forces to ensure continuity (p_2). In the case of low Mach number, the second order pressure, p_2 , reduces to the standard pressure variable as used in incompressible pressure-based methods that satisfies the well-known Poisson equation. Under certain conditions (e.g., less complex geometry) the acoustic variations represented by the first order, p_1, take the form of a linearised acoustic wave equation. By employing these asymptotic limit equations rather than solving the full equations, the acoustic effects are either completely suppressed or computed by post-processing as higher order corrections. The apparent Inability of this method to solve for the acoustic contribution fully/directly seems to makes the asymptotic approach unsuitable for the current project.

In the third category of Unified methods, the incompressible pressure-based method is extended to introduce compressible effects. Obviously, this gives the best prospects for handling low Mach number flows as it completely recovers to the incompressible scheme under zero Mach number conditions. The first exploration of this approach was carried out using a staggered grid system, in order to avoid the need for stabilising measures to avoid spurious spatial pressure oscillations (e.g., Rhie and Chow smoothing, Rhie et al. (1983). This kind of approach was first introduced by Harlow et al. (1968). In pressure-based methods, pressure is always used as a primary dependent variable for both incompressible as well as compressible flow. The continuity equation (for compressible flow with the density linked to pressure via an ideal gas law) is converted into an equation for pressure-correction by combining the discretised continuity and momentum equations. The classical incompressible version of this approach is the SIMPLE algorithm (Patankar and Spalding (1972)). Issa (1985), in order to improve the performance of the basic SIMPLE algorithm

when applied to unsteady compressible flow, developed an improved version of the basic pressure-correction method referred to as the PISO algorithm, which was particularly suited to solutions of unsteady compressible flows in IC engines. In the PISO method an implicit operator splitting semi-iterative (two-step) solution of the Poisson equation for pressure-correction was developed. This was specifically aimed at high Mach No. but subsonic (no shocks) mean flows. The operator splitting approach, involving solution of two pressure-correction equations did not require inner iterations for larger time steps as needed by the standard SIMPLE approach. No application of this method to acoustic problems has been made and, unless the time-step restrictions are severe (for example requiring many tens of inner iterations of SIMPLE), PISO offers similar performance as the standard approach. Later, Karki et al. (1989) used the compressible form of the pressure-correction equation to establish complete linkage between pressure, velocity and density by employing a fully iterative and still conservative discretisation. This was accomplished by linearising the mass flux term (ρu) by neglecting the second order correction product ($\rho' u'$). At low Mach number the modified pressure-correction equation will be elliptic (Poison equation) whereas for higher Mach number it assumes a hyperbolic nature. At the same time, McGuirk and Page (1990), proposed a similar Unified method which performs well even in transonic flows containing shocks. In their approach, the non-linear pressure/velocity contribution which was previously neglected by Karki et al. (1989) was effectively included by choosing momentum components (e.g. ρu) as the primary variables as opposed to the traditionally used velocity components. The resulting pressure correction equation remains elliptic at all speeds and the hyperbolic behaviour of the system of equation in supersonic flow condition was introduced via a "retarded pressure" dependent on local Mach number. The new retarded pressure was used in the momentum and pressure correction equations, where the real pressure was used to calculate density through equation of state. In general both Karki et al. and McGuirk and Page (1990) methods seems to work well for compressible flows, although neither has been demonstrated successfully on acoustic problems.

For solving low Mach number flows with low frequency acoustics, Wall et al. (2002), proposed a method which avoids both the acoustic CFL limitation and artificial damping of pressure waves. The artificial damping was reduced by using central difference in both time and space. In order to increase the accuracy and stability of the time-dependent continuity equation, a novel configuration of grid staggering of velocity components was introduced. Each velocity component was staggered in space by one-half grid point with respect to the scalar variables (as usual), but additionally the velocity components were staggered in time also by one-half time step with respect to the scalar variables. To eliminate the acoustic CFL requirement, the pressure was interpolated in time twice, before inserting into the momentum equations. In conventional notation, this means that the velocity is advanced from t^n to t^{n+1} using the gradient of a weighted average of pressure at times $t^{n-1/2}$, $t^{n+1/2}$, $t^{n+3/2}$„

Wall et al. (2002). By employing this three level time staggering, for linear acoustics they were able to demonstrate good prediction without artificial attenuation of the pressure waves. In an Large Eddy Simulation (LES) version of the calculation, however, dissipation had to be introduced into the pressure gradient term of the momentum equation, since without this unphysical small-scale oscillations in the scalar variables due to the presence of short-wavelength acoustics modes was observed.

Moureau et al. (2007) developed a semi-implicit pressure-based scheme for compressible flow by solving a Helmholtz equation for pressure implicitly using large time steps which drastically reduced the computational time. They separated the acoustics from the flow (advection) by using a fractional-step method (see, Kim et al. 1985) which was based on characteristic splitting and as a result obtained a second-order spatial and temporal convergence for linear acoustics without any inner loop. For the advection step, a kinetic energy conserving step was used. Finally, Armitage et al. (2006) applied a compressible pressure-based method to obtain flame transfer functions for a premixed combustion process by imposing velocity fluctuations at the inlet. Even though full compressible equations were solved, it is not clear how the crucial (for compressible effects) pressure/density linkage nature was retained in their model. This is because it seems that the variable gas mixture density was obtained from a Bray-Moss-Libby (BML) flamelet relationship, which is usually derived using a constant thermodynamic pressure. Thus the density would vary essentially only due to temperature and species (molecular mass) variations rather than due to pressure variations.

Based on the above discussion on various Unified CFD methods, it is clear that, although density-based methods have a natural link to acoustic phenomena, the inherent computational inefficiencies when using these methods for low Mach number flows does not make them so attractive to analysis of acoustic damping problems in low Mach gas-turbine combustor applications. The natural advantages of pressure-based methods for nearly incompressible flow analysis, and the evidence that these have been extended to capture strongly compressible flows (Karki et al. (1989), McGuirk and Page (1990)), encourages further development and assessment of the pressure-based approach for acoustic wave propagation and damping applications. Such a development would also be of great interest to the gas-turbine engine industry, since pressure-based methods still retain a dominant part in their routine CFD design and analysis tools.

1.7.2 Numerical Schemes For Accurate Wave Propagation

Before selecting an appropriate discretisation scheme for use in the present work for application to low Mach number acoustic problems it is necessary to consider a few key features of acoustic pressure waves as encountered inside combustors. At present

particular emphasis is given to spatial discretisation methods as required for the non-linear convective terms.

One important characteristic of acoustic waves is that: the amplitudes of associated pressure and velocity perturbations can be orders of magnitude smaller than the level set by the time- mean flow conditions. In addition, in a highly turbulent flow there is a wide range of time and length scales present due to the nature of turbulence alone; in general some will be larger and some smaller than the time and length scales of the acoustic perturbations (Wagner et al. 2007). In a CFD approach which adopts a statistical time-averaged turbulence modelling approach (e.g Reynolds Averaged Navier-Stokes (RANS) or its unsteady variant URANS), this will not be an issue. In LES this will complicate the separate identification of acoustic and turbulent scales. Acoustic waves propagate at the speed of sound in all directions relative to the local flow velocity, compared to convective perturbations which propagate at the local flow velocity. Finally, acoustic waves can travel long distances maintaining both amplitude and frequency (low diffusion and dispersion). Due to the above properties of perturbations associated with acoustic waves, traditional convection spatial discretisation schemes (e.g., conventional upwind or second-order schemes) have been found to be inefficient for acoustic wave propagation. Most conventional schemes require roughly 60-70 grid points per acoustic wavelength in order to propagate acoustic disturbance accurately (see Huang et al. 1998).

Although the order of a scheme (based on a Taylor expansion) indicates the error reduction with grid size, it gives only partial information on the separate dispersive and dissipative behaviours of the scheme. These two aspects are very important in order to simulate acoustic waves properly. This information, which is related to resolution aspects of the discretistation as opposed to the order of accuracy (Adam et al. 1996), can be obtained from a Fourier mode analysis. Resolution may be viewed as the ability of the scheme to represent various Fourier modes for a range of increasing wave numbers accurately. The dispersive errors of the scheme cause an error in the frequency and phase of the Fourier modes as compared with their exact solution, whereas dissipative errors cause an error in the amplitude of the Fourier modes (see Moin, 2001 for more information).

An enormous amount of work has been done on numerical methods for acoustic wave applications (in the field referred to as Computational Aero- Acoustics (CAA)) to address the above issues by extending schemes primarily designed for solving the strongly compressible hyperbolic flow equations (e.g Roe-type schemes, Monotone-Upstream-centred Schemes for Conservation Laws (MUSCL) schemes and Godunov-type scheme, see Hirsch (1998), for details). New approaches have also been developed specifically for CAA problems. A high band-width, central method called Dispersion-Relation-Preserving

(DRP) by Tam et al. (1993) is one scheme specifically developed for CAA which has become a popular approach in acoustic wave propagation problems. A few details of the DRP schemes are provided here for illustration.

In general the 1st order spatial derivative of a variable ϕ (as occurring in the convection terms) can be discretised as:

$$\left(\frac{\partial \phi}{\partial x}\right)_i \approx \frac{1}{\Delta x}\sum_{j=-M}^{M} a_j \phi_{i+j}$$

where M defines the discretisation stencil width and a_j are the co-efficients which determine the scheme. The basic idea of DRP schemes is to use only part of the available co-efficients a_j of the stencil to fix the order of the scheme. The remaining co-efficients are tuned to minimise the resolution error which is interpreted as the difference between the physical wave number and the numerical wave number ($\bar{k} = -\frac{1}{\Delta x}\sum_{j=-M}^{M} a_j e^{Ijk\Delta x}$) in a wave propagation test problem. This error is to be minimised by suitable choice of the a_j via a least square error assessment: $E = \int_{-\beta}^{\beta} \left| k\Delta x - \bar{k}\,\Delta x \right|^2 d(k\Delta x)$. In their paper Tam et al.1993 chose $\beta = \pi/2$, which means that the optimisation can be performed only for waves with a wavelength larger than 4Δx. Reasons for not optimising the complete wave number range (-π, +π) have been pointed out by Wagner et al. (2007) e.g., the numerical wave number goes to zero for kΔx =π. The main drawback of this central DRP scheme is that it has no dissipation mechanism to eliminate spurious short-wavelength numerical waves. This results in piling up of energy in the high wave number range and might cause the scheme to be unstable. The remedy for this is to add a variable (but as small as possible) amount of dissipative terms.

An alternative method to the DRP approach has seen increasing use recently in acoustic wave applications. An example of this alternative approach is the WENO (Weighted Essentially Non Oscillatory) scheme (Liu et al. (1994), Jiang et al. (1996), Johnsen et al. (2006)), which is an extension of the ENO (Essentially Non Oscillatory) scheme (Harten et al. 1987). The basic idea of ENO schemes is that, for each cell face, the total variation of each of a range of possible spatial stencils is assessed and the one with the lowest variation ('smoothest' stencil) is used to calculate the cell-face values. This leads to high order accuracy and avoids spurious oscillations near discontinuities where a lower order stencil is naturally selected. The main drawback of the ENO scheme is that it proposes a freely adaptive stencil, which could change even due to round-off perturbations near zeros of the solution and its derivatives; also free adaption of stencils is not necessary in regions where

the solution is smooth. WENO schemes address these flaws by choosing a weighted-average of a range of selected stencils rather than selecting one best possible stencil. The relative weighting given to each stencil is determined by the smoothness of the data within the stencil. Even though WENO schemes are slightly more expensive than their ENO equivalent they provide a greater order of accuracy for the same overall stencil size. Since it is likely that an improved convection discretisation approach (compared to those traditionally used in pressure-based method) will be needed for accurate acoustic wave propagation there the evidence seems to indicate that DRP or WENO method are worth exploring in the context of the present research.

1.7.3 Acoustic Boundary Conditions

Specifying appropriate boundary conditions is a critical aspect in the numerical solution of acoustic problems. Spurious (i.e. unphysical) reflections of disturbances resulting from inappropriate numerical boundary conditions on the chosen solution domain will contaminate the flow field and may entirely spoil the flow computation. Hence, in this section focus is given to various methods for boundary condition specification which can be used effectively at inflow and outflow boundaries of the solution domain without causing any hindrance to the numerical solution.

Much of the published work on acoustic boundary conditions has been connected to this problem of reflected waves at solution domain boundaries. If the main interest is in obtaining steady-state solution of the compressible flow equations, then the main motivation is in fact to damp out any acoustic waves which are excited during the solution or make sure they leave the domain completely. This has prompted significant work on non-reflective acoustic boundary conditions. In one-dimensional flow, Enquist et al. (1977) & Hedstrom (1979) proved that a boundary condition which is non-reflecting is equivalent to saying that the characteristic variables propagating along the incoming characteristic curve remain constant across the boundary. In the characteristic form of the Euler equations, the characteristic variables propagate at three different speeds: (1) the local flow convective speed (u), (2) the acoustic flow speed in the direction of the flow (u+c), and (3) the acoustic flow speed opposed to the local flow (u-c). Thus, for a subsonic inlet boundary, in order to avoid any spurious reflections at the boundary it is necessary to relate the numerically obtained left propagating wave component to the other two right propagating wave components. Similarly at a supersonic outlet, extrapolation from the internal side to the external side of boundary results in a true physical representation of the characteristics, since all three characteristic propagation velocities point outwards. For multi-dimensional flow, the above mentioned 1-D Euler equation based technique must be combined with dimension splitting in order to produce a non-reflective boundary condition treatment (see Hirsch (1988)). This multi-dimensional characteristic approach for an Euler system was later extended to the Navier –

Stokes equations by Poinsot and Lele (1992) by taking viscous terms into consideration. Poinsot et al. (2005) applied the Navier-Stokes based characteristic technique to subsonic isothermal (single and multi-species) as well as reacting flows. Many other approaches to achieve non-reflecting boundaries have been proposed and tested. The most used of these is to incorporate a technique which diminishes the strength of the waves/disturbances before they reach the boundary, thus minimising the reflection effect. Usually, the wave strength is decreased by increasing numerical damping in a zone between the core solution domain and the boundary (the buffer zone), (Colonius 2004). The so-called Perfectly Matched Layer (PML) method achieves this by using a specially designed equation system in the buffer zone to guarantee exponential decay of the disturbances; Hu (1996) and Hesthaven (1998) is an example of this. Even-though both the buffer zone technique and the PML method are efficient in supressing any spurious reflections at computational domain boundary, these methods are not suitable for imposition of external acoustic wave input into the computational domain as is generally required for the current problems of interest. An excellent review article covering the entire range of non-reflective boundary conditions proposed for use in subsonic and supersonic isothermal flow conditions can be found in Colonius (2004).

In the current work, the primary interest is in ensuring correct physical characterisation of, for example, input acoustic excitation due to sirens or loudspeakers, or accurate estimation of the correct physical amplitude of acoustic waves which the analysed system allows to reflect from or transmit through the boundaries. In this case, the characteristic technique of Poinsot et al. (2005) forms the ideal basis. In fact, if attention is initially focused on plane acoustic waves, then a 1D version of characteristic boundary conditions as described by Hirsch (1988) represents an optimum starting point. If necessary, the same approach could be easily modified to incorporate more complex multi-directional treatments following Poinsot et al. (2005).

1.8 AIM OF CURRENT RESEARCH

The aim of the current work is to examine and identify the optimum components of a pressure-based CFD technique for capturing acoustic wave propagation and absorption accurately, in complex geometries relevant to gas turbine combustion systems. In what follows this is for convenience referred to as a “mildly compressible pressure-based CFD approach”.

Based on the aim stated above, as well as on the basis of the literature review in previous sections, the following primary objectives were set:

- Identify a suitable method for pressure-density linkage appropriate to pressure-based CFD of acoustics and incorporate this into an existing pressure-based

incompressible CFD code, previously proven for gas turbine combustor relevant flow problems.

- Investigate and incorporate an appropriate discretisation schemes suitable for propagating acoustic waves with low numerical dissipation and dispersion errors and verify the scheme's performance against suitable simple test cases.

- Incorporate an appropriate boundary condition treatment which will allow acoustic waves to enter and leave through inlet/outlet boundaries of the solution domain whilst representing correct physical characteristic conditions and allowing physically correct reflection and transmission processes to be specified; the selected method should be verified for appropriate acoustic behaviour in a well-chosen test case.

- Finally, the developed mildly compressible methodology should be
    1. tested against a practically relevant problem for which suitable measurement data are available- acoustic damping by an orifice is the selected flow problem.
    2. used to demonstrate how the method might be used to analyse acoustic wave propagation through the complex geometry turbulent flow typically of a gas turbine combustion system- a dump diffuser flow is the selected flow problem.

1.9 THESIS STRUCTURE

An in-house structured multi-block incompressible pressure-correction CFD code (referred here as Fuel-3D) was available and modified to incorporate the mildly compressible algorithm. Chapter 2 contains a description of the baseline incompressible code. Modifications which were carried out to convert this into a mildly compressible version have been outlined in Chapter 3. Chapter 3 also contains preliminary tests on the code modifications such as selected discretisation scheme both (spatial and temporal), acoustic boundary conditions as well as tests carried out to validate prediction of acoustic input-output relationship and entropy-acoustic input-output relationships for a variable cross section duct flow at different inlet Mach numbers and different excitation acoustic frequencies.

Chapter 4 demonstrates the capability of the newly developed method via URANS predictions of recent experimental data (Rupp et al. (2010)) which have documented the flow and acoustic pressure absorption characteristics of a circular orifice in a plate located in a duct with a mean flow through it-typical of many apertures found within gas-turbine

combustion systems. The unsteady velocity field and acoustic absorption coefficient are shown to be well predicted using the current methodology for a range of bias flows.

In Chapter 5, the ability of the developed method is illustrated via a numerical study of the influence of acoustic wave excitation on combustor external aerodynamics (dump diffuser flow). This study demonstrated strong synchronisation between the unsteady response of the shear-layer produced in the dump region to external acoustic perturbation when the frequency of the excitation matched the convective time in the shear-layer.

Finally, in Chapter 6, conclusions are drawn and recommendations made for further work.

2. BASELINE INCOMPRESSIBLE PRESSURE-BASED CFD ALGORITHM/CODE

2.1 INTRODUCTION

At the start of the current project, a standard, incompressible, pressure-correction 3D CFD code (referred to here as “Fuel-3D”) was available for use as the “baseline” code/algorithm to be further developed for acoustic analysis. This was an in-house code developed at Loughborough University and is described in the PhD thesis of Baird (2001). This chapter describes the modelling and numerical approaches adopted in the basic version of this code before any modifications for accurate simulation of acoustic propagation were introduced. The choice of this CFD code was based on its proven capability to predict incompressible flows in complex flow configurations of relevance to combustor flows such as dump diffuser flows (McGuirk et al. 2001) and hybrid diffuser flows (Denman et al. 2003).

In order to solve complex geometries Fuel-3D uses a curvilinear non-orthogonal co-ordinate system, which leads to a multi-block structured grid system where the geometry and grid are defined via contiguous control volumes at cell vertex points. All solution variables are co-located at the centre of the control volumes and boundary nodes are located at the centre of the solution domain edge control volume faces. Pressure-velocity decoupling associated with the co-located system is prevented using the Rhie & Chow (1983) pressure smoothing procedure. The pressure-correction methodology adopted for the pressure-based CFD algorithm follows that of the standard SIMPLE method (Patankar and Spalding (1972)) to satisfy mass conservation. In addition to laminar flow, the code can also solve for turbulent flow by using the Reynolds Averaged Navier-Stokes (RANS) approach. Two RANS models are available in Fuel-3D, the standard k-ε model (Jones et al. 1972) and a Reynolds Stress Transport model. A thorough discussion of the various approaches to predicting the Reynolds stresses using the RANS approach can be found in Pope (2000). Both of the RANS models have been implemented using a high Reynolds number wall function approach (Ferziger et al. 2002) to apply wall boundary conditions. Important numerical details of the code necessary to understand the modifications introduced during the current research are covered in the rest of this chapter.

2.2 GOVERNING DIFFERENTIAL EQUATIONS

The fundamental equations that are solved in Fuel-3D are continuity, momentum and a conserved scalar transport equation, shown below in Cartesian co-ordinates as applicable to a laminar flow or to the instantaneous flow properties in a turbulent flow [note gravitational body force has been neglected here as negligible in the flows considered].

Continuity equation:

$$\frac{\partial \rho}{\partial t} + \frac{\partial (\rho U_i)}{\partial x_i} = 0 \qquad (2.1)$$

Momentum equations:

$$\frac{\partial (\rho U_i)}{\partial t} + \frac{\partial (\rho U_i U_j)}{\partial x_j} = -\frac{\partial p^*}{\partial x_i} + \frac{\partial}{\partial x_j}\left\{\mu\left[\frac{\partial U_i}{\partial x_j} + \frac{\partial U_j}{\partial x_i}\right]\right\} \qquad (2.2)$$

Scalar transport equation:

$$\frac{\partial (\rho \varphi)}{\partial t} + \frac{\partial (\rho U_j \varphi)}{\partial x_j} = \frac{\partial}{\partial x_j}\left(\frac{\mu}{\sigma_\varphi}\frac{\partial \varphi}{\partial x_j}\right) \qquad (2.3)$$

summation of repeated indices applies, a Newtonian law of viscosity has been assumed for viscous stresses and a constant diffusion coefficient for scalar diffusive transport $(\frac{\mu}{\sigma_\varphi})$ where σ_φ represents the Prandtl/Schmidt number for φ diffusion, note p* = $(p + \frac{2}{3}\mu\frac{\partial U_k}{\partial x_k})$ is a modified static pressure.

The baseline version of Fuel-3D has been written to solve these equations for incompressible flows in which fluid density does not depend on the fluid static pressure. However, density variations are allowed and are taken into account where these occur due to, for example, temperature or fluid species variation. In this case the scalar (φ) variable represents a mixture fraction or progress variable in a combusting flow where fluid density variations due to species or temperature changes are determined via a combustion/thermo-chemistry model, which usually assumes a constant (thermodynamic) static pressure. If appropriate, for non-reacting flows density can be chosen and treated as a constant in the code.

For solving turbulent flows the instantaneous variables such as (U,V,W etc) are first decomposed into mean quantities ($\overline{U}, \overline{V}, \overline{W}$) and fluctuating quantities (u',v',w') (e.g., $U = \overline{U} + u'$) in the Reynolds Averaged (RANS) approach (for more details, see Pope 2000).

By applying the above decomposition to U_i, p, φ in the instantaneous continuity, momentum and scalar transport equations (assuming for simplicity a constant density), it is possible to obtain the RANS continuity and momentum and scalar equations for incompressible constant fluid density flow, which are shown below (note if density fluctuations need to be taken into account, Favre (mass-weighted) averaging is needed instead of Reynolds averaging, see next chapter).

Continuity equation: $$\frac{\partial (\rho \overline{U_i})}{\partial x_i} = 0 \qquad (2.4)$$

Momentum equations:

$$\frac{\partial(\rho\overline{U}_i)}{\partial t}+\frac{\partial(\rho\overline{U_i}\overline{U_j})}{\partial x_j}=-\frac{\partial\overline{p}}{\partial x_i}+\frac{\partial}{\partial x_j}\left\{\mu\left[\frac{\partial\overline{U_i}}{\partial x_j}+\frac{\partial\overline{U_j}}{\partial x_i}\right]\right\}-\frac{\partial(\rho\overline{u'_i u'_j})}{\partial x_j} \qquad (2.5)$$

Scalar transport equation:

$$\frac{\partial(\rho\overline{\varphi})}{\partial t}+\frac{\partial(\rho\overline{U_j}\overline{\varphi})}{\partial x_j}=\frac{\partial}{\partial x_j}\left(\frac{\mu}{\sigma_\varphi}\frac{\partial\overline{\varphi}}{\partial x_j}\right)-\frac{\partial(\rho\overline{u'_j\varphi'})}{\partial x_j} \qquad (2.6)$$

Note that an unsteady term has been retained in the momentum/scalar transport equations (not in continuity equation as constant density assumption used). This implies that these are the unsteady RANS (URANS) equations. Comparing (2.5) with (2.2) and (2.6) with (2.3), the URANS equations contain extra terms (last terms on right hand side of 2.5 & 2.6) because of momentum or scalar transport due to turbulent fluctuations. These extra terms lead to the 'closure problem' in turbulence, having more unknowns than equations, which is addressed in Fuel-3D using a statistical turbulence model.

2.3 RANS or URANS TURBULENCE MODELLING

In order to solve the RANS or URANS equations, it is necessary to prescribe the Reynolds stresses ($\rho\overline{u'_i u_j'}$) and turbulent scalar flux terms ($\rho\overline{u'_j\varphi'}$) to avoid the well-known turbulence closure problem. Boussinesq (see Pope 2000) proposed the following approximation to relate the Reynolds stresses to the mean rate of strain through a turbulent viscosity (for constant density flow):

$$-\rho\overline{u'_i u_j'}=\mu_t\left(\frac{\partial\overline{U_i}}{\partial x_j}+\frac{\partial\overline{U_j}}{\partial x_i}\right)-\frac{2}{3}\delta_{ij}\,\rho\,k \qquad (2.7)$$

where k is the turbulent kinetic energy; $k=\frac{1}{2}\overline{u'_i u'_i}$ and μ_t is the turbulent viscosity.

One turbulence model implemented in Fuel-3D and used in the present work to calculate μ_t is the high Reynolds number k-ε model of Jones et al. (1972), in which μ_t is taken as proportional to $\rho\left(\frac{k^2}{\varepsilon}\right)$, where ε is the turbulent energy dissipation rate.

k & ε are obtained by solving the following modelled equations

$$\frac{\partial\rho k}{\partial t}+\frac{\partial\rho\overline{U_j}k}{\partial x_j}=\frac{\partial}{\partial x_j}\left\{\left(\mu+\frac{\mu_t}{\sigma_k}\right)\frac{\partial k}{\partial x_j}\right\}+P-\rho\varepsilon \qquad (2.8)$$

$$\frac{\partial\rho\varepsilon}{\partial t}+\frac{\partial\rho\overline{U_i}\varepsilon}{\partial x_j}=\frac{\partial}{\partial x_j}\left\{\left(\mu+\frac{\mu_t}{\sigma_\varepsilon}\right)\frac{\partial\varepsilon}{\partial x_j}\right\}+\frac{\varepsilon}{k}(C_{\varepsilon1}P-C_{\varepsilon2}\rho\varepsilon) \qquad (2.9)$$

where P is the turbulence production , $=\mu_t\left(\frac{\partial\overline{U_i}}{\partial x_j}+\frac{\partial\overline{U_j}}{\partial x_i}\right)\frac{\partial\overline{U_i}}{\partial x_j}$ (2.10)

and the turbulent viscosity is: $\mu_t = \rho C_\mu \frac{k^2}{\epsilon}$ (2.11)

The model constants are (Jones et al. 1972):

$$C_\mu = 0.09, \quad C_{\varepsilon 1} = 1.44, \quad C_{\varepsilon 2} = 1.92, \quad \sigma_k = 1.0, \quad \sigma_\varepsilon = 1.3$$

Similarly, a turbulent scalar diffusion coefficient is defined to model the scalar flux term by introducing the concept of a turbulent Prandtl number for φ, as done already for k,ε,

$$\Gamma_t = \frac{\mu_t}{\sigma_{t,\varphi}} \frac{\partial \varphi}{\partial x_i} \qquad (2.12)$$

The URANS equations therefore become:

$$\frac{\partial \rho \overline{U_i}}{\partial x_i} = 0 \qquad (2.13)$$

$$\frac{\partial \rho \overline{U_i}}{\partial t} + \frac{\partial \rho \overline{U_i}\,\overline{U_j}}{\partial x_j} = -\frac{\partial \overline{p}}{\partial x_i} + \frac{\partial}{\partial x_j}\left\{(\mu + \mu_t)\left[\frac{\partial \overline{U_i}}{\partial x_j} + \frac{\partial \overline{U_j}}{\partial x_i}\right]\right\} \qquad (2.14)$$

$$\frac{\partial (\rho \overline{\varphi})}{\partial t} + \frac{\partial (\rho \overline{U_j} \overline{\varphi})}{\partial x_j} = \frac{\partial}{\partial x_j}\left(\left(\frac{\mu}{\sigma_\varphi} + \frac{\mu_t}{\sigma_{t,\varphi}}\right)\frac{\partial \overline{\varphi}}{\partial x_j}\right) \qquad (2.15)$$

with modified mean pressure , $\bar{p} = \bar{p} + \frac{2}{3}\rho k$.

2.4 COMPLEX GEOMETRIES – NON-ORTHOGONAL CO-ORDINATES

Although the Cartesian version of the governing equations above are very useful and capture all essential information in simple flows, they are not suitable for numerical discretisation of flow in complex geometries. For this purpose, the structured mesh approach uses a general curvilinear non-orthogonal co-ordinate transformation from a Cartesian (x,y,z) system to a "geometry-fitted" (ξ, η, ζ) system, where the boundaries of the complex geometry coincide with grid lines of the transformed co-ordinates, making boundary condition implementation much-easier. Details of this approach are given in full in Ferziger et al. (2002), so only the detail necessary to describe clearly the capabilities and implementation practices used in the Fuel-3D code are included here; more details can be found in the thesis of Baird (2001).

Transformation between the Cartesian system (x,y,z) and the curvilinear (computational) system (ξ, η, ζ) as shown in Fig 2.1 is characterised by the determinant J, also called the Jacobian determinant and its inverse J^{-1} as defined by:

$$J = \begin{vmatrix} x_\xi & x_\eta & x_\zeta \\ y_\xi & y_\eta & y_\zeta \\ z_\xi & z_\eta & z_\zeta \end{vmatrix} \quad \text{and} \quad J^{-1} = \begin{vmatrix} \xi_x & \xi_y & \xi_z \\ \eta_x & \eta_y & \eta_z \\ \zeta_x & \zeta_y & \zeta_z \end{vmatrix} \qquad (2.16)$$

where, $x_\xi = \frac{\partial x}{\partial \xi}$ etc.

Figure 2. 1 - Cartesian to curvilinear co-ordinate transformation.

Using the J^{-1} determinant a 2-point space separation vector in Cartesian space (Δx, Δy, Δz) can be transferred into a separation vector in computational space $(\Delta\xi, \Delta\eta, \Delta\zeta)$ and vice-versa. Similarly, spatial derivatives with respect to (x,y,z) can be transformed into derivatives with respect to (ξ, η, ζ) in the governing equations eqn. 2.1 – 2.3 or eqn. 2.13 – 2.15. For example the Cartesian spatial derivatives of a general variable Φ can be transformed using J as follows:

$$\frac{\partial \Phi}{\partial x} = \frac{\partial \Phi}{\partial \xi}\frac{\partial \xi}{\partial x} + \frac{\partial \Phi}{\partial \eta}\frac{\partial \eta}{\partial x} + \frac{\partial \Phi}{\partial \zeta}\frac{\partial \zeta}{\partial x} = \frac{\partial \Phi}{\partial \xi_j}\frac{\beta_i^j}{J} \qquad (2.17)$$

where β_i^j represents the transpose of the cofactor of each element $\frac{\partial x_i}{\partial \xi_j}$ in the Jacobian J.

Using these rules the transport equations in Cartesian co-ordinates (eqn. 2.13 – 2.15) are transformed to the following in the curvilinear system:

Continuity equation:

$$\frac{1\partial}{J\partial \xi_j}\left(\varrho \overline{U_J}\right) = 0 \qquad (2.18)$$

Momentum equations:

$$\frac{\partial \rho \overline{u_\iota}}{\partial t} + \frac{1}{J}\frac{\partial}{\partial \xi_j}\left(\rho \overline{U_m}\beta_m^j \overline{u_\iota}\right) =$$

$$-\frac{1}{J}\frac{\partial \bar{p}\beta_i^j}{\partial \xi_j} + \frac{1}{J}\frac{\partial}{\partial \xi_j}\left[\left(\frac{\mu+\mu_t}{J}\right)\beta_k^m\beta_k^j\frac{\partial \overline{u_\iota}}{\partial \xi_m}\right] + \frac{1}{J}\frac{\partial}{\partial \xi_j}\left[\left(\frac{\mu+\mu_t}{J}\right)\beta_i^m\beta_k^j\frac{\partial \overline{u_k}}{\partial \xi_m}\right] \qquad (2.19)$$

Scalar transport equation:

$$\frac{\partial \rho \bar{\varphi}}{\partial t} + \frac{1}{J}\frac{\partial}{\partial \xi_j}\left(\rho \overline{U_m}\beta_m^j \bar{\varphi}\right) = \frac{1}{J}\frac{\partial}{\partial \xi_j}\left[\left(\frac{\frac{\mu}{\sigma_\varphi}+\frac{\mu_t}{\sigma_{t,\varphi}}}{J}\right)\beta_k^m\beta_k^j\frac{\partial \bar{\varphi}}{\partial \xi_m}\right] \qquad (2.20)$$

For the solution variables in the momentum equations (e.g. u,v,w), the velocity vector is retained in its Cartesian form, thus:

$\bar{u}_j$ are Cartesian velocity components e.g. u,v,w

$\overline{U_J}$ are velocity components normal to surfaces ξ_j = constant, related to Cartesian components via:

$$(\overline{U_J} = \bar{u}\beta_1^j + \bar{v}\beta_2^j + \bar{w}\beta_3^j) \qquad (2.21)$$

Although these equations look substantially more complex than their Cartesian counterparts, for discretisation purposes they may be treated as having: (1) a transient term, (2) 1st order spatial derivative convective terms, (3) 2nd order spatial derivative diffusion terms, (4) source terms. It is convenient to consider complex terms such as cross-derivative diffusion terms as extra source terms. The second implication for numerical solution is that a suitable geometry-fitted and usually non-orthogonal mesh has to be generated. Use of a multi-block structured mesh increases the complexity of geometry that can be treated and the Fuel-3D code was written to allow this complexity (Baird 2001). More details of this are given below.

2.5 FINITE VOLUME METHOD

The computational solution of the above equations requires that the partial differential equations are transformed into algebraic approximations by means of various discretisation schemes, on discrete (multi-block) structured meshes which are generated to cover the whole solution domain. In the finite volume method, the domain is divided into a number of discrete control volumes (CV) and the conservation equations are discretised within each CVs. Figure (2.2) and (2.3) shows typical mesh, CV layout for Cartesian 2D and 3D structured grids as well as typical cell with corresponding cell faces.

The computational nodes lie at the centroid of each CV in which all variables ($\overline{U_i}$, $\bar{p}$, $\bar{\varphi}$ etc.,) are stored, as shown in Fig 2.1. Note that the grid generation process determines co-ordinate values at vertex locations and nodal information is derived from these by interpolation. After integrating the transport equations over the cell volume, the discretised algebraic equations are derived by approximating the volume integral of the transient and source terms and the cell face convection and diffusive fluxes. In order to calculate the fluxes through CV faces it is necessary to approximate the surface integrals of convective and diffusive fluxes. This requires the variable values at the CV faces, so interpolation is used to express these in terms of nodal values. How this is done depends on the choice of spatial discretisation scheme and the options available in Fuel-3D are explained below. For simplicity the descriptions below are given for a 1D Cartesian system. How this is generalised to 3D and to curvilinear co-ordinates is presented fully in Ferziger et al. (2002).

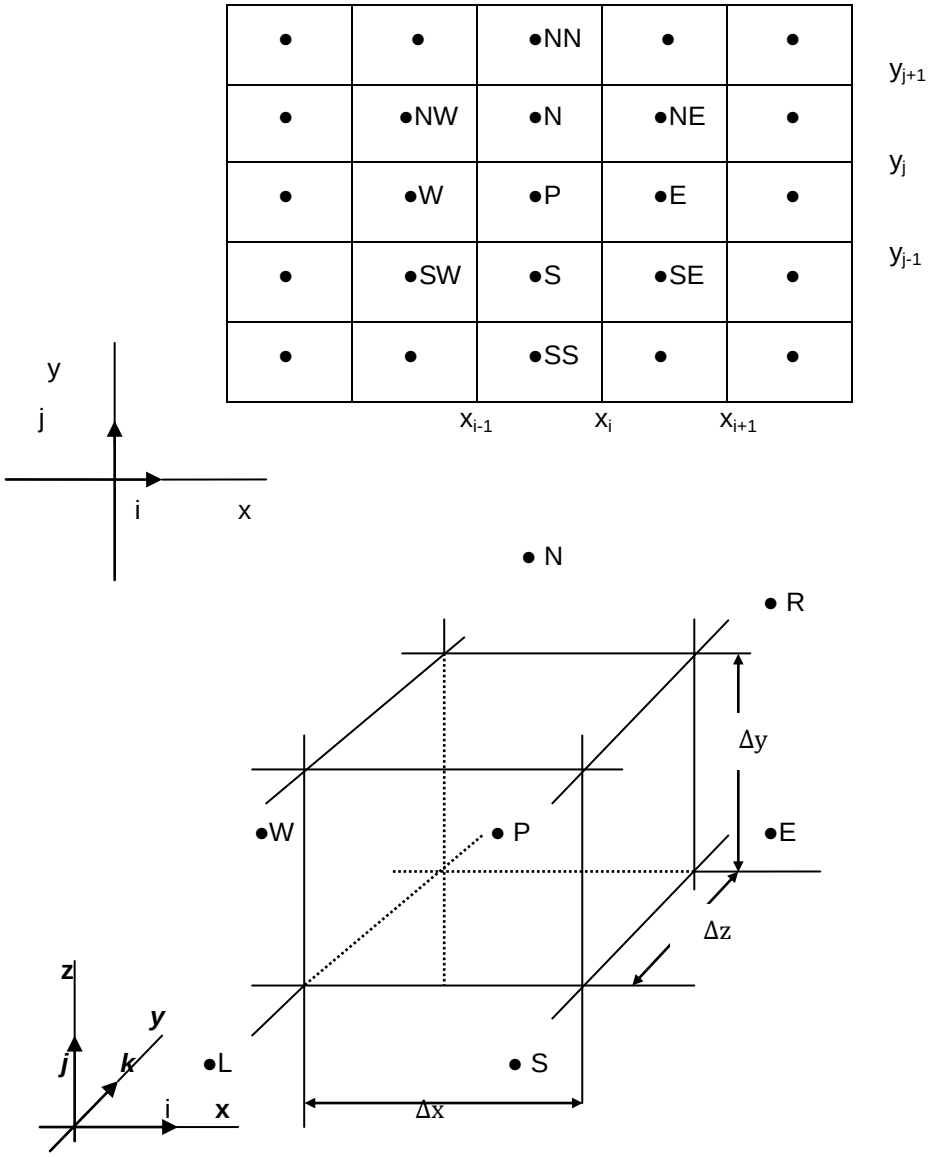

Figure 2. 2 - Typical control volumes for a Cartesian 2D & 3D grid

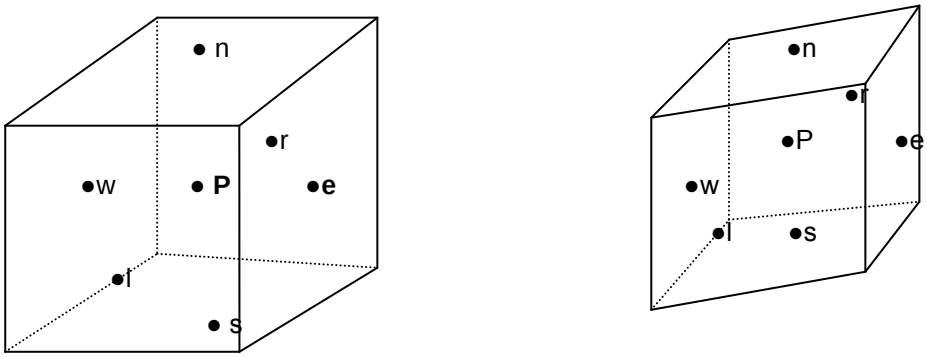

Figure 2. 3 - Labelling of faces for a cell P (left-Cartesian co-ordinates, right-general non-orthogonal co-ordinates).

2.6 TRANSIENT TERM DISCRETISATION

The temporal derivative, e.g. $\left(\frac{\partial(\rho\bar{\varphi})}{\partial t}\right)$, in the transport equations is discretised in Fuel-3D using a 1st order implicit or backward Euler method (Ferziger et al. 2002), for example: $\int_v \frac{\partial\rho\bar{\varphi}}{\partial t} = \rho\frac{(\bar{\varphi}^{n+1}-\bar{\varphi}^{n})}{\Delta t}V$. With such a method, all other terms in the transport equations such as convective, diffusive terms are also evaluated using future time, 'n+1' values. The main advantage of this is it is unconditionally stable. However, this method is only 1st order accurate so that solutions may be obtained with large Δt, but these will usually "smoothed" due to higher numerical errors at large Δt. This scheme is therefore incorporated into Fuel-3D as a convenient and simple method whereby a transient solution is only used as a means to achieve a steady state solution, rather than as an accurate method for time-resolved solutions. This is unlikely to be acceptable in the current context and a modified temporal scheme will be needed.

2.7 CONVECTIVE TERM DISCRETISATION

After integrating the transport equations over the cell volume, the first derivative terms lead to six convective fluxes through the six cell faces of the CV. The cell face convective flux (c^f) through the east (e) face of the 'P' CV for a generic transport variable (φ) may, for example be written (1D flow assumed for convenience) :

$$c^f_{P,e} = \int_S \rho\overline{U^n_e}\overline{\varphi^{n+1}_e}\,\mathrm{ds} \qquad (2.22)$$

In which, $\int_S \rho\overline{U^n_e}\,dS$, is the mass flux through the surface (assuming the $\bar{U}$ velocity is normal to ds) and is approximated using previous time values. The discretised form at the east face of the 'P' CV is:

$$c^f_{P,e} \approx (\rho\overline{U})^n_e s_e\,\bar{\varphi}^{n+1}_e \;=\; G_e\bar{\varphi}^{n+1}_e \qquad (2.23)$$

The lower-case subscripts in (2.22, 2.23) indicate the control volume face and upper – case subscripts denote the centre of control volume. Term 'G' in (2.23) represents the mass flux corresponding to the east face of the control volume. The cell face unknown convected variable '$\bar{\varphi}^{n+1}_e$' is obtained using a user-selected option available in Fuel 3D, either Hybrid or QUICK differencing as detailed below, all cell face convective velocities ($\bar{U}^n_e$) are interpolated using central differencing.

2.7.1 Hybrid Differencing

To reduce numerical oscillations which can be triggered by dispersion errors if the 2nd order central difference scheme were used at high cell Peclet number, (Pe = $\frac{\rho\bar{U}\Delta x}{\Gamma}$), a hybrid scheme may be selected, which switches between conventional central differencing and 1st order upwind differencing (Feriger et al. 2002). When the cell Peclet number is greater than two, this scheme reduces to a pure 1st order upwind scheme.

For east face

For Pe ≥ 2 :

$$\bar{\varphi}_e^{n+1} \sim \begin{cases} \bar{\varphi}_P^{n+1} if \;\; G_e > 0.0 \\ \bar{\varphi}_E^{n+1} \;\; if \;\; G_e < 0.0 \end{cases} \qquad (2.24)$$

For Pe < 2 :

$$\bar{\varphi}_e^{n+1} \sim \frac{1}{2}(\bar{\varphi}_P^{n+1} + \bar{\varphi}_E^{n+1}) \qquad (2.25)$$

2.7.2 Quadratic Upwind Interpolation (QUICK) Differencing

As the name suggests, this scheme (Ferziger et al. 2002) uses quadratic interpolation for the cell face value rather than the linear interpolation of central differencing. In order to construct a parabola one additional point is introduced, which is taken on the upstream side of the face, based on the face mass flux. The QUICK scheme for an east face can be written as:

For $G_e > 0.0,$ then

$$\bar{\varphi}_e^{n+1} = \bar{\varphi}_P^{n+1} + g_1(\bar{\varphi}_E^{n+1} - \bar{\varphi}_P^{n+1}) + g_2(\bar{\varphi}_P^{n+1} - \bar{\varphi}_W^{n+1}) \qquad (2.26)$$

The coefficients g_1 and g_2 are expressed in terms of nodal coordinates:

$$g_1 = \frac{(x_e - x_P)(x_e - x_W)}{(x_E - x_P)(x_E - x_W)} \;\; \& \;\; g_2 = \frac{(x_e - x_P)(x_W - x_e)}{(x_P - x_W)(x_E - x_W)}$$

For $G_e < 0.0,$ then

$$\bar{\varphi}_e^{n+1} = \bar{\varphi}_E^{n+1} + g_1(\bar{\varphi}_P^{n+1} - \bar{\varphi}_E^{n+1}) + g_2(\bar{\varphi}_E^{n+1} - \bar{\varphi}_{EE}^{n+1}) \qquad (2.27)$$

$$g_1 = \frac{(x_e - x_E)(x_e - x_{EE})}{(x_P - x_E)(x_P - x_{EE})} \;\; \& \;\; g_2 = \frac{(x_e - x_E)(x_{EE} - x_e)}{(x_E - x_{EE})(x_P - x_{EE})}$$

2.8 DIFFUSIVE TERM DISCRETISATION

Second derivative terms in the transport equations are discretised at control volume faces using two-point central differencing. This discretisation is shown below for simplicity for a Cartesian system, for a general curvilinear non-orthogonal system, see Baird (2001); one normal flux $2\mu\left(\frac{\partial \bar{\varphi}}{\partial x}\right)$ and two shear fluxes $\left[\mu\left(\frac{\partial \bar{\varphi}}{\partial x} + \frac{\partial \bar{\varphi}}{\partial y}\right), \mu\left(\frac{\partial \bar{\varphi}}{\partial x} + \frac{\partial \bar{\varphi}}{\partial z}\right)\right]$ may be considered to act on the east face of the CV.

$$\left(2\mu\left(\frac{\partial \bar{\varphi}}{\partial x}\right)\right)_e \sim 2\mu \frac{\overline{\varphi_E} - \overline{\varphi_P}}{x_E - x_P} \qquad (2.28)$$

$$\left(\mu\left(\frac{\partial \bar{\varphi}}{\partial x} + \frac{\partial \bar{\varphi}}{\partial y}\right)\right)_e \sim \mu\left[\left(\frac{\overline{\varphi_E} - \overline{\varphi_P}}{x_E - x_P}\right) + \left(\frac{\overline{\varphi_{ne}} - \overline{\varphi_{se}}}{y_{ne} - y_{se}}\right)\right] \qquad (2.29)$$

$$\left(\mu\left(\frac{\partial\overline{\varphi}}{\partial x}+\frac{\partial\overline{\varphi}}{\partial z}\right)\right)_e \sim \mu\left[\left(\frac{\overline{\varphi_E}-\overline{\varphi_P}}{x_E-x_P}\right)+\left(\frac{\overline{\varphi_{re}}-\overline{\varphi_{le}}}{z_{re}-z_{le}}\right)\right] \quad (2.30)$$

Due to the collocated arrangement of solution variables, subscripts ne, se, re, le are not nodal values, thus further interpolations (linear) are required to calculate these terms in eqn. 2.29 & 2.30.

2.9 PRESSURE GRADIENT AND OTHER SOURCE TERM DISCRETISATION

After integrating over the cell volume, the pressure gradient term reduces to differences between cell face pressures. The pressure at cell faces is obtained using linear interpolation. For example at the east face it is written as $\bar{p}_e \sim \frac{1}{2}(\bar{p}_P + \bar{p}_E)$. Source terms are also discretised using two-point central differencing approximations similar to those in the diffusion terms.

2.10 BOUNDARY CONDITIONS

2.10.1 Fixed Inflow

For an incompressible solver, the fixed inflow condition requires the user to specify all convected quantities at all appropriate boundary nodes. All quantities (velocity components, turbulent kinetic energy, k, ϵ and φ) are assigned once at the start of the computation and not altered during the calculation.

2.10.2 Zero Gradient Outflow

For incompressible flows, a zero gradient extrapolation of all flow variables (except pressure) is the most commonly used outflow boundary condition. When the flow at the outlet is free from re-circulation, all quantities except pressure are given by $\frac{\partial\varphi}{\partial n}=0$; where n is the outflow surface normal vector.

To satisfy overall mass conservation, the velocity component normal to the boundary obtained at the outflow through the zero gradient approximation is scaled to match the mass flow at the inlet.

2.10.3 Wall Boundaries

No slip boundary conditions are applied at solid walls by implicitly specifying all velocity components to be zero at the boundary location during the initialisation of the calculation. During the course of calculation, the flow solver does not solve for the boundary cell thus maintaining the no slip condition throughout the calculation.

For high Reynolds number turbulent flow a wall function approach is adopted assuming a 'log-law' relationship instead of resolving the near-wall boundary layer region accurately by using a very fine grid (and a low Reynolds turbulence model). The wall function formulation used for the high Reynolds number k- ε model is presented below:

The Log law of the wall (see Hinze 1975 & Pope 2000) may be written as:

$$u^+ = \frac{\overline{u_t}}{u_\tau} = \frac{1}{\kappa}\ln\left(Ey^+\right) \qquad (2.31)$$

where E is a wall roughness factor, $\overline{u_t}$ is the mean velocity tangential to the wall, u_τ is the friction velocity given by $u_\tau = \sqrt{|\tau_w|/\rho}$, where $\tau_w$is the shear stress at the wall, κ is the von Karman constant (0.41) and y^+ is the non-dimensional wall normal distance, given by $y^+ = \frac{\rho u_\tau y}{\mu}$.

If it is assumed that the region near the wall where turbulent shear stress dominates is in local equilibrium (production and dissipation of turbulence are nearly equal), it can be shown that the friction velocity can be related to local near-wall turbulent kinetic energy via:

$$u_\tau = C_\mu^{1/4} k^{1/2} \qquad (2.32)$$

Using eqns. (2.31 & 2.32) a relation for wall shear stress can be obtained:

$$\tau_w = \frac{\overline{u_t} u_\tau \rho \kappa}{ln(Ey^+)} \qquad (2.33)$$

In discretised form, the wall shear stress can also be expressed as:

$$\tau_w = \mu_t^* \frac{\left(\overline{u_{t,n}} - \overline{u_{t,wall}}\right)}{y_n - y_{wall}} \qquad (2.34)$$

$\overline{u_{t,wall}}$, y_{wall} are the tangential mean velocity and the y co-ordinate at the wall respectively, μ_t^* is the value of the turbulent viscosity which is approximated in eqn. 2.34 using eqn. 2.33.

$$\mu_t{}^* = \frac{\tau_w y_n}{\overline{u_{t,n}}} \qquad (2.35)$$

Thus, this implementation of the wall function adopts a modified value for the wall node turbulent viscosity:

$$\mu_t{}^* = \frac{C_\mu^{1/4} k^{1/2} \rho \kappa y}{ln\left(Ey\rho C_\mu^{1/4} k^{1/2} \mu^{-1}\right)} \qquad (2.36)$$

The above represents the wall function procedure for momentum; a similar local equilibrium condition and log-law velocity profile assumption is made to evaluate the production term in the k equation, and this then leads to:

$$P = -\tau_w \frac{C_\mu^{1/4} \mathrm{k_P}^{1/2}}{k y_n} \qquad (2.37)$$

For the dissipation (ε), the high Reynolds number wall function approach is to fix ε in the control volume next to the wall, where it is set to the following value:

$$\varepsilon = \frac{C_\mu^{3/4} k_P^{3/2}}{\kappa y_n} \qquad (2.38)$$

2.10.4 Cyclic Boundaries

Cyclic boundary conditions can be used in order to reduce the size of the flow configuration to be simulated and to allow consideration of swirling flow problems. In Fuel-3D, a cyclic boundary condition applied for example in the z-direction is expressed by a variable transfer as shown in fig 2.4.

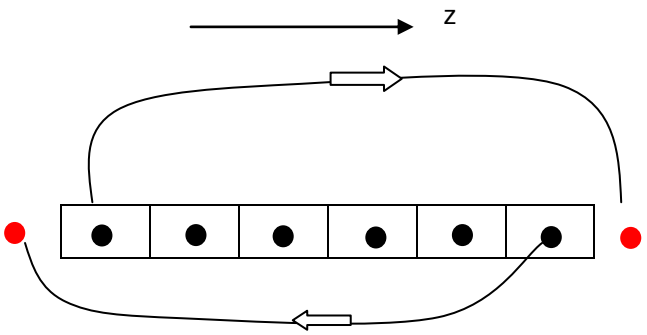

Figure 2. 4 - Data transfer methodology for cyclic boundary condition; see fig 2.3 for cell – colour information.

2.11 PRESSURE VELOCITY DE-COUPLING – A REMEDY- RHIE & CHOW SMOOTHING

The pressure gradients in the momentum equations are an important driving term; in general 2nd order central differencing (linear interpolation) is applied to pressure gradient discretisation. This approach works well with staggered grids and variable storage, but in a collocated arrangement leads to pressure-velocity de-coupling and checkerboard pressure oscillations. Rhie and Chow (1983) developed a methodology which suppresses this de-coupling, by using an alternative interpolation for the cell face convecting mass flux (see eqn. 2.18). Presented below is the method applied at the east face for the X-direction on a uniform grid, extension to other situations is straightforward.

In order to obtain the mass flux, G_e at the east face, cell face normal velocity is usually obtained by linear interpolation:

$$U_e = \frac{1}{2}(U_P + U_E) \qquad (2.39)$$

The discretised momentum equations from which U_P & U_E used in the above interpolation takes the form:

$$U_P^{n+1*} = \widetilde{U_P^{n+1*}} - \frac{1}{A_{PU}}\left(\frac{\partial p^n}{\partial x}\right)_P \qquad (2.40)$$

$$U_E^{n+1*} = \widetilde{U_E^{n+1*}} - \frac{1}{A_{PU}}\left(\frac{\partial p^n}{\partial x}\right)_E \qquad (2.41)$$

where superscript * indicates that the velocity so obtained will not generally satisfy the continuity equation and superscript ~ indicates the velocity contribution from all other terms except the pressure gradient.

Substituting (2.40) & (2.41) into eqn. (2.39) gives the cell face velocity in the discretised momentum equation form:

$$U_e^{n+1*} = \overline{\widetilde{U_e^{n+1*}} - \frac{1}{A_{PU}}\left(\frac{\partial \mathrm{p}^n}{\partial x}\right)_e} \qquad (2.42),$$

where an over-bar indicates linear interpolation.

It has been found that a cell face velocity evaluated as in eqn. (2.42) leads to decoupling due to the linear interpolation of pressure gradients; Rhie & Chow (1983) suggested replacing eqn. 2.42 by:

$$U_e^{n+1*} = \overline{\widetilde{U_e^{n+1*}} - \frac{1}{A_{PU}}\left(\frac{\partial \mathrm{p}^n}{\partial x}\right)_e - \frac{1}{A_{PU}}\left[\left(\frac{\mathrm{p}_E^n - \mathrm{p}_P^n}{\Delta x}\right) - \overline{\left(\frac{\partial p^n}{\partial x}\right)}\right]} \quad (2.43)$$

If this method is followed in determining the cell face velocities used to evaluate the mass fluxes (G_e etc), then the decoupling between velocity and pressure is avoided.

2.12 CONTINUITY EQUATION SOLUTION – PRESSURE-CORRECTION METHOD (SIMPLE)

For a fully implicit incompressible segregated solver, a pressure-correction method is typically used to enforce mass continuity (Patankar and Spalding (1972)). The pressure gradient term appearing in the momentum equation (eqn. 2.5) is evaluated using a guessed pressure field (pressure values taken from the previous time step), resulting in an approximate 'predicted' velocity field. The task now is to correct the predicted velocity (U_i^{n+1*}) and pressure (p^n) field such that mass conservation over the control volumes surrounding each node P is satisfied.

Based on a constant density (or density independent of pressure) incompressible assumption, the discretised form of the momentum equations solved to produce the approximate (non-continuity satisfying) velocity field is:

$$A_{P(i)}U_{i,P}^{n+1*} + \sum_l A_l U_l^{n+1*} = Q_{u_i}^n - \left(\frac{\partial p^n}{\partial x_i}\right)_P \qquad (2.44)$$

where the superscript n+1* represents the approximate predicted value for the n+1 time step and l denotes the neighbour points around P. Q represents all terms that are calculated based on last time-step information. The A_p coefficient in the first term of the above equation contains discretised convective and diffusive term contributions which involve the P node.

The velocities predicted by solving eqn. 2.44, do not satisfy the continuity equation due to the fact that a guessed pressure field has been used.

For convenience eqn. (2.44) may be written as

$$U_{i,p}^{n+1*} = \widetilde{U_{i,p}^{n+1*}} - \frac{1}{A_{p(i)}}\left(\frac{\partial P^n}{\partial x_i}\right)_p \qquad (2.45)$$

Here, $\widetilde{U_{i,p}^{n+1*}}$ represents the contribution from all terms in eqn. 2.44 except the pressure gradient term.

Adopting a predictor-corrector approach, the predicted velocity field (U_i^{n+1*}) is corrected so that it satisfies the continuity equation. To apply this predictor-corrector approach, velocity and pressure at the n+1 time-step are decomposed as follows:

$$U_i^{n+1} = U_i^{n+1*} + U_i{}' \qquad (2.46)$$

$$p^{n+1} = p^n + \mathrm{p}' \qquad (2.47)$$

These relations are substituted into the discretised momentum equation, eqn. (2.44), to obtain a relation between velocity and pressure corrections as:

$$U_{i,p}' = \widetilde{U_{i,p}'} - \frac{1}{A_{p(i)}}\left(\frac{\partial P'}{\partial x_i}\right)_p \qquad (2.48)$$

where $\widetilde{U_{i,p}'} = -\frac{\sum_l A_l U_l'}{A_{p(i)}}$

Finally, by substituting the velocity decomposition as shown in eqn. (2.46) into the discretised continuity equation with velocity corrections taken as in eqn. (2.48), a discrete Poisson equation for pressure correction equation is obtained:

$$\frac{\partial}{\partial x_i}\left[\frac{\rho}{A_{p(i)}}\left(\frac{\partial P\prime}{\partial x_i}\right)\right]_p = \left(\frac{\partial\left(\rho U_i^{n+1*}\right)}{\partial x_i}\right)_p + \left(\frac{\partial\left(\rho U_i'\right)}{\partial x_i}\right)_p \qquad (2.49)$$

The second term on the right hand side of the above Poisson equation is unknown and in common practice it is neglected (leading to the so-called SIMPLE algorithm). After solving the algebraic equation which results from eqn. 2.49, the pressure-correction field is obtained and hence the approximate velocity field can be corrected to produce a continuity satisfying velocity field.

2.13 MULTI-BLOCK STRUCTURED MESHES

Fuel-3D adopts a multi-block mesh to allow analysis of flow through complex geometries. A short description of the procedure to transfer data between the blocks is presented here, full details on the multi-block solver procedure and its implementation can be found in Baird (2001).

For ease of data transformation between blocks, halo cells are created in the mesh generated to fit the geometry, creating extra boundary cells. Thus each block contains (1) interior cells (●), (2) first halo cells (●) in which all the boundary conditions are applied as well as used for transferring data across blocks, and (3) second halo cells (●) for transferring data across blocks, see fig 2.5 for a 2D illustration.

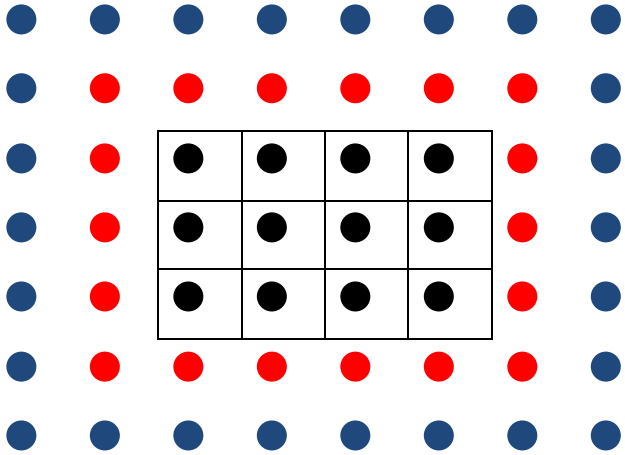

Figure 2. 5 - 2-D representation of interior and Halo cells.

Note there are reason that two halo cells are necessary is related to the way the Rhie and Chow smoothing term is evaluated, and this must be transferred properly across block boundaries. Because of the presence of cross-derivative diffusion terms corner point values in two or three locations are needed and care must be taken when solving variables which are non-zero at corner locations.

2.14 SOLUTION METHODOLOGY

To predict and analyse flow phenomena using CFD involves three basic stages: 1. Pre-processing, which consist of creating the geometry, generating the mesh to fit the geometry and applying boundary conditions, 2. Solving the discretised flow equations and 3. Post-processing, which involves analysing the solution obtained from flow solver.

The Fuel-3D code described here falls under the second part of the above process. A simple flow chart describing the steps involved is shown in Fig 2.6. An external mesh generator (ICEM) is used to generate the geometry of the solution domain and the associated grid point co-ordinate information. For post-processing the required data have been extracted and fed into Tecplot for visualisation and analysis.

Pre-Processor

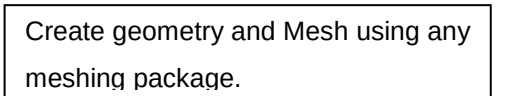

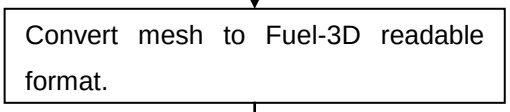

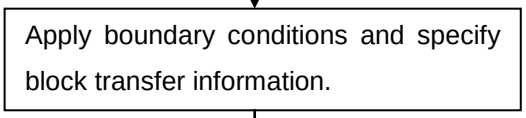

Fuel-3D

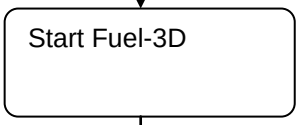

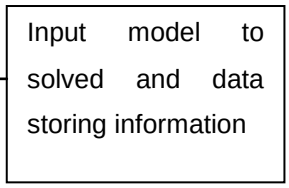

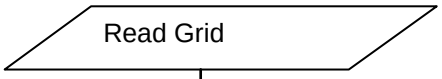

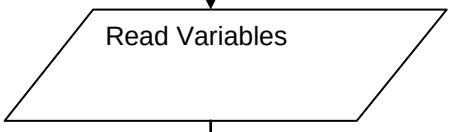

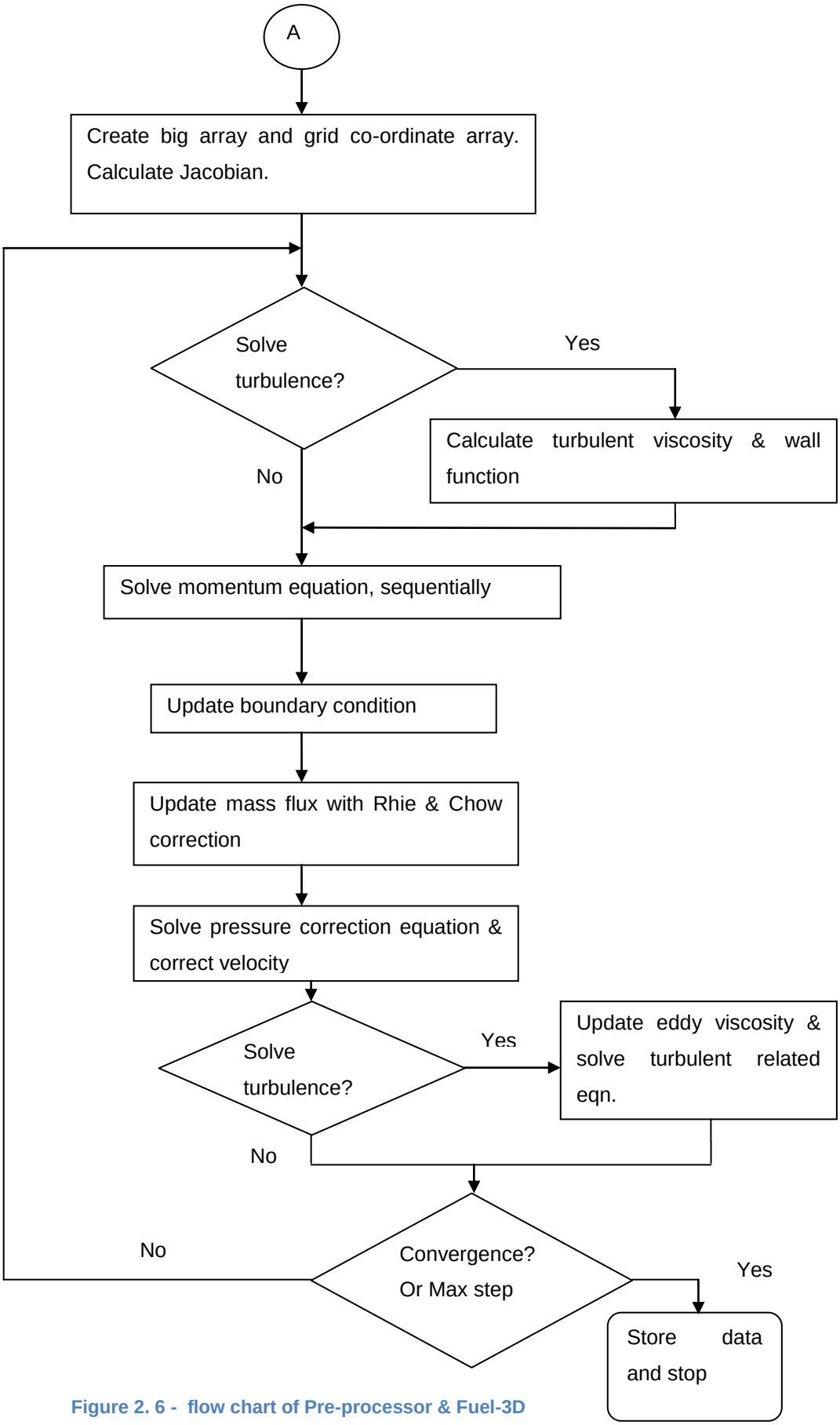

Figure 2. 6 - flow chart of Pre-processor & Fuel-3D

3. SELECTION AND VALIDATION OF BASELINE CFD ALGORITHM MODIFICATIONS FOR PREDICTION OF ACOUSTIC WAVE DYNAMICS.

3.1 INTRODUCTION

This chapter describes the various steps taken to convert the incompressible CFD code described in chapter 2 to a mildly compressible CFD code suitable for the prediction of unsteady acoustic wave propagation.

Firstly the modified set of governing differential equations appropriate to this type of flow problem are outlined. In order to achieve accurate numerical solution of acoustic wave propagation through space and time it is required that the numerical algorithm has to have the capability to preserve the shape and frequency of acoustic waves during propagation, for a wide range of wavelengths, with an affordable number of grid points per wavelength. Two alternative convection discretisation schemes were chosen to study their suitability for acoustic wave propagation, these are (i) the Weighted Essentially Non-Oscillatory (WENO) scheme (Shu,1997), since this is a higher order scheme appropriate for preservation of wave amplitude, and (ii) the Total Variation Diminishing (TVD) scheme (Branley et al.1997). Based on the results of Branley et al. (1997) and Dianat et al. (2006), which minimises the numerical dispersion associated with the second order Central Difference Scheme (CDS), and is thus optimised for use in complex turbulent flows containing shear layers and scalar mixing.

Initially using a simple implicit first order temporal scheme, the baseline pressure-correction algorithm was then modified to allow density dependency on pressure, as demanded by compressible equations. The modified pressure-correction equation was chosen to convert the Fuel-3D code into one valid for low-medium Mach number flows not containing shocks.

The third important issue addressed was provision of appropriate boundary conditions so that the acoustic waves could enter and leave the solution domain at amplitude/frequency conditions pre-specified by the user and without causing any numerical reflections or distortions. This issue was addressed by use of characteristic boundary conditions (Hirsch 1988). Once this mildly compressible version was fully developed and tested, a second order fully implicit temporal discretisation scheme (Ferziger et al. 2002) was implemented

and this version of the Fuel- 3D was then tested and validated for the test case of acoustic and entropy wave input-output relationships in a varying cross-section duct with mean flow.

3.2 COMPRESSIBLE FLOW GOVERNING EQUATIONS

The URANS equations for conservation of mass, momentum, energy and other scalar variables for compressible flow are modified versions of the incompressible flow versions given in chapter 2. It is usual to adopt a modified, mass-averaged (or density-averaged) form of time-averaging for compressible (and in general variable density) flows- Favre-averaging (see Pope (2000)); the instantaneous variable decomposition is now defined for any quantity φ as:

$$\varphi_{inst} = \tilde{\varphi} + \varphi" \qquad (3.1)$$

where, $\tilde{\varphi} = \frac{\overline{\rho\varphi}}{\bar{\rho}}$ and the overbar indicates usual Reynolds time-averaging as defined earlier.

With this modified statistical mean definition, the governing equations become:

Continuity equation:

$$\frac{\partial \bar{\rho}}{\partial t} + \frac{\partial \bar{\rho}\tilde{U}_i}{\partial x_i} = 0 \qquad (3.2)$$

Momentum equations:

$$\frac{\partial \bar{\rho}\widetilde{U_i}}{\partial t} + \frac{\partial\left(\bar{\rho}\widetilde{U_i}\widetilde{U_j}\right)}{\partial x_j} = -\frac{\partial \bar{p}}{\partial x_i} + \frac{\partial \overline{\tau_{ij}}}{\partial x_j} - \frac{\partial\left(\bar{\rho}\widetilde{u"_i u"_j}\right)}{\partial x_j} \qquad (3.3)$$

Energy equation:

$$\frac{\partial \bar{\rho}\tilde{E}}{\partial t} + \frac{\partial\left(\bar{\rho}\tilde{U}_j\tilde{H}\right)}{\partial x_j} = \frac{\partial\left(\overline{\tau_{ij}}\tilde{U}_i - \bar{q}_i\right)}{\partial x_j} - \frac{\partial}{\partial x_j}\left(\bar{\rho}\widetilde{u"_j e"}\right) - \frac{\partial}{\partial x_j}\left(\tilde{U}_i\bar{\rho}\widetilde{u"_i u"_j}\right) + \mathrm{D} \qquad (3.4)$$

Scalar transport equation:

$$\frac{\partial}{\partial t}\left(\bar{\rho}\tilde{\varphi}\right) + \frac{\partial}{\partial x_j}\left(\bar{\rho}\tilde{U}_j\tilde{\varphi}\right) = \frac{\partial}{\partial x_j}\left(\frac{\mu}{\sigma_\varphi}\frac{\partial\tilde{\varphi}}{\partial x_j}\right) - \frac{\partial}{\partial x_j}\left(\bar{\rho}\widetilde{u"_j\varphi"}\right) \qquad (3.5)$$

Finally the fluid properties are linked via the ideal gas law:

$$\bar{p} = \bar{\rho}R\tilde{T} \qquad (3.6)$$

where $\bar{p}$ is mean static pressure; τ_{ij} is the viscous stress tensor; $\tilde{E}$ is total energy ($\tilde{E} = \tilde{e} + \frac{1}{2}\tilde{U}_i\tilde{U}_i + \frac{1}{2}\tilde{k}$); H is total enthalpy ($\tilde{H} = \tilde{E} + \frac{\bar{p}}{\bar{\rho}}$); $\bar{q}_j$ is the heat flux vector ($= -\frac{k\partial\tilde{T}}{\partial x_j}$); R is the fluid gas constant; e is the specific internal energy ($e=C_vT$) and D is the dissipation function (usually neglected for low Mach number flows).

If a gradient diffusion approximation is used for modelling the turbulent fluxes:

$$-\bar{\rho}\widetilde{u"_i u"_j} = \mu_t\left(\frac{\partial\widetilde{U_i}}{\partial x_j} + \frac{\partial\widetilde{U_j}}{\partial x_i}\right) - \frac{2}{3}\mu_t\frac{\partial\widetilde{U_i}}{\partial x_j}\delta_{ij} - \frac{2}{3}\bar{\rho}\tilde{k}\delta_{ij} \qquad (3.7)$$

$$-\bar{\rho}\widetilde{u''_i e''} = C_p \frac{\mu_t}{\sigma_{t,T}} \left(\frac{\partial \tilde{T}}{\partial x_j}\right) \quad (3.8)$$

$$-\bar{\rho}\widetilde{u''_i \varphi''} = \frac{\mu_t}{\sigma_{t,\varphi}} \left(\frac{\partial \tilde{\varphi}}{\partial x_j}\right) \quad (3.9)$$

then the Favre-averaged URANS equations relevant to compressible flows assume a form very similar to their incompressible counterparts viz:

$$\frac{\partial \bar{\rho}}{\partial t} + \frac{\partial \bar{\rho}\widetilde{U_i}}{\partial x_i} = 0 \quad (3.10)$$

$$\frac{\partial \bar{\rho}\widetilde{U_i}}{\partial t} + \frac{\partial \left(\bar{\rho}\widetilde{U_i}\widetilde{U_j}\right)}{\partial x_j} =$$

$$-\frac{\partial \bar{p}}{\partial x_i} + \frac{\partial}{\partial x_j}\left\{(\mu + \mu_t)\left[\left(\frac{\partial \widetilde{U_i}}{\partial x_j} + \frac{\partial \widetilde{U_j}}{\partial x_i}\right) - \frac{2}{3}\frac{\partial \widetilde{U_i}}{\partial x_j}\delta_{ij}\right]\right\} - \frac{\partial}{\partial x_j}\left(\frac{2}{3}\bar{\rho}\tilde{k}\right)\delta_{ij} \quad (3.11)$$

$$\frac{\partial \bar{\rho}\tilde{E}}{\partial t} + \frac{\partial \left(\bar{\rho}\widetilde{U_j}\tilde{H}\right)}{\partial x_j} = \frac{\partial}{\partial x_j}\left\{C_p\left[\frac{\mu}{\sigma_T} + \frac{\mu_t}{\sigma_{t,T}}\right]\left(\frac{\partial \tilde{T}}{\partial x_j}\right)\right\} + W_f + \mathrm{D} \quad (3.12)$$

$$\frac{\partial}{\partial t}\left(\bar{\rho}\tilde{\varphi}\right) + \frac{\partial}{\partial x_j}\left(\bar{\rho}\widetilde{U_j}\tilde{\varphi}\right) = \frac{\partial}{\partial x_j}\left(\left[\frac{\mu}{\sigma_\varphi} + \frac{\mu_t}{\sigma_{\varphi,t}}\right]\frac{\partial \tilde{\varphi}}{\partial x_j}\right) \quad (3.13)$$

where W_f is the term which accounts for work done by the mean velocity field against both mean and turbulent stresses.

For the mildly compressible low Mach flows of primary interest here (acoustic wave propagation), the incompressible Fuel-3D code has been modified to solve the above versions of the governing URANS equations, with appropriate discretisation practices introduced. The density must be allowed to depend on both pressure and temperature as seen in the ideal gas law. This density/pressure linkage is then also used to modify the pressure-correction equation following Karki et al. (1989) and by including also solution of the energy equation with appropriate assumptions. Since the flow problems of interest here have low Mach number mean flow, and the compressible effects enter only via the acoustic waves, and these are traditionally assumed to be characterised well by inviscid, isentropic, adiabatic assumptions, then a reduced form of the energy equation may be adopted, viz:

$$\frac{\partial \rho \tilde{E}}{\partial t} + \frac{\partial \bar{\rho}\tilde{E}\widetilde{U_j}}{\partial x_j} = -\frac{\partial \bar{p}\widetilde{U_j}}{\partial x_j} \quad (3.14)$$

It is this form of the energy equation which has been solved in all the flow problems described below where the energy equation was required. Then using the predicted total energy ($\tilde{E}$) and corrected absolute pressure ($\bar{p}$), density was obtained through equation of state as described in eqn (3.6), where temperature $(\tilde{T})$ is obtained from specific internal energy $(\tilde{e}) = C_v \tilde{T}, and\ \tilde{e} = \tilde{E} - \frac{\widetilde{U_{mag}}^2}{2}$. In the case of incompressible flow it is common practice in RANS CFD codes to merge pressure with a turbulence energy term but for compressible flow the pressure term must be kept separate for use in the ideal gas law. The

following section describes the various parts of the CFD algorithm detailed in chapter 2 that were modified to introduce appropriate numerical treatments for the acoustic wave phenomena problems of interest in this thesis.

3.3 SPATIAL DISCRETISATION SCHEMES

Two modified convection discretisation schemes have been introduced and are detailed below:

3.3.1. Total Variation Diminishing (TVD) Scheme

The discretisation schemes originally used in pressure-based methods are either too dissipative (eg: 1st order Upwind scheme) or too dispersive (e.g., 2nd order central difference scheme) when the numerical solution displays steep gradients. In order to capture steep gradient regions accurately, fine grids become necessary, which results in higher computational cost. Based on the concept of Lax (1973) that the total variation of any physically admissible solution does not increase in time:

$$TV(\varphi) = \sum_i \left| \varphi_{i+1} - \varphi_i \right| \qquad (3.15)$$

$$TV(\varphi^{n+1}) \le TV(\varphi^n) \qquad (3.15a)$$

where TV(φ) is the Total Variation of the scalar quantity, φ.

Harten (1983) introduced a class of schemes (called TVD), in which the variation of the numerical solution between consecutive time steps was controlled by a limiter function. Many limiter functions have been identified, for example: minmod, superbee (both from Roe, 1981), Chakravarthy and Osher (1983). For a complete description of various limiter functions, see Hirsch, (1988). In the current work, the limiter introduced by Branley et al. (1997) was employed and this will be briefly described here. The choice of this limiter function was based on a study by Dianat et al.(2006) who showed that a TVD scheme with the Branley and Jones (1997) was superior to a DRP scheme of higher order in a test problem which emphasised convection of steep gradient regions at varying angles to the mesh sizes.

The Branley and Jones (1997) TVD approach involves a baseline scheme (2nd order central differencing (CDS)), with a limiter to suppress the unwanted dispersion oscillations of CDS. To illustrate the concept of the scheme, consider the discretised form of an inviscid scalar profile propagating in the positive x-direction with constant wave speed c. The governing equation is:

$$\frac{\partial \varphi}{\partial t} + c\frac{\partial \varphi}{\partial x} = 0 \qquad (3.16)$$

Adopting a TVD approach for discretisation of the convective term and an Euler backward difference (explicit) scheme for the transient term gives:

$$\varphi_i^{n+1} = \varphi_i^n - C_0\{[\varphi_i^n + \frac{1}{2}\psi_{ef}(\varphi_{i+1}^n - \varphi_i^n)] - [\varphi_{i-1}^n + \frac{1}{2}\psi_{wf}(\varphi_i^n - \varphi_{i-1}^n)] \qquad (3.17)$$

where $C_0 = \frac{c\Delta x}{\Delta t}$ is the Courant number, ψ_{wf}, ψ_{ef} are coefficients in the Branley et al. (1997), limiter function for the west face and east face of the cell.

e.g., $$\psi_{ef} = \max(0, \min(2r_{ef}, 1) \qquad (3.18)$$

where r_{ef} is the ratio of φ gradients at the west and the east faces;

$$r_{ef} = \left(\frac{\partial\varphi}{\partial x}\right)_{wf}^n / \left(\frac{\partial\varphi}{\partial x}\right)_{ef}^n \qquad (3.19)$$

$$\left(\frac{\partial\varphi}{\partial x}\right)_{ef}^n = \frac{\varphi_{i+1}^n - \varphi_i^n}{x_{i+1} - x_i} \qquad (3.19a)$$

if r_{ef} is ≥ 0.5, then the limiter function at the east face, ψ_{ef}, of Eqn (3.2), will be equal to 1, leading to pure central differencing. When $r_{ef} \leq 0$, then the limiter function becomes 0 which results in a pure upwind differencing (UDS) form for the east face, which will suppress the unwanted oscillations. In between 0 and 0.5 the limiter weights the cell flux value between UDS and CDS schemes.

3.3.2 Weighted Essentially Non-Oscillatory (WENO) Scheme

A third order WENO scheme was first developed by Liu et al. (1994) for solving hyperbolic equations. Later, it was modified and used in many applications varying from incompressible flows to Hamilton-Jacobi equations and magneto-hydrodynamics applications. As described in chapter 1 WENO schemes use a combination of several stencils, each stencil being assigned a nonlinear weight depending on the local smoothness of the numerical solution based on that stencil, (Jiang et al. 1996). The interest in applying the WENO scheme for the present application is it offers the possibility of reducing numerical diffusion and dispersion for the propagation of a given acoustic wavelength with a smaller number of grid points per wavelength.

For an east face of a control volume P, based on a required order of accuracy (identified here as N) the WENO scheme can be constructed by the following procedure (for a

complete description see, Shu 1997), for ease of explanation a 1D convective term in Cartesian co-ordinates is considered:

Identify several stencils S_j, (j = 1,….,q) around the P control volume, such that the sum of left and right control volumes plus the main cell equals the required order of accuracy N. After identifying these base stencils, construct a larger stencil which contains all the cells from the selected smaller stencils. Using a Lagrange polynomial (Shu (1997)) construct a lower-order polynomial approximation '$p_j(x)$' for each selected stencil. Find a combination of coefficients (linear weights) γ_j such that for the Gaussian point G_k on the control volume boundary:

$$Q(G_k) = \sum_{j=1}^{q} \gamma_j p_j(G_k) \qquad (3.20)$$

for all possible given cell averages in the stencil. These linear weights depend only on the point G_k and the specific reconstruction requirements but not on the given solution data in the stencils.

Compute the smoothness indicator β_j for each stencil S_j, which measures the smoothness of the function p_j in the target cell. The smaller the smoothness indicator the more smooth the function p_j.:

$$\beta_j = \sum_{1 \le k} \int_{\Delta} \Delta \left(D^{\alpha} p_j \right)^2 dx \qquad (3.21)$$

where k is the degree of the polynomial p_j, Δ is the cell distance in 1D, $D^{\alpha} = \partial_x^{\alpha}$, and α is multi-index in d space dimensions. (See, Shu (1997), for more details about the smoothness indicator and its derivation.)

Now calculate the nonlinear weight based on the smoothness indicators (β_j) and linear weights (γ_j):

$\omega_j = \dfrac{\tilde{\omega}_j}{\sum_j \tilde{\omega}_j}$, $\tilde{\omega}_j = \dfrac{\gamma_j}{\left(\varepsilon + \beta_j\right)^2}$; where ε is a small number used to avoid a zero denominator.

The final WENO approximation for the east face of control volume P is:

$$R(x) = \sum_{j=1}^{q} \omega_j p_j(x) \qquad (3.22)$$

Based on the above procedure, a fifth order WENO scheme can be constructed using a stencil of five cells {WW,W,P,E,EE}with the target cell containing the point e, for a positive U velocity. Following the above procedure three small stencils identified as:

$$S_1 = \{WW, W, P\}, \quad S_2 = \{W, P, E\}, \; S_3 = \{P, E, EE\}. \tag{3.23}$$

together these make up the larger stencil:

$$T = \{WW, W, P, E, EE\}. \tag{3.24}$$

The next step is to create the polynomial, whose cell averages agree with that of the function u in the three cells of each stencil. The Lagrange polynomials are given by:

$$\begin{aligned} p_{1e} &= \frac{1}{3}\varphi_{WW} - \frac{7}{6}\varphi_W + \frac{11}{6}\varphi_P, \\ p_{2e} &= -\frac{1}{6}\varphi_W + \frac{5}{6}\varphi_P + \frac{1}{3}\varphi_E, \\ p_{3e} &= \frac{1}{3}\varphi_P + \frac{5}{6}\varphi_E - \frac{1}{6}\varphi_{EE}. \end{aligned} \tag{3.25}$$

The higher order polynomial approximation for the larger stencil Q, is thus:

$$Q = \frac{1}{30}\varphi_{WW} - \frac{13}{60}\varphi_W + \frac{47}{60}\varphi_P + \frac{9}{20}\varphi_E - \frac{1}{20}\varphi_{EE}. \tag{3.26}$$

Linear weights are then obtained by the linear combination of Eqn (3.23) and (3.24).

$$\gamma_1 = \frac{1}{10}; \qquad \gamma_2 = \frac{3}{5}; \quad \gamma_3 = \frac{3}{10}. \tag{3.27}$$

From Eqn (3.8) the three smoothness indicators are:

$$\begin{aligned} \beta_1 &= \frac{13}{12}(\varphi_{WW} - 2\varphi_W + \varphi_P)^2 + \frac{1}{4}(\varphi_{WW} - 4\varphi_W + 3\varphi_P)^2 \\ \beta_2 &= \frac{13}{12}(\varphi_W - 2\varphi_P + \varphi_E)^2 + \frac{1}{4}(\varphi_W - \varphi_E)^2 \\ \beta_1 &= \frac{13}{12}(\varphi_P - 2\varphi_E + \varphi_{EE})^2 + \frac{1}{4}(3\varphi_P - 4\varphi_E + \varphi_{EE})^2 \end{aligned} \tag{3.28}$$

And thus flux at ‘e’ face is:

$$F_e = \omega_1 p_{1e} + \omega_2 p_{2e} + \omega_3 p_{3e} \tag{3.29}$$

The above constructed WENO scheme produces sharp and non-oscillatory solutions at steep gradients which should be very effective in solving acoustic wave propagation. This method will be compared with the TVD method and other alternatives below.

3.4 PRESSURE-CORRECTION ALGORITHM FOR MILDLY COMPRESSIBLE FLOW

To simulate compressible flow using a pressure-based method it is necessary to couple pressure and density together, an aspect missing in traditional incompressible pressure-correction methods (see section 2.12). This section deals with the extension of the pressure-based method (SIMPLE) already incorporated into the Fuel-3D code to allow prediction of subsonic bulk flow and acoustic waves.

For ease of explanation, the pressure-correction equation derived below is again presented for an unsteady, one-dimensional situation using a Cartesian grid. Similar to the incompressible version (section 2.12) the velocities obtained from segregated solution of the momentum equations with a guessed pressure field are just "estimates predictions" at the new time level and "don't" satisfy the continuity equation (eqn. 3.10). Since the density at the new time step is also unknown, the predictor – corrector approach is also used for density. Thus, density at the new time step is represented as a sum of density at previous time plus a density correction, $\overline{\rho}^{n+1} = \overline{\rho}^{n} + \overline{\rho}'$. Velocity at the new time step is also so represented as initial predicted velocity ($\widetilde{U}^{*}$) plus a velocity correction ($\widetilde{U}'$); $\widetilde{U}^{n+1} = \widetilde{U}^{*} + \widetilde{U}'$. Substituting these decompositions into 1D continuity equation:

$$\frac{\partial \overline{\rho}}{\partial t} + \frac{\partial \overline{\rho}\widetilde{U}}{\partial x} = 0 \qquad (3.30)$$

gives $\frac{\overline{\rho}'}{\Delta t} + \frac{\partial}{\partial x}\left[\left(\overline{\rho}^{n} + \overline{\rho}'\right)\left(\widetilde{U}^{*} + \widetilde{U}'\right)\right] = 0$. (3.31)

The nonlinear term $\left(\overline{\rho}^{n} + \overline{\rho}'\right)\left(\widetilde{U}^{*} + \widetilde{U}'\right)$ = $\overline{\rho}^{n}\widetilde{U}^{*} + \overline{\rho}^{n}\widetilde{U}' + \overline{\rho}'\widetilde{U}^{*} + \overline{\rho}'\widetilde{U}'$, is significantly different from the incompressible version which contains only $\overline{\rho}^{n}\widetilde{U}^{*} + \overline{\rho}^{n}\widetilde{U}'$. The additional terms are due to inclusion of density variation. The second order correction term, $\overline{\rho}'\widetilde{U}'$ in eqn. (3.31) is neglected as a linear approximation which will not be important for small time-steps.

Thus, the continuity equation is: $\frac{\overline{\rho}'}{\Delta t} + \frac{\partial}{\partial x}\left[\overline{\rho}^{n}\widetilde{U}^{*} + \overline{\rho}^{n}\widetilde{U}' + \overline{\rho}'\widetilde{U}^{*}\right] = 0$ (3.32)

From the 1-D Momentum Equation (assuming inviscid for convenience):

$$\frac{\partial \overline{\rho}\widetilde{U}}{\partial t} + \frac{\partial \overline{\rho}\widetilde{U}^{2}}{\partial x} = -\frac{\partial \overline{p}}{\partial x}, \qquad (3.33)$$

and by using $\widetilde{U} = \widetilde{U}^{*} + \widetilde{U}'$, it is possible to obtain the relationship between velocity and pressure corrections U' and p':

$$\tilde{U}'^{n+1}_{i,j} = -\frac{1}{\dfrac{\bar{\rho}^{n}_{i,j}}{\Delta t} + \dfrac{\bar{\rho}^{n}_{i,+1/2,j}\tilde{u}^{n}_{i,+1/2,j}}{\Delta x}}\frac{\partial \bar{p}'}{\partial x} \qquad (3.34)$$

A relationship between density and velocity correction may be written ($\bar{\rho}'$ and $\bar{p'}$) as

$\bar{\rho}' = k\bar{p'}$, where k = $\dfrac{\partial \bar{\rho}}{\partial \bar{p}}$

the quantity k in the above relation may be recognised as related to the speed of sound (c), a key property for compressibility and acoustic waves:

$$c^2 = \frac{\partial \bar{p}}{\partial \bar{\rho}} = \gamma R\tilde{T} \qquad (3.35)$$

Substituting these correction relations back into the continuity equation (eqn. 3.32) the following equation for pressure correction (p') is obtained.

$$\frac{\bar{p}'}{\gamma R\tilde{T}\Delta t} + \frac{\partial}{\partial x}\left[-\frac{1}{A_P}\frac{\partial \bar{p}'}{\partial x}\right]\bar{\rho}^{n} + \frac{\partial}{\partial x}\left[\frac{\bar{p}'}{\gamma R\tilde{T}}\right]\tilde{U}^{*} = -\frac{\partial \bar{\rho}^{n}\tilde{U}^{*}}{\partial x} \qquad (3.36)$$

Comparing the above equation with the incompressible version of the pressure-correction equation shows that pressure-velocity-density coupling results in two added contributions. The first term in eqn.3.36 is due to the temporal variation of density in continuity, and the third term is due to the spatial variation of density. The second term is similar to diffusion-like term with the third term similar to a convection term. The ratio of these two terms is proportional to the inverse of the square of Mach number. At low Mach numbers, the diffusion term is dominant and the pressure-correction equation will be elliptic as in incompressible flow. As the Mach number increases, the convection term becomes progressively more dominant and the equation becomes hyperbolic. This pressure-correction equation may be solved using similar numerical techniques as for the constant density case.

3.5 CHARACTERISTIC BOUNDARY CONDITIONS

In solving acoustic problems it is essential to use appropriate boundary conditions at flow inlets/outlets to provide correct representation of acoustic excitation waves, and to represent physically correct reflected and transmitted waves at these solution domain boundaries. Many researchers have studied this issue; comprehensive reviews can be found in Hirsch (1988), Poinsot et al. (2005) and Colonius (2004). In the current work, where we are mainly interested in ensuring accurate characterisation of the amplitude of plane acoustic waves entering and leaving the solution domain, a simple 1D approach to implementation of characteristic boundary conditions for subsonic inlets and outlets within a pressure-based formulation forms the optimum starting point. If necessary, the same

approach could be easily modified to incorporate more complex characteristic treatments (e.g. Hirsch (1988), Poinsot et al. (2005)).

The characteristic boundary conditions which will be used are derived from 1-D Euler equations written in characteristic form as (Hirsch 1988):

$$D^0\rho - \frac{1}{c^2}D^0 p = 0 \tag{3.37}$$

$$D^+U + \frac{1}{\rho c}D^+ p = -\frac{Uc}{s}dS \tag{3.38}$$

$$D^-U - \frac{1}{\rho c}D^- p = \frac{Uc}{s}dS \tag{3.39}$$

where D^0, D^+, D^- defined as follows:

$$D^0 = \partial_t + U\partial_x; D^+ = \partial_t + (U+c)\partial_x; D^- = \partial_t + (U-c)\partial_x$$

and S represents the cross-sectional area of the 1D flow.

From the above equations it is clear that all variables propagate at three different velocities U, U+c, U-c. In the case of supersonic flow, all three propagation velocities are in the same direction, whereas for subsonic flow, two of these velocities (U, U+c) travel in the same direction and the other propagates (U-c) in the opposite direction, as shown in fig 3.1, (assuming U is positive):

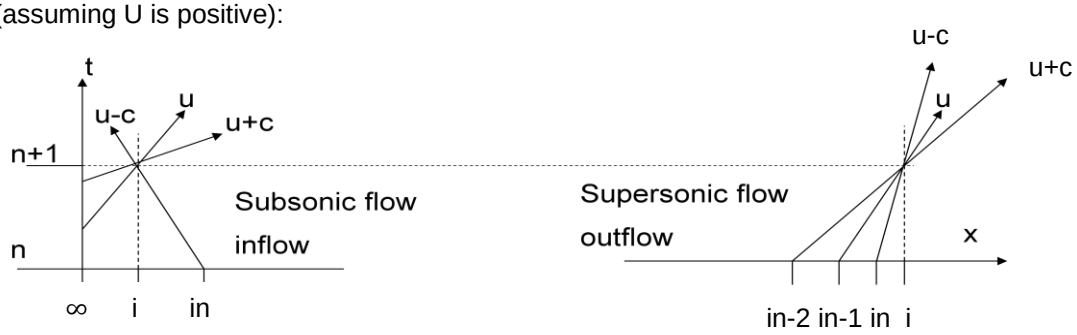

Figure 3. 1 - Influence of characteristic velocities at subsonic (inlet) and supersonic (outlet condition) flows.

The equation (3.37) relates the variation of entropy, which propagates along the path line at a speed determined by the convection velocity (U) and is conserved along this characteristic, as long as discontinuities do not appear. Thus in systems with constant entropy at the boundaries (i.e., no shock or discontinuity), the acoustic contribution to the primitive variables (pressure and velocity) at the boundary can be obtained by relating the right and left propagating characteristic variables (eqn 3.38 and 3.39) as shown below, as long as the boundary has a constant cross-sectional area (making the right-hand side of eqn 3.38 and 3.39 to zero):

$$\frac{\partial \tilde{u}}{\partial t}+\frac{1}{\overline{\rho c}}\frac{\partial \tilde{p}}{\partial t}+(\bar{U}+\bar{c})(\frac{\partial \tilde{u}}{\partial x}+\frac{1}{\overline{\rho c}}\frac{\partial \tilde{p}}{\partial x})=0 \quad (3.40)$$

$$\frac{\partial \tilde{u}}{\partial t}-\frac{1}{\overline{\rho c}}\frac{\partial \tilde{p}}{\partial t}+(\bar{U}-\bar{c})(\frac{\partial \tilde{u}}{\partial x}-\frac{1}{\overline{\rho c}}\frac{\partial \tilde{p}}{\partial x})=0 \quad (3.41)$$

where a tilde (~) here indicates the acoustic contribution to the Favre-averaged primitive variables shown with an overbar (-). Equations 3.40 and 3.41 are discretised using a first order Euler method in time and an upwind difference method in space. The example procedure described below is for applying this characteristic based acoustic boundary condition for a subsonic inflow. In the following equations the subscript indicates the spatial index of the CV (where 'i' is the boundary CV, 'in' is the first interior CV and '∞' is for the upstream value of the variable) and the superscript indicates the temporal index.

The convective part of two equations 3.40 and 3.41 are discretised as follows, assuming unit grid size:

$$w_{right}=(\bar{U}^{n}+\bar{c}^{n})((\tilde{u}_{i}^{n}-\tilde{u}_{\infty}^{n})+\frac{1}{\overline{\rho^{n}c^{n}}}(\tilde{p}_{i}^{n}-\tilde{p}_{\infty}^{n})) \quad (3.42)$$

$$w_{left}=(\bar{U}^{n}-\bar{c}^{n})((\tilde{u}_{in}^{n}-\tilde{u}_{i}^{n})-\frac{1}{\overline{\rho^{n}c^{n}}}(\tilde{p}_{in}^{n}-\tilde{p}_{i}^{n})) \quad (3.43)$$

Thus, equations 3.40 and 3.41 become:

$$\frac{\tilde{u}_{i}^{n+1}}{\Delta t}-\frac{\tilde{u}_{i}^{n}}{\Delta t}+\frac{1}{\overline{\rho^{n}c^{n}}}(\frac{\tilde{p}_{i}^{n+1}}{\Delta t}-\frac{\tilde{p}_{i}^{n}}{\Delta t})=-w_{right} \quad (3.44)$$

$$\frac{\tilde{u}_{i}^{n+1}}{\Delta t}-\frac{\tilde{u}_{i}^{n}}{\Delta t}-\frac{1}{\overline{\rho^{n}c^{n}}}(\frac{\tilde{p}_{i}^{n+1}}{\Delta t}-\frac{\tilde{p}_{i}^{n}}{\Delta t})=-w_{left} \quad (3.45)$$

By adding and subtracting equations 3.44 and 3.45 the acoustic velocity and pressure components are obtained:

$$\tilde{u}_{i}^{n+1}=\tilde{u}_{i}^{n}-\frac{\Delta t}{2}(w_{right}+w_{left}) \quad (3.46)$$

$$\tilde{p}_{i}^{n+1}=\tilde{p}_{i}^{n}-\frac{\Delta t\overline{\rho^{n}c^{n}}}{2}(w_{right}-w_{left}) \quad (3.47)$$

The remaining variables can be obtained using the thermodynamic relations $\frac{\rho_i}{\rho_{in}}=\left(\frac{p_i}{p_{in}}\right)^{\frac{1}{\gamma}}$ and the equation of state; p = ρ RT. For example, to input a plane acoustic wave, such as from a loudspeaker, a harmonic acoustic pressure to match the required amplitude level of

the plane wave as well as its corresponding acoustic velocity field are specified in the above equation for the pressure and velocity variables having ∞ as subscript. Similarly, infinite acoustic pressure and velocity contribution to the above equation must be taken as zero to represent an infinite acoustic duct entry/termination.

For the case of a subsonic outflow, the primitive variables can be obtained in a similar manner to the subsonic inlet described above, just by interchanging variables such as $\tilde{f}_{in} \rightarrow \tilde{f}_{\infty}$ and $\tilde{f}_{\infty} \rightarrow \tilde{f}_{in}$ in eqns. 3.42 -.3.47. Alternatively other methods, which are specifically designed for an outflow condition, are available, such as:

1. Based on Rudy and Strikwerda (1980), $\tilde{p}_i^{n+1}$, $\tilde{\rho}_i^{n+1}$ are obtained by extrapolating $\tilde{u}_i^{n+1}$, $\tilde{v}_i^{n+1}$, $\tilde{w}_i^{n+1}$, $\tilde{T}_i^{n+1}$

$$\tilde{p}_i^{n+1} = \left[\tilde{p}_i^{n} + \alpha \Delta t \tilde{p}_{\infty} + \overline{\rho^n \; c^n}\left(\tilde{u}_i^{n+1} - \tilde{u}_i^{n}\right)\right]\frac{1}{1+\alpha\Delta t} \qquad (3.48)$$

2. Similar to the zero-gradient outflow condition commonly used in incompressible flows, all variables can be extrapolated from the interior.

However, the Rudy and Strikwerda (1980) method as well as complete extrapolation of variables produced numerical reflections when incorporated in a simple 1D flow analysis. Thus in the rest of this thesis only the characteristic boundary condition was considered. Commonly used acoustic boundary conditions in a duct flow such as an open-ended duct termination or a closed duct can be specified in a straight forward way by relating characteristic information from $w_{right,}$ w_{left} in eqns. 3.43 and 3.44 to obtain acoustic pressure and acoustic velocity. In the case of an open duct termination, a pressure node is assumed to be present at the boundary. Based on the available information from left/right travelling waves it can be arranged that the acoustic pressure at the boundary becomes zero. For example, to apply an open end condition at a duct exit located in a y-z plane, information on w_{right} in eqn 3.44 and 3.47 can be obtained through eqn. 3.42. In order to satisfy zero acoustic pressure corresponding to an open end termination, w_{left} (which is unknown) must be equal to $w_{right.}$ Acoustic velocity corresponding to an open end termination can then be obtained using eqn. 3.46. Similarly, for the case of an acoustically closed end condition, there will be an acoustic pressure anti-node at the boundary, whereas the acoustic velocity will have a nodal point. Hence, by relating the w_{left} information to w_{right} to obtain zero acoustic velocity at the boundary, the acoustic pressure can be calculated. Thus, using these characteristic boundary conditions a wide range of acoustic boundary treatment can be specified.

3.6 VERIFICATION AND VALIDATION TEST CASES

At each stage of introducing the above modifications bench-mark test cases were carried out. The following sub-section contains details of these verification and validation predictions.

3.6.1 1-D Linear Wave Propagation

To study the ability of the newly implemented discretisation schemes such as TVD and WENO to predict wave propagation, and to compare with traditional second order Central difference scheme (CDS) (for completeness a pure Upwind scheme (UDS) was also studied), a linear one-dimensional convective wave equation problem was solved using a simple first-order implicit scheme for time. The 1D linear convective wave equation for a scalar property (T) being convected at a constant velocity (u) is:

$$\frac{\partial T}{\partial t} + u\frac{\partial T}{\partial x} = 0 \qquad (3.49)$$

The scalar variable was initialised as a Gaussian profile with a specified width in the X direction and its convection at speed 'u' analysed:

$$T = 0.5\exp\left[-\ln 2\left(\frac{x - x_0}{r}\right)^2\right] \text{; at t = 0} \qquad (3.50)$$

where r is the rms (Root Mean Square) of the Gaussian shape. This is the parameter which characterises the X direction wavelength of the perturbation in T, x_o is the location of the peak in the Gaussian profile. The amplitude was taken as 0.5. The exact solution of this linear wave equation is:

$$T = 0.5\exp\left[-\ln 2\left(\frac{x - x_0 - ut}{r}\right)^2\right] \qquad (3.51)$$

In general, the frequency of acoustic pressure perturbations of most interest falls between a few Hertz to kilo Hertz; thus the spatial wavelength that needs to be resolved can vary from a few mm to of order 1 metre. The numerical scheme to be used for capturing the waves should possess the capability of capturing both long and short wavelength accurately on a given grid. Three classes of waves were tested, they are

1. Long wave $\left(r/\Delta x\right) \geq 15$
2. Intermediate wave $6 < \left(r/\Delta x\right) < 15$
3. Short wave $\left(r/\Delta x\right) < 6$

These three classes were based on Tam and Webb (1993). In the current work, the above three wave classes are achieved by varying the grid spacing. By reducing the CFL number

$\left(\frac{u\Delta t}{\Delta x}\right)$ (by decreasing the time step (Δt)), the temporal accuracy of the schemes was improved until solution behaviour become asymptotic. Since only a simple 1st order temporal discretisation was used here, the temporal efficiency was not of primary interest.

The CDS and WENO solutions for short wave and CDS, TVD and WENO solutions for intermediate waves displayed asymptotic behaviour at CFL = 0.05. This low value of CFL is due to the 1st order accurate time discretisation scheme employed. For convenience all the results described below were obtained using this CFL. Figures (3.2 - 3.4) depict the Gaussian profile propagation after 10 sec for all three wavelengths compared to the exact solution. For a long wavelength (r/dx=15), three schemes (CDS, TVD and WENO) except UDS capture the waveform well with hardly noticeable dispersion and dissipation errors (fig 3.2). For the intermediate wavelength (as the number of mesh points per wavelength decreases from 15 to 6), the performance of all schemes decreases. Phase error is dominant in the case of CDS. Phase error is minimal for TVD scheme at the expense of decreased amplitude. The WENO method out-performs the other schemes in this case without any oscillations and with minimal numerical diffusion (fig 3.3).

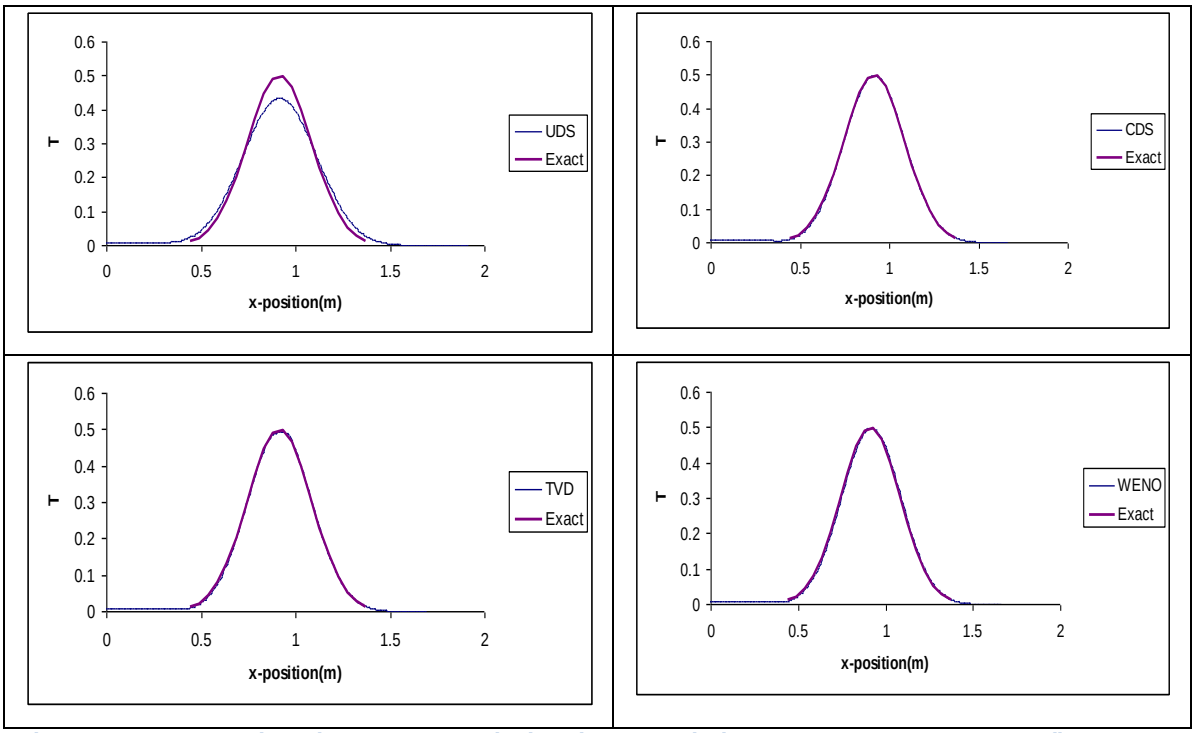

Figure 3. 2 - Comparison between numerical and exact solution at CFL 0.05 at t =10sec, (long wave: r/dx =15)

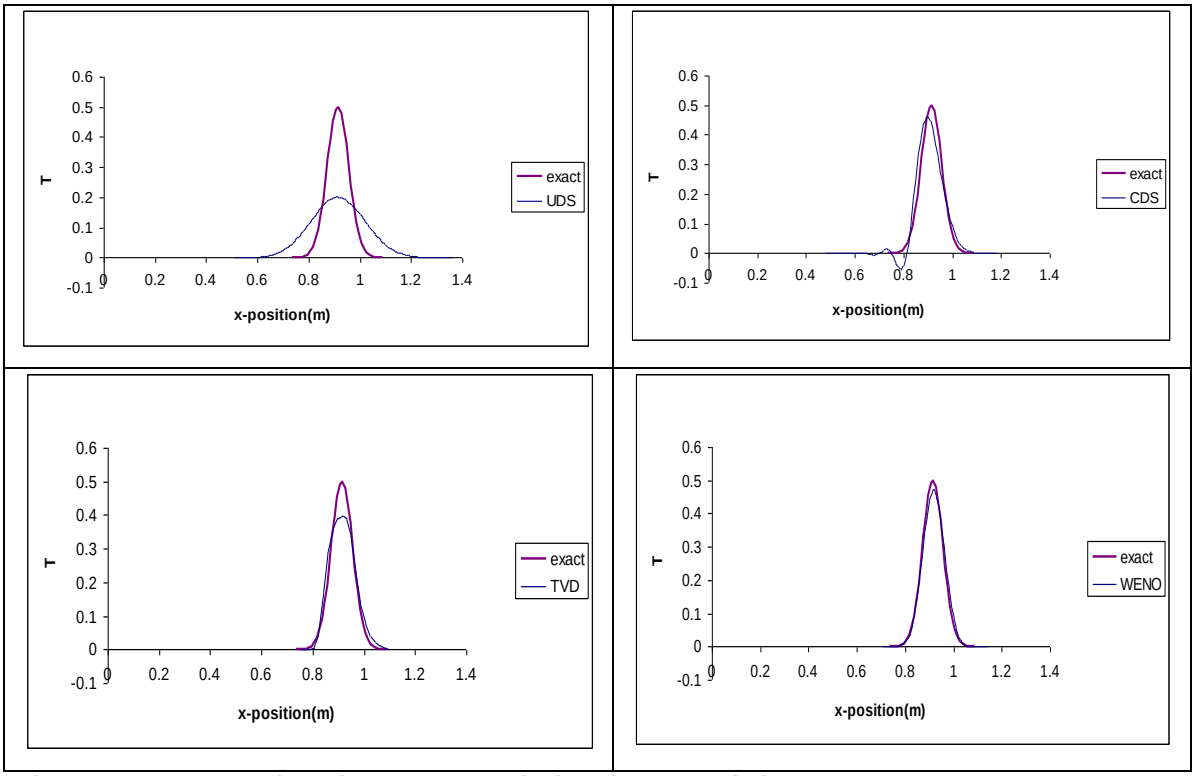

Figure 3. 3 - Comparison between numerical and exact solution at CFL 0.01, at t =10sec (intermediate wave: r/dx=6)

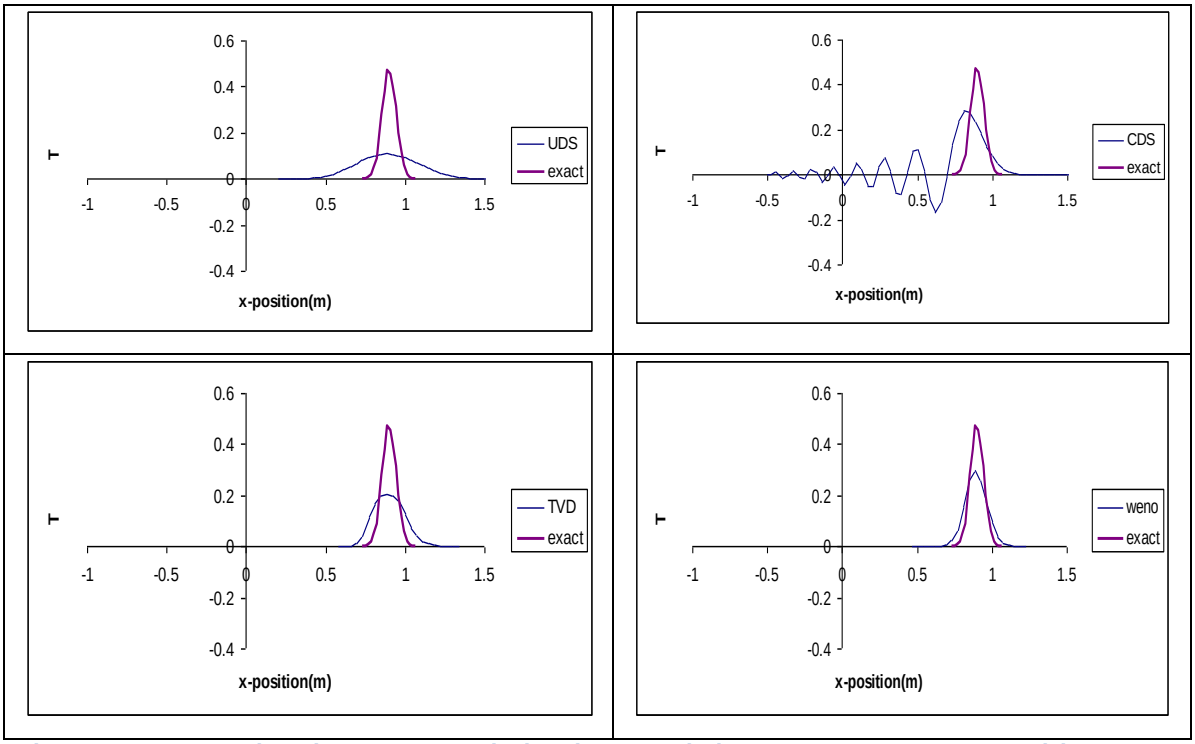

Figure 3. 4 - Comparison between numerical and exact solution at CFL 0.01 at t =10sec, (short wave:r/dx=3)

For short wavelength it can be clearly seen in fig 3.4, that artificial viscosity in the case of UDS dominates the solution and completely smears out the wave. For CDS, phase

distortion is introduced by the strong oscillations at the rear of the wave, which also reduce the amplitude of the wave. In the case of the TVD scheme, which blends the positive features of both UDS and CDS, it can be seen that the rear and front of the wave are diffused. This is due to the limiter function switching to UDS to prevent the unwanted oscillations of the CDS scheme, however due to the introduction of artificial diffusion the amplitude error is higher compare to CDS and the Gaussian profile also flattens out at the peak. For the WENO scheme, numerical diffusion is much reduced compared to the other schemes and even though a slight oscillation can be seen at the rear of the wave, the wave form is reasonably well captured considering the fact the test was performed on such a coarse mesh (ie. r/dx =3).

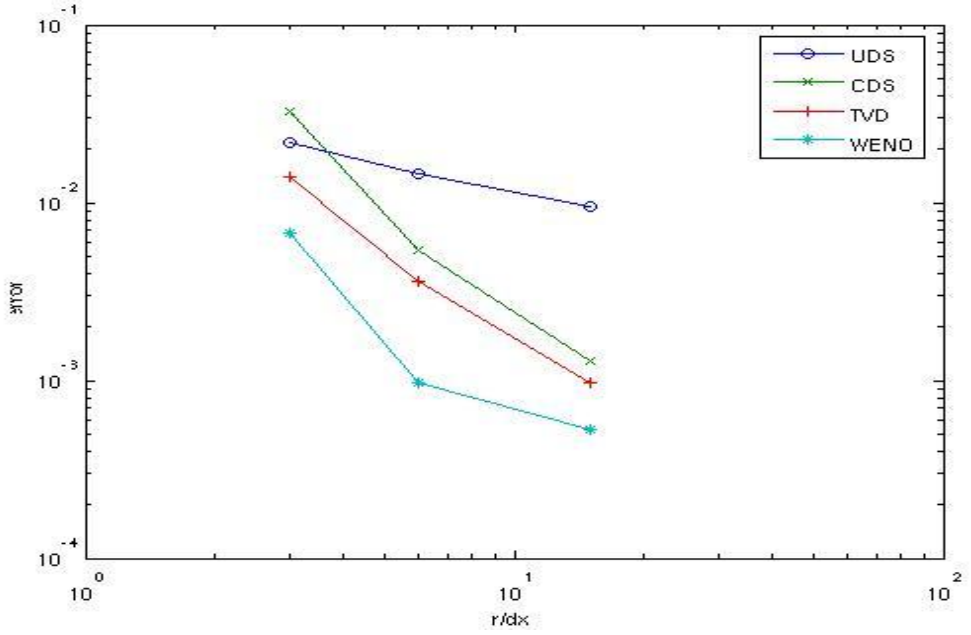

Figure 3. 5 - Error Vs r/dx, at t = 10 sec.

Figure 3.5 present an error (amplitude) chart against points per wavelength. The error was calculated based on the following:

$$\text{Error} = \frac{\sum_{i-1}^{N} |T_i - t_i|}{N}$$

where T_i is the exact solution at the point i, t_i is the numerical solution at the point i and N is the number of grid points. This chart displays the dissipation of the scheme. It can be seen that the WENO scheme performs better in terms of dissipation and dispersion as the number of points per wavelength decreases. This is a promising aspect of WENO for the acoustic problems of interest here.

3.6.2 2-D Linear Convection – A steady flow

In the previous section, numerical schemes were tested to study their dissipation and dispersion behaviour using a 1-D linear convection problem. In this section, the schemes were tested against a steady pure scalar convection in 2D. The purpose of this test case is to study the behaviour of TVD and WENO along with 2nd order CDS and 1st order UDS in a test problem which has been found appropriate for scalar equation solution in a complex flows where the velocity vector convecting scalar gradients to be resolved accurately is at various angles to the mesh lines. In order to predict accurately acoustic wave propagation in complex flow conditions it is paramount to choose a numerical scheme whose ability is not limited to acoustic wave phenomena but performs well in general scalar convection/diffusion regimes. Thus, schemes such as DRP initially developed by Tam et al. (1993) and Bogey et al. (2004) specifically for acoustic wave resolution may not perform so well in this type of problem.

The test problem is defined as follows. The solution domain is defined by $-1 \leq x \geq 1$ and $0 \leq y \geq 1$. The velocity field is specified through-out this domain using the following expressions:

$$U(x,y) = 2y(1-x^2)$$
$$V(x,y) = -2x(1-y^2) \qquad (3.52)$$

A specified scalar inflow boundary condition was specified along y =0 and x = -1 to 0. The above mentioned velocity field convecting the scalar profile 180° and through a zero gradient outflow boundary condition was specified along y =0 and x =0 to 1. Remaining boundaries are specified using the exact solution. The predicted scalar must coincide with the flow streamlines since this problem assumes zero physical diffusion of the scalar so any spread of the scalar field in the domain is due to numerical dissipation and dispersion, (over or undershoots in the scalar). Figure 3.6, illustrates the scalar field contours and streamlines obtained using a 40 X 20 (X,Y) grid for different numerical schemes.

The global error was evaluated using $\frac{\sum|\phi_{comp} - \phi_{exacti}|}{\sum \phi_{exact}}$ by comparison with the exact solution and is shown in Fig. 3.7, comparing different numerical schemes and different mesh sizes. 1st order UDS clearly leads to large errors. The 2nd order CDS and TVD schemes perform better, with errors an order of magnitude smaller on a given grid, and also a steeper gradient for error reduction. TVD shows smaller errors because it reduces the high dispersion errors of CDS. The DRP schemes of (Tam et al. (1993) & Bogey et al. (2004)) perform no better than the WENO scheme unless a fine mesh is used. This is because, although the DRP schemes formally have a 6th or even higher order of accuracy, the added

dissipation to produce acceptable stability interferes with this. Only for the finest mesh does the DRP 8th order scheme show any benefit, and then only marginally. In general the WENO scheme is better on coarse meshes than the DRP schemes; hence the WENO scheme was selected for further simulations reported in this work.

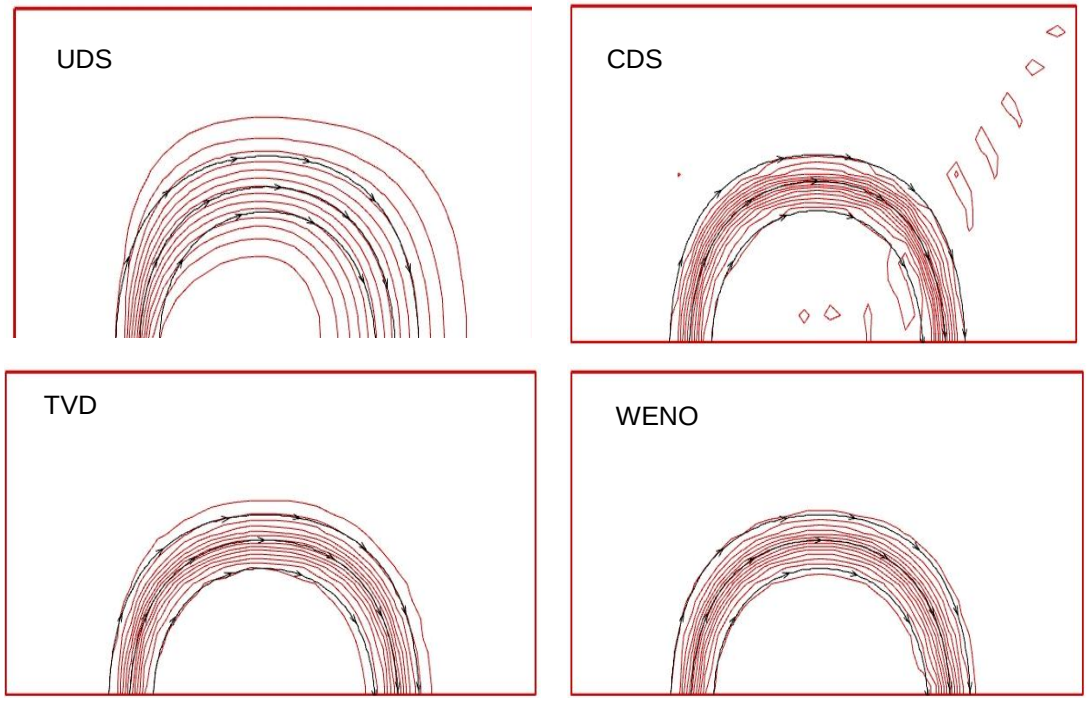

Figure 3. 6 - Scalar field contour on 40 X 20 mesh, (Black line with arrow – Streamline & Red line–Numerical solution.

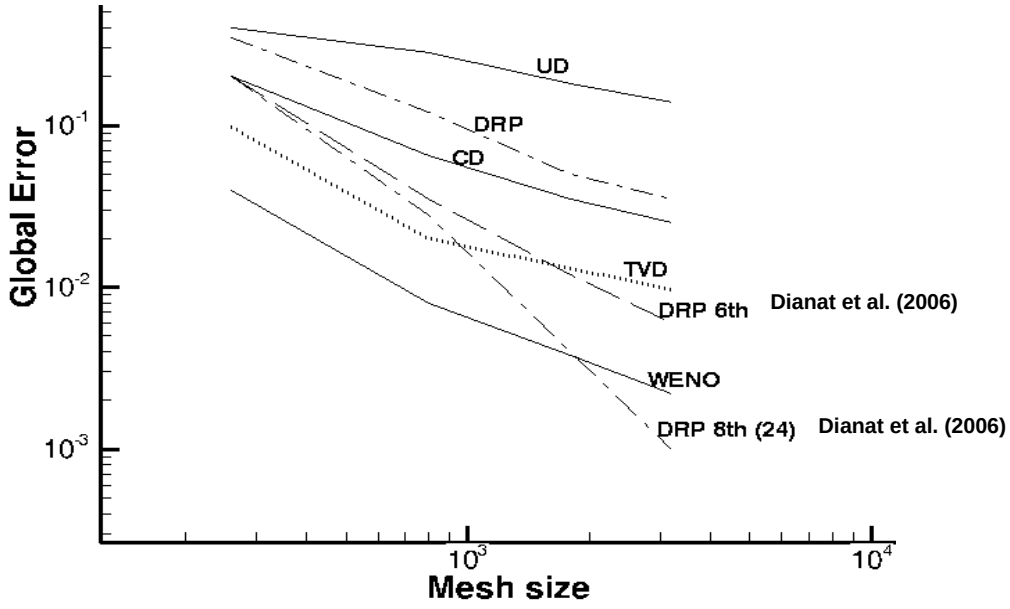

Figure 3. 7 - Global Error vs Mesh size for various schemes.

3.6.3 1-D Non- Linear Wave Propagation

This test case represents a nonlinear propagation of an initial Gaussian waveform. It is a test case selected from Category 2 of the NASA (Tam et al. 1995) workshop on benchmark problems in CAA (Computational Aero Acoustics). Fully compressible URANS equations 3.10 - 3.12 were used to solve this problem. The initial conditions are given as

At t = 0;

$$\frac{U}{c_\infty} = 0.5\exp\left[-(\ln 2)\left(\frac{x}{\Delta x 5}\right)^2\right] \tag{3.53}$$

$$\frac{p}{\rho_\infty c_\infty^2} = \frac{1}{\gamma}\left(1+\frac{\gamma-1}{2}\frac{U}{c_\infty}\right)^{\frac{2\gamma}{\gamma-1}} \tag{3.54}$$

$$\frac{\rho}{\rho_\infty} = \left(1+\frac{\gamma-1}{2}\frac{U}{c_\infty}\right)^{\frac{2}{\gamma-1}} \quad ; \gamma = 1.4 \tag{3.55}$$

where subscript ∞ represents, values at infinity and Δx is the grid spacing.

A computational domain of $-50 \le x \le 350$ is used. The initial Gaussian profile propagates nonlinearly due to the high amplitude of disturbance (50% of ambient level). A shock will form and then propagate (see figure 3.8). An approximate analytical solution is given in NASA (1995) as well as obtained using Whitham's equal area rule (Whitham 1974) and is shown below along with the predicted numerical solution. Any deviation in computed shock position to that of the analytical solution is an indicator of dispersion error and the shock amplitude deviation is a measure dissipation error.

Computation was performed using a grid spacing $\Delta x = 1$, and a non-dimensional time step $\Delta t \frac{c_\infty}{\Delta x} = 0.05$. Figure 3.9 shows the non-dimensional velocity and density predictions after t = 200, using TVD for spatial discretisation and fully implicit first order temporal discretisation. Figure 3.10 was obtained using the WENO scheme. In both cases the numerical solution compares very well with the analytical solution. Since the nonlinear flow disturbances are much larger compared to the numerical errors, effects of the numerical schemes are hardly noticeable.

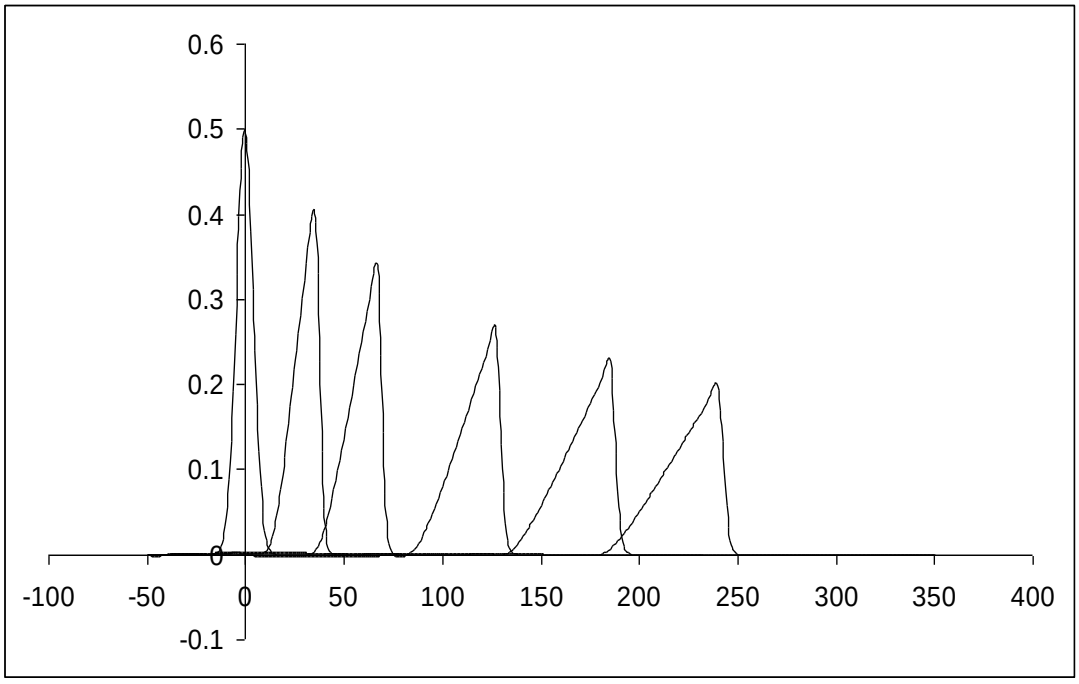

Figure 3. 8 - Nonlinear wave propagation, Initial Gaussian disturbance at time = 0 to shock wave propagation at time = 200.

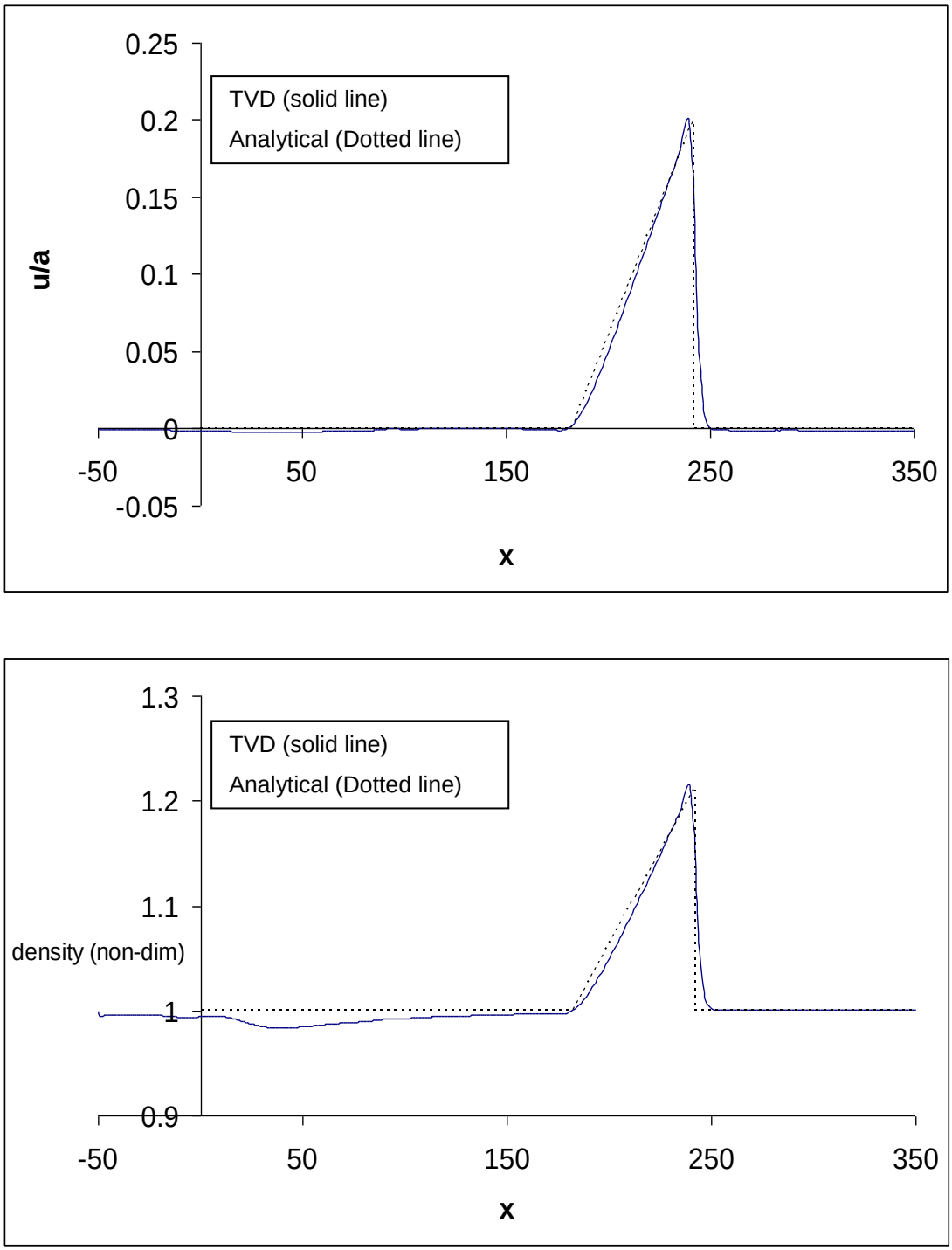

Figure 3. 9 - Comparison between CFD using TVD and analytical solution at non-dimensional time = 200 for velocity and density.

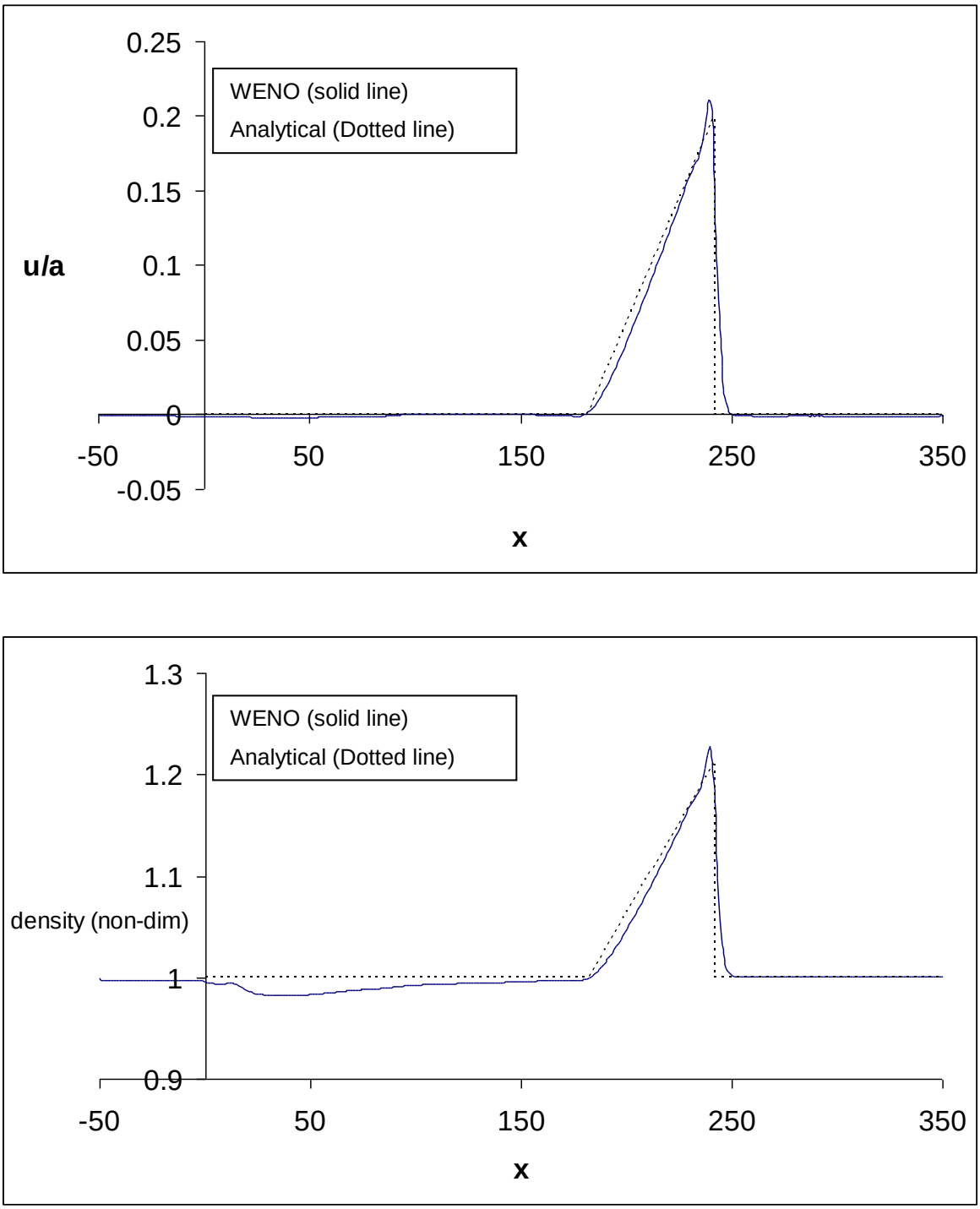

Figure 3. 10 - Comparison between CFD with WENO and analytical solution at non-dimensional time = 200 for velocity and density.

3.6.4 Acoustic Wave Entering a Solution Domain.

In subsonic flows, acoustic perturbations can enter into the computational domain from the outlet and can propagate against the mean flow. The boundary conditions used should allow waves to enter the solution domain without causing any spurious effects. This is therefore a simple test case for the newly implemented characteristic boundary conditions.

A computational domain was selected consisting of a rectangular duct with length from $0 \le x \le 1$ and equal height and width but both much smaller than the axial dimension of the duct. A grid spacing of Δx 0.007 was used in the axial direction whereas the cross-section was meshed with just 5 cells in each direction. In order to test the behaviour of the characteristic boundary conditions for an acoustic wave entering the duct against the mean flow; a mean flow Mach number of 0.11 was chosen. A sinusoidal upstream propagating pressure perturbation was prescribed at the outlet with peak amplitude of 2% of the mean pressure and a frequency of 2400 Hz, which corresponds to a resolution of 20 points per wavelength. The computation was carried for a time corresponding to 5 periods of the incoming perturbation with an acoustic CFL number of 0.04. Figure 3.11 shows the solution obtained using various discretisation schemes, with the temporal scheme being unaltered and kept at first-order fully implicit. Once again WENO performs better than the rest of the schemes. It is also evident from the Figure 3.11 that the characteristic boundary condition allows external waves to enter the domain without spurious effects at the boundary, only the 1st waveform shows any evidence of change from the incoming wave, as expected for the initial transient.

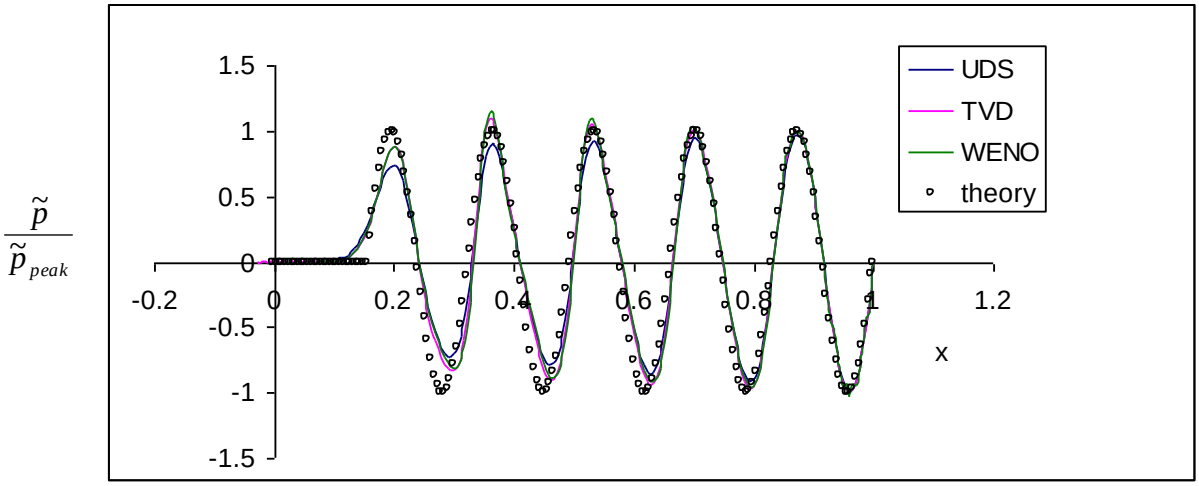

Figure 3. 11 - Waves through outlet using characteristic bc's and various numerical schemes.

3.6.5 2nd Order Temporal Discretisation

In spite of using a fully implicit scheme, it is clearly necessary to increase the order of temporal accuracy to 2nd order for application to more complex acoustic problems. A three time level (Ferziger et al. 2002) 2nd order accurate time scheme was introduced. This scheme was obtained by using a quadratic backward approximation in time. The discretised form of a 1D Burgers equation appears as shown below:

$$\frac{3u_P^{n+1}-4u_P^{n}+u_P^{n-1}}{2\Delta t} = -\left(u\frac{\partial u}{\partial x}\right)^{n+1} \qquad (3.56)$$

Note that to use this time scheme, it is necessary to store previous time step values of the solution variables.

To verify the implication of the second order time scheme, a test was performed by repeating the problem described in section 3.7.4. This was carried out this time with two different acoustic CFL numbers and with WENO for spatial discretisation. It can be seen from figure (3.12), that the wave form is well captured even when using twice the time-step of the first order prediction.

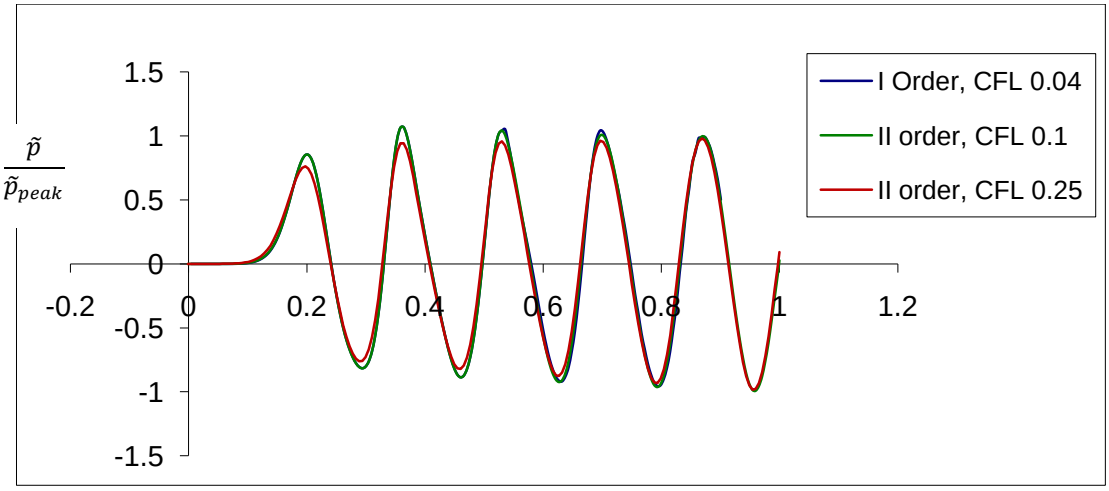

Figure 3. 12 - Comparison between 1st & 2nd order temporal scheme.

3.6.6 Assessment of Dissipation/Dispersion Error in Acoustic Wave Propagation

The initial validations on simple 1D or 2D flow problems shown in the previous section demonstrates successful conversion of the incompressible CFD code to a mildly compressible CFD code. The ability to capture acoustic wave propagation accurately using the current mildly compressible of CFD code was further estimated by repeating the test case suggested by Foeller et al. (2010) to determine dissipation and dispersion errors for linear acoustic pressure wave propagation in a simple 1D duct. Foeller et al. (2010) used a 2nd order Lax-Wendroff scheme and a density based CFD solver, so this forms a useful first comparison between pressure-based and density-based compressible algorithm for acoustic problems.

A rectangular duct similar to that used by Foeller et al. (2010) was chosen for this study; the choice of mesh in the cross-sectional directions was also similar. The axial grid spacing was altered to yield explicitly a defined number of points per wavelength. A pure downstream propagating sinusoidal acoustic wave was specified as an input boundary condition at x=0 using the characteristic approach, with acoustic velocity and pressure amplitudes calculated based a wave amplitude of 0.2m/s which for a downstream travelling wave. The frequency (1200Hz) was chosen such that within the axial length of the duct 10 complete periods of sinusoidal wave fit exactly inside the duct. The mean flow field was initialised with a velocity of 0.25 m/s. Four simulations were carried out, with the grid resolution varying from 10 to 40 points per wavelength. All simulations were carried out for TVD as well as WENO scheme

with the 2nd order time scheme. During the simulation the time series of acoustic pressure and velocity were extracted at various positions along the duct. The predicted time series and spatial information after a distance of 10 acoustic wavelengths were post-processed to evaluate acoustic dissipation (from predicted wave amplitude) and dispersion (from predicted wavelength) relative to the exact values. Fig 3.13 shows results for all four simulations. The WENO scheme, as expected, performs at lower error than TVD, particularly with coarse resolution (see 10 points per wavelength plot). The associated dissipation and dispersion errors are shown in Table 3.1. Comparison between the current 2nd order TVD and 5th order WENO schemes as well as the 2nd order Lax-Wendroff scheme used in Foeller et al. (2010) are shown in Table 3.1. In general the WENO scheme produces dissipation errors half those of the 2nd order schemes at the same resolution. Dispersion errors for all schemes are very small except for the most under-resolved mesh for the 2nd order Lax-Wendroff method. Based on this and the performance described in the other test cases abvoe, the WENO scheme was selected as providing best overall performance.

Δ/λ	Dissipation error (%)			Dispersion error(%)		
	Foeller et al. (2010)	TVD	WENO	Foeller et al. (2010)	TVD	WENO
10	34.7	23.2	14.7	2.89	0.02	0.04
20	2.8	5.4	1.7	0.08	0.02	0.03
30	1.2	1.5	0.6	0.05	0.02	0.02
40	0.4	0.6	0.2	0.05	0.02	0.02

Table 3. 1 - Percentage of numerical dissipation error after 10 periods for TVD and WENO compared at different grid point per wavelength as well as with the results of Foeller et al. (2010).

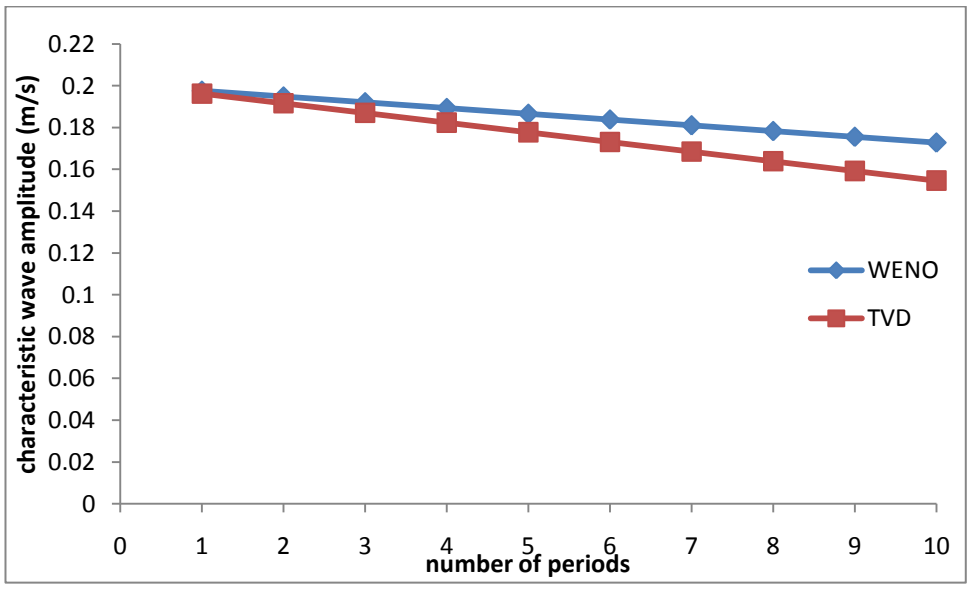

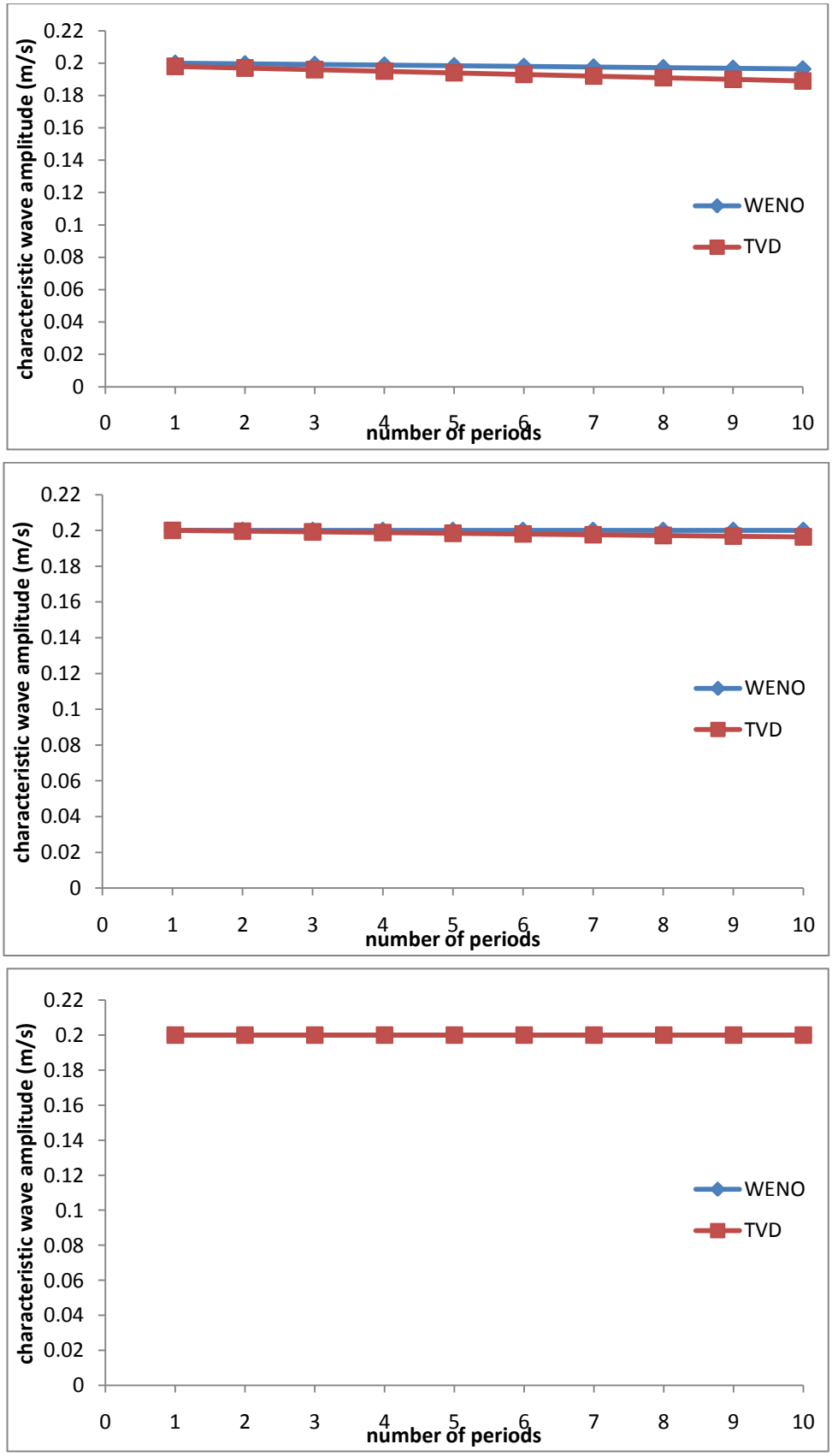

Figure 3. 13 - Dissipation of acoustic wave amplitude for TVD and WENO at various grid resolution.

3.6.7 Acoustic and Entropy Wave Refection and Transmission Relationships in Varying Cross-section Duct Flow.

As described in Chapter 1, the acoustic waves in gas turbine combustors are influenced by many complex processes. During propagation through the complex geometry of the combustor the acoustic waves can gain or reduce strength. In addition local regions of hot gas (entropy waves) produced by the combustion process propagates at the mean flow speed and create acoustic waves when this convect through regions with mean-flow gradients, such as flow through variable area transition nozzle. These indirect acoustic waves propagate upstream against the mean flow and can superimpose on already existing pressure waves and intensify the pressure fluctuations they will also convect downstream and cause noise in downstream turbine components. It is of interest therefore to examine the performance of the current method for acoustic and entropy wave propagation in a variable area duct. In this section CFD simulations to predict the acoustic input-output response (transmission and reflection coefficients) for flows in variable area ducts (i.e. with mean velocity gradients) as well as the entropy – acoustic wave input - output response is examined. Barton (1986) has studied such a problem using a numerical solution of the classical linear acoustic approach to analyse quasi-1D duct flows (nozzles and diffusers); these solutions are therefore available to compare with current CFD predictions. In order to predict the acoustic input-output response it is of paramount importance to have proper boundary conditions which will allow acoustic waves to enter and leave the solution domain without causing any spurious effects otherwise they may destroy the entire flow calculation or will influence the predicted reflection and transmission coefficients. Accurate prediction of acoustic input-output response directly relates to the ability of the characteristic boundary conditions implemented in the modified CFD code to process acoustic information accurately at inflow and outflow boundaries.

3.6.7(a) Acoustic Input and Output Response.

The geometry of a nozzle of unit length and area ratio of 4:1 as well as the mean flow conditions for velocities, pressure and density at the inlet are taken from Barton (1986). The nozzle exit Mach number varies from 0.18 for a low velocity inlet test case to 0.89 for a high velocity test case. The flow in the nozzle is assumed to be inviscid for this test problem. Both a nozzle and a diffuser test problem were considered. For the diffuser case the geometry (and also mean flow conditions) were reversed from the nozzle case specification. The ratio of any input pressure fluctuation relative to the mean pressure is <<1 to satisfy the linear assumption employed by Barton (1986) in his study. The input wave frequencies were chosen as 100 rad/sec and 1000 rad/sec. To avoid any problems associated with abruptly ending the geometry, a short length of constant area duct was connected at both inlet and outlet.

The approach adopted in the current study to calculate the input-output wave response is to divide the problem into two smaller tests. In the first test a pure downstream propagating acoustic wave is input at the inlet of the duct. In the second test, a pure upstream propagating acoustic wave is input at the outlet of the duct.

If a pure downstream propagating acoustic wave is input at the constant area section of the inlet, in order to calculate its reflection and transmission coefficients an acoustic boundary condition must be specified at the outlet. The characteristic boundary conditions were used to prescribe no upstream propagating acoustic waves entering into the duct outlet (see Figure 3.14, where a diffuser geometry is shown rather than a nozzle). The input pure downstream wave will split into a transmitted wave as well as a reflected wave due to the change in duct area at the nozzle inlet (Lighthill 1978). Inside the nozzle/diffuser, in the variable cross-section domain the transmitted wave propagates downstream and part of it will be transmitted and part gets reflected at the nozzle/diffuser outlet. By taking the ratio of calculated reflected acoustic wave at inlet to the input pure downstream acoustic wave, a reflection coefficient at the inlet, r_{ud} can be calculated. Similarly, by taking the ratio of the downstream transmitted acoustic wave at the outlet to the input acoustic wave, a transmission coefficient, t_{dd}, is obtained.

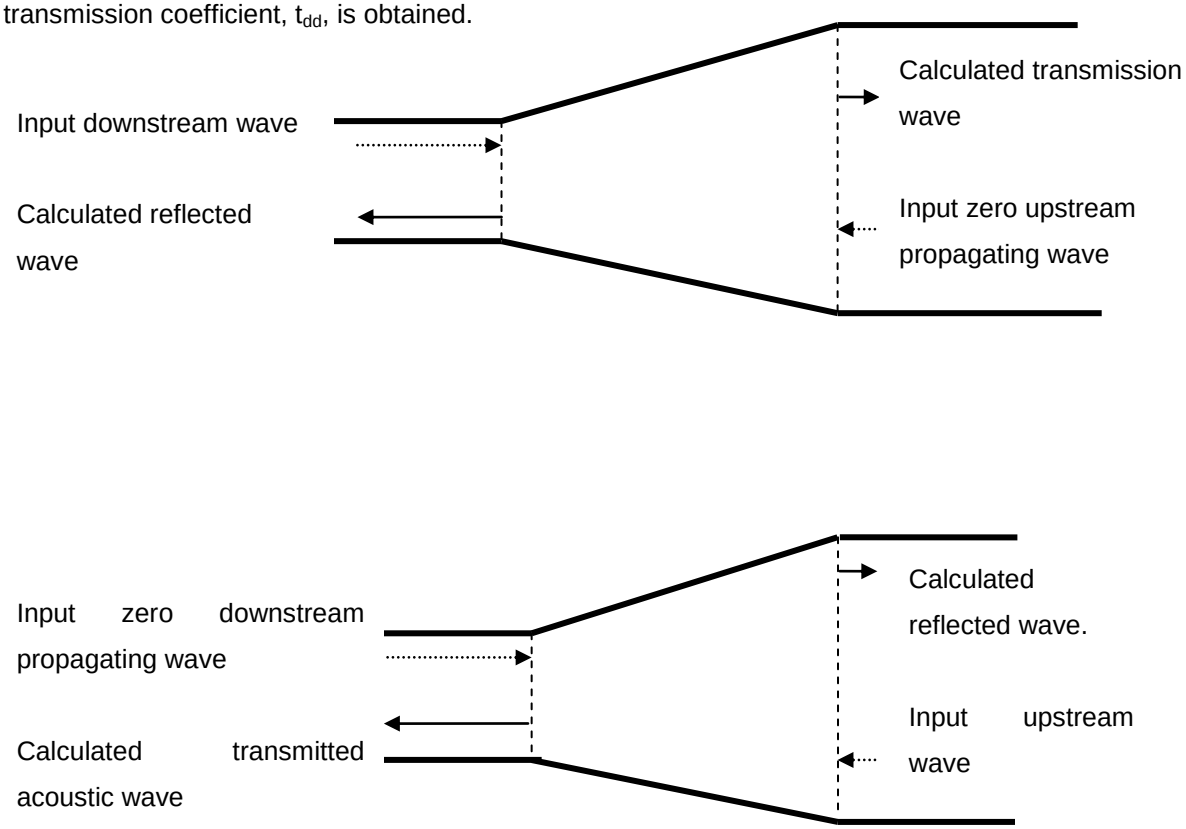

Figure 3. 14 - Schematic of diffuser with acoustic boundary conditions.

In the same way, by specifying a pure upstream propagating wave at the outlet and with prescribed zero downstream propagating wave input at the inlet using the characteristic boundary condition, the reflection coefficient at the outlet r_{du} and the transmission coefficient t_{uu} at the inlet can be calculated. All CFD calculations were performed using WENO for spatial discretisation and with 2nd order fully implicit scheme for time and 20-30 grid points per wavelength to capture the waves. For an inlet Mach number of 0.04 and 100 rad/sec and a nozzle flow the waveforms for input pure downstream propagating wave and its corresponding transmitted and reflected waves are shown in Figure 3.15. It can be seen that the reflected wave has a 180^{o} phase shift with respect to the input wave whereas only a slight shift in phase is seen for the transmitted wave, which corresponds to the time it takes the input acoustic wave to reach the outlet.

Predicted input/output response coefficients are shown in fig 3.16 for nozzle and compared with the Barton (1986) for two frequencies (100 rad/sec & 1000 rad/sec)and various inlet Mach numbers. It can be seen that excellent agreement between CFD and linear acoustic analysis was achieved. Except for the high velocity test cases, the downstream propagating wave is transmitted with increased amplitude and the upstream propagating wave is transmitted with decreased amplitude.

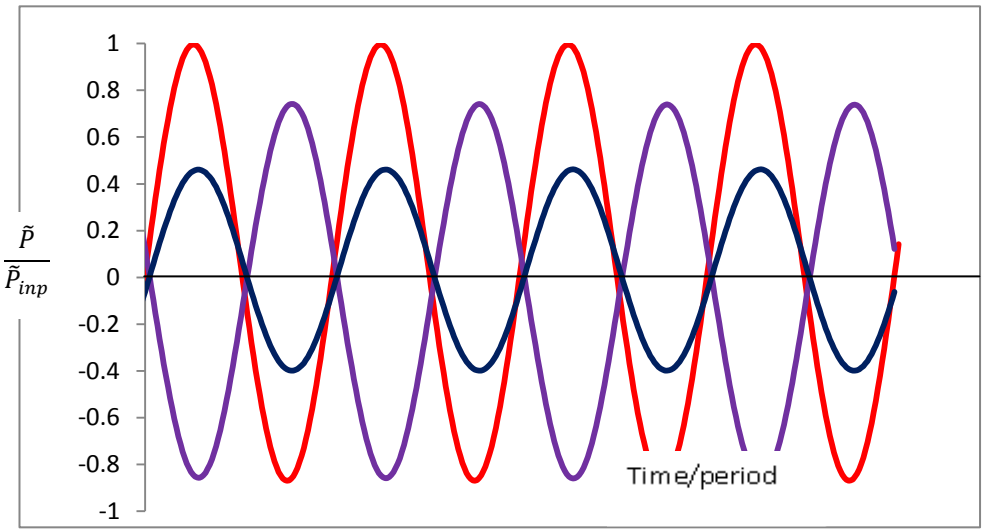

Figure 3. 15 - Inputted and Calculated waves for nozzle and their phase relation. Red – Inputted downstream wave, Dark blue – Transmitted wave at outlet & Purple – Reflected wave at inlet.

Similarly for a diffuser case (1:4 area ratio) the coefficients obtained using the present CFD algorithm and the comparison with respect to Barton (1986) is shown in fig 3.17. Again excellent agreement between CFD and exact solution was obtained for wide range of frequency and inlet Mach number. Opposite to the nozzle case the downstream propagating wave is transmitted with decreased amplitude while the upstream propagating wave is transmitted with increased amplitude. Transmitted and reflected waves gain strength at

higher inlet Mach numbers. For upstream propagating waves, irrespective of the inlet Mach number and wave frequency, the transmitted wave amplitude was always greater than the inputted wave with the strength of waves increasing sharply at higher Mach number (>0.6). For reflection coefficients, the strength increases greatly, much higher than the input wave for the downstream propagating condition, whereas the opposite occurs for upstream travelling acoustic waves.

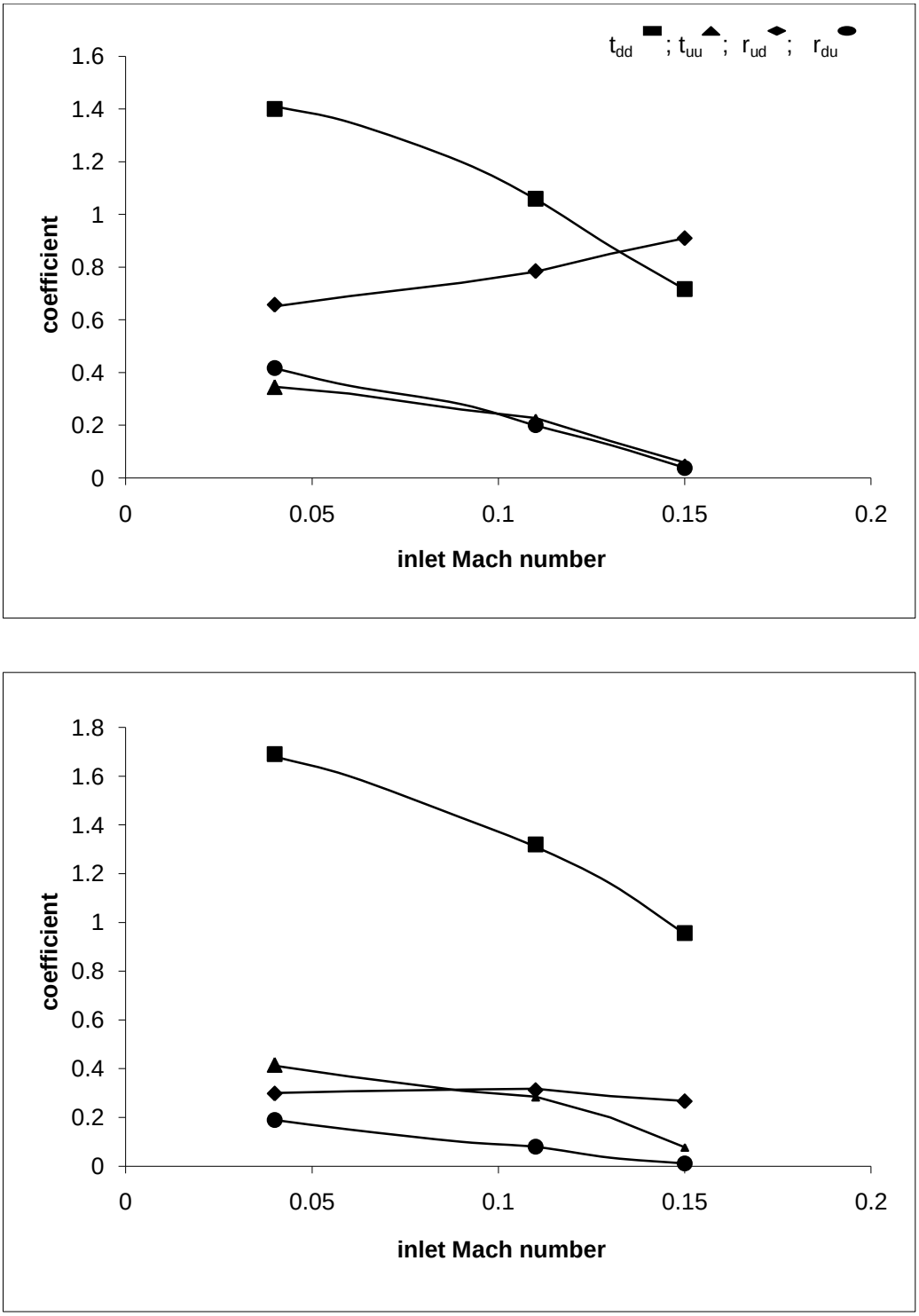

Figure 3.16 - Reflection and Transmission coefficients for acoustic wave in nozzle, wave frequency 100 rad/sec (top) & 1000 rad/sec (bottom); symbols- Barton (1986); solid line –CFD.

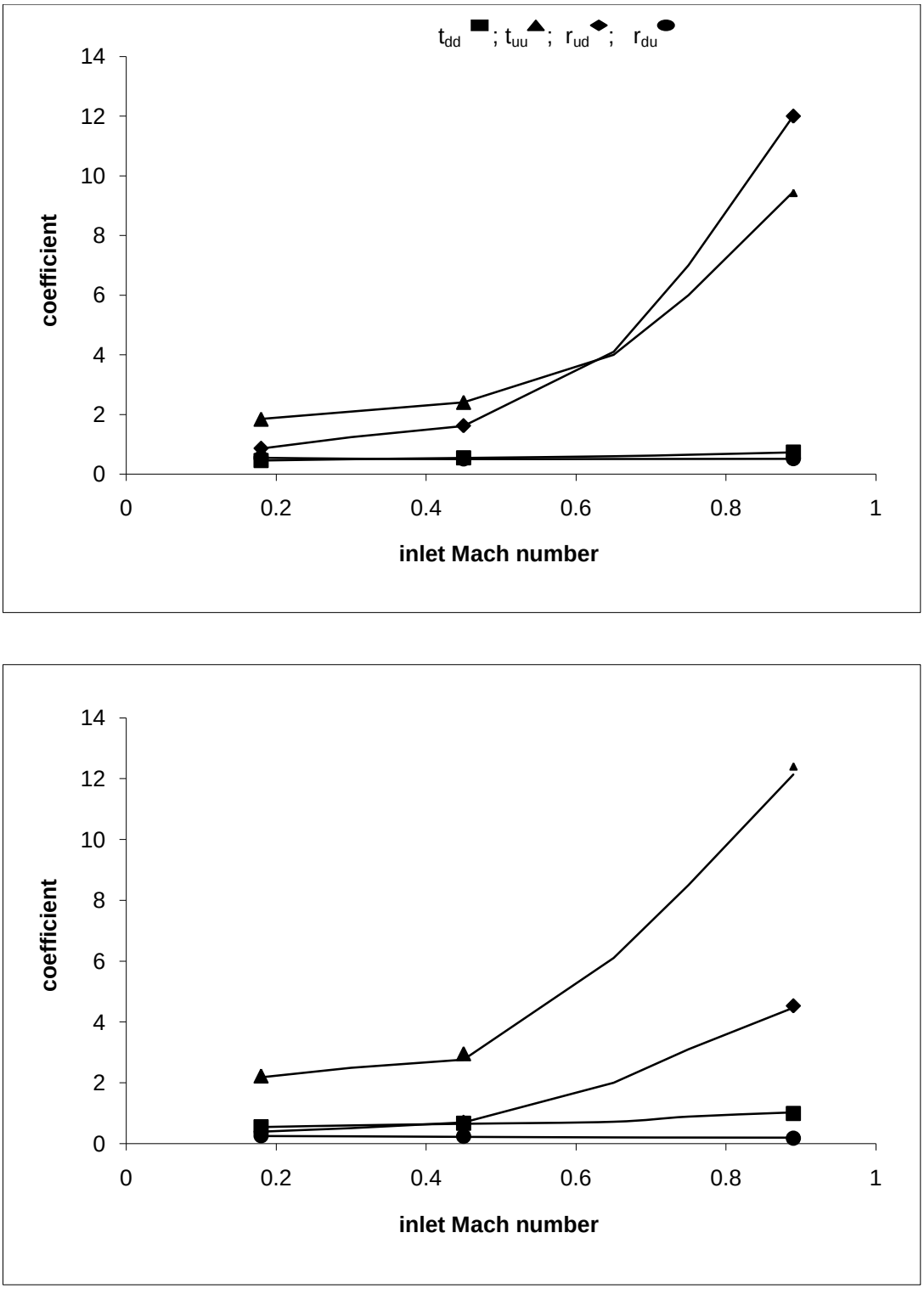

Figure 3. 17 - Reflection and Transmission coefficients for acoustic wave in diffuser, wave frequency 100 rad/sec (top) & 1000 rad/sec (bottom); symbols- Barton (1986); solid line –CFD.

3.6.7(b) Entropy Input-Output Response

By following a procedure similar to that described above for acoustic input-output response, it is possible to obtain an entropy input-output response for both nozzle and diffuser geometry. Now, instead of input of a pure acoustic wave, an entropy wave was specified by varying the inlet temperature about a mean value. Due to the change in duct cross-section, this input entropy wave generates acoustic waves as represented pictorially in Fig 3.18. These acoustic waves then propagate both upstream and downstream along with the downstream propagating entropy wave. This allows calculation of reflection and the transmission coefficients of the entropy wave, where t_{de} represents transmission coefficient which is defined as ratio of downstream propagating acoustic wave at outlet to convected entropy wave at inlet and r_{ue} represents reflection coefficient and can be defined as the ratio of upstream propagating acoustic wave at inlet to convected entropy wave at inlet.

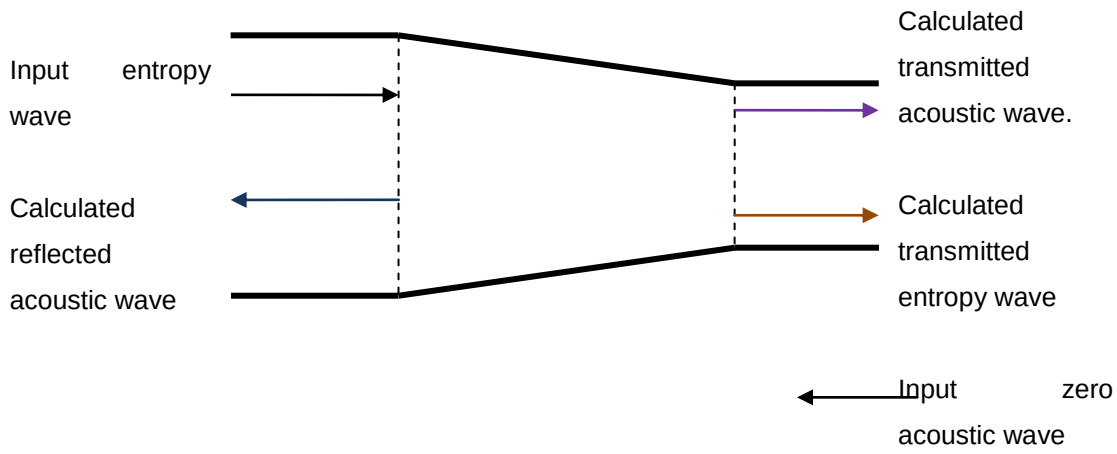

Figure 3. 18 - Nozzle with pure entropy inputted wave.

Similar to the previous test case, all simulations were carried out, using WENO for spatial discretisation and 2nd order implicit for time, for a wide range of inlet Mach numbers with wave frequencies of 100 rad/sec & 1000 rad/sec. The wave-forms of all four waves are shown in fig 3.19 for inlet Mach number of 0.15 and with wave frequency of 1000 rad/sec, 1. Green - input entropy wave, 2. Brown - transmitted entropy wave at outlet, 3.Purple - transmitted acoustic wave at outlet and 4. Blue - reflected acoustic wave at inlet. (Note that for better viewing the transmitted acoustic wave (Ta) as well as the reflected acoustic wave (Ra) are scaled as shown in the figure). For the nozzle flow configuration, coefficients obtained by CFD and Barton (1986) are shown in Fig 3.20; again excellent agreement was obtained for all flow conditions.

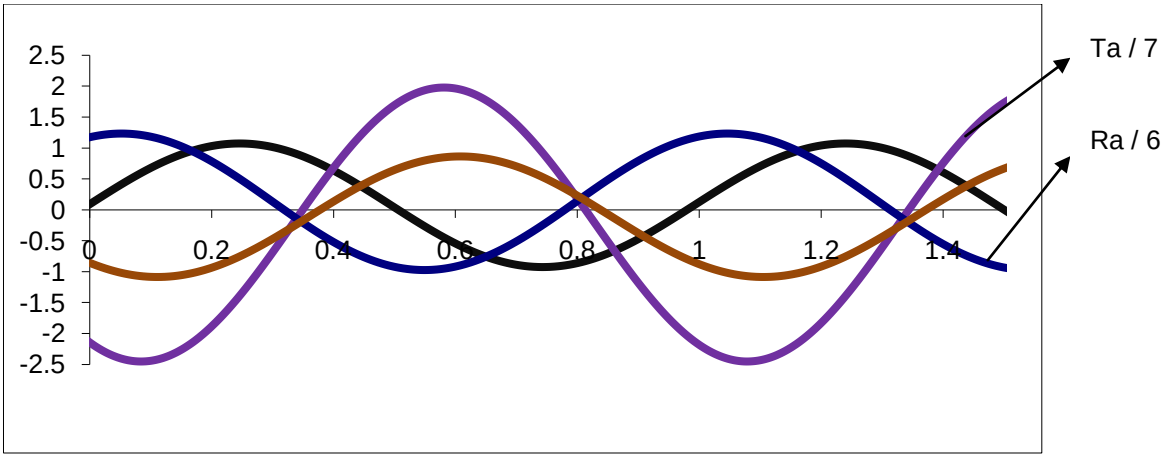

Figure 3. 19 - Wave form for Inlet Mach number 0.15, with frequency 1000rad/sec.

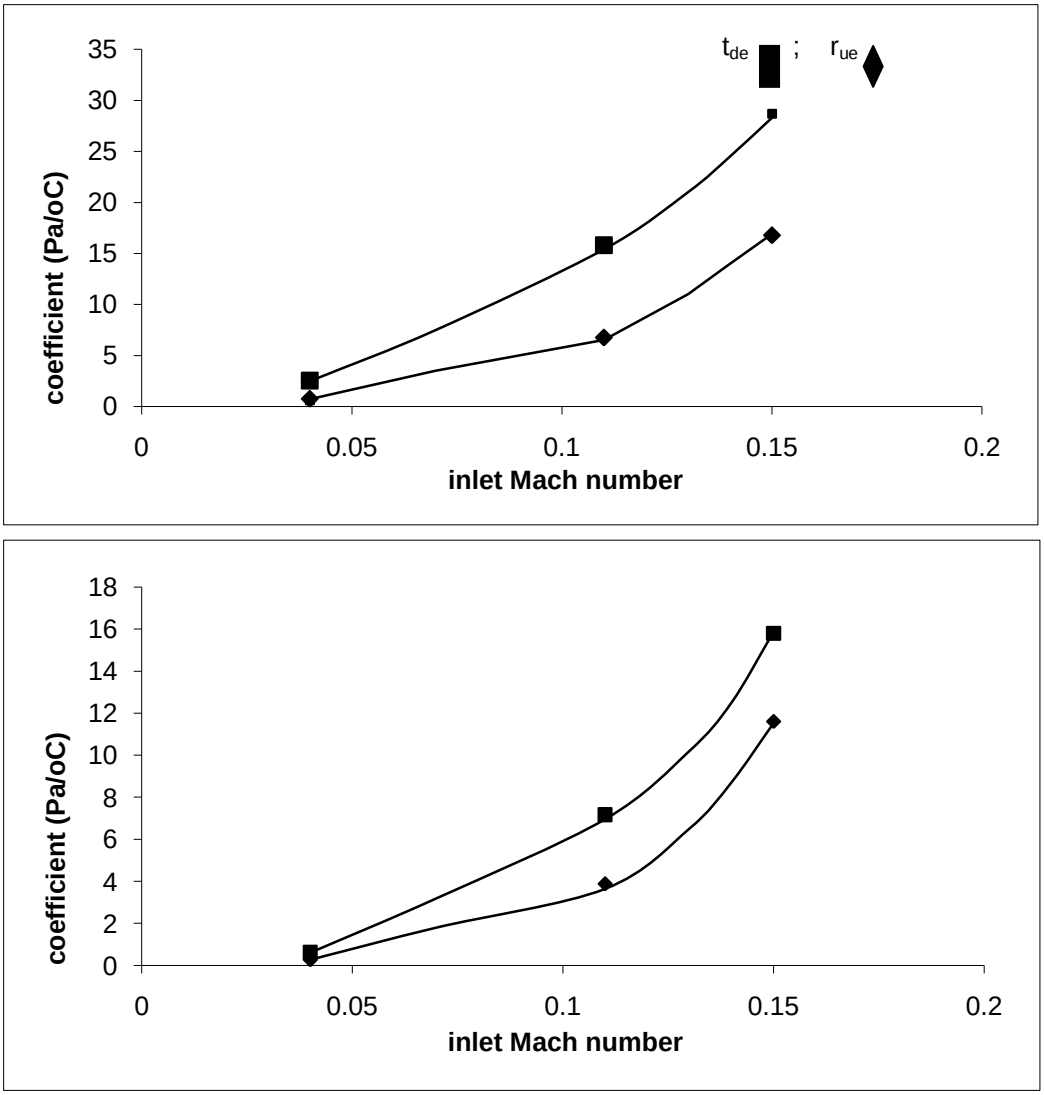

Figure 3. 20 - Reflection and Transmission coefficients for entropy – acoustic relationship, wave frequency 100 rad/sec (top) & 1000 rad/sec (bottom); symbols- Barton (1986); solid line – CFD.

The solutions show how a propagating entropy wave can excite a significant acoustic response – a factor of 10-20 amplification in terms of Pa/K. This problem is an important test case; the phenomenon of 'entropy noise' as examined in this test problem is attracting increasing attention in the gas turbine combustor community (Fischer et al. 2008).

3.7 SUMMARY

This chapter has described several modifications made to the baseline incompressible CFD code to capture compressible and acoustic propagating phenomena. All modifications were tested against a range of simple flow pattern and performed well. The accurate prediction of transmission and reflection coefficients for acoustic and entropy waves at various mean Mach numbers and various frequencies in a variable area duct illustrates the completion of the task of modifying the existing incompressible Fuel-3D CFD code to a mildly compressible code for solving acoustic flow phenomena. The remaining part of this thesis describes work carried out to demonstrate the prediction capability and applicability of the developed mildly compressible CFD code for problems relevant to acoustics in gas turbine combustion system components.

4. FLOW THROUGH AN ORIFICE ACOUSTIC DAMPING

4.1 INTRODUCTION

Using the developed mildly compressible pressure-based method simulations have been carried out to study the capability of this new method in predicting acoustic phenomena in complex flow configurations, in particular containing acoustic/ mean flow interactions, and with flow recirculation present. Acoustic waves passing through an orifice in a plate in a duct with mean flow involves all the above, including the presence of rapid acceleration/deceleration, recirculation, and formation of jet shear layers. Such orifice configurations are common features of combustion geometries (e.g. various cooling holes in the flametube) and can play a key role in terms of reducing the amplitude of acoustic waves associated with combustion instability, by converting acoustic energy into vortical flow kinetic energy which is eventually dissipated by viscosity into internal energy. Thus, the flow serves as an ideal practically relevant validation case for the newly developed method. This chapter contains a detailed study describing the application of the developed method to the prediction of acoustic damping due to an orifice, for which appropriate experimental data is available (Rupp et al. (2010)).

4.2 SOUND ABSORPTION BY AN ORIFICE - AN OVERVIEW

The basic principle on which passive dampers operate (e.g., Helmholtz resonators or perforated liners), is based on conversion of sound energy into kinetic energy of fluid vortex motion. For design purpose, it is essential to understand the performance of the apertures in perforated liners under various flow and operating conditions. Vorticity is produced where the fluid experiences a sudden expansion, such as at corners and sharp edges. Similarly vorticity is generated when a sound wave is incident on a sharp edge (Howe (1979), Bechert(1980), Hughes et al. (1990)). When the bulk fluid is stationary, dissipation of acoustic energy is generally weak; sound absorption can be significantly increased in the presence of mean flow through a perforated plate (see, Howe 1995). On the other hand, for a single orifice Rupp et al. (2010) found that sound absorption without a bulk mean through flow was higher than with a mean motion at higher incident sound amplitudes. In general, there are two types of mean flow of relevance: (i) flow parallel to the orifice axis, which is known as ‘bias’ flow (focus of the current work), (ii) flow perpendicular to the orifice axis, commonly known as ‘grazing’ flow. In general both will be present, but the emphasis in Rupp et al.’s experiments, chosen for detailed study here, was just on bias flow effects. Starting in 1870 (Rayleigh 1945), a large amount of work has been carried out to study the influence of incoming sound waves (at small noise amplitudes where linear behaviour was

expected) on flow through an orifice. This work was initially predominantly analytical (Rayleigh (1945), Howe (1979), Bechert (1980), Mani (1976)) with more recently experimental studies preferred (Bechert et al. (1977), Howe (1998)). Most of the analytical work has made use of the concept of Rayleigh conductivity, defined as the ratio of the fluctuating volume flux through the orifice to the fluctuating pressure difference across it. Nearly all analytical work assumes fluid motion near the orifice is essentially incompressible. The Influence of various complexities such as orifice wall thickness, shape, and orifice diameter to duct ratio on sound absorption is often addressed by introducing various “end corrections” based on minimum Rayleigh conductivity (for example, the circular aperture has the minimum conductivity for apertures of given area and an ellipse has 3% larger conductivity - this suggests that the conductivity of any elongated aperture will be larger) and the minimum kinetic energy principle of inviscid, incompressible flow (see Howe (1998), Wendoloski (1998)). Using the Rayleigh conductivity idea Ffowcs Williams (1972) and Leppington et al. (1973) predicted sound absorption by a perforated screen for low frequency incident sound with a ‘grazing’ mean flow. In the case of bias flow through an orifice, where flow is much more complex (due to formation of mean jet shear layers), additional fluctuations are produced by an applied time harmonic pressure perturbation, which leads to generation of a succession of vortex rings. For this situation, to estimate the conductivity, the interaction of these vortex rings with the orifice flow must be determined. Howe (1979) proposed a theoretical model in which conductivity was decomposed into an inertial part and a resistance part, where the attenuation of sound due to vortex shedding was included. In order to calculate the strength of the vortex shedding, Howe adopted a simplified approach by neglecting the variation in radius of the vortex rings, which were taken equal to orifice radius. Good agreement with experiment was obtained (Hughes et al. 1990). Using this theory, Howe (1979), determined the dependence of the absorption coefficient, which characterises the amount of acoustic energy absorbed, on the Strouhal number ($\omega R/U$) of the excitation, where ω is acoustic excitation frequency, R - the orifice radius and U- the vortex ring convection velocity. Hughes et al. (1990) greatly increased the absorption efficiency of a perforated plate by using a rigid backing wall (cavity-backed screen) with bias flow.

Recently, using incompressible Large Eddy Simulation for simulating acoustic sources and combining with low-order acoustic models, Eldredge et al. (2007) calculated the Rayleigh conductivity for an orifice in bias flow by taking into account the effects of a large array of perforated liner holes as well as the tilting of the orifice in the tangential flow direction. A variation to the Howe (1979) model was suggested to include more geometrical sophistication like aperture thickness and tilt angle as well as obtaining considerable improvement over existing linear acoustic methods. Even though integration of LES with computational aeroacoustic techniques substantially improved the linear acoustic model, the

linear acoustic models failed drastically to capture properly the effects under some circumstances of orifice thickness and tilt angle and when more complex flow phenomena appeared inside the orifice such as shear layer instability.

At higher acoustic input amplitudes, non-linear mechanisms can be important for small orifices if the acoustic Reynolds number $\omega R^2/v$ is large; viscosity has little control over the dynamic interaction except for its role in generating vorticity at the surface. Predominantly work at such high acoustic amplitudes have been carried out using experiments (Ingrad et al. (1967), Ingrad (2008)) since analytical work failed to predict the complex fluid flow phenomena such as shear layer instability, vortex shedding etc. (Cummings (1986), Howe (1995)). Non-linearity also causes a pure sinusoidally varying pressure signal incident on the orifice to produce reflected and transmitted waves containing harmonics of the incident wave frequency (Howe 1995). The sound absorption then can be higher in comparison with linear behaviour. For the case of a perforated plate flow, a proper choice of the bias flow velocity will yield large absorption at low frequencies, irrespective of the incident sound amplitude (Howe 1998). Numerically, Tam et al. (2001) analysed acoustic losses due to vortex shedding at nonlinear sound amplitude for a resonator using a “2D” Direct Numerical Simulation and provided further insight in to vorticity shedding at the rim of an aperture. The calculated vortical energy was compared with measurements conducted within an impedance tube and showed good agreement for the high amplitude test cases. An excellent review of nonlinear acoustics can be found in Ingard (2008). Based on the previous work reviewed above it is apparent that little effort has been made to correlate fluid flow phenomena such as the strength of the generated vorticity/shear layer instability with loss in acoustic energy using theoretical/numerical study. The developed mildly compressible algorithm gives an opportunity to predict the unsteady velocity field associated with a small orifice in both linear and non-linear regimes of acoustic amplitude. Recent experimental study in such flow configuration (Rupp et al. 2010) gives an ideal validation test condition for the developed algorithm and was chosen for prediction test.

4.2 SELECTED EXPERIMENTAL GEOMETRY AND ASSOCIATED COMPUTATIONAL DOMAIN

The experiment of Rupp et al. (2010) has been selected for use as validation data in the present work and hence a brief introduction to their experimental set-up is needed. The test rig consisted of a 120mm x 120mm rectangular duct which was flanged to allow insertion of a 6mm thick plate in which a single round orifice of 12.7mm diameter was centrally located. In order to avoid any unwanted acoustic interference, both ends of the rectangular duct were connected to large plenums which provided a good approximation to an open end termination for acoustic quantities (acoustic pressure becomes close to zero corresponding to 180° phase shift between right and left propagating waves at the boundary interface between the duct end and the plenum). Mean flow through the duct (and orifice hence a

bias flow) was established by using a fan to draw air from the upper plenum, exhausting into the lower plenum. The orifice was subjected to acoustic excitation using a loudspeaker located near the lower plenum end which generated plane axial waves along the duct. The frequency of the wave was kept at 125 Hz throughout the Rupp et al. (2010) experiments while the acoustic excitation amplitudes ranged from 115dB to 143dB. The orifice plate was purposely chosen to be located 1323mm downstream of the duct inlet, since this then corresponded to a half wavelength (after end correction due to a bell mouth entry in the upper plenum) for the 125 Hz acoustic excitation, so that a pressure node would be formed on the upstream side of the orifice throughout the experiments. The purpose of this pressure node was to avoid any influence of orifice upstream pressure fluctuation in driving flow through the orifice, so that flow through orifice varies only due to the input loudspeaker oscillation.

This experimental flow configuration was captured computationally by choosing the domain for numerical simulation shown in Fig 4.1. To represent the loudspeaker in the CFD solution, an upstream propagating pressure wave was specified at the downstream end of the solution domain (x = 880mm). Throughout this section, the x – coordinate represents the main flow direction and wall normal coordinates are represented by y and z. The frequency and amplitude range of the incoming wave were specified from experimental values. A pressure node at the plane upstream of the orifice will be formed either by using an upstream quarter wave or half wave tube. In the experimental rig, it is far easier to realise a half wave (pressure node at the upstream end) than a quarter wave (pressure anti-node at the upstream end). In the present CFD approach, an acoustically closed condition (pressure anti-node) was easily realised via the characteristic boundary conditions method described in chapter 3. To utilise the advantage of this capability and to reduce the size of the computational domain the rectangular duct length upstream of the orifice was selected as 687mm in the numerical set-up (as opposed to the 1323mm of experimental duct length, the duct was connected to the upper plenum via a bell mouth and due to this end effect the duct length is not exactly half of the experimental setup) and a pressure anti-node condition fixed there. The mean flow enters the solution domain at the same location, at a magnitude fixed by the steady mean pressure drop driving flow through the orifice as measured in the experiment. Similarly, the downstream duct length was taken as 70 orifice diameters so that any flow recirculation due to the jet exiting the orifice has disappeared and the flow has filled the duct cross-section, allowing the mean flow boundary condition at downstream duct exit to be set as a zero gradient outflow, with the characteristic boundary condition treatment specifying the incoming acoustic excitation (see below). The lengths of both downstream and upstream ducts surrounding the orifice were thus reduced in comparison with the experiment to reduce the computational cost but without modifying any flow or acoustic

behaviour near orifice. Fig 4.1 shows a schematic of both experimental test rig as well as the chosen computational domain.

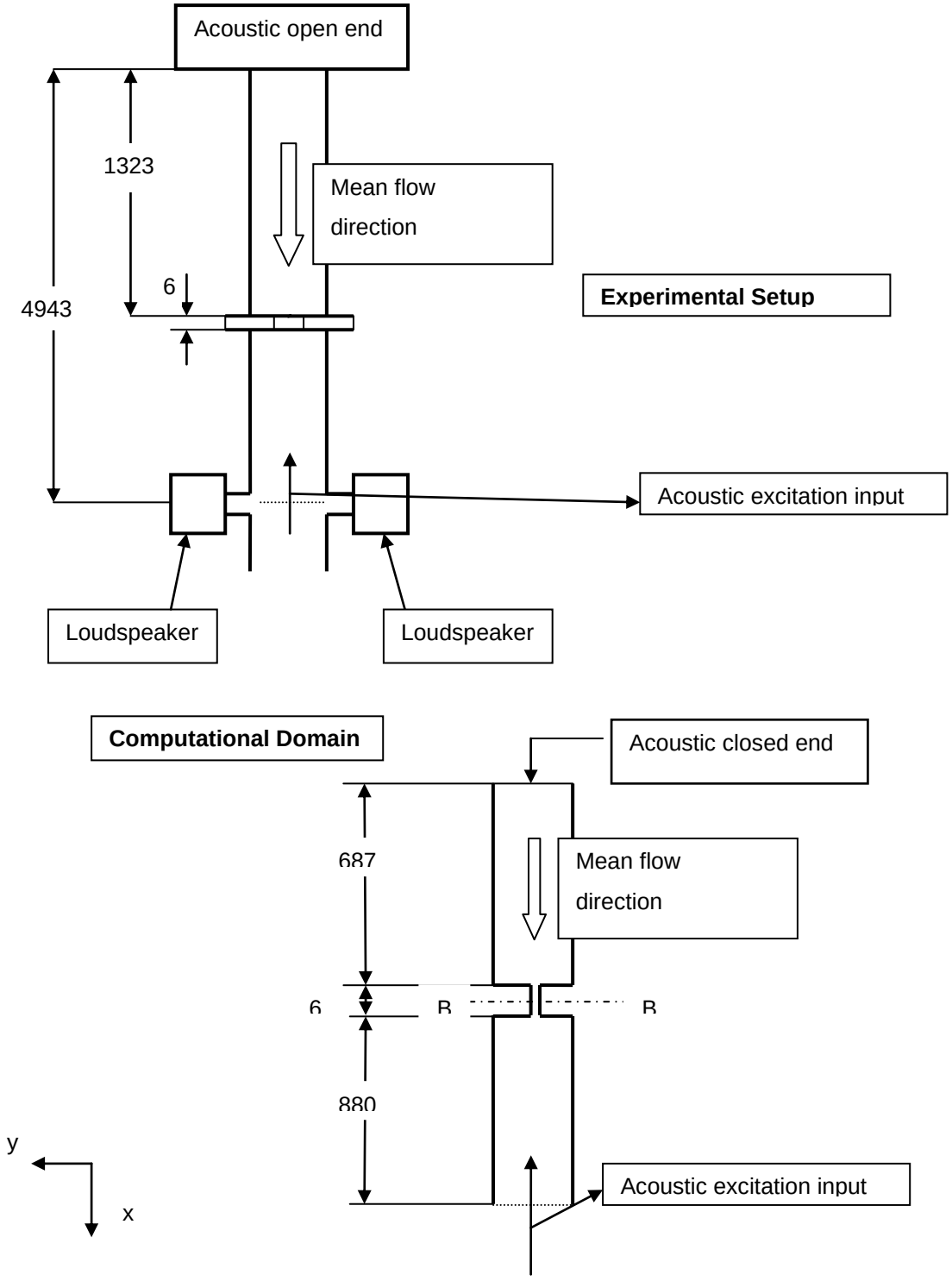

Figure 4.1 - Schematic of orifice and duct configuration, experimental rig (top) & computation (bottom), all dimensions are in mm and are shown not in scale.

4.3 GRID GENERATION

A multi-block structured grid was generated using the commercial grid generator software ICEM-CFD. Any centre-line singularity in the grid configuration was avoided using an O-H grid topology which generated an 'H' mesh in the centre of the orifice (see Fig 4.2). The same O-H mesh formation was maintained throughout the computational domain including upstream and downstream ducts. This resulted in 23 individual blocks (9 blocks each for both upstream and downstream rectangular ducts 5 blocks for the orifice) to represent the entire solution domain as shown in Fig 4.3.

In the current study, the excitation acoustic wave, input through the downstream duct exit boundary conditions, was at a frequency of 125 Hz. At this frequency the wave-length of the acoustic wave is roughly 2.75m at atmospheric pressure & temperature conditions, whereas the entire solution domain is roughly half a wave-length. A grid resolution of 20 - 30 points per wave-length was considered sufficient for high accuracy amplitude resolution of acoustic waves without dissipation/dispersion; this was therefore not a challenging constraint in choosing the grid resolution. Total grid nodes, grid spacing and grid distribution were defined to allow accurate resolution of the steady mean flow behaviour rather than acoustic phenomena. Thus, grid parameters were chosen in accordance with the resolution requirements for the jet and shear layer flow characteristics that were expected downstream of the orifice. Fig 4.4, shows mean axial velocity contours predicted in the near downstream orifice region using two different y-z plane mesh spacing. The velocity contours in the top picture were obtained using a 10 X 10 mesh in the central 'H' grid block on the y-z plane for the entire computational domain and the bottom contours were obtained by doubling the mesh count to 20 X 20 mesh in y-z plane throughout the domain (see Fig 4.2) which resulted in circumferential grid refinement but the axial grid point and grid distribution was kept same for both the conditions with 10 grid points for the entire length of the orifice and 190 grid points each for both upstream and downstream rectangular duct with dense mesh near the orifice and progressively coarsening towards the inlet and exit of the duct as shown in Fig 4.3. In terms of prediction of the emerging jet and associated shear layers downstream of the orifice both coarse and fine grids produced similar results; the finer grid showed a slightly longer potential core. Thus, results shown below were all obtained using the finer grid configuration.

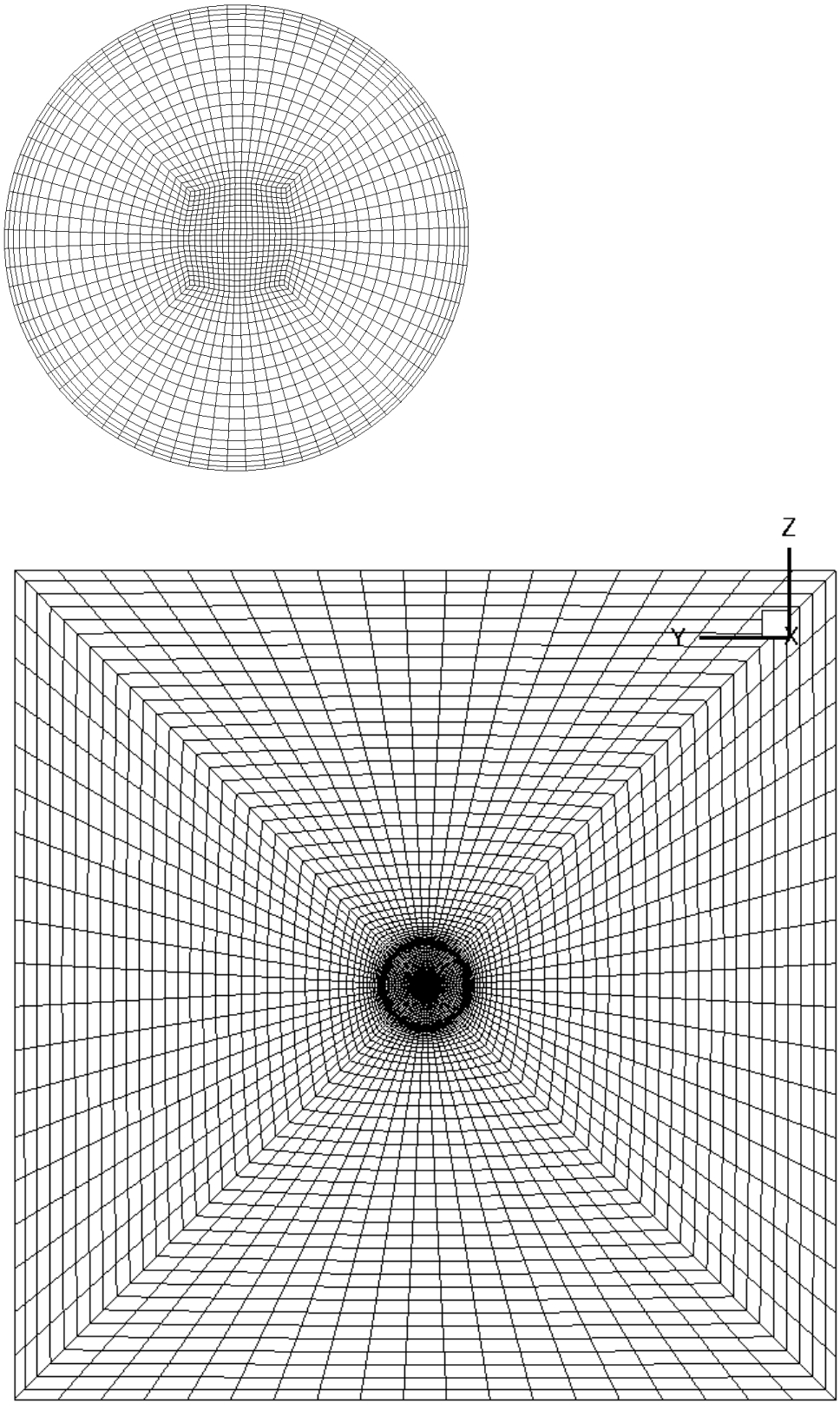

Figure 4.2 - 'O-H' - Grid at the orifice cross section B-B (top) and at rectangular duct cross section (bottom).

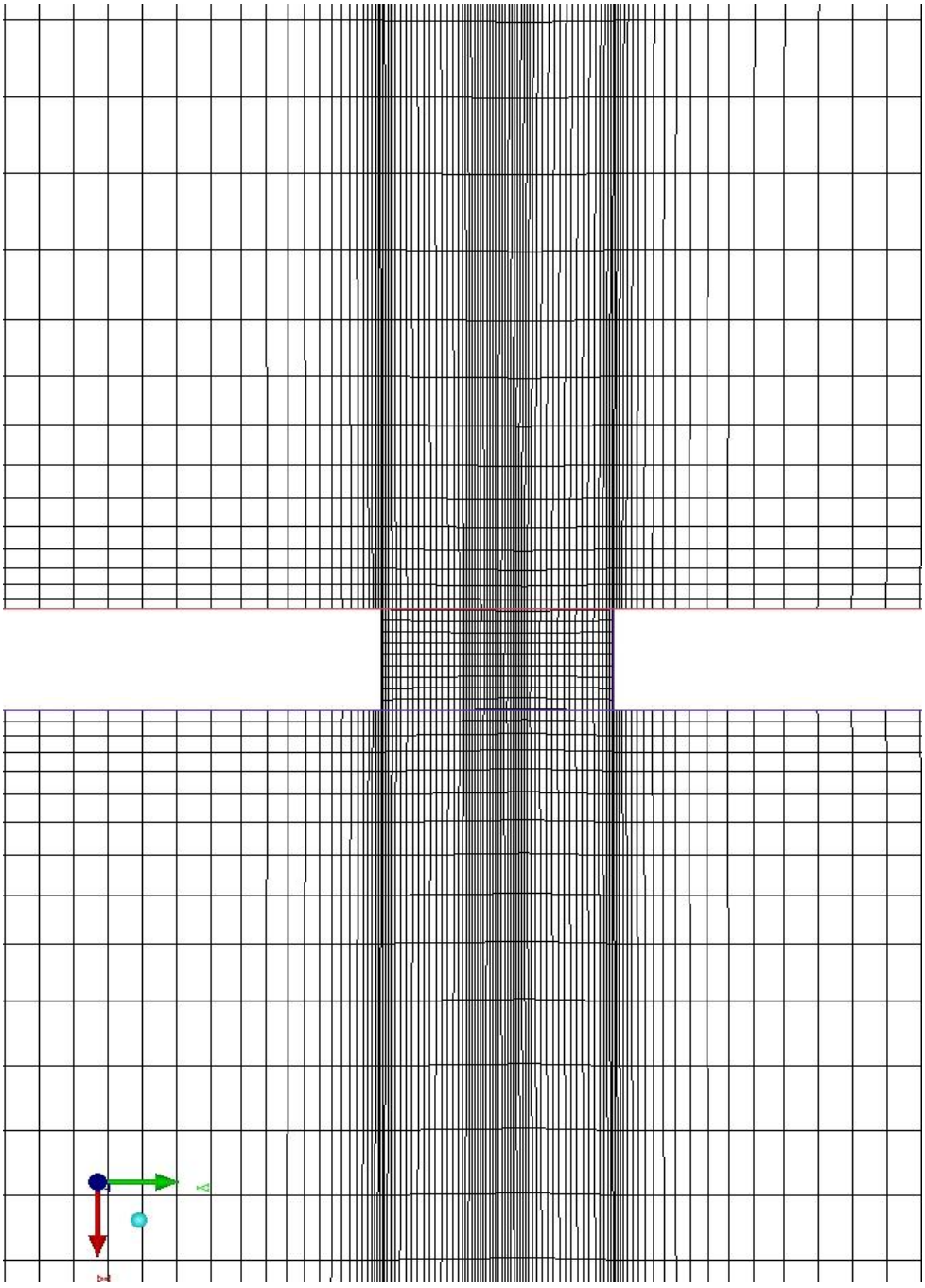

Figure 4.3 – Illustration of grid and grid distribution at middle of x-y plane (enlarged near orifice).

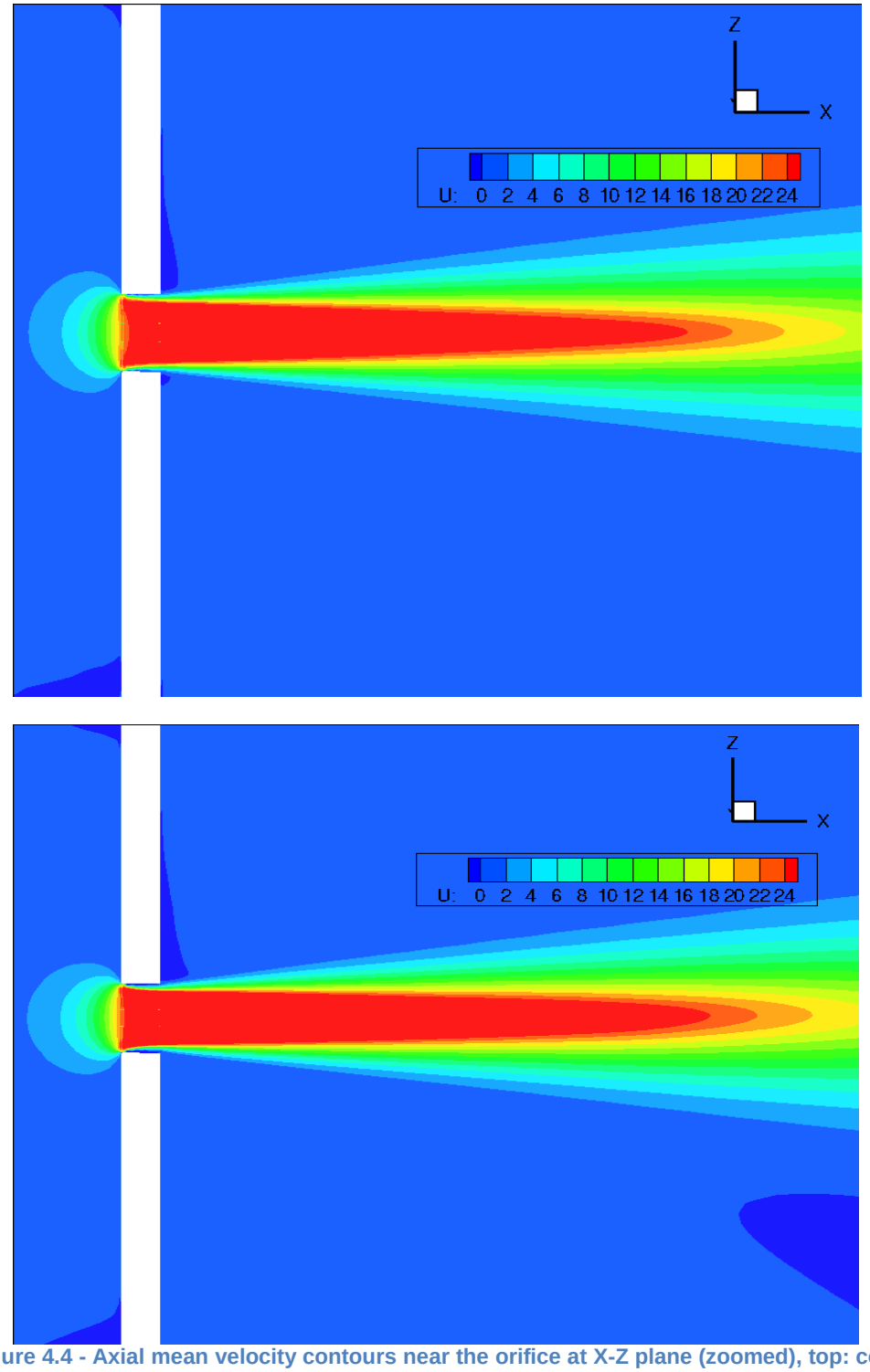

Figure 4.4 - Axial mean velocity contours near the orifice at X-Z plane (zoomed), top: coarse y-z plane grid distribution, bottom: fine y-z plane grid distribution.

4.4 DURBIN'S REALIZABLE k-ε

In the case of bias flow through the orifice, due to the large area ratio between the orifice and the rectangular duct, the flow field upstream of the orifice is subjected to high acceleration. It is well known that the standard high Reynolds number k-ε formulation of Jones et al. (1972) does not perform well in region of high acceleration/deceleration (Pope 2000). For example in an impinging jet flow, turbulent kinetic energy (k) is over-predicted (Pope, 2000) which can influence the overall flow field. Evidence of this effect can be seen in the present predictions; Fig 4.5 shows predicted contours of mean axial velocity & turbulent kinetic energy near the orifice using the standard k-ε formulation for a bias flow condition. The highest predicted 'k' (but due to spurious generation) is at the entrance to the orifice. This high turbulent kinetic energy is then convected downstream into the jet flow. The very high k at the centre of the orifice leads to enhanced turbulent diffusion and a shorter potential core length. In general, the highest kinetic energy in such a flow would be expected to occur in the shear layers on the edges of the jet. To remove the high "spurious" prediction of k in highly strained flows, Durbin (1996) proposed a modification to the standard k-ε model. He pointed out that the strained flow anomaly was due to the occurrence of large values of unphysical turbulent time scale (k/ε) with the standard k-ε model. By imposing a realisability constraint ($2k \geq \overline{u'u'} \geq 0$), a constrained turbulent time scale formulation was derived:

Turbulent time scale (T) = $min\left(\frac{k}{\varepsilon}, \frac{2k}{3kC_\mu}\sqrt{\frac{3}{8|S|^2}}\right)$ (4.1)

where |S| is the trace of the rate of strain tensor.

When the turbulent time scale as constructed in eqn 4.1 is used in the current CFD predictions, the unrealistic high turbulent energy in the highly strained flow approaching the orifice is eradicated. Fig 4.6 shows contours of mean axial velocity and turbulent kinetic energy near the orifice. The spurious production of k in the orifice entry region has been suppressed and the production of turbulence is highest in the jet shear layer. As a consequence of this a much longer jet with a potential core region ~ 5-6 orifice diameters occurs, as expected for jet flow with low flow turbulent intensity. Note that the predicted solution asymmetry (seen particularly in the k contours in Fig. 4.6) is due to the fact that the results shown in Figs 4.5 and 4.6 were obtained with a steady RANS solver that was not run to complete convergence. The purpose of these calculations was to illustrate the benefit brought about by the Durbin turbulence model modification. The key aspect was the suppression of the spurious turbulence at the orifice entry. This was already obvious in the solutions shown in Figs. 4.5 and 4.6. The asymmetry in the k contours was slowly disappearing as iterations continued, but it was not viewed necessary to run this to complete convergence as the key point had already been proved. Because of the improved results obtained using the Durbin time-scale correction, all further calculations shown below included this, but all were now run in unsteady solution mode with sufficient time steps for

the solution to be fully converged, or to display true periodically repeating conditions over several cycles.

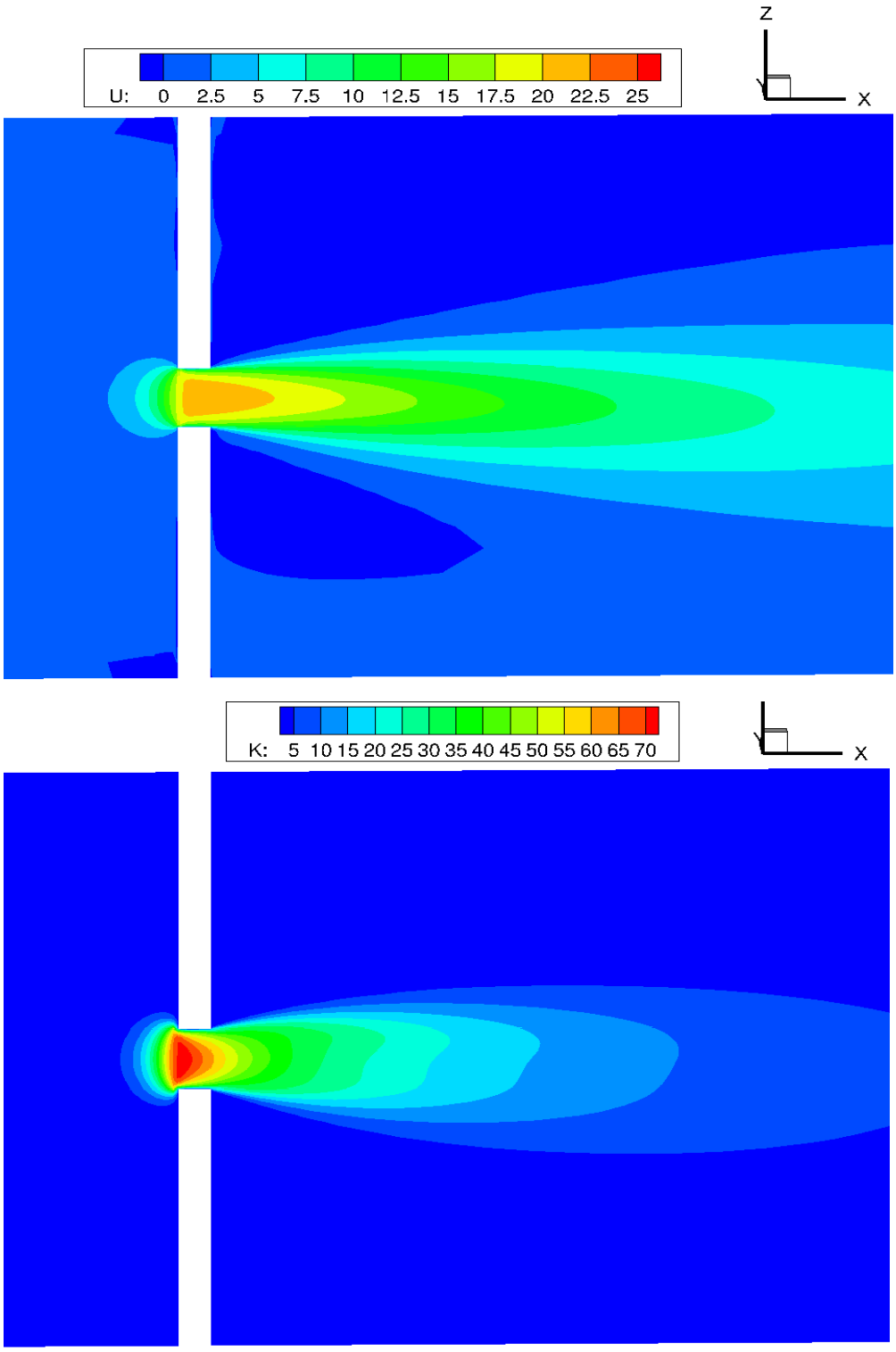

Figure 4.5 - Contours of mean axial velocity (top) and turbulent kinetic energy (bottom) from standard k-ε.

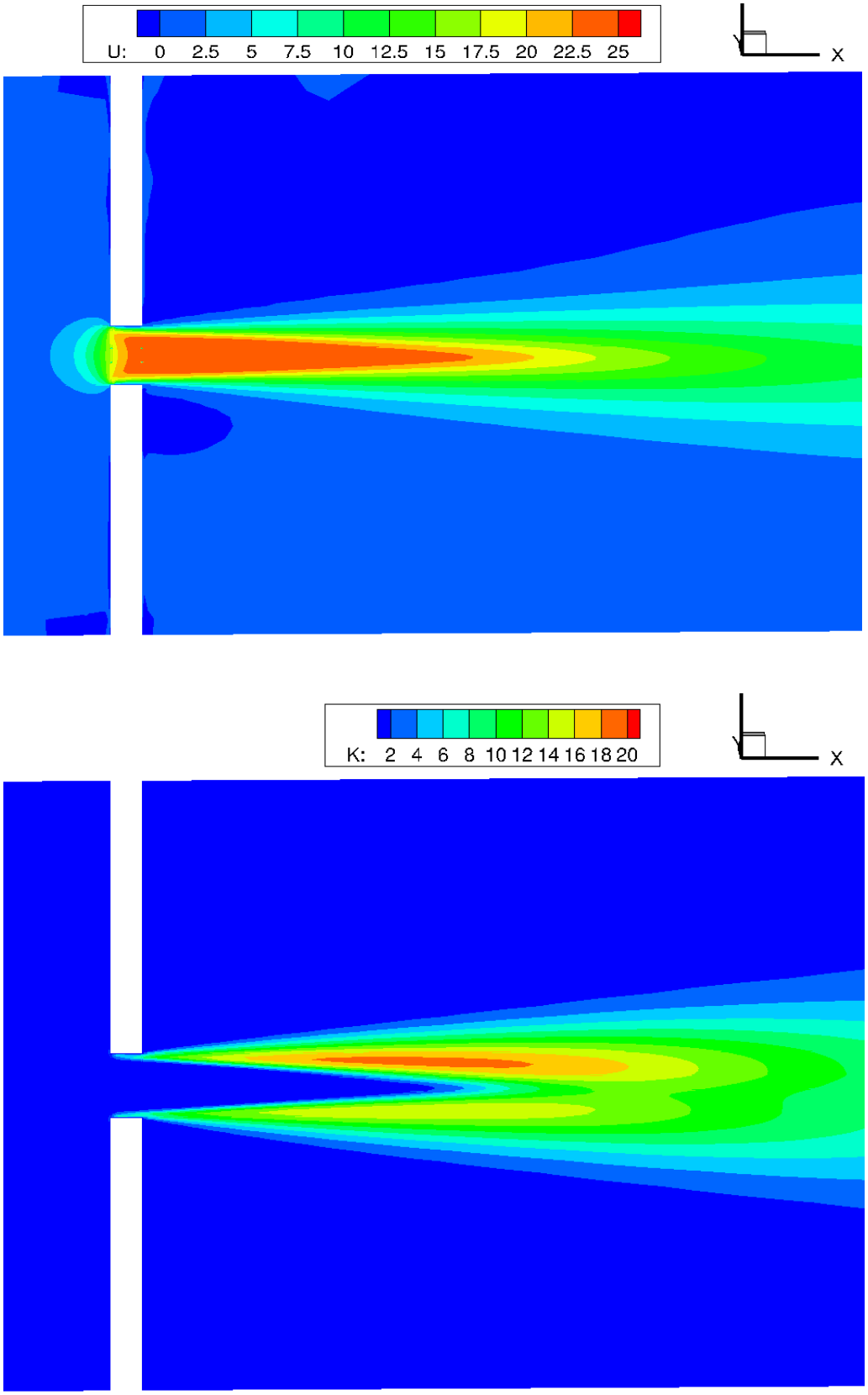

Figure 4.6 - Contours of mean axial velocity (top) and turbulent kinetic energy (bottom) after including Durbin's correction.

4.5 ABSORPTION COEFFICIENT

The mildly-compressible Fuel-3D code was now applied to calculate the acoustic absorption coefficient of a single orifice as in the experiments of Rupp et al (2010). The experiements studied acoustic behaviour for various mean pressure drops across the orifice ranging from zero to 2900 Pa. Two mean flow conditions (zero Δp and 500 Pa Δp across the orifice) were chosen for study. The reason for this choice is related to the value of Δp at which non-linear behaviour of the absorption coefficient was observed (see Rupp et al 2010). The absorption coefficient was calculated as in the experiments using the difference between acoustic power propagating towards the orifice and acoustic power propagating away from the orifice relative to the acoustic power propagating towards orifice.

Acoustic power of an upstream propagating wave is:

$$W^- = \left(\frac{cs\ area\ of\ duct}{2\bar{\rho}\bar{c}}\right)(|\tilde{p}^-|^2)(1-M)^2 \qquad (4.2)$$

Acoustic power of a downstream propagating wave is:

$$W^+ = \left(\frac{cs\ area\ of\ duct}{2\bar{\rho}\bar{c}}\right)(|\tilde{p}^+|^2)(1+M)^2 \qquad (4.3)$$

Thus the absorption co-efficient is calculated as:

$$\Delta = \frac{W_{di}^- + W_{ur}^+ - W_{dr}^+ - W_{ut}^-}{W_{di}^- + W_{ur}^+} = 1 - \frac{W_{dr}^+ + W_{ut}^-}{W_{di}^- + W_{ur}^+} \qquad (4.4)$$

The overall acoustic pressure can be decomposed into downstream propagating acoustic wave ($\tilde{p}^+$) and upstream pressure wave ($\tilde{p}^-$) using plane wave acoustic relationship as shown below:

In plane acoustic waves, acoustic pressure can be represented as

$$\tilde{p} = \tilde{p}^+ + \tilde{p}^- \qquad (4.5)$$

and acoustic velocity as:

$$\tilde{u} = (\tilde{p}^+ - \tilde{p}^-)/\bar{\rho}\bar{c} \qquad (4.6)$$

Using eqn (4.5) and (4.6), the downstream propagating acoustic wave component is:

$$\tilde{p}^+ = (\tilde{p} + \tilde{u}\ \bar{\rho}\bar{c})/2 \qquad (4.7)$$

and the remaining part in the eqn 4.5 corresponds to the upstream propagating acoustic wave.

For the case of 500 Pa Δp across orifice the mean flow was first established without input of any acoustic perturbation with turbulence modelled using the k-ε model in which eddy viscosity was modified using Durbin's (1996) realizable constraint, and using pressure boundary conditions as given in Table 1. WENO was used for the convective terms and transient terms were discretised using 2nd order implicit method. Once the mean flow was established, acoustic wave excitation was then applied. In the case of no mean flow condition, the Reynolds number at the duct was only 150 even at the highest sound amplitude level tested. This Reynolds number is very low even for low Reynolds turbulence models. Thus, the absorption coefficients were predicted assuming a laminar mean flow.

Table 4.1 summarises the various boundary conditions used for mean flow and for acoustic simulations. As detailed above, in Rupp's (2010) experimental set-up, air was drawn into the duct from a large plenum using a well-designed bell-mouth entry. Typically such well-defined duct entrance conditions have weak turbulence and since exact level of turbulence in duct entry is unknown different levels of turbulent intensity (2- 7%) and viscosity ratio (10 - 500) were tested to study the influence of inflow boundary condition. Higher levels of turbulence are generated within shear layers than inflow boundary, making the result of the calculation relatively insensitive to the inflow boundary values, thus the turbulence quantities at inlet were calculated assuming 5 % turbulent intensity and a viscosity ratio (eddy / molecular viscosity) of 100.

The pure upstream propagating acoustic wave (p_{di}^{-}) which was input at the downstream end of the duct (representing loud-speaker excitation) will be partly transmitted through the orifice and propagate into the upstream duct (p_{ut}^{-}); the remaining acoustic energy will be reflected and propagate to the right towards the exit of the downstream duct (p_{dr}^{+}). Because of imposition of an acoustic closed boundary condition at duct inlet (pressure anti-node condition), the transmitted wave will be fully reflected (p_{ur}^{+}) back towards the orifice as shown in fig 4.7 (a). Fig 4.7 (b) shows the waveform of the overall acoustic pressure signal as well as decomposed upstream and downstream propagating pressure wave in the downstream duct (top) as well as in the upstream duct (bottom) taken at 30 * orifice diameter upstream and downstream of the orifice. All results were collected over a sequence of at least five full cycles, and test runs over longer times revealed no tendency for the cycle to change. The decomposition was carried out using eqn 4.5 - 4.7. It can be seen that there is significant phase difference between the input upstream propagating pressure wave(p_{di}^{-}) and the reflected pressure wave(p_{dr}^{+}) in the downstream duct. In the upstream duct, due to the imposed boundary condition, the reflected downstream pressure wave(p_{ur}^{+}) is in-phase with the transmitted wave (p_{ut}^{-}), it is also evident from Fig 4.7, that the transmitted wave is not a pure sinusoidal form but contains contributions from higher harmonics.

	Mean flow	***Acoustics***
Duct inlet	Total pressure inlet	Characteristic wave inlet for velocity, pressure & density
Duct outlet	Fixed static pressure	Characteristic wave outlet for velocity, pressure & density
k at inlet	5 % turbulent intensity	Same as mean flow
ε at inlet	Obtained assuming μ_t/μ_{mol}= 100	Same as mean flow

Table 4. 1 - Boundary conditions used to prescribe velocity and turbulence quantities for mean flow and mildly compressible simulations.

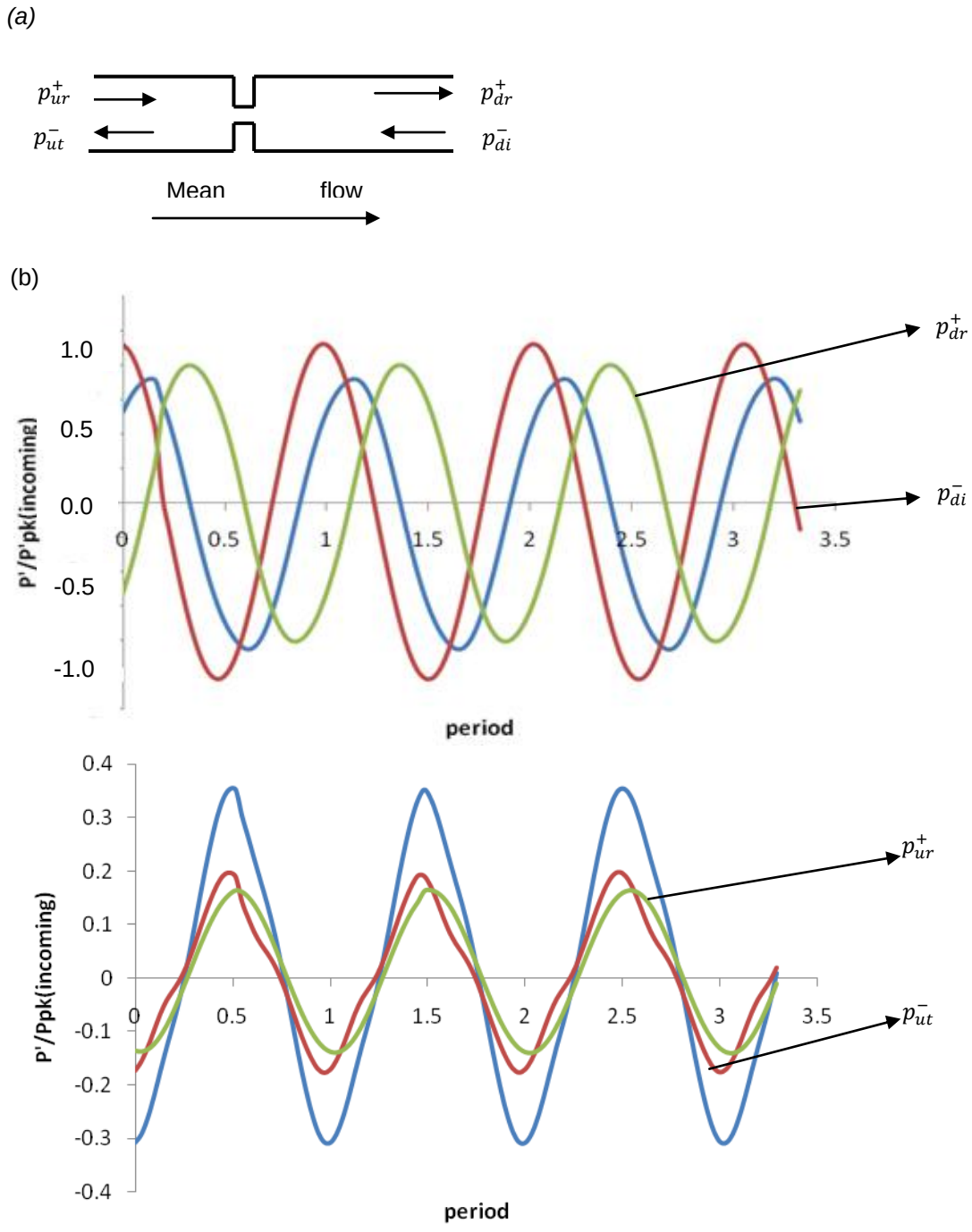

Figure 4.7 - (a): Wave decomposition in the duct & (b): Decomposed waves at downstream of orifice (top) as well as upstream of orifice (bottom). Overall acoustic pressure in blue; upstream propagating wave in red & downstream propagating wave in green.

Figure 4.8 shows a comparison between the absorption co-efficient predicted using the current CFD approach and the measurements of Rupp et al. 2010. Good agreement can be seen across all excitation amplitudes as well as both mean flow conditions. At 500 Pa mean

pressure drop, the absorption tends to be constant at a predicted value of 0.29 until an excitation level of 140dB. This indicates a linear acoustic phenomenon. Further increase in excitation amplitude begins to show non-linear effects as the absorption coefficient starts to increase slightly. Note that this behaviour is observed to occur at the same excitation level in the CFD predictions as in the test data. Rupp et al (2010) commented that this onset of non-linearity is associated with the excitation amplitude increasing to a level where the unsteady pressure change at the downstream orifice face is able to reverse the flow through the orifice overcoming the effect of the mean Δp.

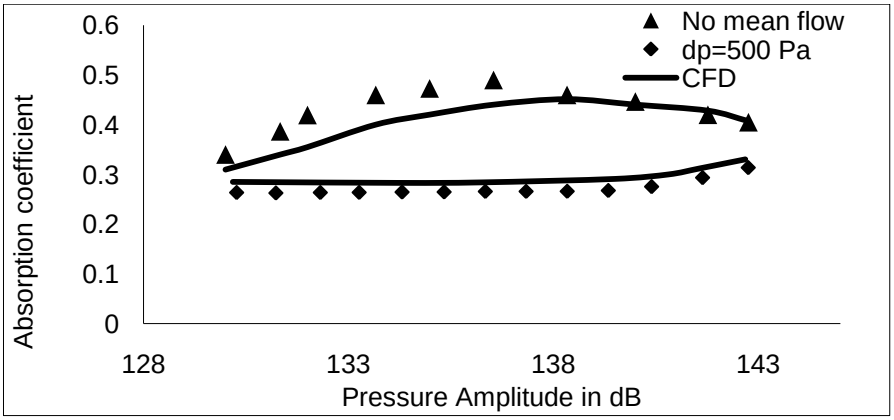

Figure 4.8 - Absorption coefficient with and without mean flow, symbol – Rupp et al. (2010) & line – CFD.

The images of CFD predicted flow structures at various stages of the acoustic cycle shown in Fig. 4.9 confirm this description. Fig 4.9 shows predicted axial velocity contours and streamline patterns for 5 points in the acoustic cycle, starting at a time when the acoustic pressure perturbation at the downstream orifice face is zero and about to start increasing. For the 5 flow-field snapshots shown, the first is at the initial time and the other 4 are separated by a phase of $\pi/2$ from the initial time. For 137dB excitation, the jet through the orifice increases and decreases in strength and width as the acoustic perturbation changes, but the flow is always forwards through the orifice, and the flow external to the jet corresponds to a pure entrainment process. Note that the streamline pattern in the region outside the jet which visualises the entrainment into the jet shear layers is not quite symmetrical. This is as expected in a 3D URANS prediction carried out assuming no symmetry planes, so the jet is free to 'wander' off centreline, and does so. For increased excitation to 143 dB, the jet flow through the orifice experiences a stronger deceleration, eventually leading to a small separation region inside the orifice (seen best at the second time instant, where the streamlines within the orifice move away from the walls and a close-up indicates negative velocities - see Fig 4.10, which shows the flow features near the orifice at the second time instant). This creates a 'starting vortex' as the jet begins to flow forward again (seen forming in the third frame). The growth in size and downstream propagation of the starting vortex ring is clearly visible in Fig 4.9 for 143dB excitation, but not present at all at the 137dB level. The kinetic energy of this vortex is responsible for the

increase in acoustic damping coefficient, since the vortex kinetic energy (subsequently dissipated into internal energy) is extracted from the acoustic energy.

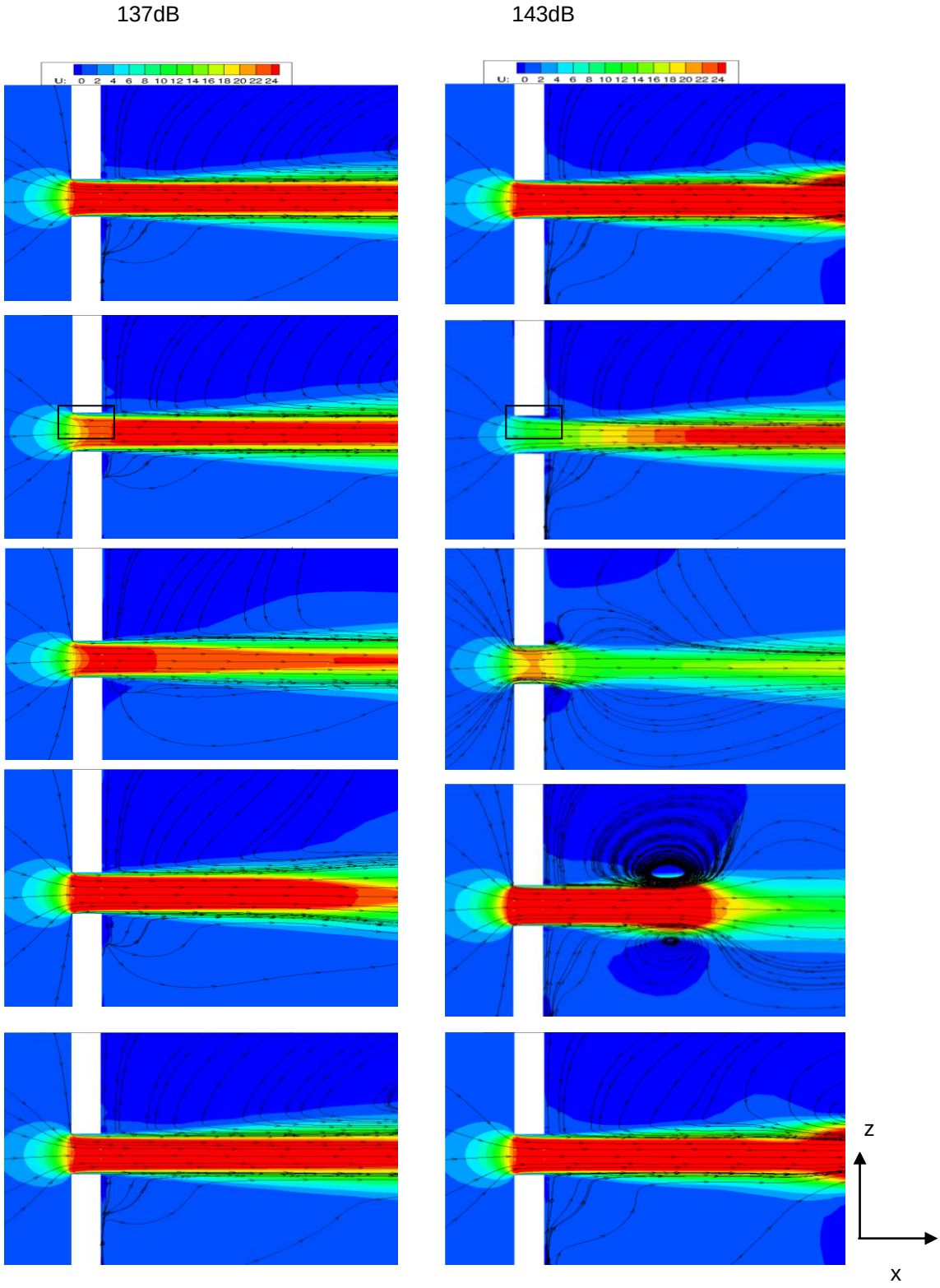

Figure 4.9 - Sequence of images showing the difference between 137 dB, left (linear) and 143dB, right (nonlinear) flow structure for 500 Pa Δp across orifice; boxed region in IInd sequence is zoomed at the orifice and shown in Fig 4.10.

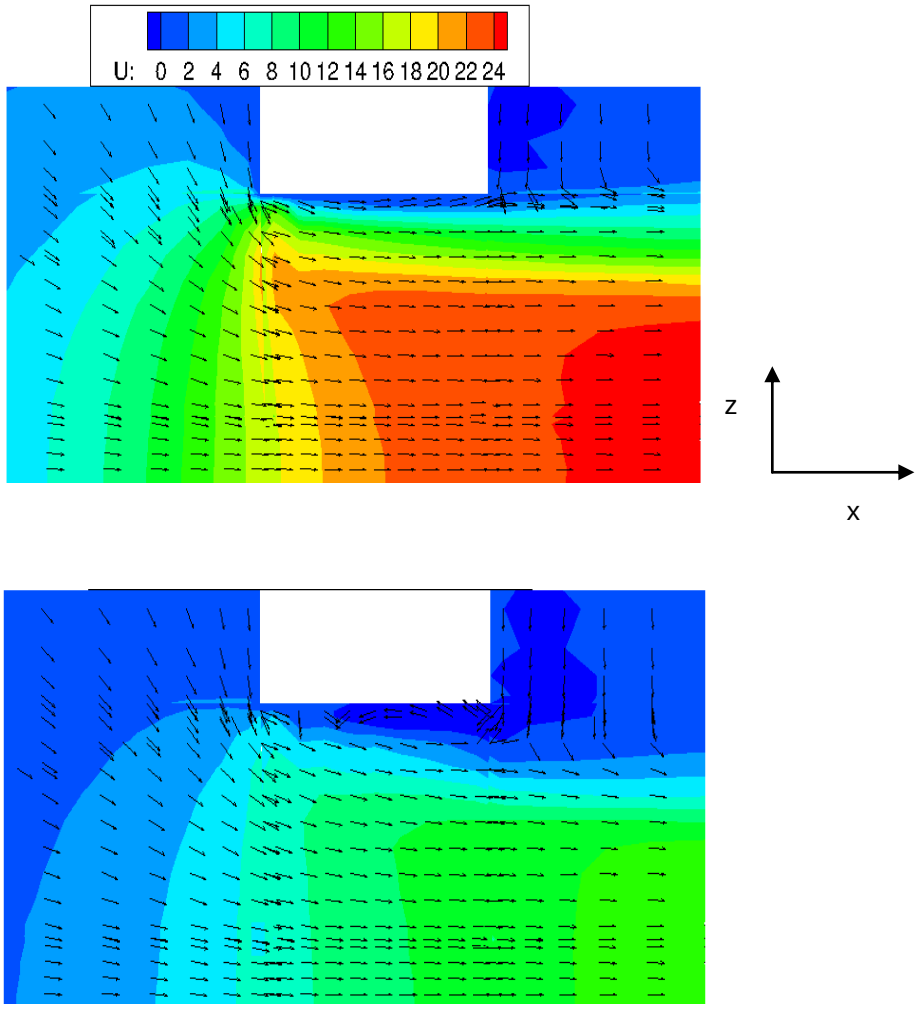

Figure 4.10 - Flow structure and velocity vectors near the orifice at the second time instant of Fig 4.9, 137dB (top) and 143dB (bottom).

The non-linear behavior of the absorption coefficient can of course be seen most clearly, and for all excitation amplitudes in the zero mean flow predictions shown in Fig. 4.8 and in the equivalent flow structure images in Fig. 4.11. Vortex rings are predicted to exist at all excitation levels and the strength of the vortex increases, leading to enhanced acoustic absorption, as the pressure level increases. However, a peak and subsequent decrease in the acoustic absorption curve is observed in the experiments at ~137dB, and in the CFD predictions at 139dB. The decrease is due (see Rupp et al. (2010) & Gharib et al. (1998)) to the fact that above a certain level of excitation, a maximum circulation in the vortex ring is reached; further increase in acoustic pressure amplitude leads more to a strengthening of the so-called secondary jet (Gharib et al. 1998), which is formed in the vortex central region and trails behind it, rather than increased vortex strength. This secondary jet is less effective at extracting energy from the acoustics, so the damping coefficient falls. Fig. 4.11 shows a stronger secondary jet is predicted for excitation above 139dB.

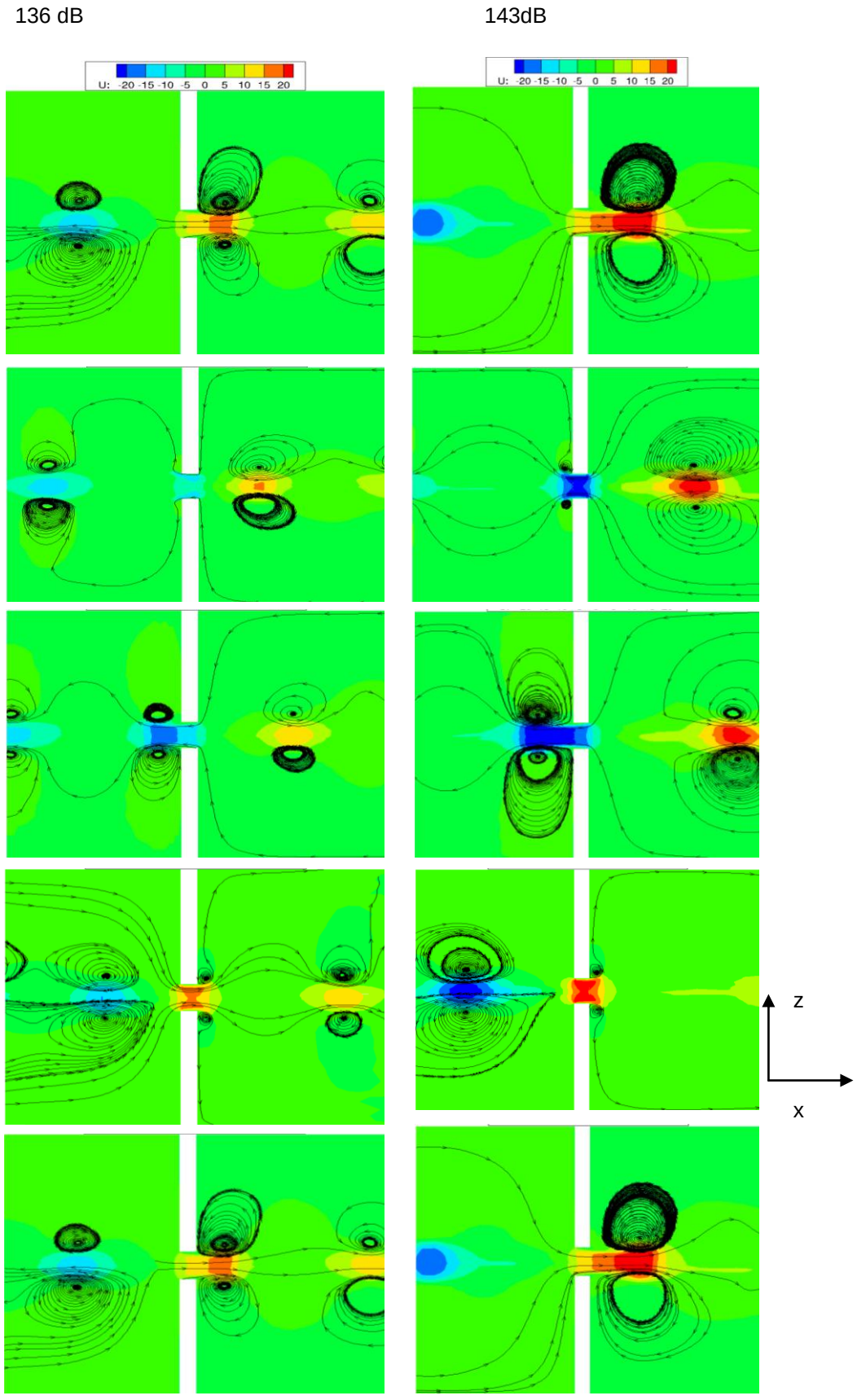

Figure 4.11 - Sequence of images showing the difference between the flow structures at 136dB, (left) & 143 dB, (right) sound level (no mean flow) .

4.6 TRANSMISSION OF HIGH-AMPLITUDE SOUND THROUGH AN ORIFICE

The detailed waveforms of transmitted and reflected waves produced due to sound absorption were analysed for all CFD simulations carried out. It was observed that with or without bias flow nonlinear behaviour of the transmitted wave was observed for sound levels above 139 dB. This is therefore discussed in detail here and is illustrated in Fig 4.12 for no mean flow (top) & 500 Pa pressure drop (bottom). The pressure signatures of the wave transmitted to the upstream duct are depicted in Fig 4.12 (amplitudes have been shifted for ease of representation) for a range of excitation amplitudes starting at 137 dB upto 143 dB. At both flow conditions, the wave profile becomes progressively distorted from a pure sinusoid as the incoming sound amplitude level increases. For the case of no mean flow at the higher sound level, transmitted waves display a saw-tooth shape whereas in the case of the bias flow, waves are stretched in the increasing part of the cycle and compressed in the decreasing part, this kind of behaviour is clearly evident above 139 dB level excitation.

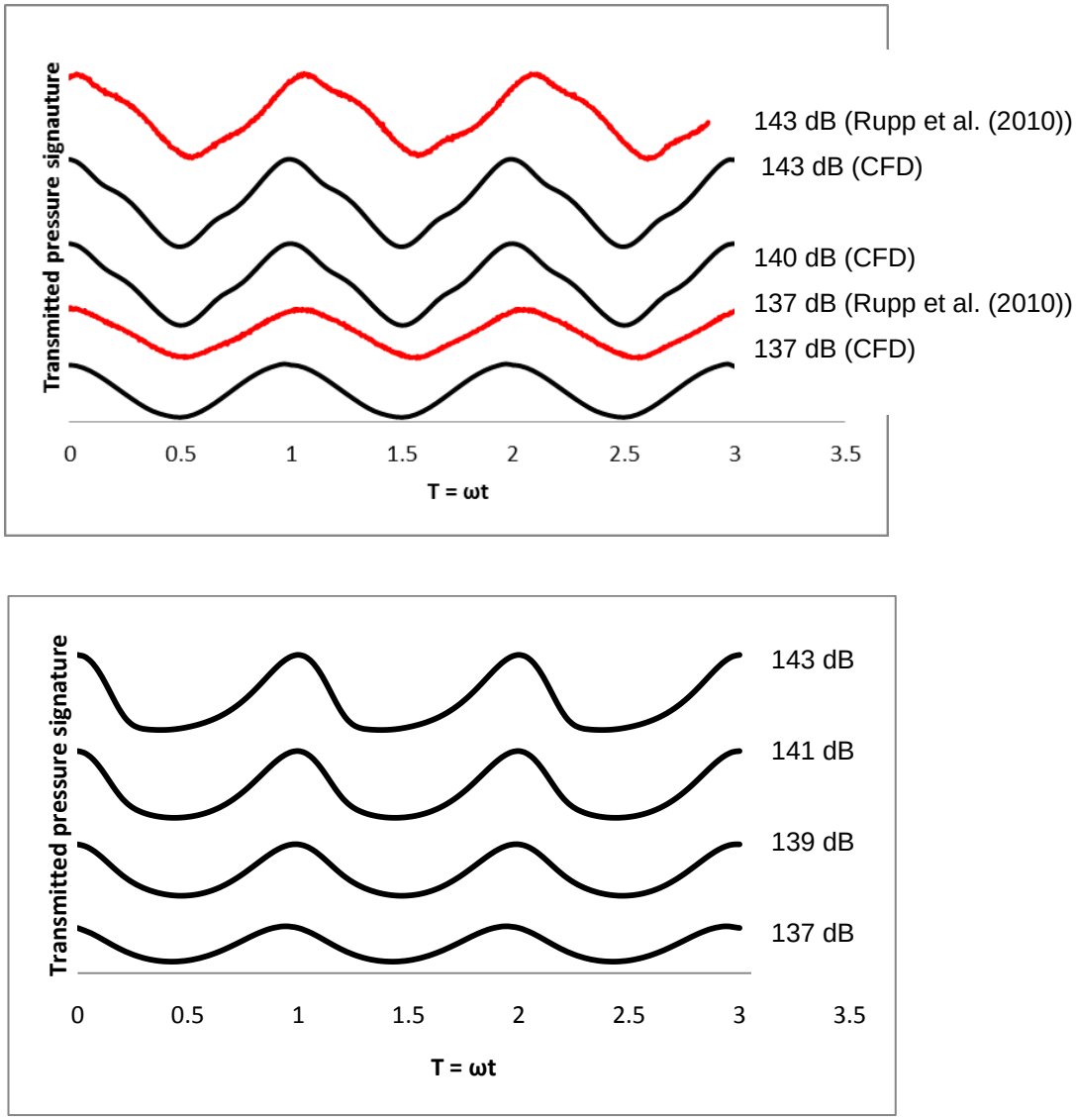

Figure 4.12 - Pressure signature transmitted through an orifice for various excitation amplitudes; zero Δp (top), 500 Pa Δp (bottom).

4.7 CONCLUSIONS

Based on the results presented above, the mildly compressible algorithm developed in this thesis has demonstrated an excellent capability for predicting acoustic damping in an orifice flow geometry. Accurate prediction of absorption co-efficients for a wide range of excitation amplitude levels and at various flow conditions (with and without bias flow) were observed. The present investigation, also demonstrated clear evidence to support Gharib et al's. (1998) and Rupp et al's. (2010) suggestion that vortex shedding was the dominant mechanism for non-linearity in orifice configuration. Finally, it was also proven, as predicted by Howe (1998) and Rupp et al.(2010) that the transmitted pressure signal can contain evidence of non-linearity via harmonics of the incident wave frequency under high amplitude excitation.

5. A STUDY OF THE ACOUSTIC SENSITIVITY OF COMBUSTOR EXTERNAL AERODYNAMICS

5.1 INTRODUCTION

As an illustration of the use of the mildly compressible CFD code developed and validated in this research project, in this chapter the sensitivity to acoustic pressure fluctuations of the aerodynamics of a dump diffuser as typically found in modern aero gas turbine combustion systems is studied. Initially, without introducing acoustic excitation, the flowfield is predicted using a two-equation URANS approach and results compared with experimental data (Manners et al.1997), with good agreement observed. The response of this mean flowfield to various acoustic excitation signals was then analysed for a selected range of excitation frequencies. After identifying the most sensitive acoustic frequency, further acoustic analysis was carried out to study the behaviour of the dump diffuser flowfield for various acoustic boundary conditions.

5.2 MOTIVATION FOR THE CURRENT STUDY

In a comprehensive experimental study, Regunath et al. (2010) have confirmed the existence and origin of aerodynamic instabilities excited by acoustic perturbations in the external aerodynamic flowfield of a typical geometry as found in modern combustors. The work presented in the present section was inspired by the idea of exploring whether such acoustically driven phenomena could be captured using the mildly compressible algorithm developed in this thesis. A brief overview of the work of Regunath et al. (2010) is therefore needed. In a geometry representative of a rich burn combustion system (e.g. Rolls-Royce Trent 500), flow measurements even without acoustic excitation indicated aerodynamic instabilities in the dump cavity and the outer annulus region, identified via regions of significantly enhanced turbulence level. The observed flowfield features were similar to those found, for example, in free shear layers and are usually associated with large scale instabilities and coherent turbulent structures. Using various frequencies of loudspeaker generated acoustic excitation propagating into the combustor system from downstream (to represent pressure fluctuations due to heat release), Regunath et al. (2010) analysed the response of the regions of instability in the dump cavity. When the input acoustic excitation was at the ‘natural’ frequency of the aerodynamic instabilities (these had been initially identified with no external acoustic input) even stronger enhanced energy levels were observed, due to the formation of highly coherent structures. The amplification was typically 1 or 2 orders of magnitude greater than the response at other frequencies.

Measurements using the same upstream combustor external aerodynamics configuration (pre-diffuser + dump diffuser) but without the flametube liner indicated no aerodynamic instabilities were present, presumably because the geometry of the corner recirculation in the dump region and the associated curved shear layers were altered. Regunath et al. (2010) concluded that the measured aerodynamic instabilities and their sensitivity to acoustic excitation were due to the particular characteristics of the curved free shear layer that separates the flow issuing from the pre-diffuser from the outer dump cavity recirculation. It is the purpose of the CFD investigation presented in this chapter to examine whether the CFD algorithm developed in this thesis is capable of reproducing the phenomena observed in Regunath et al. (2010)'s experimental study.

5.3 FLOW GEOMETRY AND GRID GENERATION

Since the observations described above indicated that the main phenomenon to be studied was closely related to the characteristics of the curved shear layer on the edge of the corner re-circulation region in a dump-diffuser, it was deemed unnecessary to represent all details of the complex rich burn combustion geometry used by Regunath et al. (2010) in the calculation to be undertaken. Instead, a simplified generic annular dump diffuser geometry tested experimentally by Manners et al. (1997) was chosen, since this configuration had detailed flow and turbulence data for validation of the zero acoustic excitation case. Combustor diffuser systems essentially begin at the exit of the compressor Outlet Guide Vane (OGV) and extend downstream and into the inner/outer annular regions surrounding the combustion chamber. A pre-diffuser is always present, followed by a relatively large expansion commonly known as the "dump region"; further downstream the combustion chamber is located in the middle of the geometry forming a blockage to stabilise flow exiting the pre-diffuser. The combustor liner divides flow into an inner and outer annulus which feeds air into ports drilled into the liner walls, as well as providing cooling air for the liner and for the turbine downstream. Note that in the simplified geometry used by Manners et al. (1997) a solid combustor liner was used, allowing no air to enter the combustor. Fig 5.1 provides a sketch of the geometry. Since the geometry is axi-symmetric, only a small circumferential sector needs to be considered in URANS calcuations. The focus of the current work is on studying external aerodynamic phenomena in a geometry which comprises the entire flow exterior to the combustion chamber, such as pre-diffuser, dump region and both annuli flows. Note that no flow features in the combustor system had to be included, (e.g., fuel injector, dilution holes etc), the liner of the combustion chamber was completely closed, thus all flow from the pre-diffuser leaves the system through the two annuli with a 65:35 mass flow split specified between outer and inner annulus respectively as dictated by the experimental conditions.

For the current study a 15 degree circumferential sector of the dump diffuser was selected . For the URANS calculations undertaken here any size of sector could have been chosen.

For LES calculations the sector size would have to be large enough not to constrain the azimuthal size of large eddies and 15 degrees was deemed sufficient (for future LES studies). Structured multi-block grids were generated for this sector using commercial grid generating software (ICEM-CFD). The computational grid consisted of 600,000 grid points (40,000 points in the x-r plane and 15 points in the azimuthal plane). The mesh distribution in an x-r plane is shown in Fig 5.2 along with the location of 5 different stations used in the measurement comparison with Manners et al. (1997) experimental data; 3 stations are located downstream of the pre-diffuser exit within the dump cavity and 2 stations are towards the downstream end of the combustor head in the outer annulus. At these 5 measurement stations, mean quantities from two-equation URANS predictions are compared with LDA data.

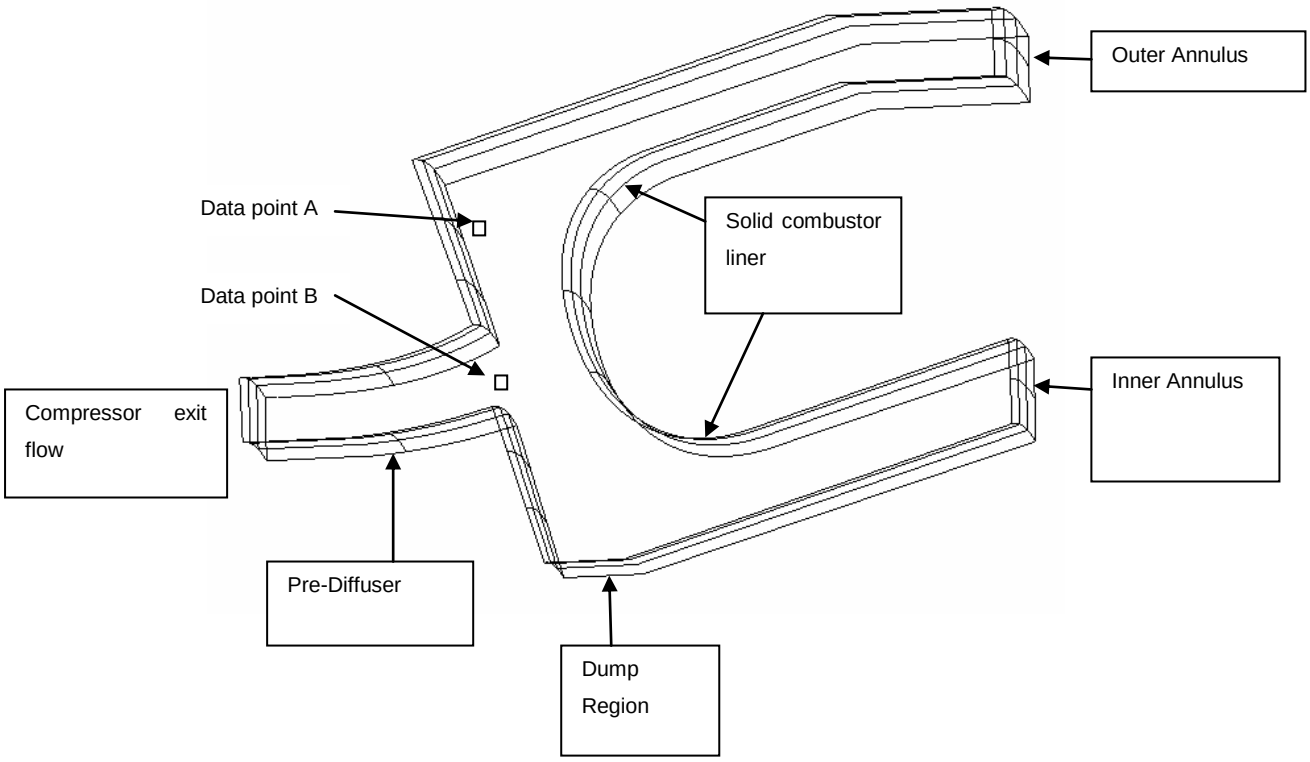

Figure 5. 1 - A sector of a dump diffuser system and associated nomenclature; (small boxes in dump region indicate pressure signal monitoring locations in acoustic simulations)

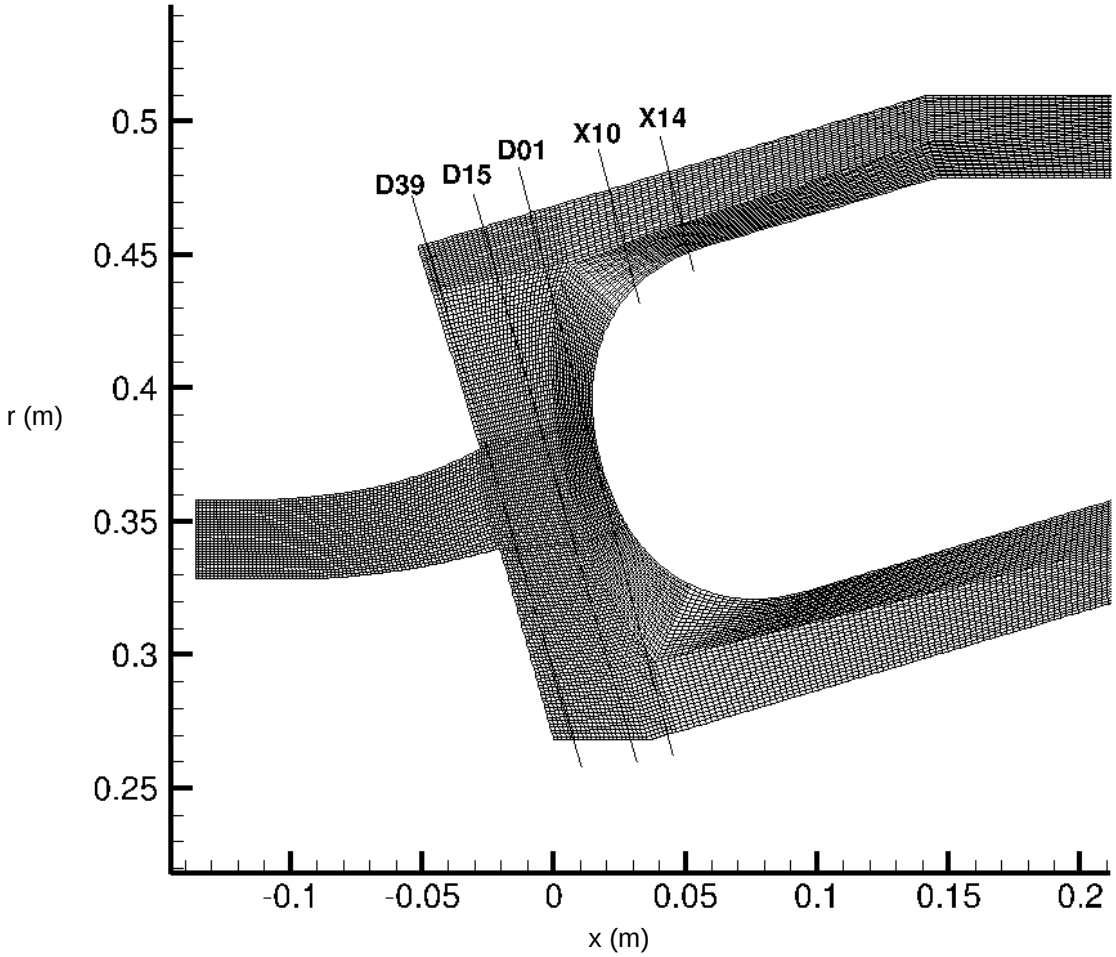

Figure 5. 2 - Computational mesh in x-r plane and measurement station locations.

5.4 RESULTS WITHOUT ACOUSTIC EXCITATION

Using the computational domain and mesh as specified in the previous section, incompressible, unsteady two-equation (k-ε) URANS simulations were performed first in order to predict the mean flowfield in the dump diffuser system. The experimental profiles of $\overline{U},\ \overline{V}\ and\ \overline{W}$ ($\overline{V}\ and\ \overline{W}$ were zero) velocity components and turbulent kinetic energy (k) were taken from the Manners et al (1997) LDA measurements and specified as fixed inlet conditions. The turbulent dissipation (ε) was estimated by assuming the ratio between eddy and molecular viscosity was 500 at the inlet. The mass flow split between the outer and inner annulus (65:35) was forced at the domain outlets. “Law of the wall” wall functions were used as well as the 2nd order accurate implicit time scheme and the WENO scheme for convective fluxes; these practices remained the same for all simulations presented in this chapter. Two side boundaries in the circumferential direction were treated as cyclic boundaries.

Fig 5.3 illustrates the various flow features present in the dump diffuser system – an expanding flow in the pre-diffuser and an emerging and impinging jet, corner flow recirculation and curved shear layers in the dump region. Fig 5.3 shows both streamlines (top) and axial mean velocity contours (bottom). The flow enters from the inlet, decelerates within the pre-diffuser and enters the dump region as a jet. The jet flow impinges on the head of the combustion chamber and splits into two streams which flow into the inner and outer annulus. In the dump region large corner recirculation regions are formed between the dump cavity walls and curved shear layers form on the outer/inner edges of the impinging jet. Note that a small third re-circulation region is predicted to occur on the combustor wall in the inner annulus due to shear layer detachment from the combustor wall.

Mean velocities predicted using the present k-ε simulation were compared with LDA measurements (Manners et al. 1997) at the locations indicated in Fig 5.2. Fig 5.4 shows the axial and transverse velocity profiles at station location D39 which is located just downstream of pre-diffuser exit. The profiles are plotted along the LDA transverse line (see Fig 5.2) and are shown on a normalised co-ordinate r/h (where h represents the pre-diffuser inlet annulus height) which has its origin at the outer wall of the dump cavity and is measured radially inwards along the transverse line. It can be seen in the case of the axial velocity that the jet issuing from the pre-diffuser is symmetric about the pre-diffuser centre-line for the CFD whereas the LDA data show a bias towards the upper pre-diffuser wall. This is due to the fact that in the experimental setup, the inner wall of the pre-diffuser had different boundary layer trips to the outer wall, which leads to an inner wall shear stress 40% greater than on the outer. This level of sophistication in inlet conditions has not been incorporated into the CFD predictions at this stage but this could easily be done. The small mean transverse velocity has been captured well in magnitude and shape in the CFD results. At the measurement plane in the middle of the dump region, D15, the comparison between mean axial and transverse velocities is presented in Fig 5.5 and again shows good agreement between CFD and experiment. Similarly, at station D01 which is located just upstream of the combustion chamber head good agreement between CFD and experiment is again observed.

Finally, stations X10 and X14 were selected to focus attention on the flow development in the outer annulus. At location X10 (Fig 5.7), both velocity profiles are surprisingly well predicted considering this location is situated within the outer re-circulation region, and an eddy viscosity RANS turbulence closure is not usually considered to be highly accurate for a such flow regime. The profiles are now plotted against a normalised co-ordinate *r/h* starting from 0 at the inner wall and reaching 1 at the outer wall so it now represents the local annulus height at X10. The mean axial velocity is slightly over-predicted near the inner wall

where a wall jet flow is formed, whereas near the outer wall a slight under-prediction of the strength of backflow is obtained.

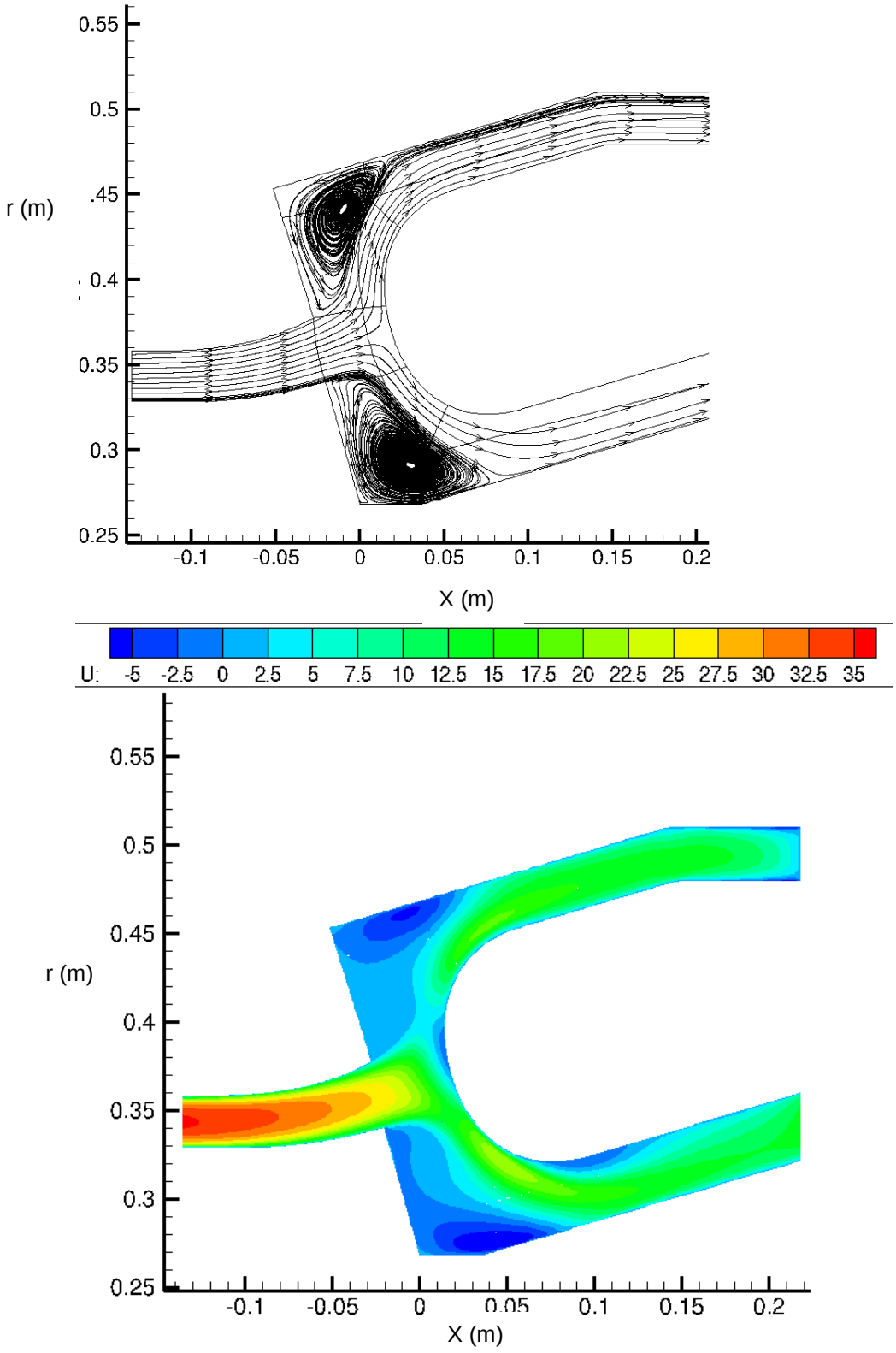

Figure 5. 3 - Flow streamlines (top) and mean axial velocity contour (bottom) at the mid-plane.

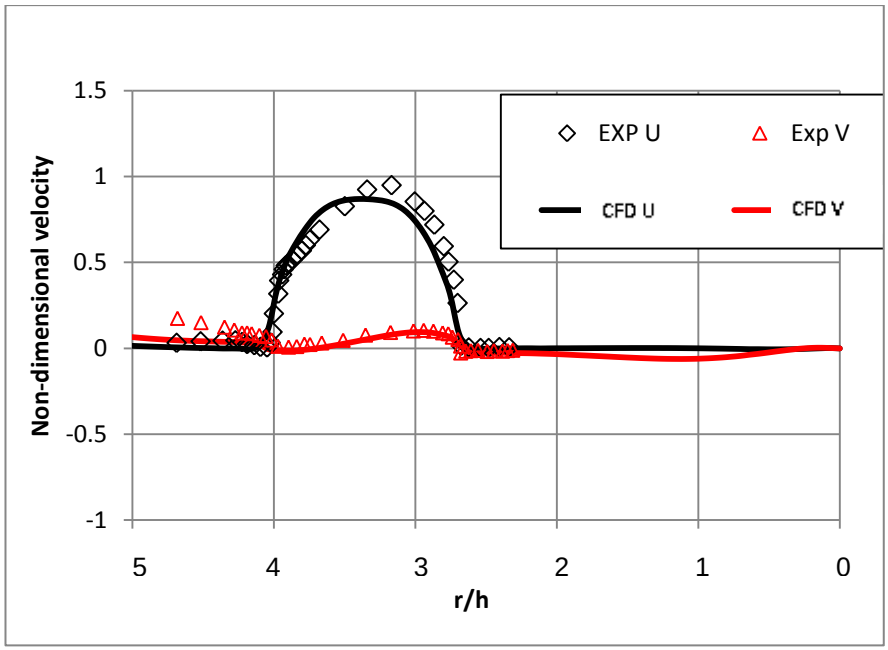

Figure 5. 4 - Mean axial and transverse velocity profiles at station D39 compared with LDA experiments (Manners et al. (1997).

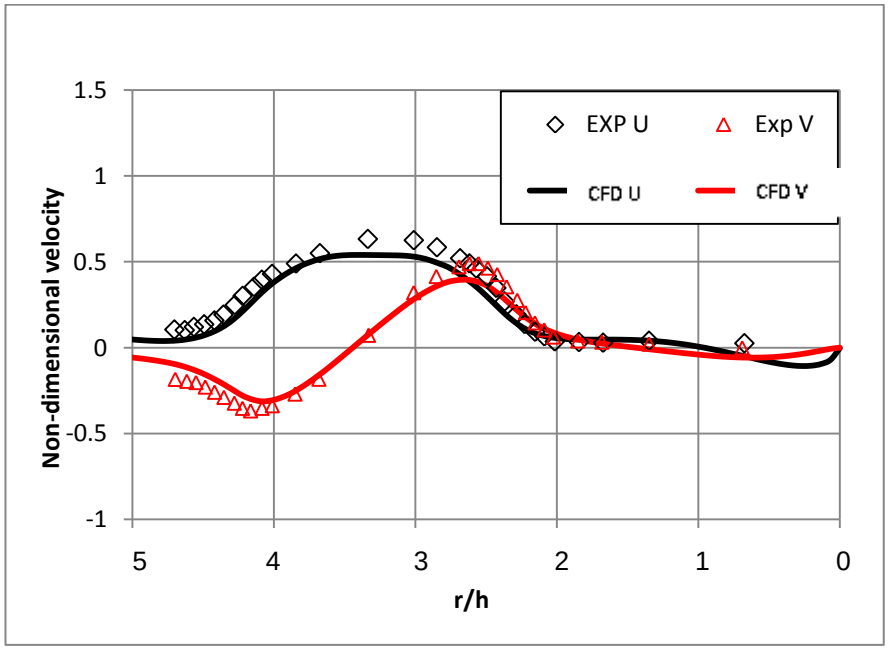

Figure 5. 5 - Mean axial and transverse velocity profiles at station D15 compared with LDA experiments (Manners et al. (1997).

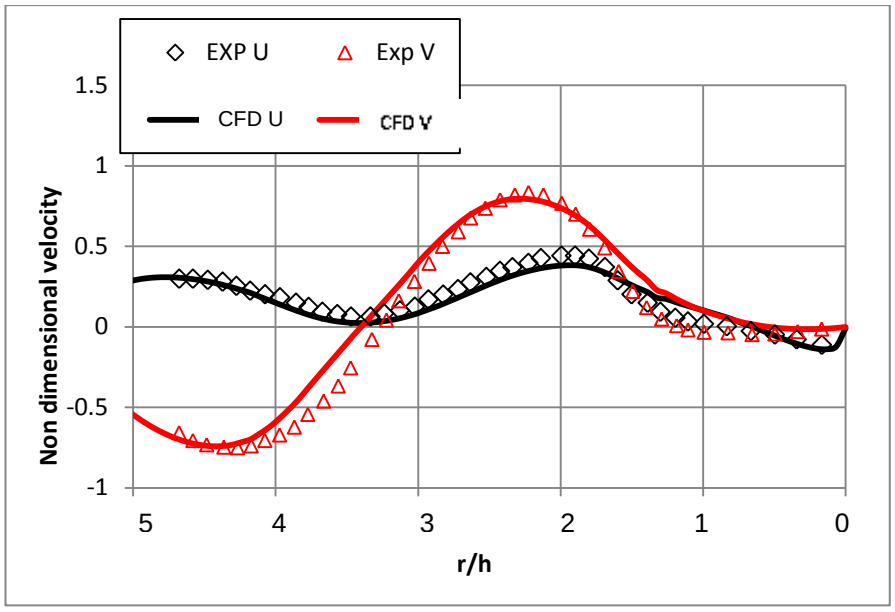

Figure 5. 6 - Mean axial and transverse velocity profiles at station D01 compared with LDA experiments (Manners et al. (1997).

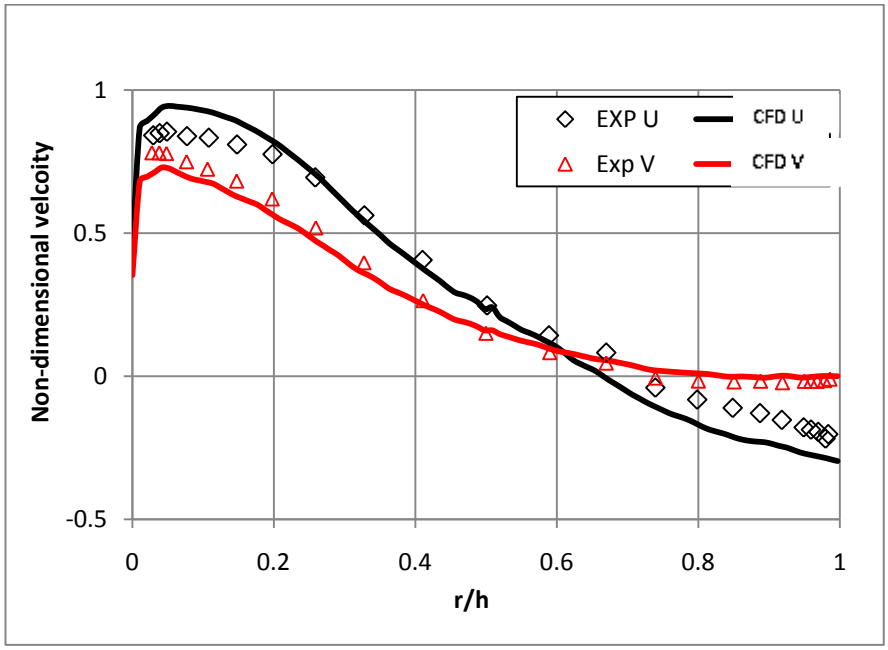

Figure 5. 7 - Mean axial and transverse velocity profiles at station X10 compared with LDA experiments (Manners et al. (1997).

The axial length of the re-circulation region is under-predicted, as is evident from comparison of CFD and LDA data at station X14 (Fig 5.8). The predictions indicate re-attachment has already happened, but the experimental data show a small negative velocity. The present predictions in Fig 5.7 and Fig 5.8 are similar to eddy viscosity calculations shown by Tang et al. (2004) using a different CFD code. They also showed that if improved prediction of the mean flow field is needed, even a Reynolds stress turbulence model is not sufficient and an LES CFD approach is required. The predicted levels of turbulent kinetic energy (k) are shown in Fig 5.9, higher turbulence energy levels are predicted in the region where the outer curved shear layer approaches the annulus wall. Since this was also observed in the experiments of Regunath et al. (2010) this is encouraging for the current investigation.

Whilst the agreement between predicted time-average flow features and experimental measurements can be improved, as stated above, it was considered sufficient for the present purpose as the k-ε model captures the overall flow pattern adequately and shows evidence of the outer curved shear layer displaying a tendency for enhanced turbulence activity. The next section therefore describes the acoustic sensitivity study of the predicted flow.

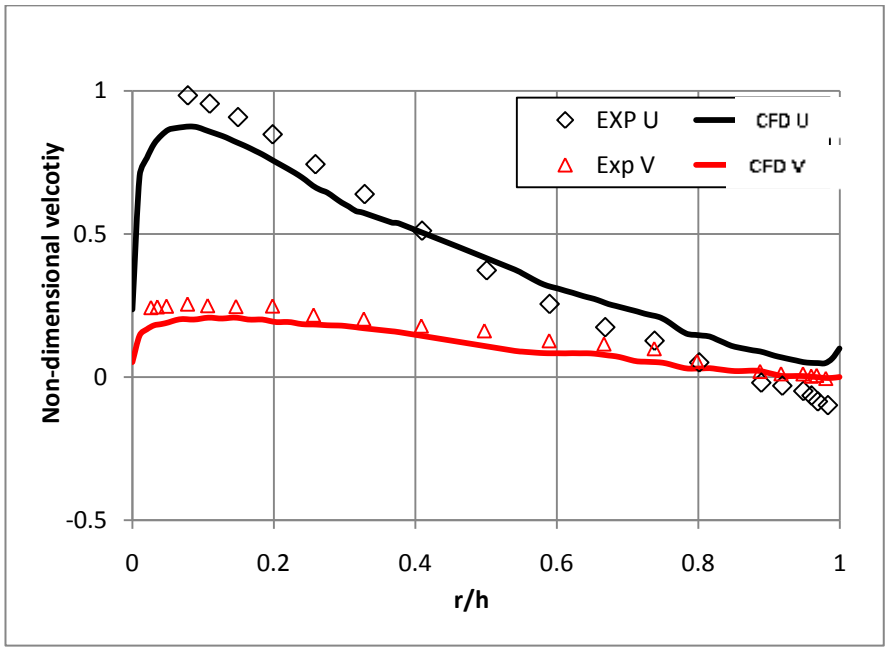

Figure 5. 8 - Mean axial and transverse velocity profiles at station X14 compared with LDA experiments (Manners et al. (1997).

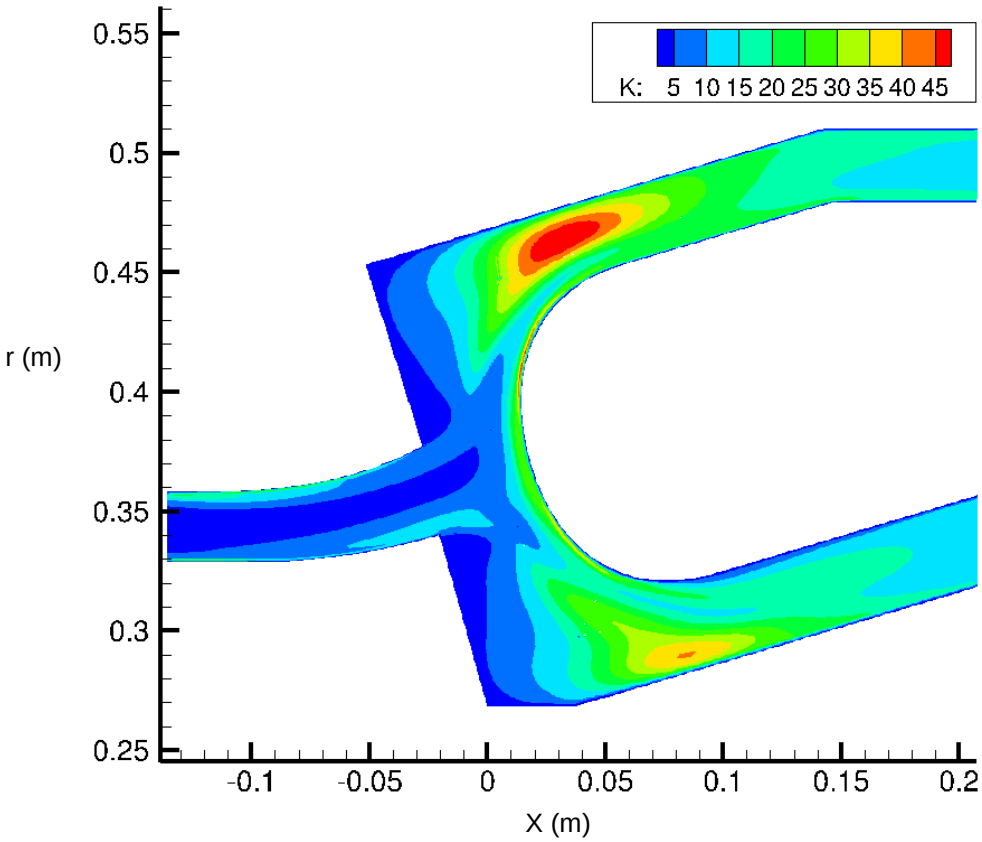

Figure 5. 9 - Contours of turbulent kinetic energy (k) in x-r plane at z = 0.

5.5 RESULTS WITH ACOUSTIC EXCITATION

Simulations to study the response of a typical dump diffuser flowfield to external acoustic excitation were carried out by using the developed mildly compressible CFD algorithm described in earlier chapters. The incompressible URANS steady state solution described in section 5.4 was taken as initial conditions for the whole flowfield. At both inner and outer annulus exit boundaries the boundary conditions were changed from zero-gradient outflow to a characteristic boundary condition with a pure left travelling plane acoustic wave as input. This simulated the presence of a loud-speaker system allowing plane acoustic waves of specified frequency and amplitude to propagate upstream through the inner and outer annulus into the dump cavity. The flow split between outer and inner annulus was maintained at 65 - 35 % respectively with reference to the steady state inlet mass flow rate. This mean flow split was retained in the unsteady solution by mapping the mean static pressure field and mean velocity components at the annulus exit predicted in the steady state URANS calculation and treating these as the mean pressure and mean velocities used in the unsteady characteristic boundary condition. Similarly mean k and ε at annulus outlets were taken from the steady state calculation. Characteristic boundary conditions were also applied at pre-diffuser inlet. In the first set of acoustically excited predictions (where excitation frequency was varied) the inlet characteristic conditions were set (as described in

section 3.5) assuming an infinitely long duct existed upstream of pre-diffuser inlet, so that left travelling acoustic waves would leave the solution domain without any reflection. In a second set of acoustically excited predictions undertaken at the "preferred" or most resonant frequency, established from the first set of simulations, acoustic reflection at pre-diffuser inlet was activated either by matching the phase of both left and right propagating pressure waves (an acoustically closed condition) or by imposing a 180º phase difference between left/right travelling pressure waves (an acoustically open condition). In all the test cases shown here, boundary conditions for mean velocities, k and ε at pre-diffuser inlet were taken from the steady state URANS solution, i.e. based on the LDA measurement of Manners et al. (1997). The characteristics of the input acoustic excitations were changed in the first set of predictions by using different frequencies (20, 65, 100, 300 Hz see below for the reasons for selecting these values) but keeping the sound amplitude level at 154 dB, which corresponds to a 1% pressure fluctuation with respect to the mean static pressure at the annuli outlets.

As mentioned in section 5.2, Regunath et al. (2010) found large scale aerodynamic instabilities in the outer annulus region and the flow scenario simulated here also for a higher mass flow through the outer annulus resulting in higher levels of turbulence near the outer annulus region as shown in Fig 5.9. This region of high turbulence activity in the upper region of the dump system might indicate a local flow pattern which is more susceptible to external acoustic excitation. Thus, in the descriptions provided below of the simulation results, focus is given to the upper region of the dump diffuser system. All results were collected over a sequence of at least five full excitation cycles, and test runs over longer times revealed no tendency for the observed flow periodic behaviour to change. Figures 5.11, 5.13, 5.15, 5.17, 5.19 below show snap-shots of axial velocity contours along with vector maps for the upper region of the dump diffuser for various input acoustic excitation frequencies. These contour maps cover one complete cycle of the input acoustic wave with each snap-shot taken at a lag of 45 degree with respect to the previous frame. The first frame shown at all excitation conditions as well as the starting point of pressure signal plots were chosen at zero phase with respect to the input acoustic excitation. The reason for choosing to plot velocity vectors as well as axial mean velocity contours is to allow better visualisation of the dynamic behaviour of the shear layer flow structures observed in the CFD. During each cycle of acoustic excitation, pressure signals were also monitored at two selected points (i) data point A at the re-circulation region near the top corner of the dump cavity, (ii) data point B at the exit of the pre-diffuser. These points are marked by boxes in fig 5.1.

5.5.1 Results for 20 Hz Acoustic Excitation (First Set)

Using the steady state URANS simulation the time for the core of the large scale recirculation in the top dump cavity to make a complete cycle was estimated and this time

scale implied a frequency of 20 Hz. Hence, to analyse possible response of the upper recirculation to external acoustic excitation, a 20 Hz left travelling acoustic wave was input through the downstream end of each annulus. Fig 5.10 shows the overall acoustic pressure signal as well as decomposed left and right propagating pressure waves at data point 'A', fig 5.1. Due to the change in geometry from annulus exit to dump region through to pre-diffuser inlet the input pure left travelling wave is both transmitted and reflected inside the dump-diffuser geometry. The acoustic pressure at data point A normalised by the input acoustic wave amplitude corresponds to amplitude of ~ 0.6 for both left and right travelling wave with little phase difference between them. The 8 frames in Fig 5.11, show the sequence of flowfield events that take place due to the 20 Hz input acoustic excitation. It can be seen from the snapshots shown that the large scale recirculation structure is squeezed and expanded, due to the imposed acoustic wave. The reattachment point on the outer wall oscillates back and forth during the cycle but only by ~ $\pm$ 3% about its mean value . Frames 1 to 4 shows the flow structure during the expansion part of the re-circulation region; it can be seen in these frames that the magnitude of negative mean axial velocity at the top of the dump region is reduced indicating the expansion of the vortex structure due to the imposed acoustic wave. Frames 5 to 8 correspond to the squeezing sequence of the large recirculation, with the strength of velocity in the re-circulation region slowly increasing during this part of the cycle. It is noticeable that the structure of the curved shear layer on the edge of the recirculation zone hardly changes during the excitation cycle.

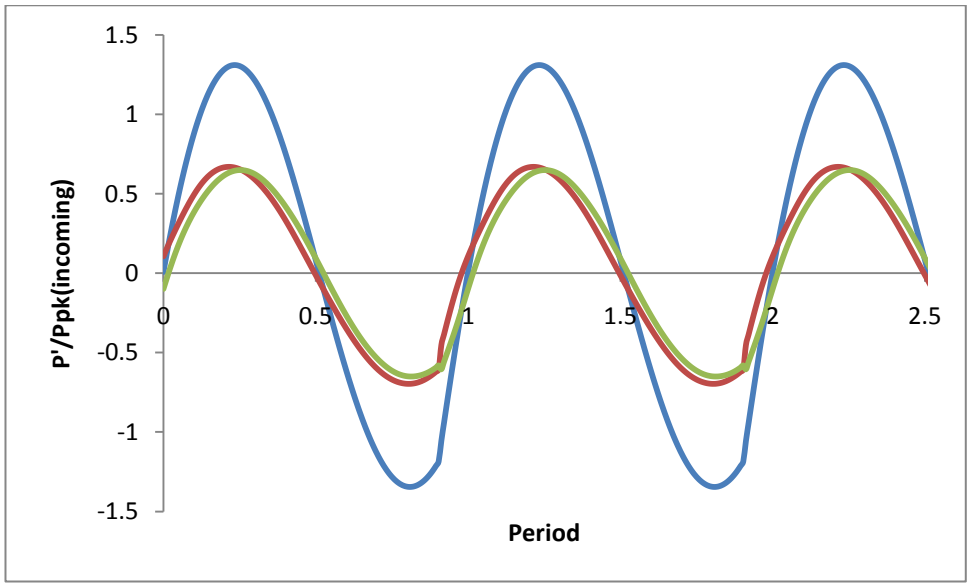

Figure 5. 10 - Pressure signal in the top dump region (see Fig 5.1 for location) for 20 Hz input frequency; blue- overall pressure wave; red- right propagating pressure wave; green – left propagating pressure wave.

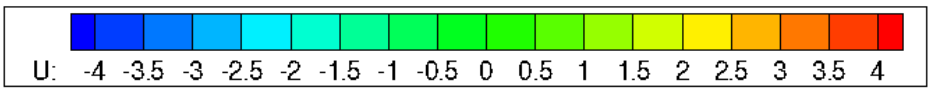

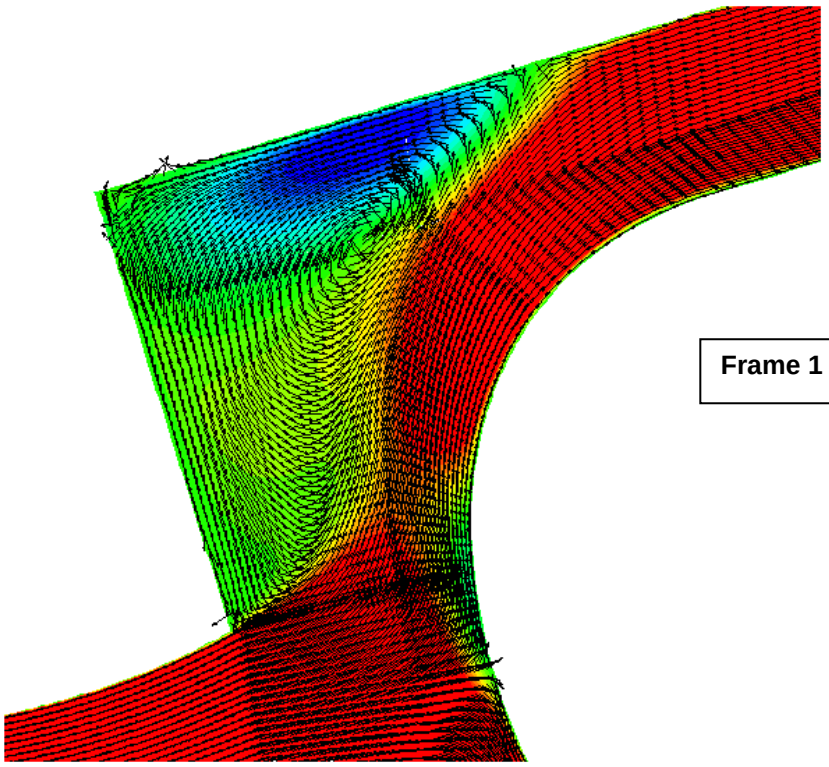

Frame 1

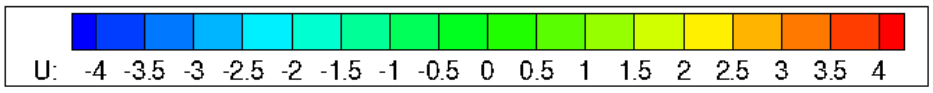

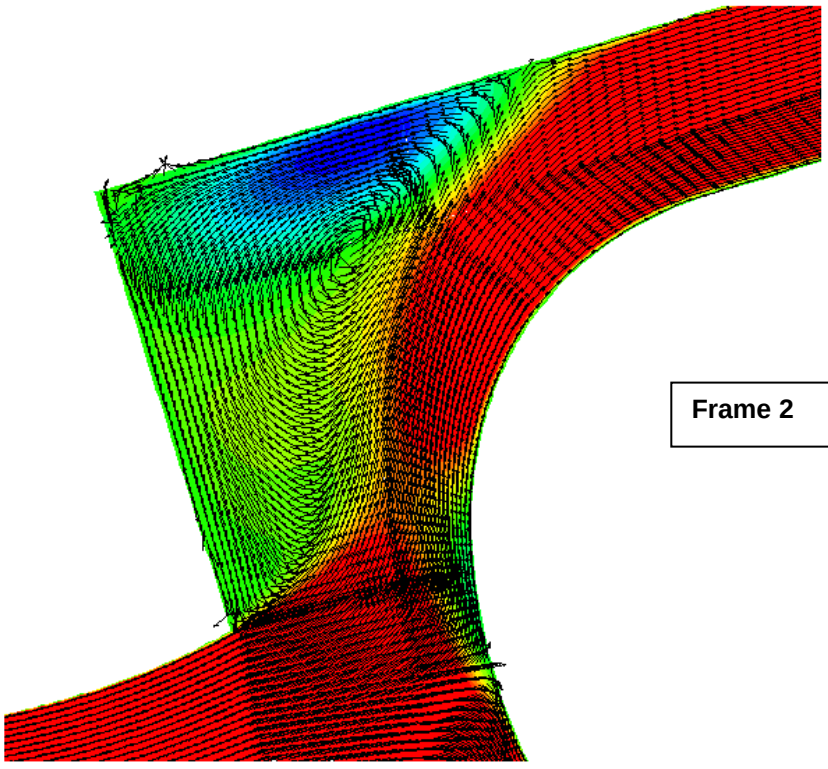

Frame 2

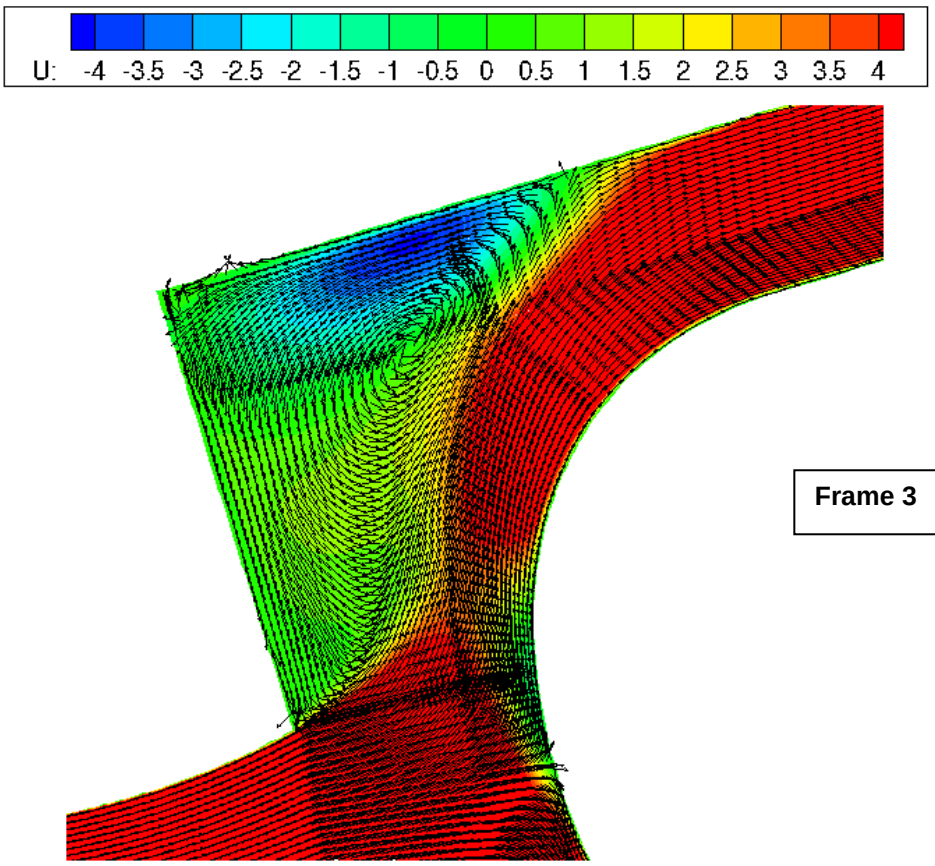

Frame 3

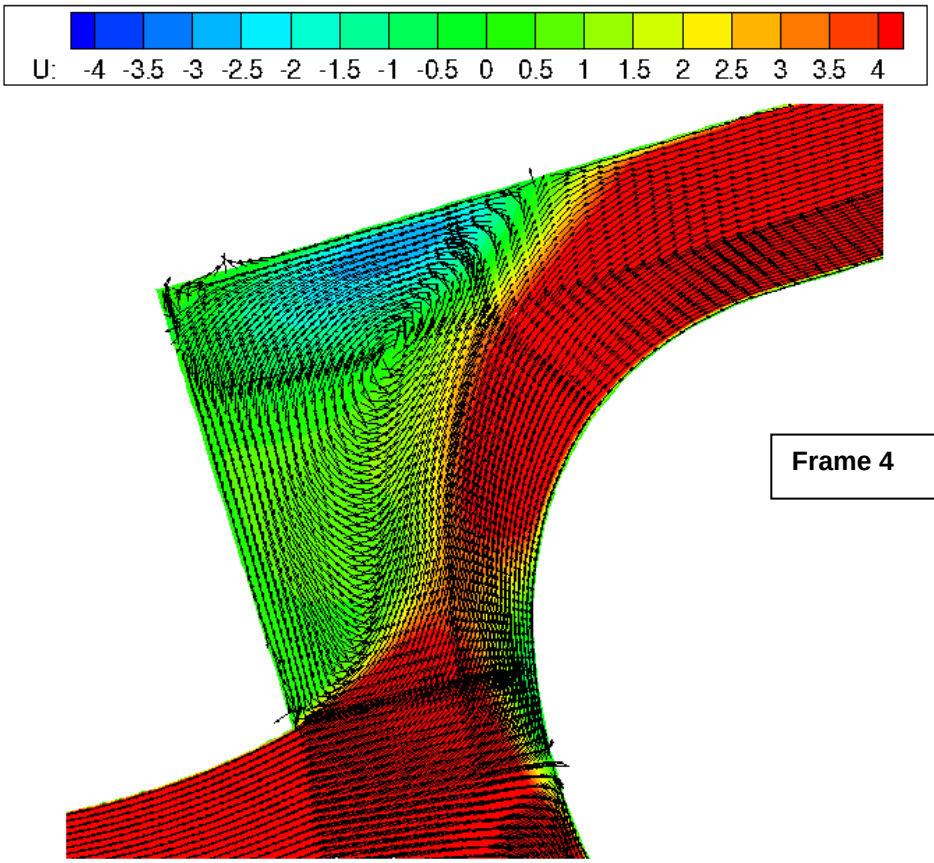

Frame 4

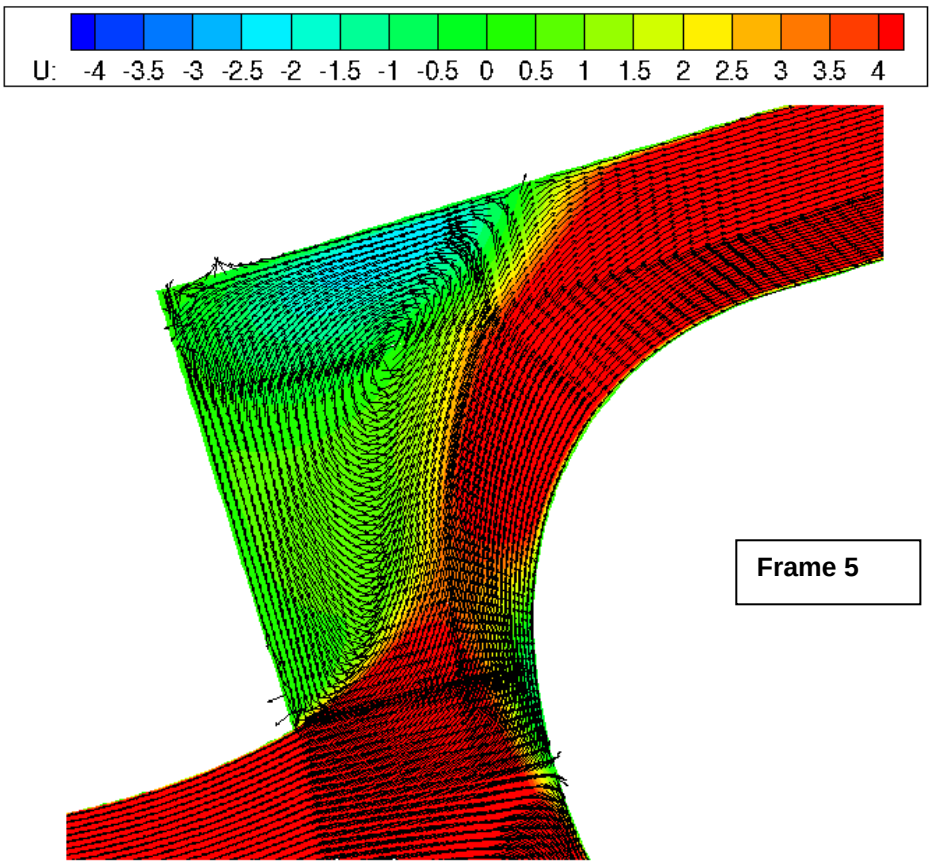
U: -4 -3.5 -3 -2.5 -2 -1.5 -1 -0.5 0 0.5 1 1.5 2 2.5 3 3.5 4
Frame 5

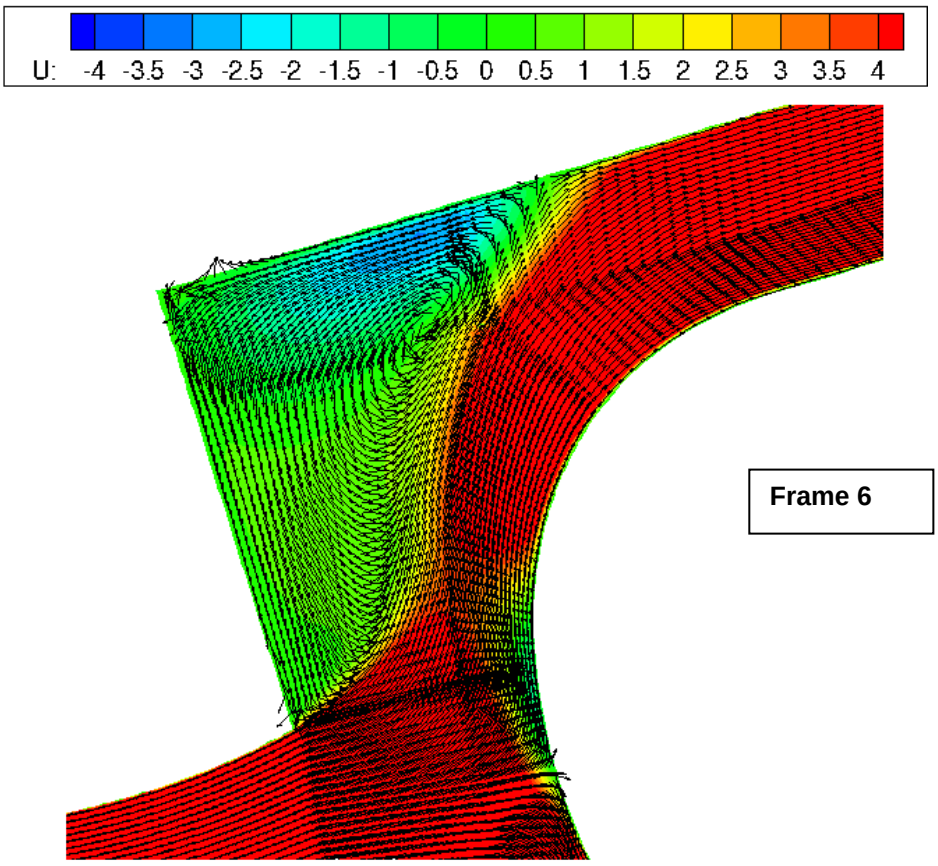
U: -4 -3.5 -3 -2.5 -2 -1.5 -1 -0.5 0 0.5 1 1.5 2 2.5 3 3.5 4
Frame 6

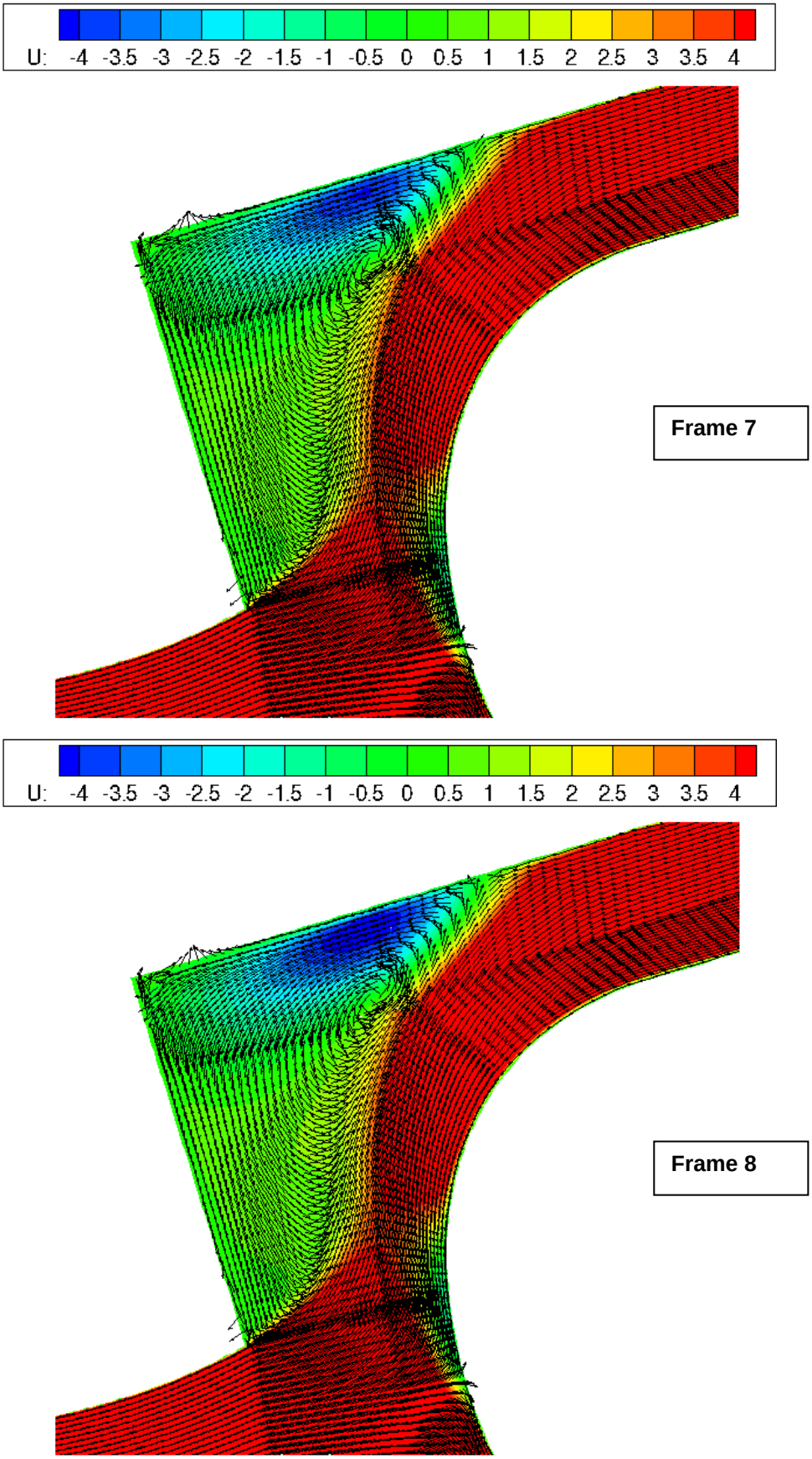

Figure 5. 11 - Sequence of snapshots of axial velocity contour and vectors for 20 Hz wave.

5.5.2 Results for 65 Hz Acoustic Excitation (First Set)

Since the imposed 20 Hz acoustic wave effectively targeting the rotational time-scale of the large re-circulation structure in the dump region did not produce much response in the dynamical behaviour of the overall dump-diffuser flowfield, simulations were next carried out at a frequency corresponding to the time-scale associated with the curved shear layer. Again using the steady state URANS results it was estimated that the convection time for a fluid particle in the shear layer starting from pre-diffuser exit to reach the wall reattachment point in the upper annulus wall was roughly 0.015 sec, corresponding to a frequency of 65 Hz. In order to examine the sensitivity of the shear-layer to external excitation, a 65 Hz acoustic wave was input at the downstream end of both annuli. Fig 5.12 shows the waveforms of the acoustic pressure signal at data point 'A' in the upper dump cavity (top) and acoustic pressure and acoustic velocity signal (bottom) for data point 'B', in the middle of the pre-diffuser exit. At data point A, the magnitude of the right travelling pressure wave is now higher than the left travelling wave by ~ 25%, indicating more complex acoustic interactions than observed at 20 Hz, but again with little phase difference between them. Due to geometric effects, the left travelling wave which enters the pre-diffuser gets partly reflected (but not near pre-diffuser inlet where all waves leave the domain due to constant cross-sectional area) and the imposed zero reflection acoustic boundary condition produces a weak right travelling wave of amplitude ~ 20% of the left propagating wave. Fluctuations in the magnitude of the acoustic velocity due to the presence of the acoustic wave at pre-diffuser exit are ~ 5 m/s peak-peak relative to a bulk mean velocity of 28 m/s. The 8 frames in Fig 5.13, show the sequence of events taking place due to the 65 Hz input left travelling acoustic wave. It can be observed in these snap-shots that a small secondary vortex structure (see Frame 6) is formed downstream of the pre-diffuser exit as well as more significant changes occurring in the curved shear layer compared to the 20 Hz simulation. The sequence of events which take place during one complete cycle of excitation leading to the appearing of this secondary vortex is as follows. Since the acoustic excitation imposed corresponds closely to a shear-layer time scale, it is expected that there should be good synchronisation between acoustic velocity fluctuations and the shear layer in the dump cavity. This can be clearly identified in fig 5.13 where notable transverse movement of the shear layer is observed at around the mid cavity location. Frames 1 to 3 show such a motion where the core of the bulk corner vortex structure moves from the middle of the dump cavity towards the upper annulus as well as being squeezed towards the corner by an upward motion of the central part of the shear layer, resulting in increased negative axial velocity in the upper part of frames 1 to 3. Further upward movement of the corner vortex structure results in weakening of the ability of this flow region to supply fluid for entrainment of the jet as it exits the pre-diffuser, resulting in a small flow reversal near the upper corner of the pre-diffuser exit, see frame 4 and more prominently in frame 5. This flow reversal results in the formation of a secondary vortex as shown in frame 6. The secondary vortex convects

downstream and is injected into the dump cavity recirculation. Over the same time period, the primary corner vortex has moved upstream (frame 7). These two opposite travelling vorticies combine together (frame 7 and 8) and form a single vortex structure as seen in frame 1. These significant flow events lead to the shape of the shear layer changing considerably in terms of curvature resulting also in greater oscillations of the shear-layer reattachment point than seen at 20 Hz.

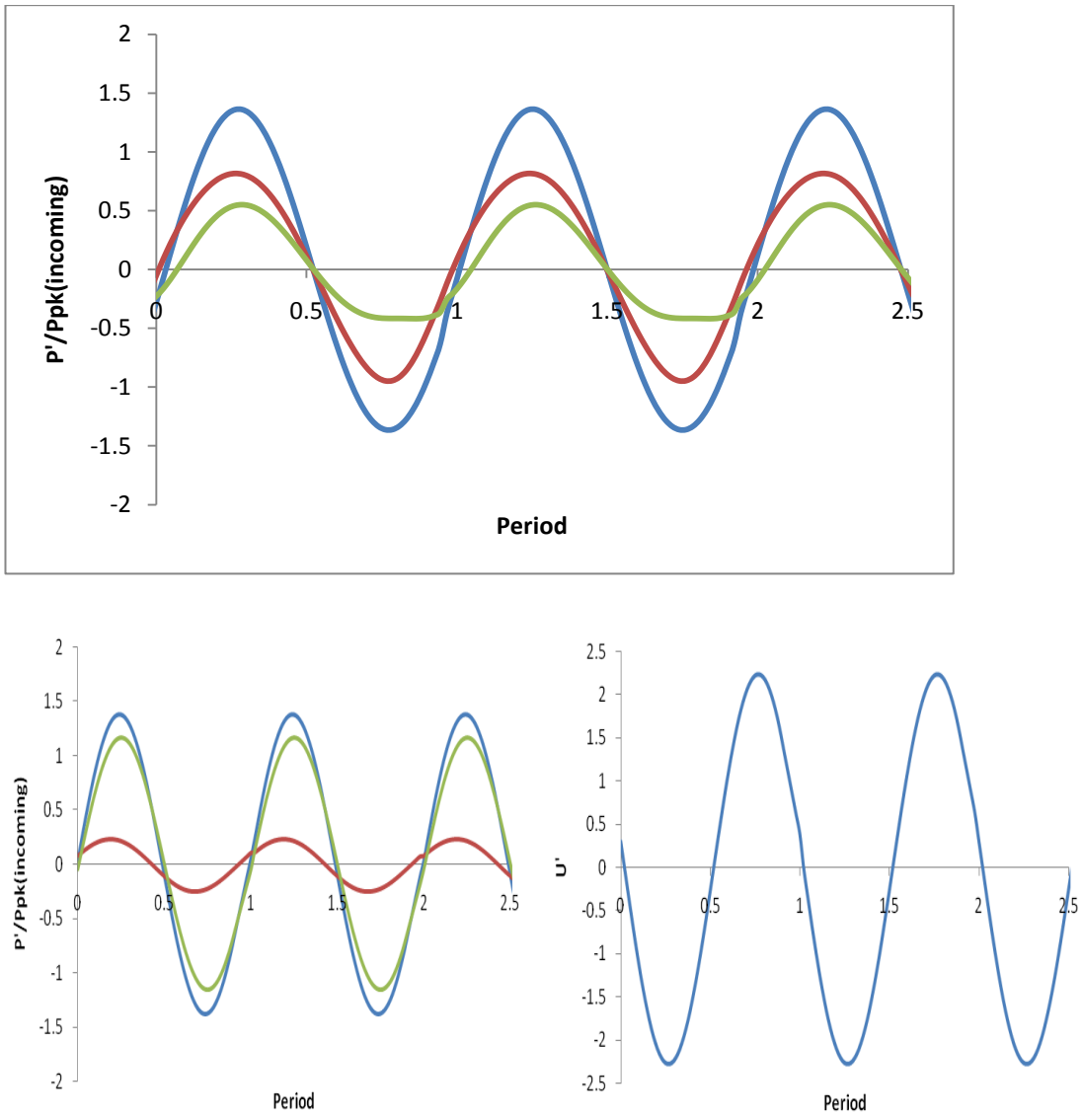

Figure 5. 12 - (top) Pressure signal in the top dump region (see Fig 5.1 for location) & (bottom) acoustic pressure and acoustic velocity at pre-diffuser exit for 65 Hz input frequency; blue- overall pressure wave; red- right propagating pressure wave; green – left propagating pressure wave.

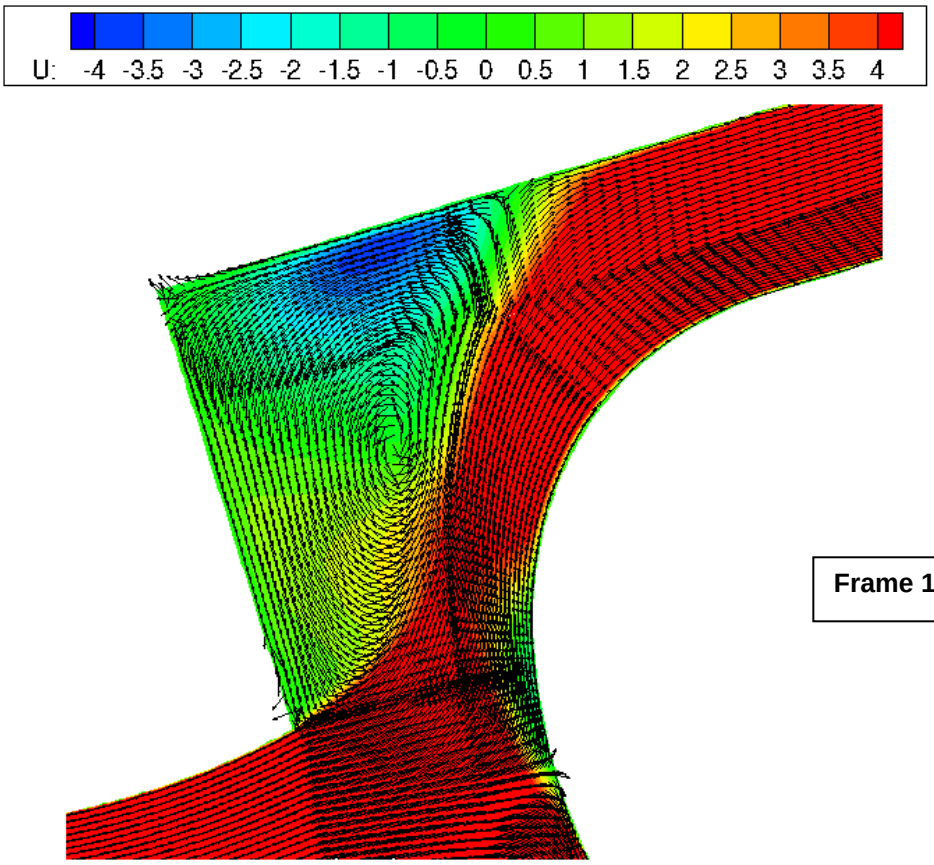

Frame 1

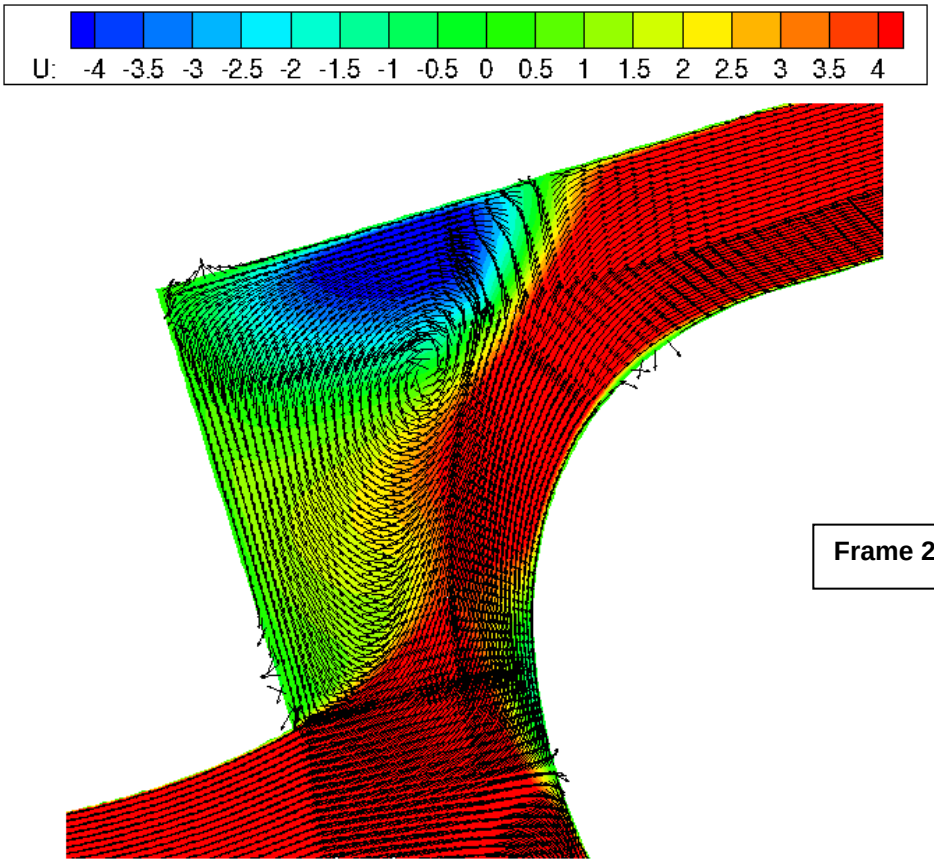

Frame 2

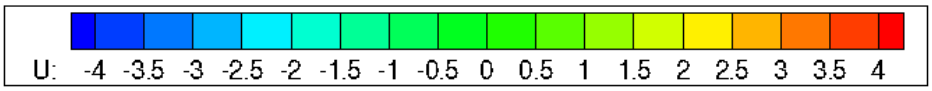

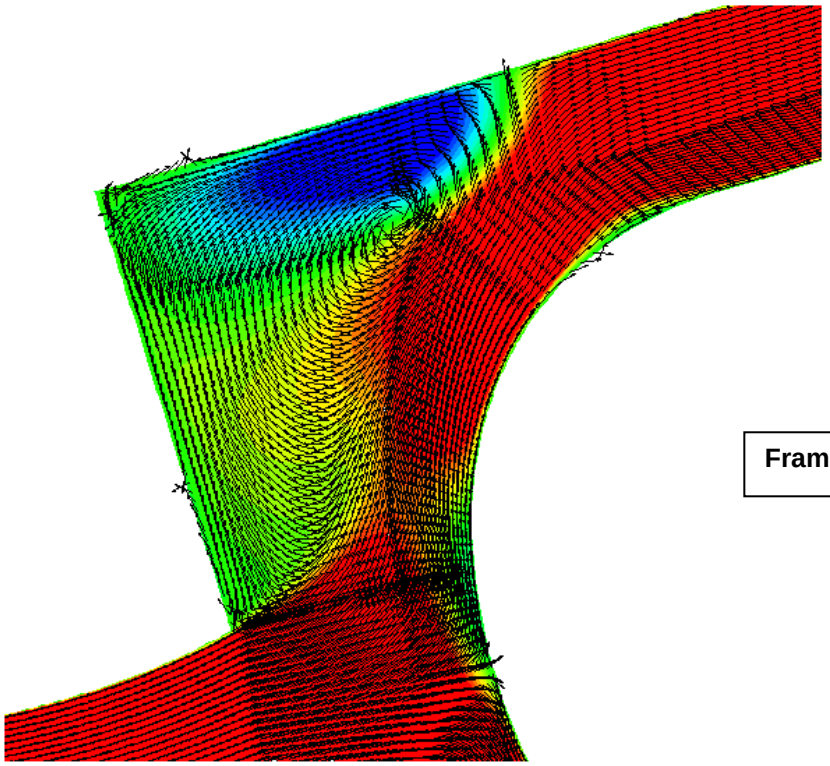

Frame 3

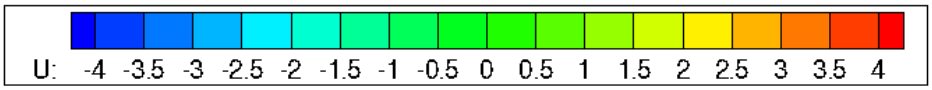

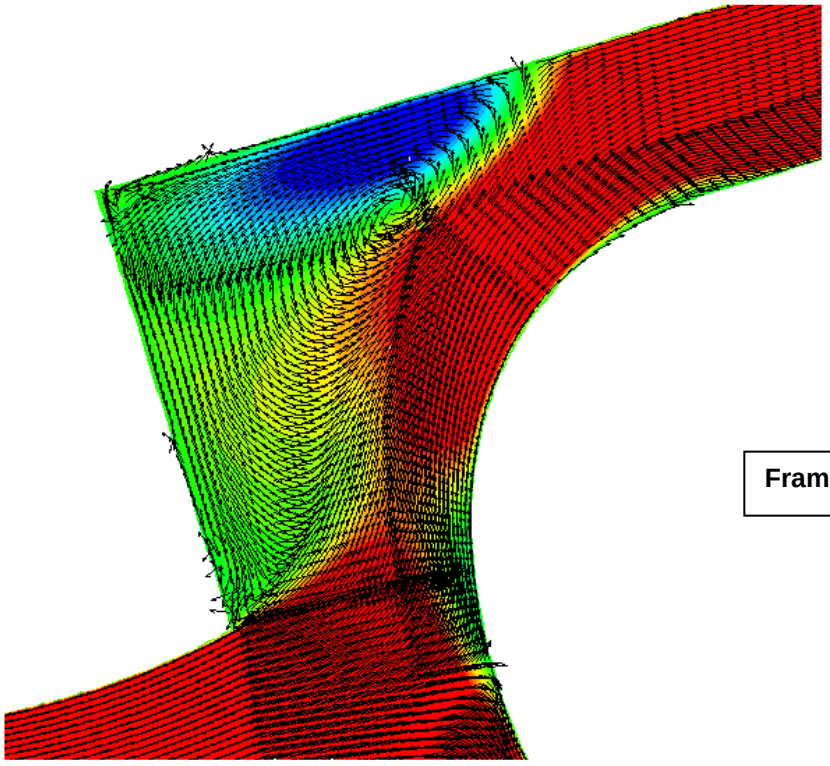

Frame 4

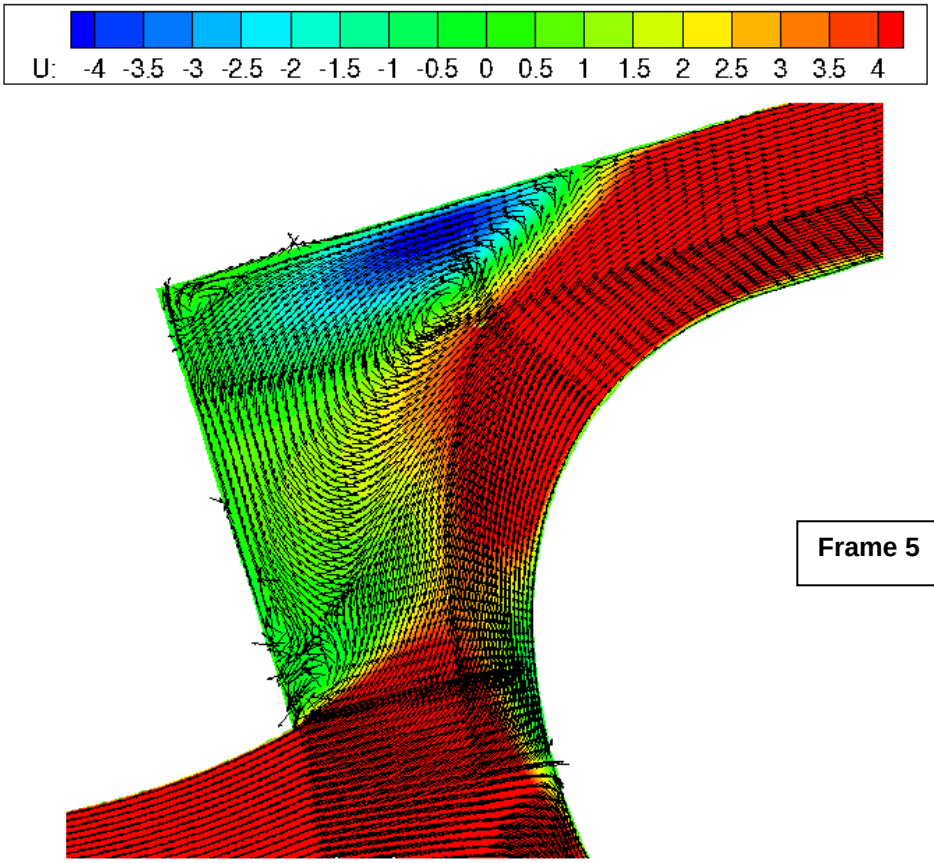

Frame 5

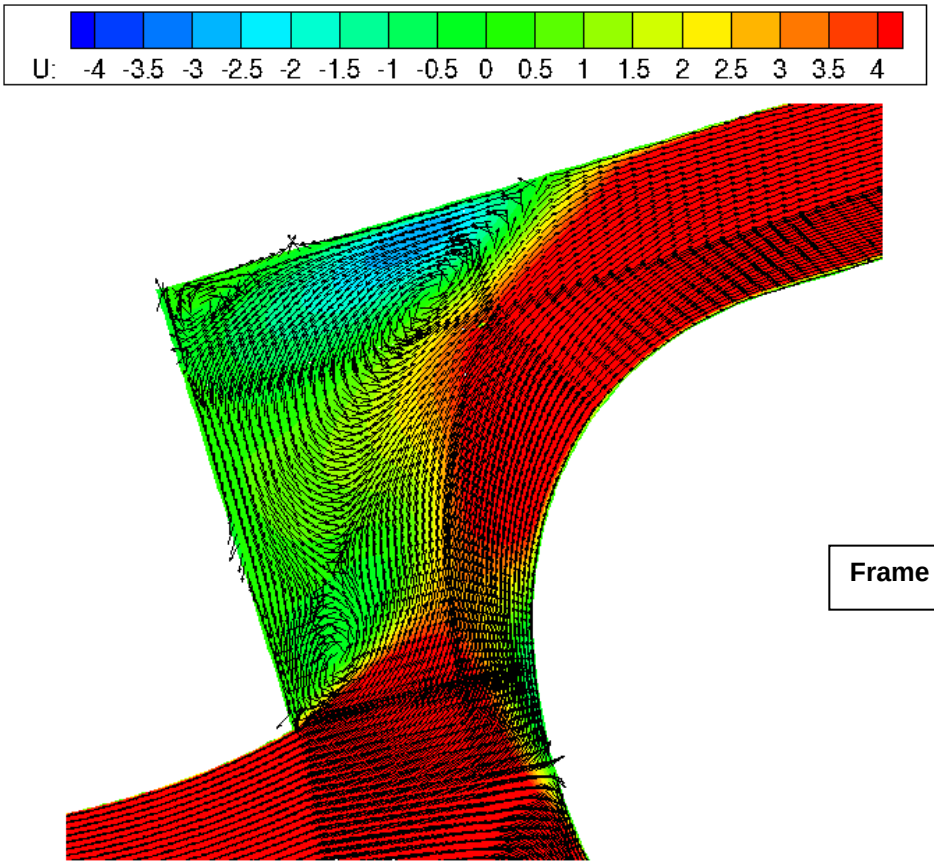

Frame 6

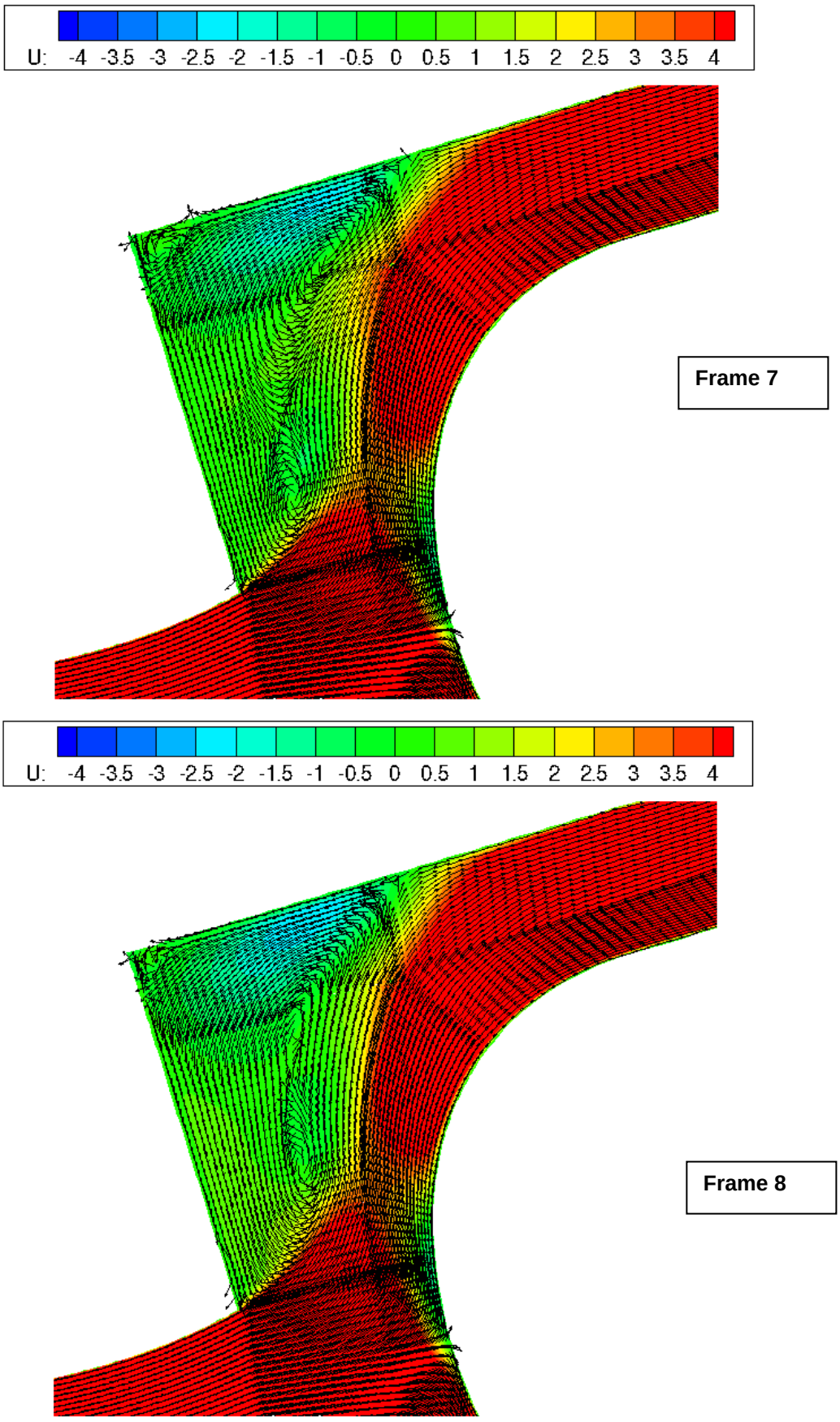

Figure 5. 13 - Sequence of snapshots of axial velocity contour and vectors for 65 Hz wave.

5.5.3 Results for 100 Hz Acoustic Excitation (First Set)

It was noticeable that the stronger response to acoustic excitation at 65 Hz was associated with the appearance of a secondary (starting-type) vortex at pre-diffuser exit, and the interaction between this and the core primary dump region vortex. To investigate whether this interaction would be influenced by the frequency of appearance of the pre-diffuser secondary vortex, an excitation simulation at 100 Hz was carried out. This frequency was selected by estimating (again from the steady state URANS flowfield) the time taken for a fluid particle to convect from pre-diffuser exit to the location of the core primary dump region vortex 'eye'. The predicted waveform of the pressure signal corresponding to the 100 Hz acoustic excitation at data point 'A' in the dump region and also at data point 'B' at pre-diffuser exit (including acoustic velocity) are plotted in Fig 5.14. A slight increase in the acoustic velocity compared to the 65 Hz test condition can be seen, as well as a notable increase in phase shift of the left/right propagating pressure oscillations at data point 'A'. This indicates a stronger acoustic response to excitation. The sequence of changes in dump cavity flow structures are given in the axial velocity contour/velocity vector snapshots in fig 5.15. The various dynamical features identified at 65 Hz excitation: formation of secondary vorticity at pre-diffuser exit, and merging of secondary and primary vortex are also observed at 100 Hz excitation, but with more vigour. This change was also reflected in the oscillation of the shear-layer reattachment point on the upper of the annulus wall, which now moved by $\pm$ 10 % about its mean value. The secondary vortex still appears in frame 7, but the transverse movement of the shear layer is now sufficiently strong that the eye of the primary vortex moves right up to the upper annulus outer wall (frame 7) and the merging of the two vortices takes up a greater fraction of the cycle time.

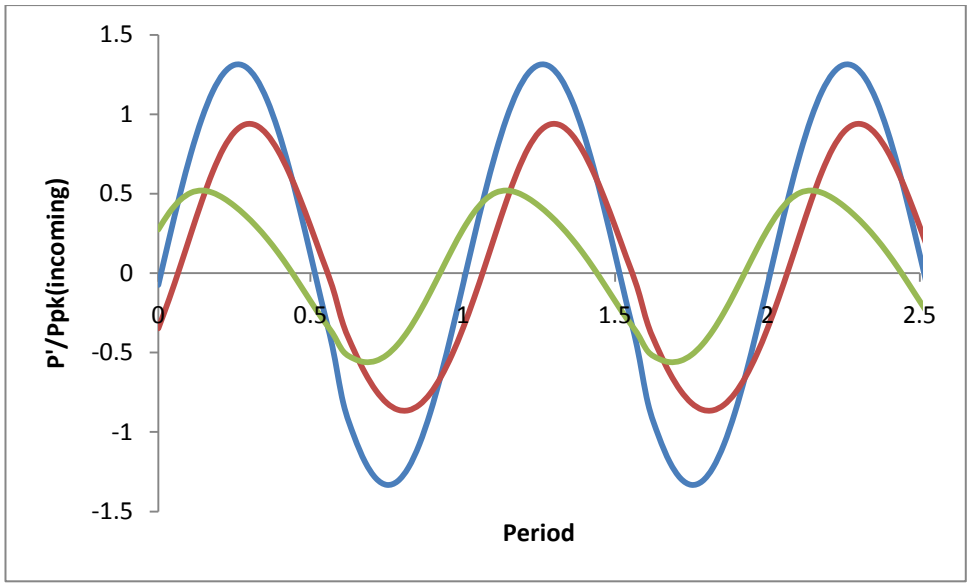

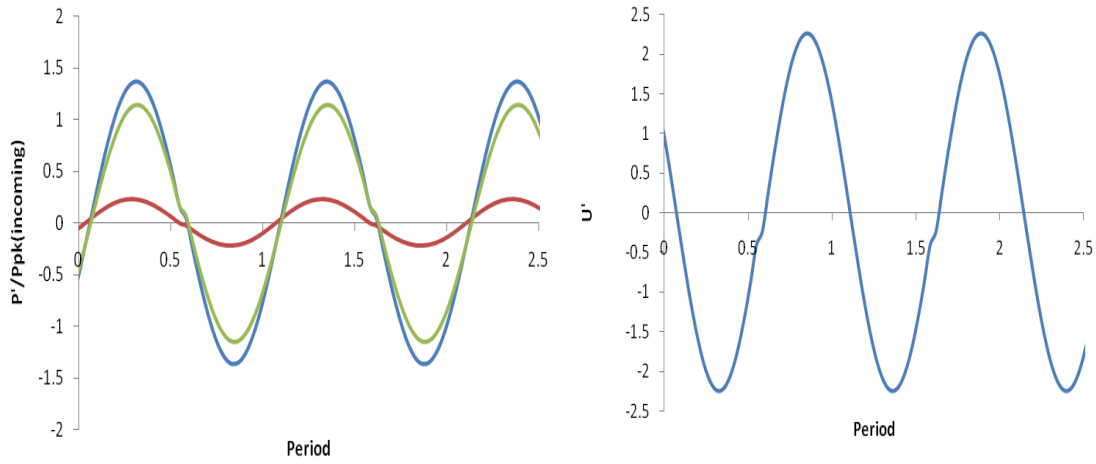

Figure 5. 14 - (top) Pressure signal in the top dump region (see Fig 5.1 for location) & (bottom) acoustic pressure and acoustic velocity at pre-diffuser exit for 100 Hz input frequency; blue- overall pressure wave; red- right propagating pressure wave; green – left propagating pressure wave.

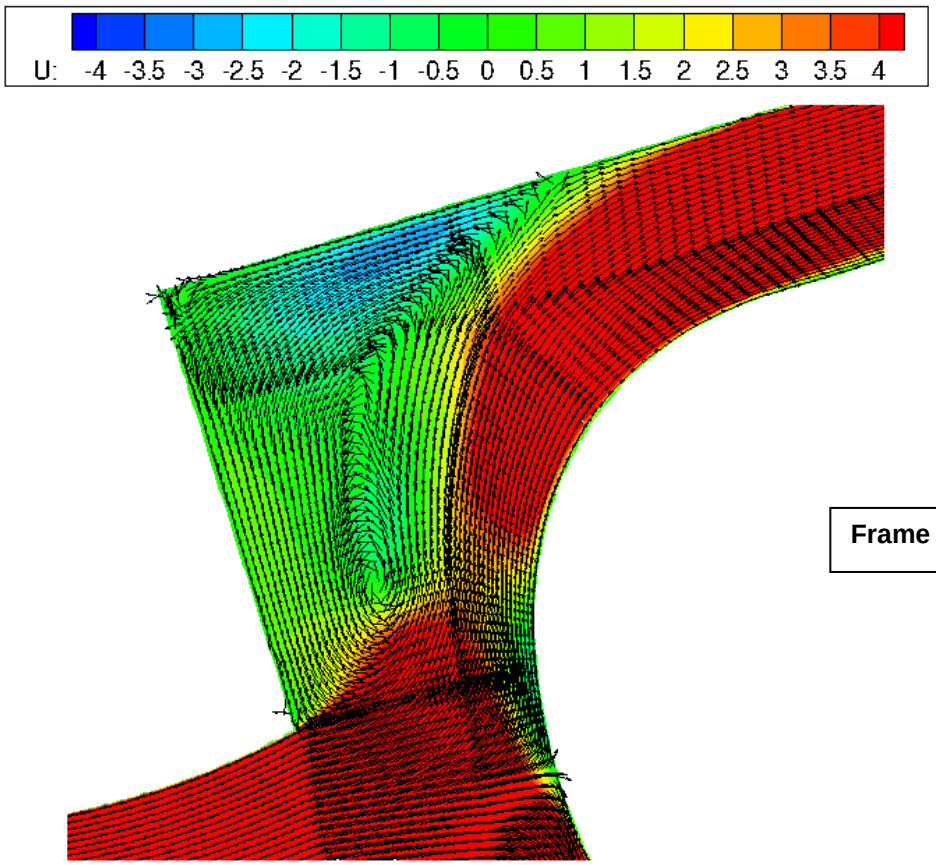

Frame 1

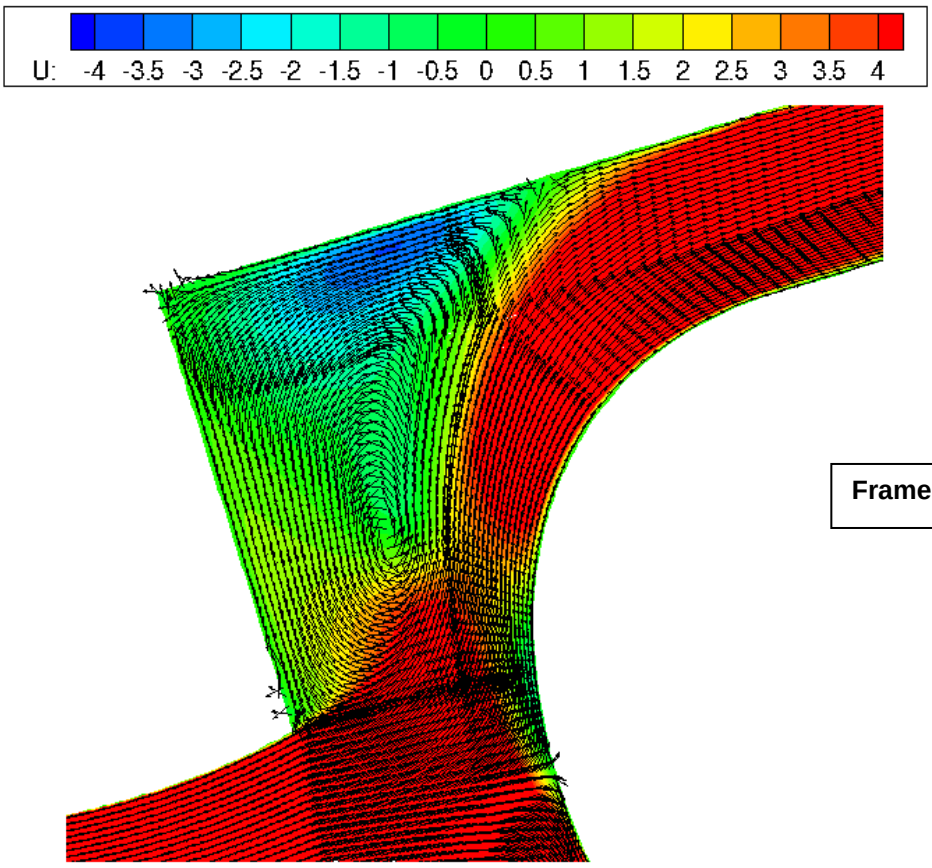

Frame 2

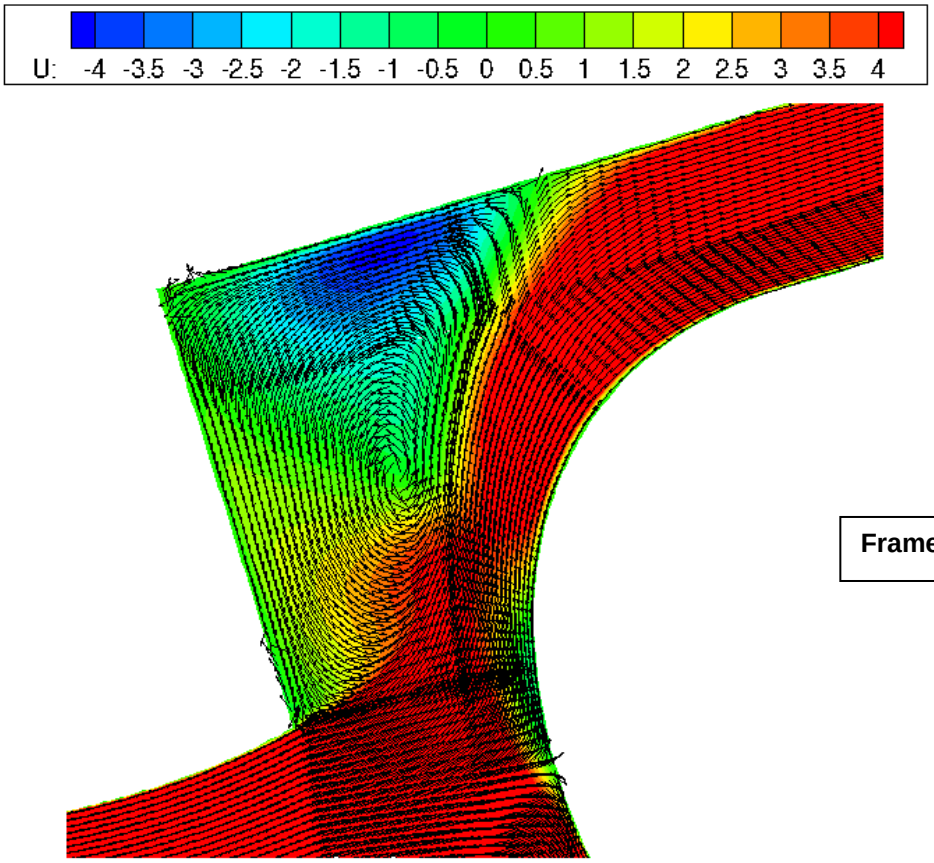

Frame 3

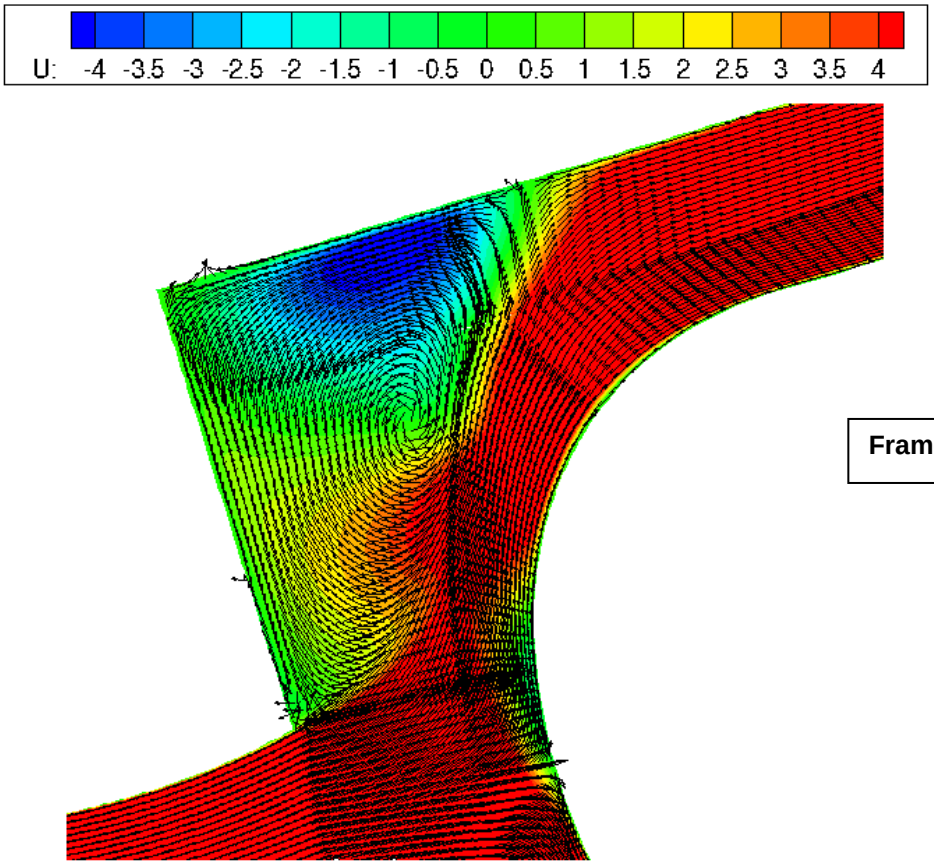

Frame 4

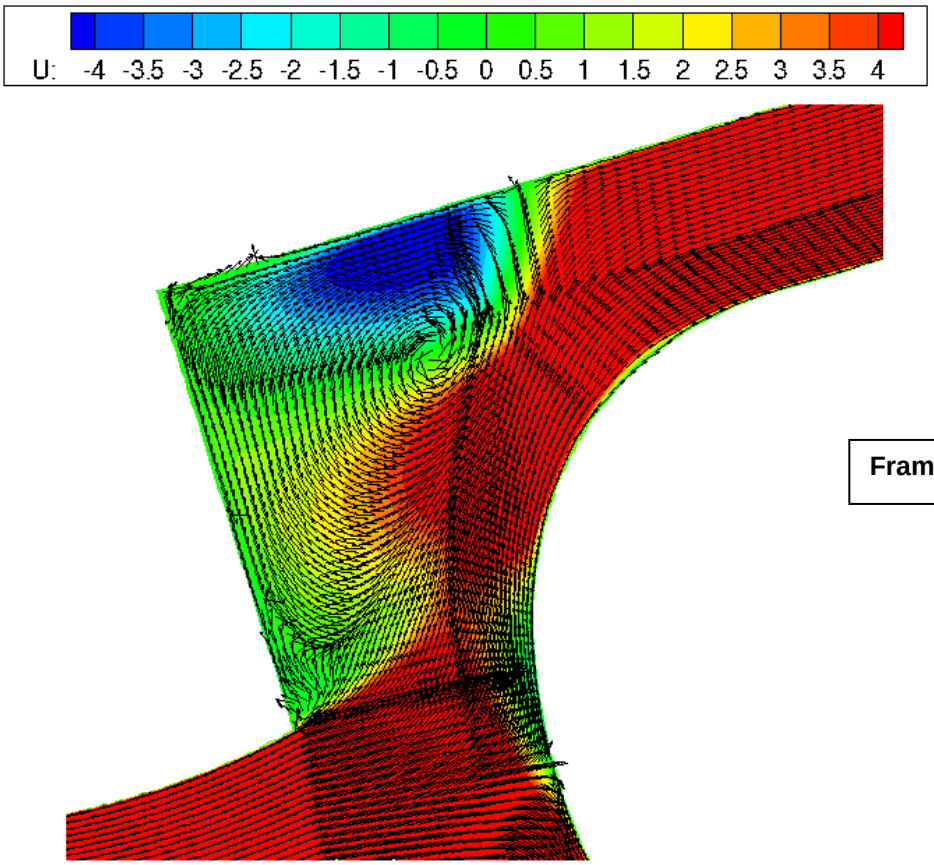

Frame 5

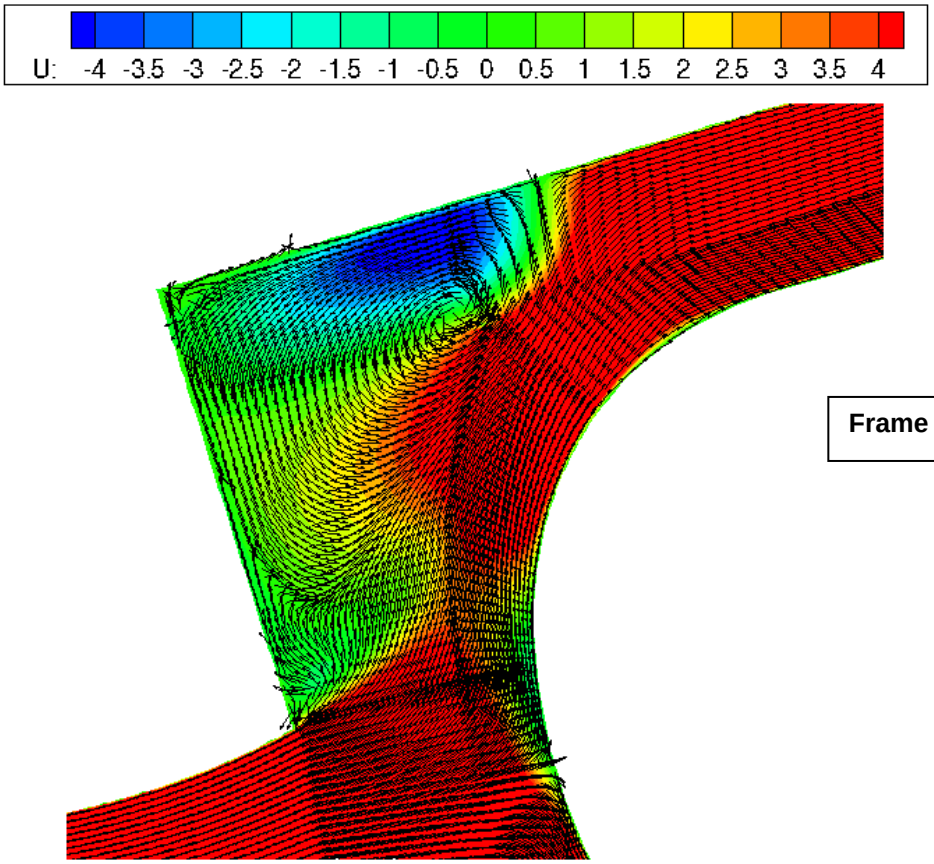

Frame 6

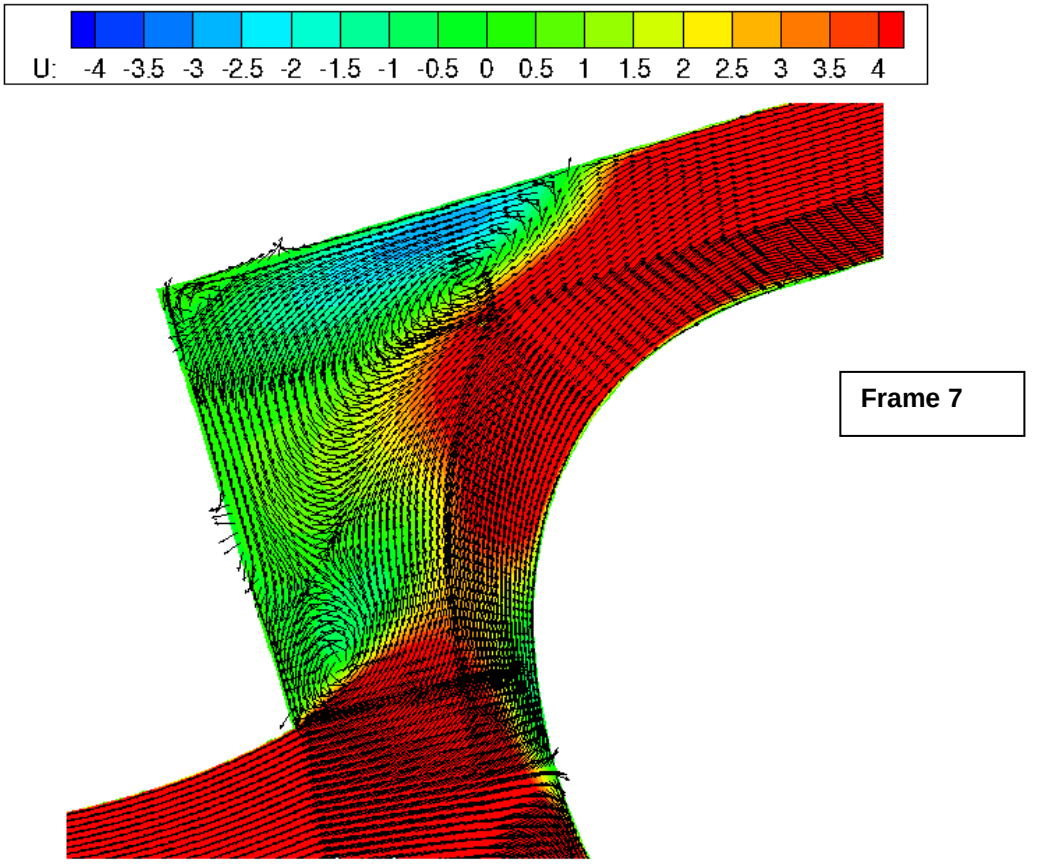

Figure 5. 15 - Sequence of snapshots of axial velocity contour and vectors for 100 Hz wave.

5.5.4 Results for 300 Hz Acoustic Excitation (First Set)

In order to study the influence of a higher acoustic excitation, a 300Hz acoustic wave was input at annuli exit. Similar to previous calculations, fig 5.16 shows the waveform of the pressure signal at data point 'A' and at data point 'B' (including acoustic velocity), as well as the usual snap-shots frames are shown in Fig 5.17. At this higher frequency acoustic excitation, most of the dynamic flow features resemble those observed at 65 and 100 Hz conditions but are now much weaker. The reduced acoustic velocity fluctuation (~3.5 m/s peak-peak variation) at pre-diffuser exit leads to reduced strength of the secondary vortex (just visible in frame 2). Due to its reduced strength, this secondary vortex dissipates before interacting with the primary vortex. Based on these tests it was concluded that the optimum excitation frequency for producing maximum response in the present dump-diffuser configuration is 100 Hz .

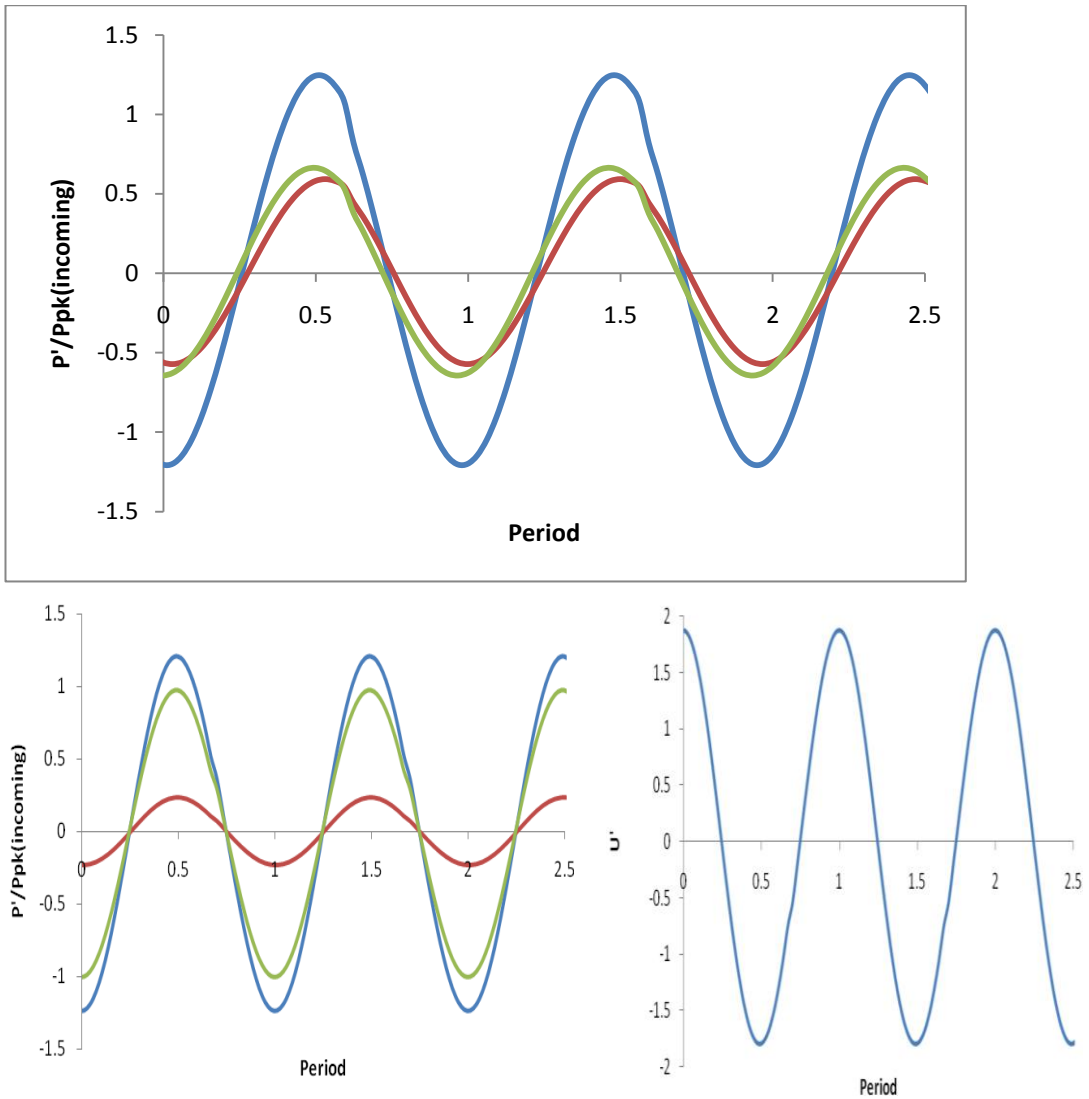

Figure 5. 16 - (top) Pressure signal in the top dump region (see Fig 5.1 for location) & (bottom) acoustic pressure and acoustic velocity at pre-diffuser exit for 300 Hz input frequency; blue- overall pressure wave; red- right propagating pressure wave; green – left propagating pressure wave.

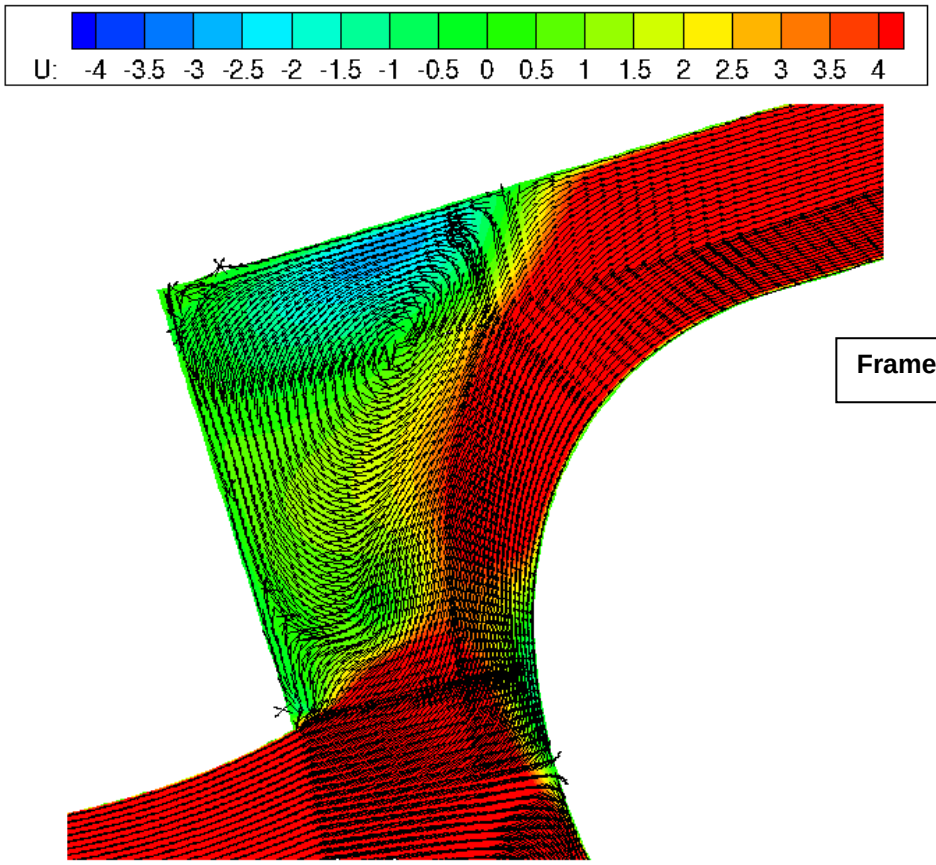
U: -4 -3.5 -3 -2.5 -2 -1.5 -1 -0.5 0 0.5 1 1.5 2 2.5 3 3.5 4
Frame 1

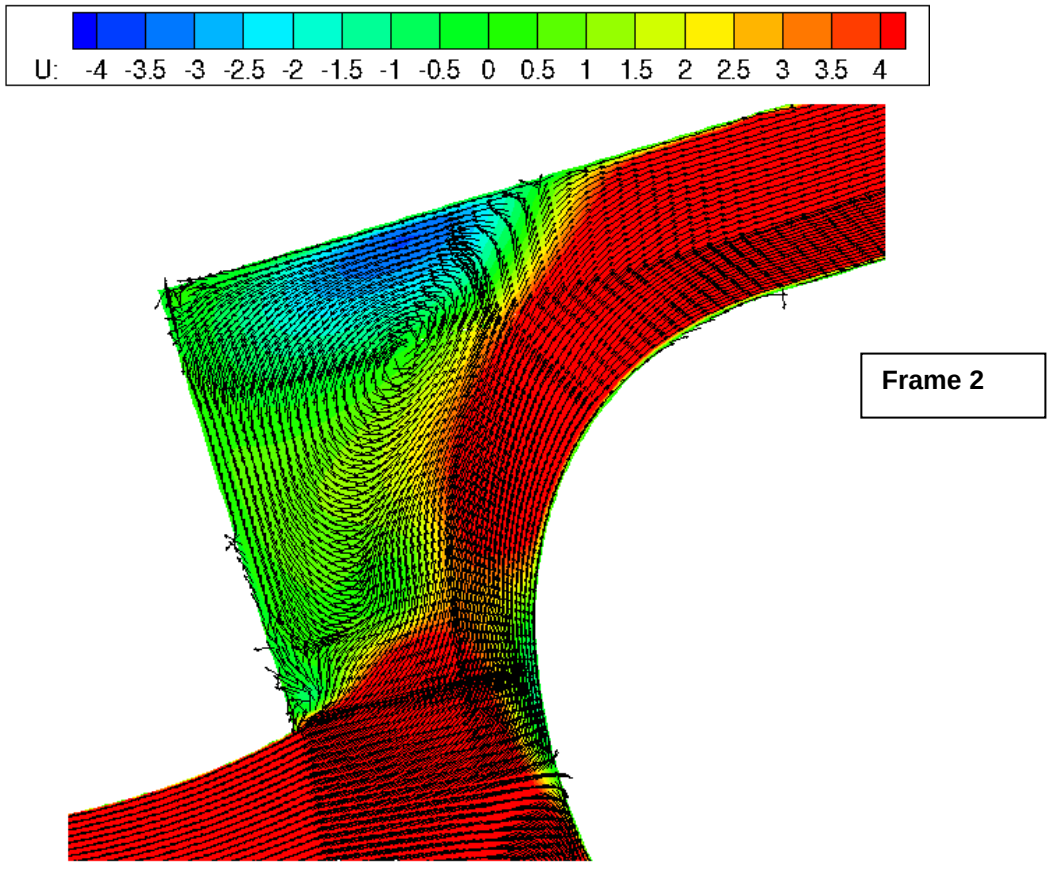
U: -4 -3.5 -3 -2.5 -2 -1.5 -1 -0.5 0 0.5 1 1.5 2 2.5 3 3.5 4
Frame 2

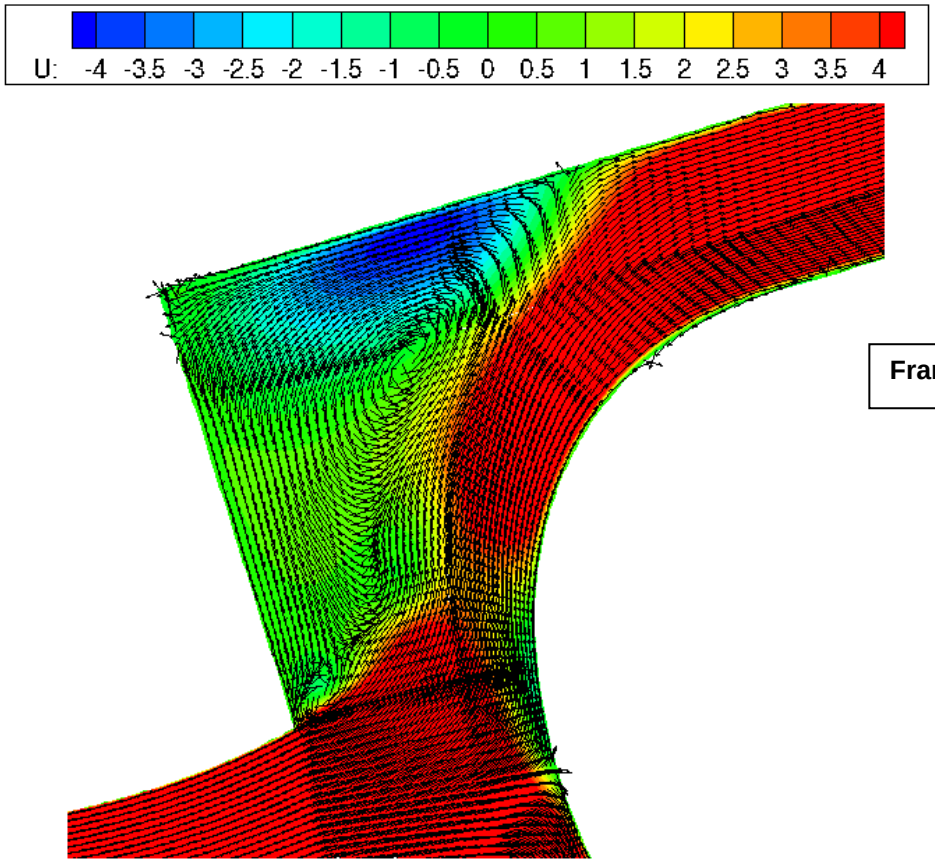
U: -4 -3.5 -3 -2.5 -2 -1.5 -1 -0.5 0 0.5 1 1.5 2 2.5 3 3.5 4
Frame 3

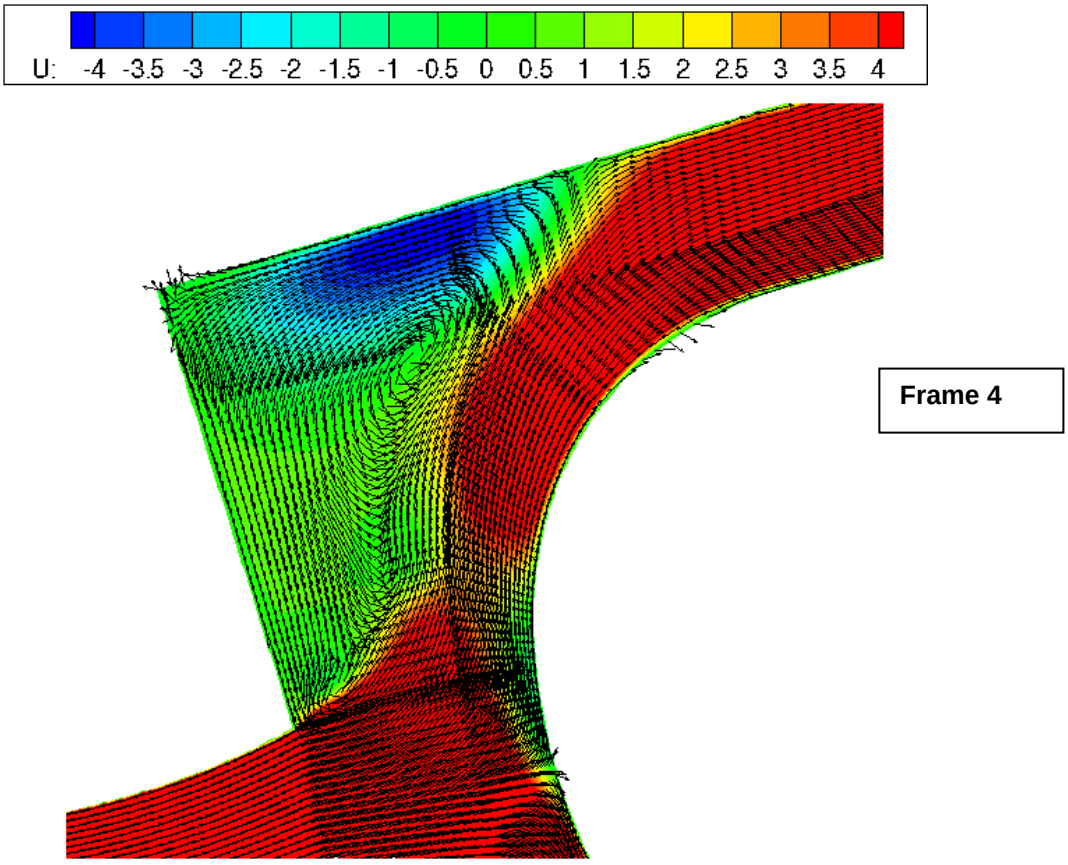
U: -4 -3.5 -3 -2.5 -2 -1.5 -1 -0.5 0 0.5 1 1.5 2 2.5 3 3.5 4
Frame 4

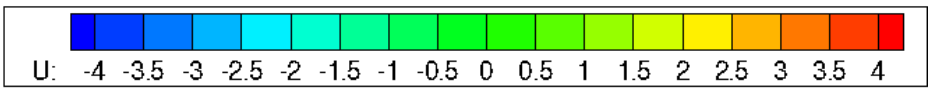

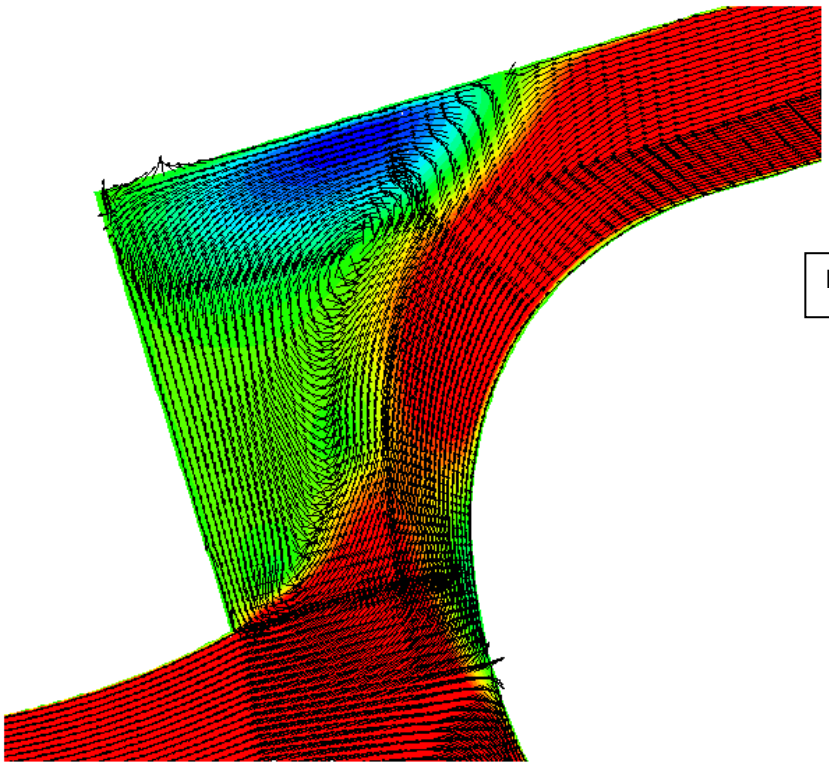

Frame 5

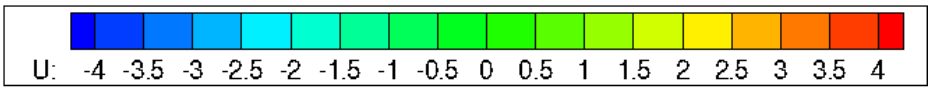

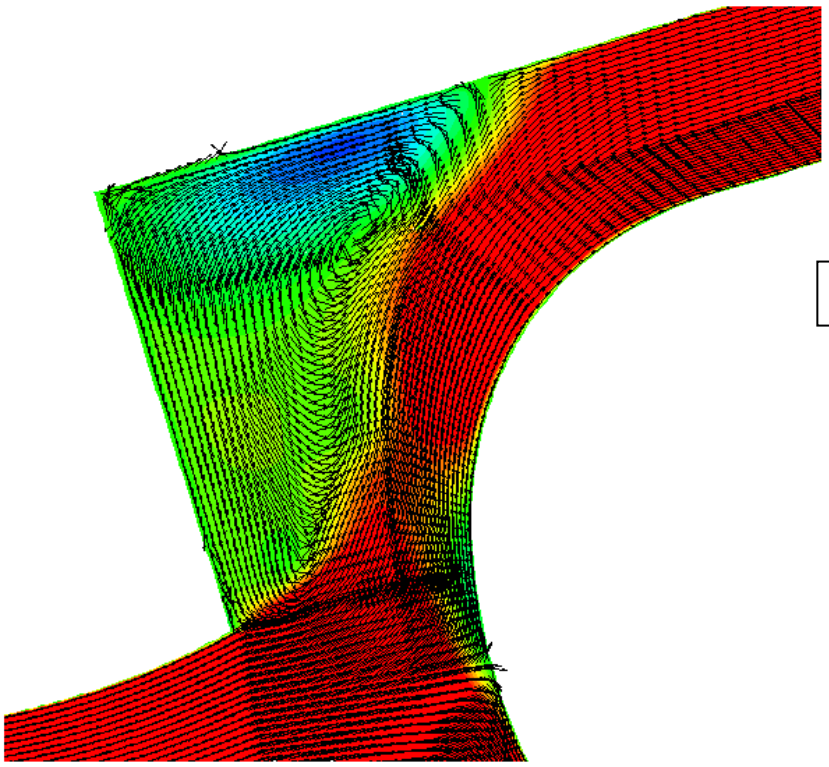

Frame 6

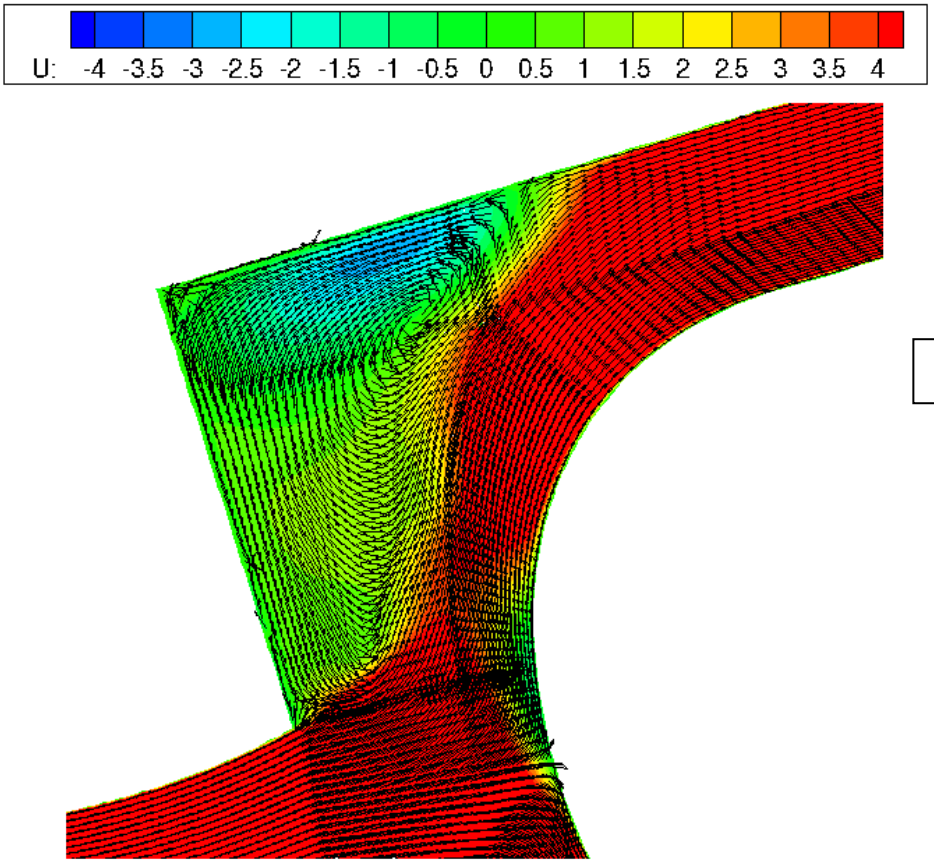

Figure 5. 17 - Sequence of snapshots of axial velocity contour and vectors for 300 Hz wave.

5.5.5 Results for 100 Hz Excitation with Acoustically Closed Inlet Boundary Condition

In all acoustic excitation simulations presented above, the acoustic boundary condition at pre-diffuser inlet was taken as corresponding to an infinite upstream supply duct which allows pressure waves to leave the solution domain without any reflection. It was found in the above studies that 100 Hz excitation produced the strongest interaction between input acoustic wave and dump cavity shear layer, a secondary vortex was created and shed from the pre-diffuser exit. In order to study the influence of changing the inlet acoustic boundary condition, a simulation was performed by setting an acoustically closed boundary condition at pre-diffuser inlet (acoustic velocity being zero and acoustic pressure determined via production of a perfectly reflecting in-phase right propagating wave). All other boundary and operating conditions were maintained as in the previously simulated 100 Hz prediction. Figure 5.18 shows the pressure signal at data point 'A' and pressure and acoustic velocity signals at data point 'B'. The influence of the closed boundary condition can be seen from the pressure signals which, as expected, show both left and right propagating wave are of equal amplitude and are in phase with each other as required to produce a pressure anti-node (acoustic velocity node) at the upstream boundary. Note also that the strength of acoustic velocity fluctuation at pre-diffuser exit has been reduced to about 1/3rd of its previous level. The sequence of flow structure plots (Fig 5.19), not surprising that now show much reduced flow oscillations in the dump cavity shear layer with a almost steady state flowfield observed. No formation of any secondary vorticity is observed and the shear layer attachment point does oscillate about it mean position but at a significantly reduced level $\sim \pm$ 1%.

An attempt was made to predict flowfield at similar excitation condition, but for an acoustically open condition at pre-diffuser inlet. This should produce a 180° phase shifted right propagating pressure wave at the pre-diffuser inlet resulting in a pressure node there as well as an acoustic velocity anti-node (i.e. maximum acoustic velocity). Unfortunately this resulted in severe oscillations in the entire dump diffuser configuration and numerical divergence resulted. Clearly this is a much more acoustically susceptible condition, but time prevented detailed examination and resolution of the problem.

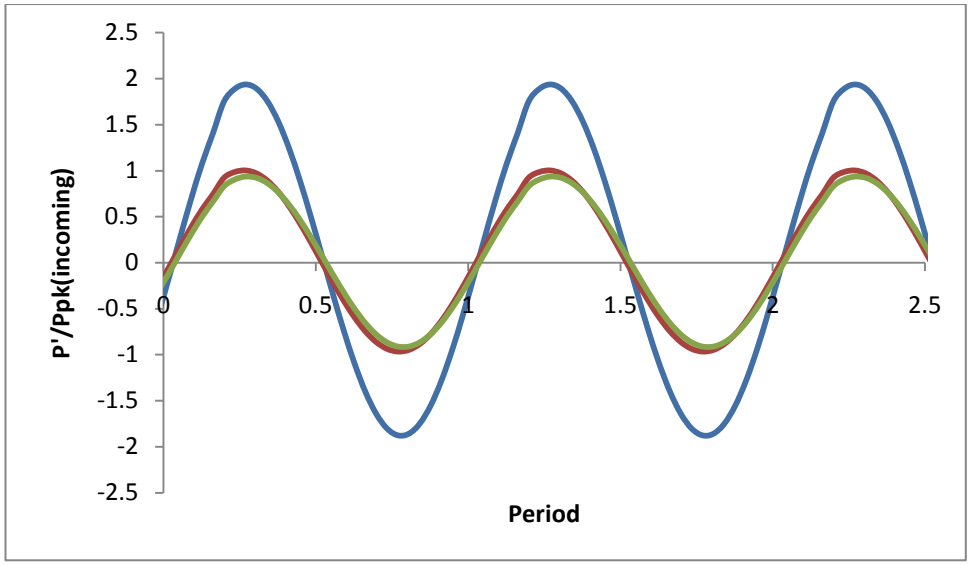

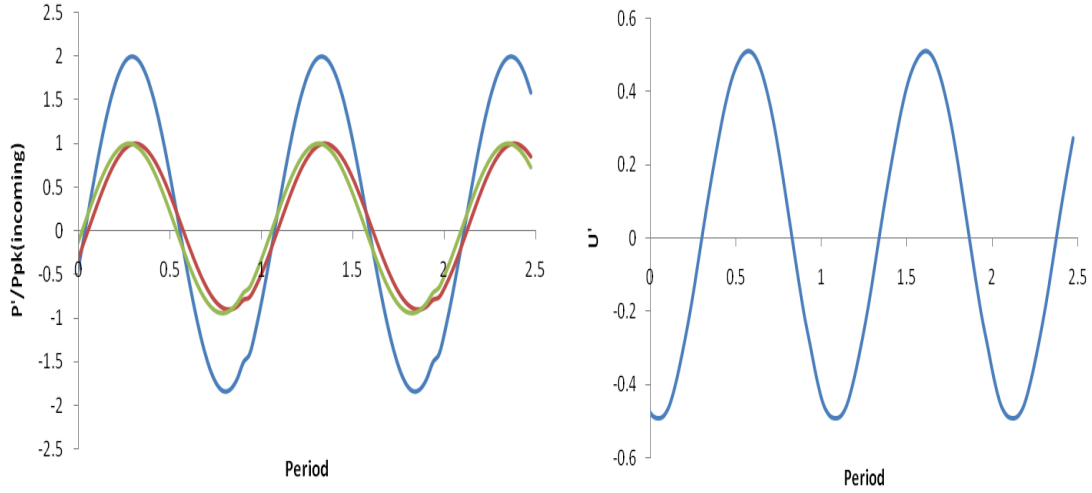

Figure 5. 18- (top) Acoustic pressure signal in the top dump region (see Fig 5.1 for location) & (bottom) acoustic pressure, acoustic velocity at pre-diffuser exit for 100 Hz input frequency; blue- overall pressure wave; red- right propagating pressure wave; green – left propagating pressure wave.

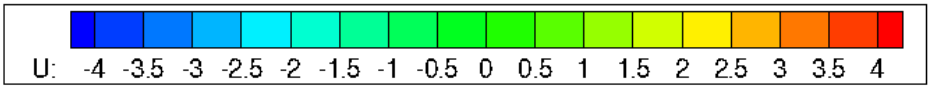

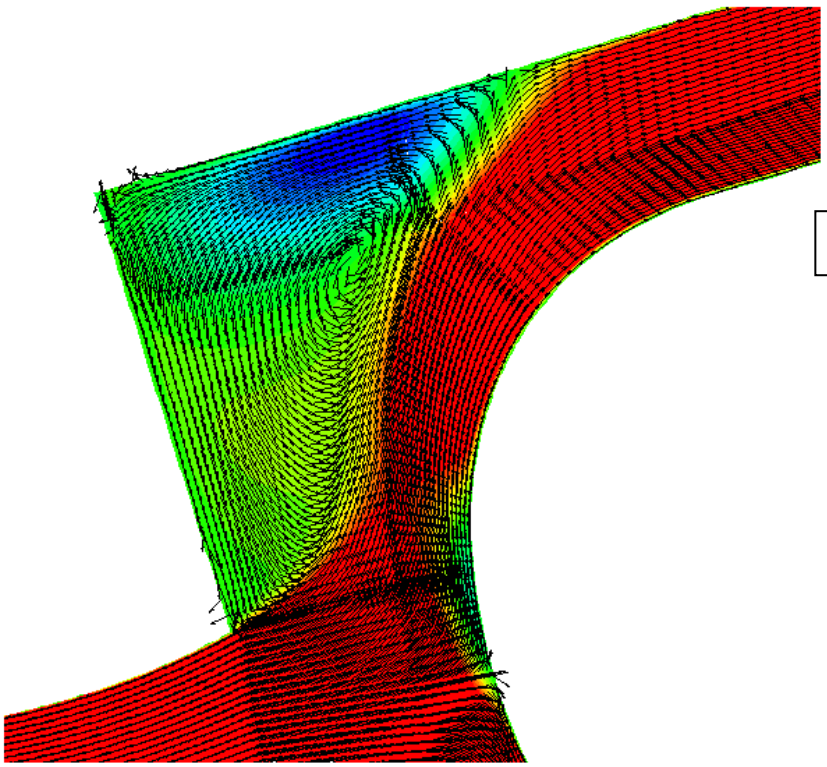

Frame 1

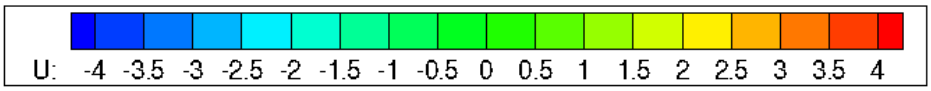

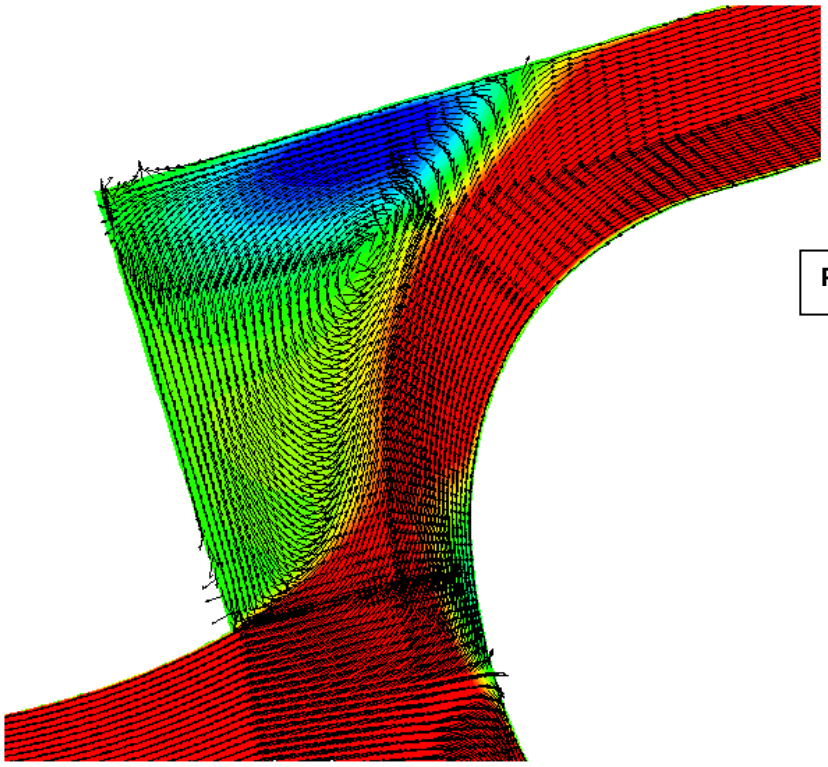

Frame 2

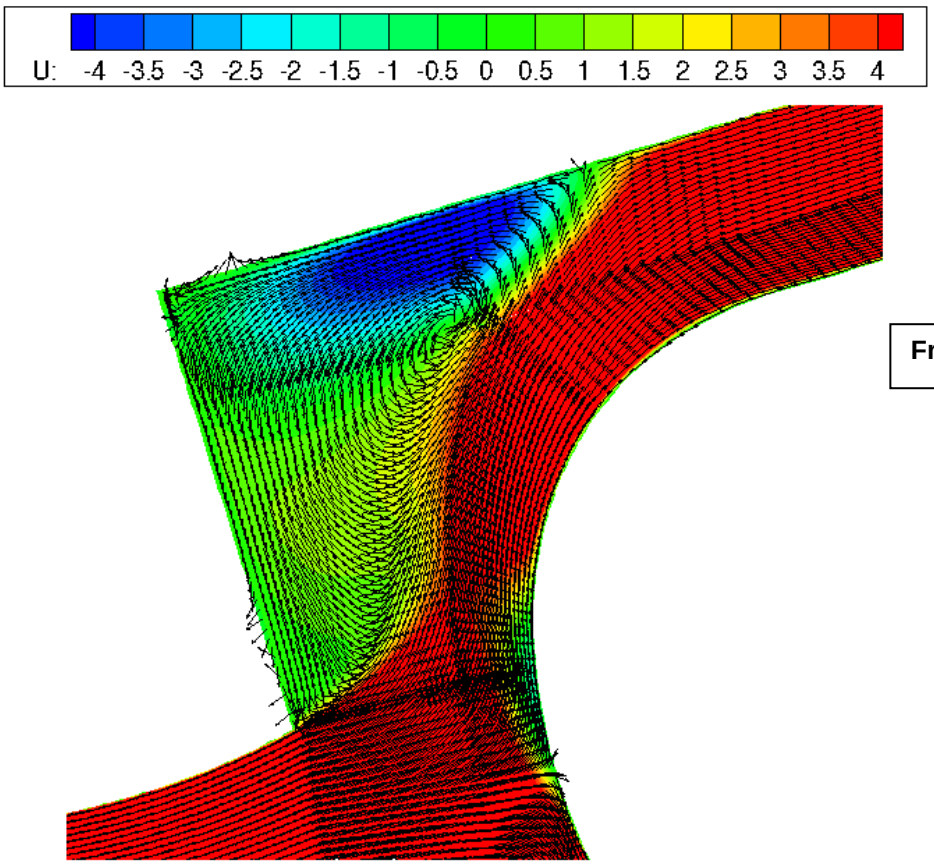

Frame 3

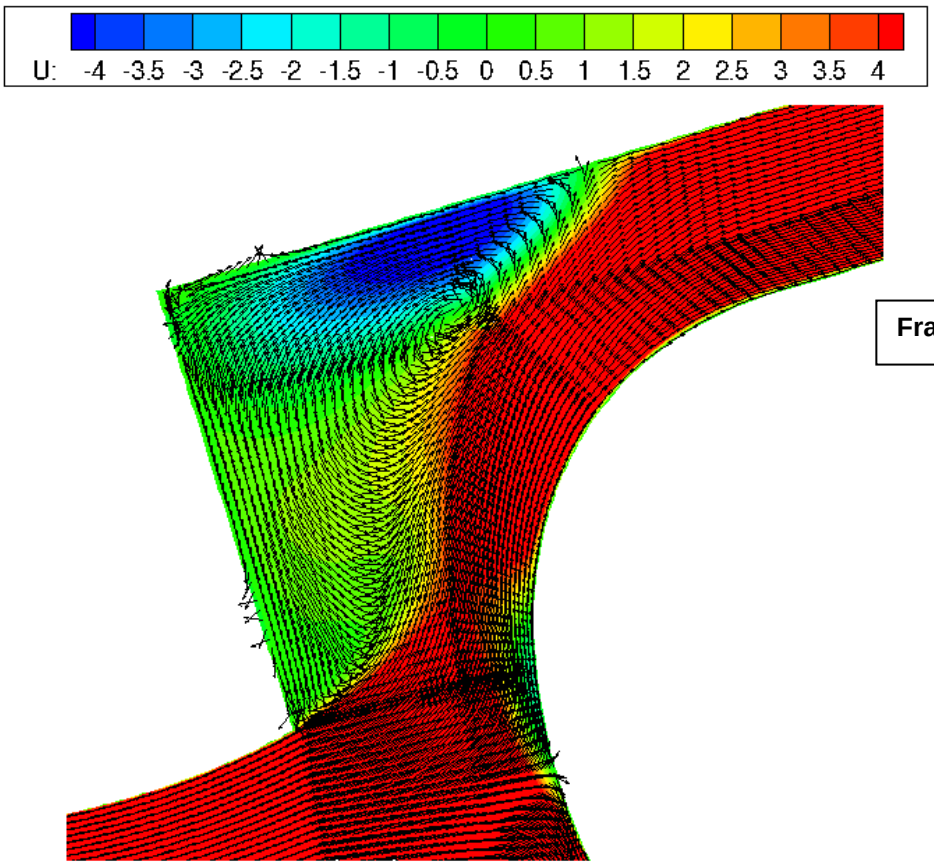

Frame 4

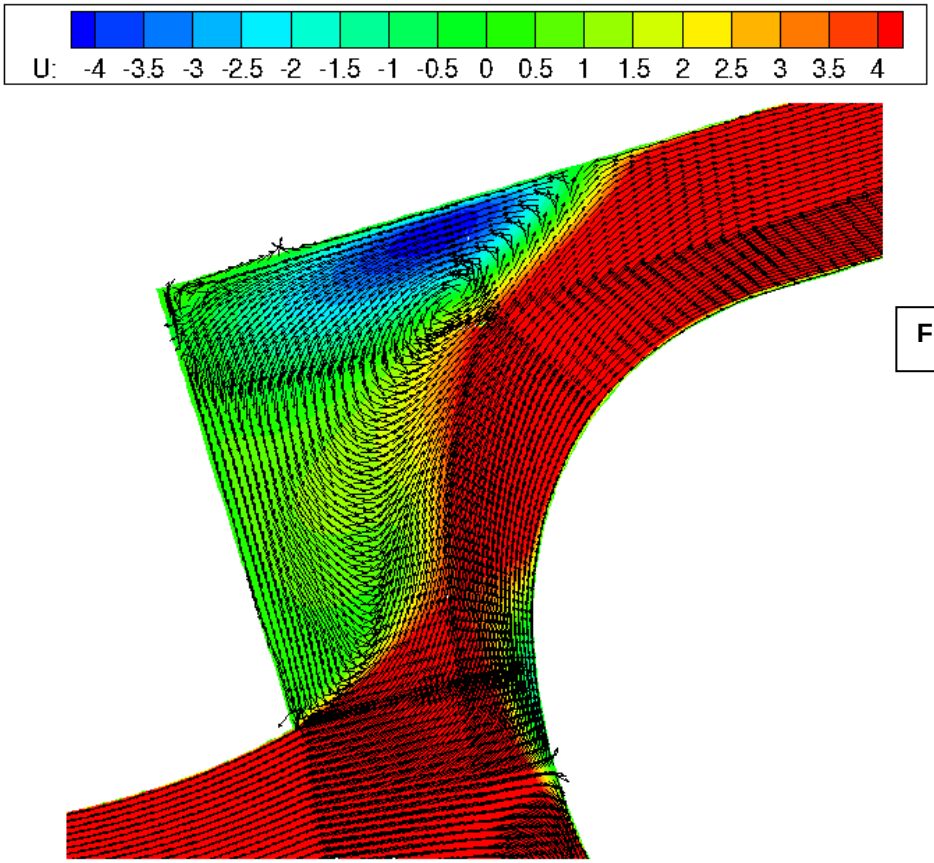

Frame 5

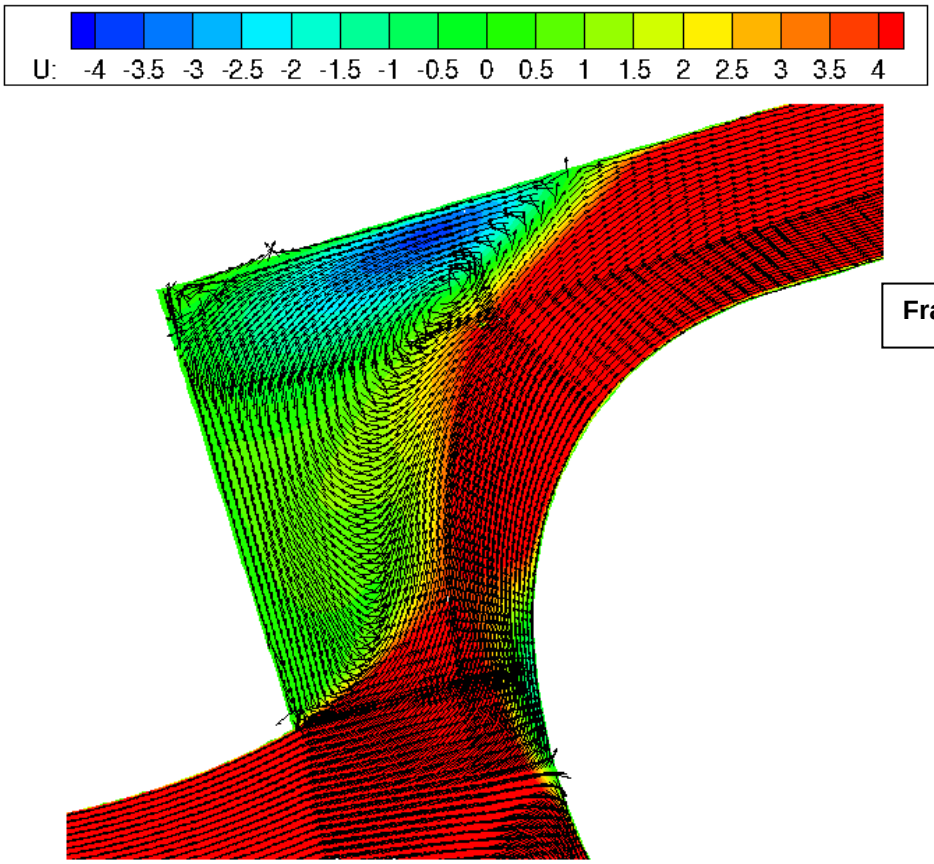

Frame 6

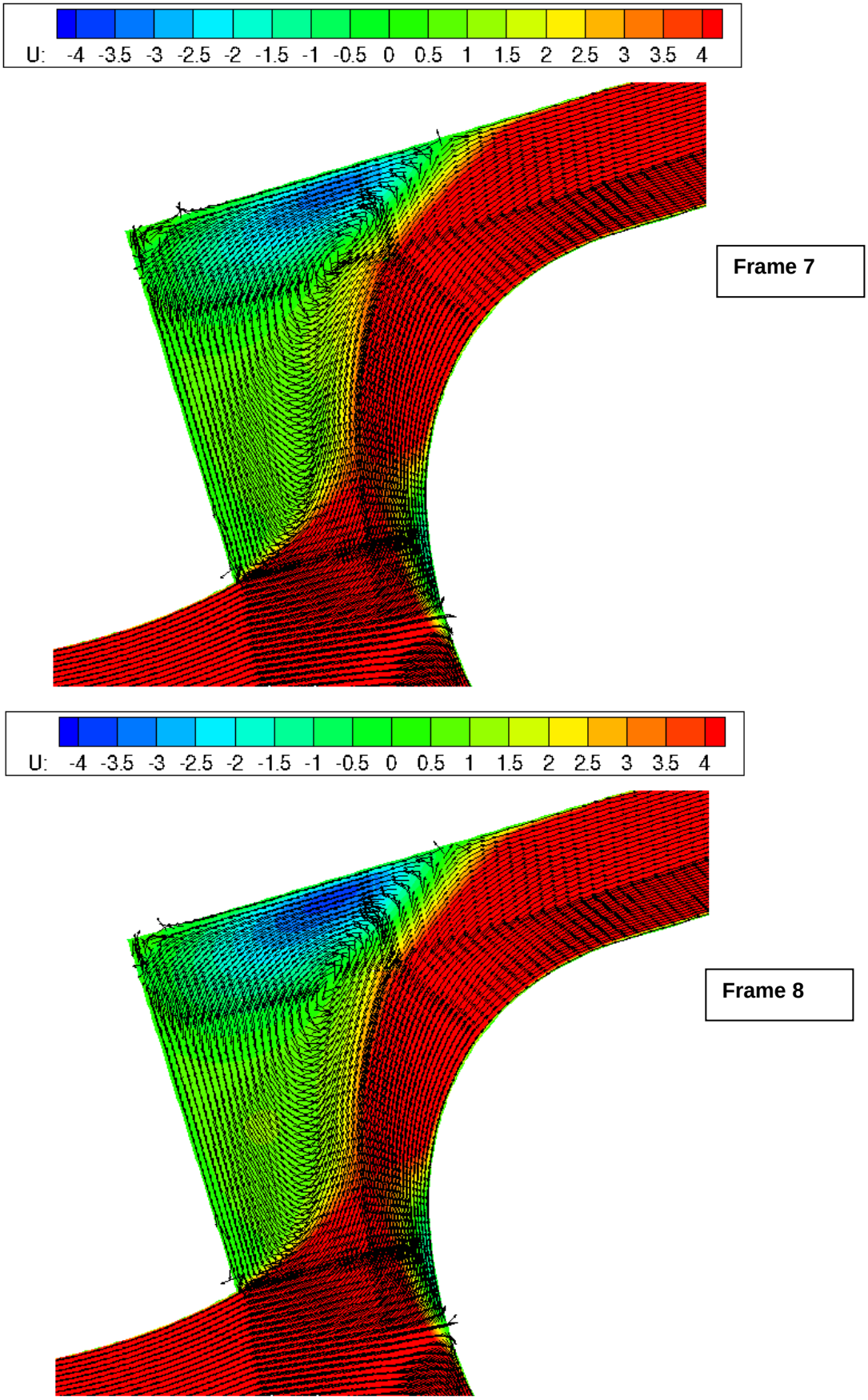

Figure 5. 19 - Sequence of snapshots of axial velocity contour and vectors for 100 Hz wave.

5.6 SUMMARY AND CONCLUSIONS

This chapter has provided a clear illustration of the ability of the pressure-based CFD method developed in this thesis to provide useful predictions of acoustic problems relevant to gas-turbine combustor systems. The case chosen for demonstrating this was pre-diffuser/dump diffuser external aerodynamics and the flowfield response to acoustic excitation. Based on the sequence of test cases detailed above, it is clearly shown that the flow feature which is most responsive to downstream acoustic excitation is not the dump cavity recirculation zone, but the curved shear layer. When combined with favourable acoustic boundary conditions input external disturbances synchronise with unsteady shear-layer dynamics and produce significant unsteady changes in flow structure. A resonant frequency of ~ 100 Hz was determined for an inlet boundary condition corresponding to zero reflections. An acoustically closed condition produced much weaker response, but the acoustically open condition response was so vigorous that it resulted in numerical divergence, the precise cause and solution of this is yet to be determined.

6. Conclusions and Future Work

In this chapter the conclusions drawn from the research reported in this thesis are summarised and suggestions for future work put forward.

6.1 SUMMARY AND CONCLUSIONS

The first part of this thesis has presented the development of a mildly compressible CFD code which has the capability of predicting both fluid flow and acoustic phenomena directly for combined gas turbine aero-acoustic combustor modelling. The mildly compressible algorithm was based on the classical pressure-correction approach. The modified CFD algorithm consisted of three key features which enabled an in-house pressure-based CFD code to be modified to enable accurate prediction of various acoustic phenomena such as acoustic propagation and damping in complex turbulent flows. These features are: (i) high discretisation accuracy to minimise wave attenuation and phase shift due to numerical dissipation and dispersion errors - this was achieved by employing a 5^{th} order accurate Weighted Essential Non-Oscillatory (WENO) scheme (Jiang et al. 1996). After a series of standard test cases it was concluded that use of the 5^{th} order WENO scheme resulted in reduction in the minimum requirement for number of grid points per wavelength from 40 – 60 (Huang et al. 1998 and Foller et al. 2010) to 20 - 30 points per wavelength, (ii) pressure-velocity-density coupling, essential for solving mildly compressible phenomena like acoustic wave propagation in low Mach number mean flow - this was established using a modified pressure-correction algorithm, (iii) characteristic boundary conditions, which enabled accurate specification of waves travelling in both directions across the solution domain boundaries were introduced. With the help of these boundary conditions a classical variable area duct flow test case (Barton 1985) showed that accurate prediction of transmission and reflection coefficients, as well as accurate prediction of the influence of an entropy wave generating an acoustic wave in a variable cross-section duct flow was achieved for a wide range of mean flow Mach numbers as well as for various frequencies of sound wave using the developed method.

Following on from the simple validation tests discussed above, transient simulations were carried out in order to calculate the acoustic absorption coefficient for a practically relevant configuration, namely an orifice with bias flow. A URANS k-ε model formulation was adopted incorporating the mildly compressible method. The predicted absorption co-efficient matched well with the experimental measurements of Rupp et al. (2010). For the case of zero bias flow, due to flow reversal inside the orifice, vortex structures were formed for all excitation sound amplitude levels. The level of absorption was closely related to the strength of the shed vortices. The strength of these structures attained an asymptotic value (as also

observed by Rupp et al. (2010)) which leads to non-linear behaviour of the absorption coefficient. With bias flow, flow reversal takes place only above a certain sound amplitude level and the acoustic excitation amplitude at which this occurred was well predicted. It was also observed that at higher amplitude levels the transmitted acoustic waves were no longer of pure sinusoidal form, instead, as observed by Rupp et al. (2010), Howe (1998) and others, these waves contained higher harmonic components, evidence of non-linear acoustic effects.

Finally, the capability of the method was demonstrated via analysis of the acoustic wave excitation of a combustor external aerodynamic flowfield as represented by a pre-diffuser and dump diffuser system. Various acoustic frequencies, each corresponding to a flow characteristic time scale in the dump region of the system, were analysed. It was found that the acoustic wave frequency corresponding to the transit time of a particle within the curved shear layer on the edge of the corner dump re-circulation had the most sensitive effect on the flow response. This finding matched with experimental work in a similar but more complex configuration (Regunath et al. 2010). At this frequency, merging of the primary vortex structure with an acoustically formed secondary vortex structure shed from pre-diffuser exit lead to amplified spatial oscillations in the flow re-attachment point on the outer wall of the annulus. In addition, at this preferred frequency, when the acoustic boundary condition at pre-diffuser inlet was changed the dynamical flow structure showed significant variation, although time prevented a complete analysis of these effects.

On the basis of the work presented here it is concluded that the methodology shows considerable promise for incorporation into pressure-based CFD codes and for use in acoustic performance assessment relevant to combustors, such as passive damper designs and external aerodynamics sensitivity assessment.

6.2 FUTURE WORK

Further Validation:

Even though concrete validation of the mildly compressible algorithm was presented in this work using a wide range of acoustic excitation conditions (in both linear and non-linear regimes), only acoustic wave frequencies up to 300 Hz were tested. Further validation is necessary for higher acoustic frequencies (> 1 kHz) to provide a complete validation of the mildly compressible algorithm; this would also result in a widening of the range of applications for simulating acoustic behaviour.

Similarly, the reason for the numerical divergence when using an acoustically open inlet condition in the dump diffuser flow needs further investigation; possible time-step alterations

or inadequate in-step iterations (or using PISO method) for the implicit solver are aspects that could be examined.

Further Development:

At present only plane acoustic wave excitation has been considered. The possibility of input of spinning waves or combined axial/spinning waves should be investigated. This would require modifications of the characteristic boundary condition implementation described here, following suggestions of Hirsch (1988) or Poinsot et al. (2005). In addition, the present work has not addressed Large Eddy Simulation (LES) formulation of the mildly compressible methodology. Use of LES to resolve turbulence could reveal more of the fundamental mechanisms of vortex formation, convection and merging in dump diffuser external aerodynamics. A key requirement which has to be addressed for a LES formulation is a methodology to separate acoustic fluctuations from mean and turbulent (stochastic) fluctuations. This decomposition is essential for successful use of the characteristic boundary condition approach in LES. Kopitz et al. (2005) have proposed a method, which enables separation of acoustic and turbulence fluctuations by identifying the acoustic as a perturbation which propagates at the speed of sound; this approach should be explored for the current method.

Further Application:

Based on the encouraging agreement between experiments and CFD prediction presented in this work, more complex flow problems should now be analysed, for example by considering a fully-featured combustion system such as used by Regunath et al. (2010). Also, gas turbine manufacturers have observed that some fuel injectors are more susceptible to thermo-acoustic combustion instability than other. Since injectors feature complex internal flow geometry and strong swirl flows, it would be of great interest to apply the mildly compressible algorithm to carry out a detailed study of dynamical flow structures excited by an input acoustic wave for different fuel injector geometries to identify the cause of injector sensitivity.

REFERENCES

Adams N.A., Shariff K.(1996), *A high resolution hybrid compact ENO scheme for shock-turbulence interaction problem*, J. of Comp. phy. 127, pp 27.

Anand, M. S., Zhu, J., Connor, C. and Razdan, M. K., (1999), *Combustor flow analysis using an advanced finite-volume design system*, ASME 99-GT-273.

Armitage C. S., Balachandran R., Mastorakos E. and Cant R.S, (2006), *Investigation of the nonlinear response of turbulent premixed flames to imposed inlet velocity oscillations,* Comb. and Flame, 146 (3), pp 419.

Baird S. (2001), *Computational modelling of fuel cell,* PhD Thesis, Loughborough University.

Barton J.P (1986), *Acoustic and entropy wave input-output relationships for quasi one-dimensional gas flows*, J. Acoust. Soc. Am 80(1), pp 340.

Bechert D.W, Michel U and PfizenmaierE, (1977), *Experiments on the transmission of sound through jets,* AIAA paper, 77-0135, pp 1278.

Bechert D.W, (1980), *Sound absorption caused by vorticity shedding demonstrated with a jet flow*, J. Sound. Vib., 70(3), pp 389.

Bellucci V., Flohr P., Paschereit C.O., Magni F .(2000), *On the use of Helmholtz resonators for damping acoustic pulsations in industrial gas turbines,* J of Eng Gas turbines and Power, 126(2), pp 271.

Bogey C., Bailly, C. (2004), *A family of flow dispersive and low dissipative explicit schemes for flow and noise computation*", Jnl. of Comp. Phys., 194, pp 194.

Branley N., Jones W.P. (1997), *LES of a turbulent non-premixed flame,* Proc. 11th TSF Symposium.

Candel S. (2002), *Combustion dynamics and control: progress and challenges*, Proc. Comb. Inst. 29, pp 1.

Chakravarthy S.R., Osher S, (1983), *High resolution applications of the Osher upwind scheme for the Euler equations,* AIAA Paper, 83-1943, pp 363.

Chong L T W., Komarek T., Kaess R., Foller S., Polifke W, (2010), *Identification of flame transfer functions from LES of a premixed swirl burner*, ASME Turbo Expo, GT2010-22769.

Choi D., Merkel C.L.(1985), *Application of time iterative schemes to incompressible flow*, AIAA J, 23(10), pp 1518.

Choi Y.H., Merkle C.L. (1993), *The application of preconditioning in viscous flows,* J. of Comp. Phys, 105, pp 207.

Crocco L., Cheng S.(1956), *Theory of combustion instability in liquid propellant rocket motors*, Butterworths Scientific.

Colonius T. (2004), *Modeling aritificial boundary conditions for compressible flow*, Annual Rev. Fluid Mechanics, 36, pp 315.

Cummings A, (1986), *Transient and multiple frequency sound transmission through perforated plates at high amplitude*, J. Acoust. Soc. Am., 79, pp 942.

Denman P.A., Barker A.G., Jayatunga, C.W., McGuirk J.J.(2003), *Modelling and measurements of combustor cooling tile flows*, ASME GT-2003-38793.

Dianat M., Yang Z., Jiang D., McGuirk J.J. (2006), *LES of scalar mixing in a coaxial confined jet,* Flow Turb. Comb., 77, pp 205.

Dowling A.P. (1995), *The calculation of thermoacoustic oscillations,* J. of Sound and Vib., 180(4), pp 557.

Dowling A.P., Stow S.R. (2003), *Acoustic analysis of Gas turbine combustors,* J of Prop. and Power, 19(5), pp 751.

Ducruix S., Schuller T., Durox D, (2003), *Combustion dynamics and instabilities: Elementary coupling and driving mechanisms*, J. Prop. and Power, 19, pp 722.

Dupere I.D.J., Dowling A.P. (2005), *The use of Helmholtz resonators in a practical combustor*, J of Eng for Gas Turbines and Power, 127, pp 268.

Durbin, P. A. (1996), *On the k-ε stagnation point anomaly*, Int. Jnl. of Heat and Fluid Flow, 17, pp 17.

Eldredge J.D., Dowling A.P. (2003), *The absorption of axial acoustic waves by a perforated liner with bias flow*, J. Fluid Mech, 485, pp 307.

Eldredge J.D., Bodony D.J. and Shoeybi M. (2007), *Numerical investigation of the acoustic behaviour of multi-perforated liner*, 13th AIAA/CEAS Aeroacoustics Conference, AIAA 2007-3683.

Engquist B., Majda A. (1977), *Absorbing boundary conditions for the numerical simulation of waves*, Math. Comp., 31, pp 629.

Ferziger J.H., Peric M.(2002), *Computational methods for fluid dynamics,* Springer-Verlag.

Ffowcs Williams, J.E, (1972), *The acoustics of turbulence near sound absorbent liner, J. Fluid Mech*., 51, pp 737.

Fischer, A., Bake, F., Roehle, I, (2008), *Broadband entropy noise phenomena in a gas turbine combustor*, ASME GT2008-50263.

Foller S., Kaess R., Polifke W, (2010), *Determination of acoustic transfer matrices via LES system identification*, AIAA/CEAS Aeroacoustic Conference, AIAA-2010-3998.

Gharib, M., Rambod, E., Shariff, K.(1998), *A universal time scale for vortex ring formation*, J. of Fluid Mech., 360, pp 121.

Harlow F.H., Amsden A.A. (1968), *A numerical fluid dynamics calculation method for all flow speeds*, J. of Comp. Phys, 8, pp 197.

Harten A, (1983), *High resolution schemes for hyperbolic conservation laws,* J. of Comp. Phys., 49, pp 357.

Harten A., Engquist B., Osher S ., Chakravarthy J. (1987), *Uniformly High Order Accurate Essentially Non-oscillatory Schemes,* J. of Comp. Phys, 71, pp 231.

Hedstrom G.W. (1979), *Nonreflecting boundary conditions for nonlinear hyperbolic systems*, J. of Comp. Phys., 30, pp 222.

Hesthaven J.S. (1998), *On the analysis and construction of perfectly matched layers for the linearized Euler equations*, J of Comp. Phys., 192, pp 129.

Hinze J. (1975), *Turbulence*, McGraw Hill, Second edition.

Hirsch C, (1988), *Numerical computation of internal and external flows*, vol 1 and 2, Wiley and sons.

Howe M.S. (1979), *On the theory of unsteady high Reynolds number flow through a circular aperture*, Proc. Roy. Soc. A, 366, pp 205.

Howe M.S, (1995), *Damping of sound and vibration of flow nonlinearity in the apertures of a perforated elastic screen*, IMA J. of App. Math., 55, pp 221.

Howe M.S. (1998), *Acoustics of fluid structure interactions*, Cambridge University Press.

Hu F.Q. (1996), *On absorbing boundary conditions for linearized Euler equations by a perfectly matched layer*, J of Comp Phys., 129, pp 201.

Huang X., Page G., Horner J., McGuirk J.J.(1998), *CFD prediction of aerofan acoustics,* Dept of Aero and Automotive Eng, Loughborough University (internal report).

Hughes I.J and Dowling A.P, (1990), *The absorption of sound by perforated linings*, J. Fluid Mech., 218, pp 299.

Ingard U, and Ising H, (1967), *Acoustic nonlinearity of an orifice*, J. Acoust. Soc. Am., 42, pp 6.

Ingard U, (2008), *Notes on Acoustics*, Infinity Science Press.

IPCC. (1999), *Aviation and the global atmosphere*, Special report.

Issa R.I, (1985), *Solution of the implicitly discretised fluid flow equations by operator-splitting,* J Comp. Phys., 62, pp 40.

James S., Anand, M. S., Sekar, B. (2008), *Towards improved prediction of aero-engine combustor performance using Large Eddy Simulations*, ASME GT2008-50199.

Jiang G.S., Shu C.W.(1996), *Efficient implementation of Weighted ENO schemes,* J. of Comp. Phys, 126, pp 202.

Jones W.P., Launder B.E, (1972), *The prediction of laminarisation with a two-equation model of turbulence,* Int. J. Heat and Mass Trans., 15, pp 301.

Johnsen E., Colonius T.(2006), *Implementation of WENO schemes in compressible multicomponent flow problems*, J. of Comp. phys. 219, pp 715.

Karki K.C., Patankar S.V.(1989), *Pressure based calculation procedure of viscous flows at all speeds in arbitrary configurations*, AIAA J, 27(9), pp 1167.

Klein R.(1995), *Semi-implicit extension of a Godunov-type scheme based on low mach number asymptotics 1: one dimensional flow*, J of Comp. Phys., 121, pp 213.

Kim J., Moin P.(1985*), Application of a fractional step method to incompressible Navier-Stokes equations*, J of Comp. Phys., 59, pp 308.

Kopitz J., Brocker E., Polifke W, (2005), *Characteristics-based filter for identification of planar acoustic waves in numerical simulation of turbulent compressible flow,* 12th Int. Cong. Sound and Vibration, 393, Lisbon.

Lax P.D, (1973), *Hyperbolic systems of conservation laws and the mathematical theory of shock waves,* SIAM Ser. Appl. Math., 11, pp 202.

Lee J,G., Santavicca D.A. (2003), *Experimental diagnostics for the study of combustion instabilities in lean premixed combustors*, J. Prop. and Power, 19, pp 735.

Lefebvre A.H.(1998), *Gas turbine combustion,* Taylor and Francis, second edition.

Lefebvre A.H., Billal D.R. (2010), *Gas turbine combustion: Alternative fuels and emissions,* CRC press, thrid edition.

Leppington F.G, and Levine H, (1973), *Reflexion and transmission at a plane screen with periodically arranged circular or elliptical apertures*, J. Fluid Mech., 61, pp 109.

Lieuwen T., McManus K.(2003). *Introduction: Combustion dynamics in lean-premixed prevaporized (LPP) gas turbines*, J. of Prop. and Power, 19(5), pp 721.

Lieuwen T.C., Cho J.H, (2003), *Modeling the response of premixed flames due to mixtures ratio perturbations*, ASME Turbo Expo, GT-2003-38089.

Lieuwen T., Yang V. (Eds), (2005), *Combustion instabilities in gas turbine engines: Operational experience, Fundamental mechanisms and Modeling*, AIAA, Series 210.

Lighthill J.(1978), *Waves in Fluids,* Cambridge University Press.

Liu X.D., Osher S., Chan T, (1994), *Weighted Essentially Non-Oscillatory schemes,* J. Comp. Phys., 115(1), pp 200.

McGuirk J.J., Page, G.J.(1990), *Shock capturing using a pressure correction method*, AIAA Journal, 27, pp 1751.

McGuirk J.J., Spencer A. (2001), *Coupled and uncoupled CFD prediction of the characteristics of jets from combustor air admission ports*, ASME Jnl. of Eng. For Gas Turbines and Power, 123, pp 327.

McManus K., Poinsot T., Candel S. (1993), *A review of active control of combustion instabilities*, Prog. Energy Comb. Sci. 19. pp 1.

McManus K.R., Magill J.C., Miller M.F, (1998), *Combustion instability suppression in liquid-fueled combustors*, AIAA 98-0642.

McMurtry C.L., Jou W.H., Riley J.J., Metcalfe R.W.(1986), *Direct numerical simulations of a reacting mixing layer with chemical heat release*, AIAA J. 24, pp 962.

Mani R, (1976), *The influence of jet flow on jet noise – Part 1 The noise of unheated jets,* J. Fluid. Mech., 73, pp 753.

Manners A.P., Carrotte J.F, (1997), *Predictions and measurements in a two dimensional axisymmetric model dump diffuser,* Lougborough University Report, TT-97-R01.

Menon, S. and Patel, N. (2006), *Sub-Grid modelling for simulation of spray combustion in large-scale combustors*, AIAA Jnl., 44, pp 709.

Merkle C.L., Choi Y.H.(1988), *Computation of low-speed compressible flows with time marching procedures*, Int. J. Num. Methods for Eng., 25, pp 293.

Moin P. (2001), *Fundamentals of engineering numerical analysis*, Cambridge University Press.

Moureau V., Berat C., Pitsch H.(2007), *An efficient semi-implicit compressible solver for LES,* J. of Comp. Phys, 226, pp 1256.

Noiray N., Durox D., Schuller T., Candel S. (2007), *Passive control of combustion instabilities involving premixed flames anchored on perforated plates*, Proc. Comb. Ins., 31, pp 1283.

Patankar S. V., Spalding, D. B. S. (1972), *A calculation procedure for heat, mass, and momentum transfer in 3D parabolic flows*, Int. J. Heat and Mass Transfer, 15, pp1767.

Paschereit C.O., Gutmark, E., Weisenstein, W. (1999), *Control of Combustion-Driven Oscillations by Equivalence Ratio Modulations*, ASME TURBO EXPO, 99-GT-118.

Preetham S., Lieuwen T, (2007), *Response of Turbulent premixed flames to harmonic acoustic forcing*, Pro. Comb. Inst., 31, pp 1427.

Pope S.(2000), *Turbulent flows,* Cambridge University Press.

Poinsot T., Lele S. (1992), *Boundary conditions for direct simulations of compressible viscous flows*, J of Comp. Phys., 101, pp 104.

Poinsot T., Veynante D(2005), *Theoretical and Numerical Combustion,* Edwards.

Rayleigh, Lord, (1945), *The theory of sound, vol. 2*, Dover Publications.

Rehman S.F., Eldredge J.D. (2007), *Numerical investigation of a bias flow perforated liner for damping of thermoacoustic instabilities*, ASME Turbo Expo, GT2007-27319.

Regunath G.S., Carrotte J.F., Rupp J, *External aerodynamic acoustics in lean systems,* 18th Annual Report, University Technology Centre, Loughborough University, July 2010.

Rhie C.M., Chow W.L.(1983), *Numerical study of the turbulent flow past an airfoil with trailing-edge separation*, AIAA Journal, 21, pp 125.

Richards G.A., Yip M.J., Robey E., Cowell L., Rawlins D.(1997), *Combustion oscillation control by cyclic fuel injection,* ASME J Eng. Gas turbine power, 119(2), pp 340.

Roe P.L, (1981), *Approximate Riemann solvers, parameter vectors and difference schemes,* J. Comp. Phys., 43(2), pp 357.

Rudy D., Strikwerda J, (1980), *A non-reflecting outflow boundary condition for subsonic Navier-Stokes calculations,* J. Comp. Phys., 36, pp 55.

Rupp J., Carrotte J.F., Spencer, A, (2010), *Interaction between the acoustic pressure fluctuations and the unsteady flow-field through circular holes*, ASME Jnl. of Eng. For Gas Turbines & Power, 132, pp 06150-1.

Schuller T., Ducruix S., Durox D., Candel S. (2002), *Modeling tools for the prediction of premixed flame transfer functions*, Pro. Comb. Ins., 29, pp 107.

Selle, L., Lartigue, G., Poinsot, T., Koch, R., Schildmacher, K-U., Krebs, W., Prade, B., Kaufmann, P., and Veynante, D. (2004), *Compressible Large Eddy Simulation of turbulent combustion in complex geometry on unstructured meshes*, *Combustion and Flame*, 137, pp 489.

Shu C W.(1997), *Essentially non-oscillatory and weighted essentially non-oscillatory schemes for hyperbolic conservation laws*, NASA, ICASE Report No 97-65.

Snyder, T. S., Stewart, J. F., Stoner, M. D. and McKinney, R. G. (2001), *Application of an advanced CFD-based analysis system to the PW6000 Combustor to optimise exit temperature distribution – Part II: comparison of predictions to full-annular rig test data*, ASME 2001-GT-64.

Sreenivasan K.R., Raghu S.(2000), *The control of combustion instability: A perspective,* Current Science, 79, pp 867.

Steele R.C., Cowell L.H., Cannon S.M., Smith C.E, (2000), *Passive control of combustion instability in lean premixed combustors*, J. Eng. Gas Turbines and Power, 122, pp 412.

Tang G., Yang Z., McGuirk J.J.(2004), *Numerical methods for LES in general co-ordinates,* Int. J. Numerical Methods in Fluids, 46, pp 1.

Tam C.K.W., Webb J.C.(1993), *Dispersion-relation-preserving finite difference schemes for computational acoustics*, J. of Comp. Phys., 107, pp 226.

Tam C.K.W., Webb J.C., Dong Z.(1993), *A study of the short wave components in computational acoustics,* J . Comp. Acoustics, 1, pp 1.

Tam C.K.W., Hardin J.C, (Eds), (1997), *Second computational aeroacoustics workshop on benchmark problems*, NASA CP-3352.

Tam C.K.W., Kurbatskii K.A, Ahuja K.K, and Geeta R.J. (2001), *A numerical and experimental investigation of the dissipation mechanisms of resonant acoustic liners*. J. Sound & Vib., 245(3), pp 545.

Venakataraman K.K., Preston L.H., Simons B.J., Lee J.G., Santavicca D.A. (1999), *Mechanism of combustion instability in a lean premixed dump combustor*, J. Prop. & Power, 15(6), pp 909.

Wall C., Pierce C.D., Moin P.(2002), *A semi-implicit method for resolution of acoustics waves in low Mach number flows*, J. of Comp. Phys., 181, pp 545.

Wagner C., Huttl T., Sagaut P (Eds), (2007), *LES for acoustics,* Cambridge University Press.

Wendoloski J.C, (1998), *Sound absorption by an orifice plate in a flow duct.* J. Acoust. Soc. of Am., 104(1), pp 122.

Whitham G.B, (1974), *Linear and Non-Linear waves*, John Wiley Publications.

Williams F.A, (1985), *Combustion Theory*, Westview Press.

www.rolls-royce.com

www.acare4europe.com

www.iata.org

www.nasa.gov

www.ipcc.ch